Thesis
about the topic

Nanomechanics of Li-ion battery materials

Submitted by
Hugues-Yanis Amanieu
Born December 12, 1987
in Grande-Synthe, France

Presented to the Faculty of Engineering of
the University of Duisburg-Essen
for award of the academic degree of
Doctor of Engineering (Dr.-Ing.)

on July 23, 2015
&
defended on October 20, 2015

1st rapporteur:	Prof. Dr. rer. nat. habil. Doru C. Lupascu	Institut für Materialwissenschaft
2nd rapporteur:	Prof. Dr. Marc Kamlah	KIT
Examiners:	Prof. Dr.-Ing. habil. Jörg Schröder	
	Prof. Dr. rer. nat. Angelika Heinzel	
Industrial supervision:	Dr. Daniele Rosato	Robert Bosch GmbH

Abstract

Active materials used in lithium ion batteries consist of micro-metric ceramic particles. Mechanical failure can happen within these brittle particles due to large internal stresses provoked by lithium intercalating in the crystalline structure during charge and discharge. Their mechanical behavior is directly related to some key intrinsic parameters, namely the elastic modulus, the fracture toughness and lithium diffusivity.

This works deals with the development of new characterization techniques to quantify these parameters at the local scale. Obtaining quantitative measurements is notably challenging for this type of specimen due to the highly heterogeneous structure of battery electrodes. For this, spinel $LiMn_2O_4$-based commercial cathodes are proposed as material of investigation.

First, composition analysis of cathode materials at different states of charge was done. In general it was noticed that commercial cells are not as consistent as laboratory cells: impurities are often present (Ni, Co,...) and particles can be porous agglomerates of nanoparticles as well as large single grains. However only spinel structure was detected by X-ray diffraction and Rietveld analysis showed a typical lattice expansion for higher lithium concentrations.

A method using nanoindentation was developed. It consists of applying a large number of indents in cathode cross-sections and subsequently filtering the measurements depending on whether they fit the set of hypotheses of the Oliver and Pharr method. It was observed that for decreasing lithium concentrations, the elastic modulus and the hardness increase from 87 GPa (0% State of Charge) to 104 GPa (100% SoC) and from 7.0 GPa (0% SoC) to 8.0 Gpa (100%SoC), respectively. With the help of contact-resonance atomic force microscopy, the elastic property could also be qualitatively mapped and it seems that the particles are homogeneous. Added to micro-raman spectroscopy, it was observed that neighboring particles can have different lithiation levels.

The fracture toughness was estimated by measuring the crack opening displacement by atomic force microscopy and applying Irwin's near field theory. A toughness of about 0.9 $MPa{\cdot}m^{1/2}$ was found but should not be taken at face-value. Irwin's theory requires a purely elastic-brittle fracture with traction-free crack walls. Unfortunately this condition cannot be met due to the size of the particles and the toughness is surely overestimated. Associated with electron backscattered diffraction, cleavage planes were also evaluated on a reference {111} wafer. It was found that cracks always propagate in the $<121>$ direction, corresponding to {101} planes just below the surface. At higher depths (> 100 nm), the crack deviates of 30 to 40°.

The last part of this work consists of developing a model to better comprehend electrochemical strain microscopy "time spectroscopy" (ESM-TS). It is the most promising technique to quantify locally ionic diffusion coefficients. An AFM cantilever is used to measure the mechanical excitation induced by lithium ions, themselves excited by an alternative current applied to the tip. The cantilever amplitude is recorded after applying a short electric potential pulse. The change in the lithium concentration field induced by the pulse has an impact in the change of the measured amplitude. If the physics binding these two events is better understood, this technique can be used to measure the diffusivity. The model draw the attention on the origin of the signal: while the pulses can change locally the concentration, our hypothesis is that it is not the case during the AC excitation, hence the signal does not originate from Vegard's deformation as originally thought. It is suggested that the signal is dependent on the Lorentz force applied on the ions by the AC excitation. We could demonstrate that the model can fit experimental data. Besides, we introduced an effective diffusion coefficient which is dependent on the lithium concentration and showed that some experimental observations can be explained with it. However we could not explain the exact physics behind ESM-TS and only pointed at some new research directions.

Contents

List of Figures

List of Tables

Acknowledgments

While I was a student at the University of Duisburg-Essen (UDE), this work has been mainly undertaken in the laboratories of the Corporate Research Department of Robert Bosch GmbH in Stuttgart, Germany. The research was supported by the European Commission within FP7 Marie Curie Initial Training Network "Nanomotion" (grant agreement n. 290158, www.nanomotion.eu). I am much obliged to these three institutions (the European Commission, Bosch and UDE) for giving me the chance to progress as a person by acquiring an international experience, industrial insights and the academic grade of Doctor of Engineering.

I am deeply grateful to my academic supervisor (Doktorvater), Prof. Doru C. Lupascu, and my first direct manager, Dr. Jan Goehler (Robert Bosch GmbH), for admitting me to this position. I am much obliged to Prof. Lupascu for the bi-annual meetings with the rest of his group and the fruitful discussions.

I would like to thank first and foremost Dr. Daniele Rosato for guiding me during the past years, for his patience and our discussion sessions. His input was very valuable in every step of my research from the smallest details to the bigger picture. His guidance extended the sole frame of my thesis and I am very thankful for that.

Sie haben mir bei der Probevorbereitung und Mikroskopie geholfen und waren auch sehr geduldig mit meinen Deutschkenntnissen (die zu katastrophalen Misverständnissen hätten führen können): Herzlichen Dank an Frau Ingrid Würhl und ihr Team Hans, Ulrike und Sven. Ich bedanke mich bei Dr. Frank Felten, meinem zweiten Vorgestezten, der immer für mich da war und mir erklärt hat, wie man Bruchzähigkeit mit einem AFM messen kann. Ich muss mich außerdem bei unseren Kollegen von der Analytik bedanken, ohne die alle Proben immer noch unbekannt wären: Herr Stefan Hinderberger mit EBSD, Dr. Nils Salingue mit dem AFM, Dr. Christiane Müller, Dr. Lars Epple und Dr. Thomas Köhler mit XRD, Dr. Malte Rolff mit Raman und Herr Stefan Tenhagen mit ICP-OES. Ich bedanke mich bei allen meinen Kollegen und Mitdoktoranden von Bosch, die mich unterstützt haben.

I am especially thankful to Prof. Kholkin from the University of Aveiro (UA), Portugal, for organizing the Nanomotion project. I must acknowledge him also for hosting me in UA during the last part of my thesis in order to further work on the Electrochemical Strain Microscopy model depicted in part V.

I would like to thank Dr. Marco Sebastiani from the University of Roma Tre, Italy. He was present from the beginning of the thesis and his background concerning nanoindentation helped me a lot with developing a method we called selective nanoindentation. He co-authored 2 articles with me and he organized a wonderful workshop in Rome led by Prof. Pharr on Nanoindentation. All of the work with focussed-ion beam was carried out by him or his students.

I greatly appreciate working with Dr. Ute Rabe and Dr. Leonardo Batista from the Fraunhofer Institut of Saarbrücken (IZFP). All the work using Atomic Force Accoustic Microscopy was carried out in IZFP with them and I hope we will keep further in touch after my PhD.

I must thank my Master student, Mohammad Aramfard, for he was here to further use *selective nanoindentation* (see part IV) on so many samples. His work was used in one of my papers. Our relationship was based on exchange and I learned as much from him than he from me and not only in Science, but also in life and geopolitics.

I need to thank all of my colleagues from the Nanomotion network as it was always a pleasure to meet them in the different places in Europe where our project meetings took place. I must particularly thank my dearest colleagues Mr. Sergey Luchkin and Mr. Huy Thai. We contributed together to better understanding ESM which led to an article. Our relationships will last beyond Nanomotion and that is frankly the real success of such projects.

I should also mention two websites that were rich in information despite little mention, or even disregard, in the scientific community: Wikipedia for being a good introduction to many technical knowledge and Stack Overflow for its rich community.

J'aimerais remercier mes parents et surtout mes frères. Du Canada, du Maroc, de l'Allemagne, du Portugal ou de la France, nous avons été si loins les uns des autres et pourtant sommes nous restés si proches.

Last but not least, I am so happy to have met such a wonderful clique of friends and my beloved Marion in Stuttgart. They helped me getting the most of this new cold land and cheered me up before I would get disheartened.

To future international students coming to Stuttgart I would like to say: behind its soulless Porsche cars and unsightly banks and shopping malls, this city has a lot of hidden treasures that only ask to be discovered.

Introduction

In the context of increased mobility and the change of energy sources, a need for robust energy storage solutions has been growing in the past decades. Lithium-ion batteries (LiBs) have been an excellent commercial candidate for small transportable devices such as laptops, cellphones and wireless tools. Their use is currently being extended to more heavy-duty applications such as in the automotive industry. It has already proven its utility in short-range electric vehicles and hybrid electric vehicles. They are still lacking many benefits of the vehicles powered by internal combustion engines in terms of fuelling time, mileage and lifetime. Mileage is thought to be extended by approaching different chemistries and design in order to increase the energy density. The time of charge can be reduced by developing batteries with limited capacity fade during fast charge and hence with more power density. In order to have a longer cycle life, fatigue phenomena during cycling must be better understood and corrected. One effect common to many different chemistries used in LiB is a mechanical fatigue activated by the multiple loads induced by lithiation and delithiation of lithium ion hosts.

In this research, mechanical and ionic characterization methods of LiB active materials are investigated to better comprehend the origin of the fatigue. This activity has been carried out within the frameworks of (1) an industrial project called *ReLiOn*, funded by the German Federal Ministry of Education and Research and lead by Robert Bosch GmbH and of (2) an academic program funded by the European Commission under the Initial Training Network called *Nanomotion*. The former targets at improving the cycle life of LiB by simulating local mechanical failure with finite element modeling (FEM). For this purpose, three important properties need to be quantified: (a) the elastic modulus, (b) the fracture toughness and (c) lithium diffusivity. The second project is similar in many ways as it addresses new methods for the characterization of battery materials at the nanoscale in order to obtain a more thorough knowledge of micro- and nanomechanical effects and lithium diffusion mechanisms. This is done in close collaboration with the university of Aveiro where electrochemical strain microscopy (ESM) is used to characterize lithium diffusivity.

The proposed material of study is spinel lithium manganese(III,IV) oxide ($LiMn_2O_4$), which is used in positive electrodes (aka cathodes). Spinel $LiMn_2O_4$ is an interesting commercial material thanks to its low cost and low toxicity. One of its main drawbacks is its short lifetime. The main issue is that $LiPF_6$-based electrolyte dissolves manganese ions by interacting with the surface of $LiMn_2O_4$ particles. Another issue is the introduction of cracks in the particles by the multiple loading/unloading cycles of lithium ions. It leads to more surface area in contact with the electrolyte and more importantly can lead to the loss of electrical contact with the current collector.

The goal of this work is to bring new characterization methods to qualitatively and quantitatively measure the elastic properties (a) and fracture toughness (b) of lithium ion host particles. Due to the structure of electrodes, the main challenge lies in measuring highly heterogeneous sample where the phase of interest, the active particles, are too small for traditional techniques (around 10 µm). In a different approach, lithium diffusivity (c) was not directly studied as experimental measurements were already carried out by the University of Aveiro. Instead an FEM model was developed in order to better understand the mechanisms behind the tool used in Aveiro. The plan was to to bring together knowledge with modeling developed by Robert Bosch GmbH and Karlsruhe Institute of Technology, notably through the work of Dr. Bohn (Bohn 2011), and, on the other hand, experimental expertise of the University of Aveiro.

In part I, the functioning of LiB will be first described. Then the state of the art concerning the properties of $LiMn_2O_4$ will be more precisely reviewed. The main instruments used during the preparation of the thesis will be thereafter detailed. Nanoindentation will be first described and then the theoretical model used to obtain quantitative measurements, the Oliver and Pharr method. Afterwards general information concerning atomic force microscopy (AFM) will be outlined before further developing on contact-resonance atomic force microscopy (CR-AFM), ESM and the measurement of fracture toughness by AFM.

In part II, the goals of the research will be listed.

part III describes the experiments. It will start by describing sample preparation. Then the different analysis methods used will be depicted followed by a description of the nanoindenter and the different AFMs used.

part IV involves *selective nanoindentation*, a method that was specifically developed in order to obtain quantitative data from indentation in highly heterogeneous composites.

part V deals with the modeling of the working principle of ESM. The thermodynamics behind the model will be detailed as well as the boundary conditions and the COMSOL model.

In part VI, the results will be listed in 4 parts: the first one will deal with chemical characterization of the samples, the second one will deal with the measurements of elastic properties and the indentation hardness of $LiMn_2O_4$, the third one will deal with the fracture toughness of $LiMn_2O_4$ and the last one will deal with the output of the FEM model and how well it fits experimental data. The different results will be also discussed in this section.

In part VII the different methods used to characterize heterogeneous samples will be comparatively analyzed . Then the origin of the ESM signal will be discussed. Finally, there will be a discussion on the global properties of $LiMn_2O_4$ extracted from the different methods.

In the conclusion, there will be a general outlook intended for people working on modeling battery systems. A perspective concerning nanoscale characterization of electrochemical materials will also be given.

Part I

Theoretical background

1 Chapter

Lithium-ion battery

A battery is a device made out of several electro-chemical cells that stores chemical energy while charging and convert it into electrical energy while discharging. There are two kinds of batteries: primary batteries can only convert chemical potential into electricity; secondary batteries are however rechargeable as it is possible to restore the initial chemical potential by applying an opposite current. Lithium-ion batteries (LiBs) have a commercial advantage as compared to other chemistries: there is no memory effect (loss of capacity due to an unfinished cycling), they have a high specific energy density (>100Wh·kg^{-1}), and a good efficiency (99 %) (SCROSATI AND GARCHE 2010).

Commercialized for the first time by Sony in 1990 (BRODD 2009), its application was for a long time limited to gadgets with a short life span such as cellphones or MP3 players. Due to an increasing interest from the automotive industry, multiple designs and chemistries have been developed to stretch its power density and cycle life.

This chapter deals with the functioning of LiBs in general. Then the key material parameters of mechanical fatigue are introduced, around which this thesis has been built. Last, a closer look is brought into one of the most used cathode chemistries: spinel $LiMn_2O_4$.

1.1 Working principle

A typical LiB consists of several elements. A negative electrode stores the lithium ions when fully charged. During charge, the negative electrode reduces. During discharge, it oxidizes. It is more commonly called the anode, even though this term is erroneous as it is not always oxidizing. The most commercialized chemical is graphite, where lithium ions are inserted between graphene sheets. The following reaction takes place during charge and discharge:

$$\mathrm{C_6(s)} + x\mathrm{Li^+} + x\mathrm{e^-} \xrightleftharpoons[\text{discharge (ox)}]{\text{charge (red)}} \mathrm{Li}_x\mathrm{C_6}. \tag{1.1}$$

The lithium ions are inserted during discharge into the positive electrode, where the opposite reaction takes place. As for the positive electrode, it is more commonly called the cathode, even though this term is as well erroneous as it is not always reducing.

They are usually made of a metal oxide of the form $\mathrm{Li}_x\mathrm{M}_y\mathrm{O}_2$, where M represents a transition metal such as Co, Ni or Mn (Park et al. 2010). On this side, the following reaction occurs:

$$\mathrm{M}_y\mathrm{O}_2(\mathrm{s}) + x\mathrm{Li}^+ + x\mathrm{e}^- \underset{\text{charge (ox)}}{\overset{\text{discharge (red)}}{\rightleftharpoons}} \mathrm{Li}_x\mathrm{M}_y\mathrm{O}_2. \tag{1.2}$$

These lithium host materials are usually in the form of micro-metric particles due to the ease of manufacturing and for a specific surface allowing a good ionic and electronic exchange. As for most oxides, electronic conductivity is similar to dielectrics and semiconductors. Cathode active materials are therefore mixed with percolated carbon black nano-powder. A binding polymer, usually Polyvinylidene fluoride (PVDF), is used to keep a certain mechanical stability and to act as a mechanical buffer. These mixtures are coated onto metallic collectors, in general aluminum on the positive side and copper on the negative side. These current collectors provide electron carriers from the electrodes to the terminals. An electrolyte provides an ion carrier between the two electrodes. It is in general a solution of LiPF_6 dissolved in mixed organic solvents such as dimethyl carbonate (DMC) and ethylene carbonate (EC) in a 1:1 ratio (DMC:EC). A porous separator, soaked by the electrolyte, electrically separates the two electrodes but is permeable to lithium ions. A schematic of the system can be seen in fig. 1.1.

An electromotive force is generated between the opposite electrodes as the system seeks a more stable (discharged) state. The system can be seen in thermodynamical terms:

$$\nabla \eta_{\mathrm{Li}} = \nabla \mu_{\mathrm{Li}} + z_{\mathrm{Li}} F \nabla \psi \tag{1.3}$$

where η_{Li} is the electrochemical potential, μ_{Li} is the chemical potential of lithium inside the hosting material, z_{Li} is the lithium ion charge (+1), F is Faraday's constant and ψ is the electric potential originating from an external active load during charge or a passive load during discharge. The electromotive force (EMF) comes from the difference of chemical potential μ_{Li} between the opposite electrodes (Huggins 2009, chapter 2, chapter 6). This difference of potential is referred to as the open-circuit voltage (OCV) when there is no external load and can be understood as follows:

$$\Delta\psi = \psi^{\text{anode}} - \psi^{\text{cathode}} = \frac{\mu_{\mathrm{Li}}^{\text{anode}} - \mu_{\mathrm{Li}}^{\text{cathode}}}{z_{\mathrm{Li}} F} \tag{1.4}$$

The potential difference $\Delta\psi$ tends to reduce upon discharge as the system tends to a more stable state. The profile of the voltage versus lithium concentration is not necessarily a strictly monotonous function. The chemical potential is derived from the Gibbs free energy as follows

$$\mu_{\mathrm{Li}} = \frac{\partial G}{\partial c_{\mathrm{Li}}}, \tag{1.5}$$

where G is the Gibbs free energy and c_{Li} is the concentration of lithium per $\mathrm{M}_y\mathrm{O}_2(\mathrm{s})$ unit. In some materials, the lithium host can experience a first-order phase transition

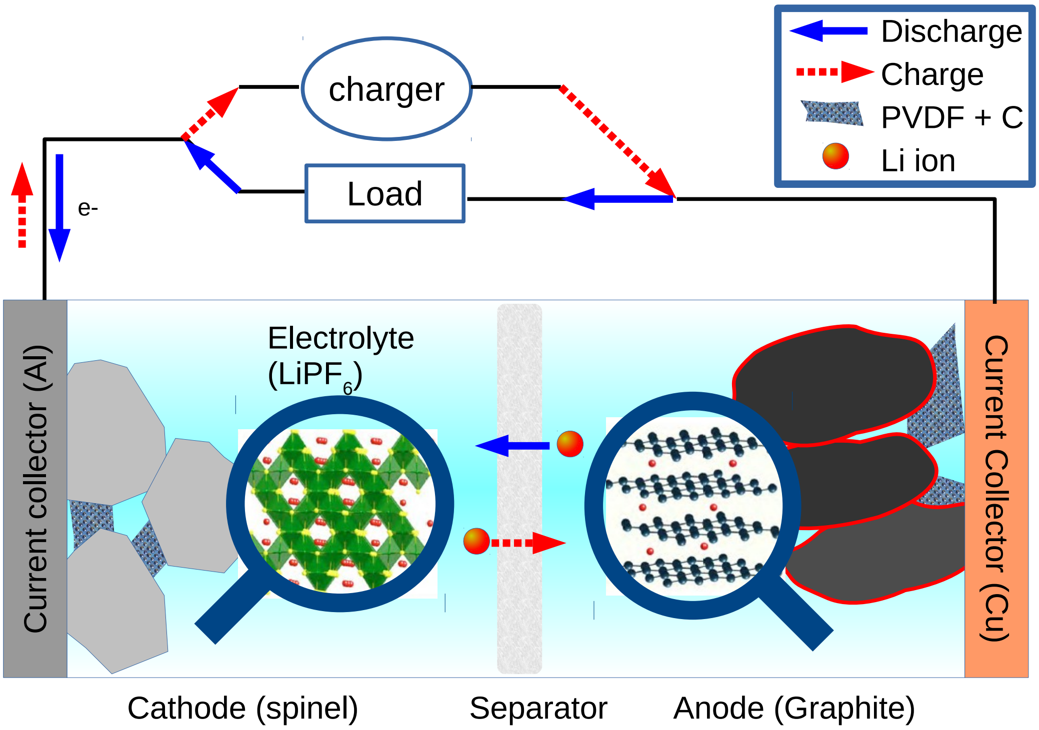

Figure 1.1: Operating lithium-ion battery. Readapted from Park et al. (2010).

to a new more stable phase upon lithiation. The material would experience a phase growing into the other one rather than a solid solution. The total free energy would linearly change between the two energy minima associated with each phase. Hence μ_{Li} will stay constant and so would the OCV. This phenomenon is illustrated in fig. 1.2. It is often more practical for commercial applications to have a regularly decreasing voltage so as a simple voltmeter can estimate the remaining capacity of the battery. Concerning the study of materials, obtaining the curve of the OCV versus lithiation concentration gives direct information about the thermodynamic properties of the materials (Van Der Ven et al. 2013).

The total capacity of the electrode is determined by the amount of reversible lithium it can store. The total energy can be simply calculated by multiplying the capacity by the average OCV. Increasing the total energy of the cell can either be done by finding a design with the highest potential or making materials that can store more lithium per unit volume/mass. In general, the chemical potential of pure metallic lithium is used as reference to characterize different chemistries. Figure 1.3 presents some material potentials versus lithium metal as well as their specific capacity (number of storable charges per mass unit). It can be observed how different chemistries can offer a variety

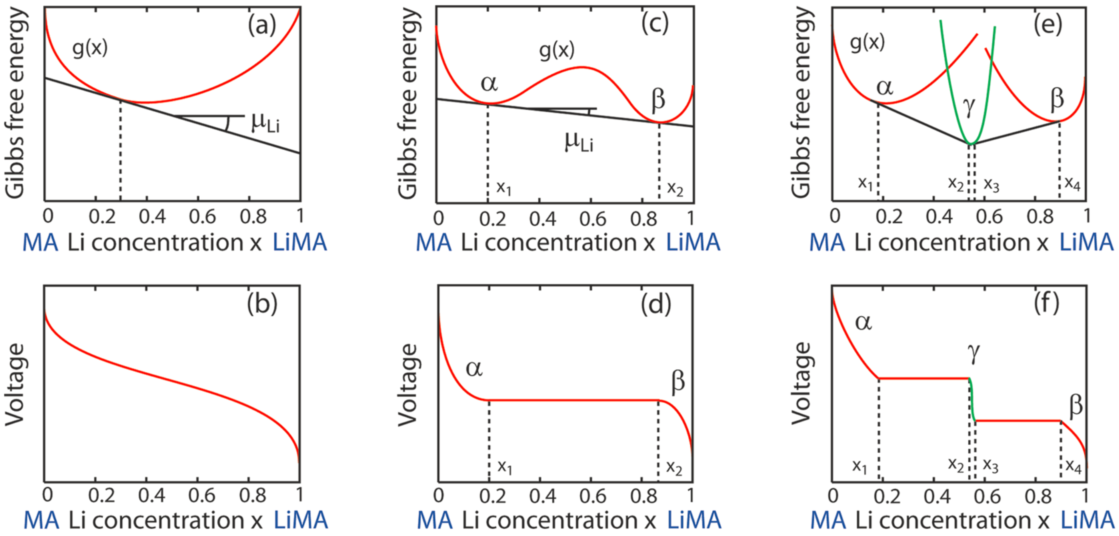

Figure 1.2: The influence of the Gibbs free energy on the voltage curve of lithium host materials upon infinitely slow (de)lithiation. Different curves are induced by the number of stable phases. From Van Der Ven et al. (2013). MA stands for the unit cell (M= Metal, A=Anion)

of specific capacity, with silicon anodes having the highest one. Besides $LiMn_2O_4$ has a relatively high potential versus lithium.

Finding the appropriate design is however not limited to maximizing the voltage or the specific capacity. The first design introduced by Sony in the 1990s consisted in graphite (-) versus lithium cobalt dioxide ($LiCoO_2$, +) because it was cheap to produce and had a relatively high voltage from 3 to 4.2V with a specific capacity of 140 $mAh \cdot g^{-1}$ (Yoshio et al. 2009, chapter 2). $LiCoO_2$ has a layered structure where lithium diffusion is facilitated in 2 dimensions. Cobalt stays a relatively expensive material and is a toxic heavy metal. It has been tried to replace it with nickel so as to reduce cost and toxicity. The specific gravity of this materials has been also showed to be higher, up to 200 $mAh \cdot g^{-1}$. However it is difficult to synthesize stoichiometric $LiNiO_2$, making it inaccessible to industrial scale production(Huggins 2009, chapter 9). This is due to a structural disorder where nickel ions take the place of lithium ions, limiting its electrochemical performance. Adding cobalt helps stabilizing the structure, but also aluminum and magnesium, structures found in the market. Olivine structures were also investigated and lead to commercial applications such as lithium iron phosphate ($LiFePO_4$). These structures only enable one-dimensional diffusion and can only be used in low power applications. They offer the advantage of being relatively inexpensive and stable upon cycling as oxygen ions are tightly bound to the phosphate. Spinel $LiMn_2O_4$ has been proposed as an alternative. Contrary to the previously discussed materials, it is based on the atomic ratios of 1:2:4 (Li:M:O) which turns into a smaller specific capacity. Spinel structure allows nonetheless a 3 dimensional diffusion path for lithium ions and hence offers a better specific power. Manganese is also less toxic than other transition metals and is more abundant(Brodd 2009). However its application is limited due to its short cycle life. The main reason is the slow manganese dissolution into the electrolyte upon cycling, leading to loss of material and structural disordering with a dramatic loss of capacity(Vetter et al. 2005). $LiMn_2O_4$ was selected as the material of study for this study and a more detailed description follows in section 1.3.

Lithium reacts easily with water. It can lead to serious safety issues as lithium hydroxide and flammable hydrogen are produced. The reactivity window of water versus lithium is [0−1.2] V, hence most materials with a potential versus lithium above 1.2V are stable. It is also sensitive to oxygen as it forms white lithium oxide in contact with air (explaining the white appearance of lithium metals) and to nitrogen, forming lithium nitride. For this reason, LiBs should be opened in a glove box with a controlled atmosphere, usually filled with argon. It is to be noted that most cathode materials, due to their high potential versus Li, are stable in air.

The electrolyte is often stable for a large potential window of [0−5]V versus Li(m). During the first cycle, a secondary electrolyte interface (SEI) is formed on the surface of the anode particles due to its instability with lithiated graphite. This new interface offers some protection to the particles against the corrosive electrolyte and is permeable to lithium cations (Vetter et al. 2005). However it can be destroyed and rebuilt upon cycling due to volume expansion, each time consuming some lithium in the process. It is believed to be one of the main reason for capacity loss on the negative electrode. SEI growth can happen also on the positive side, yet at a lower extend (Lei et al. 2005).

As graphite is relatively cheap and stable, most of the research has been therefore focused on improving cathode material although some new and promising high-energy anode chemistries based on lithium alloys (Si-Li or Sn-Li) have diverted some of this focus.

The cathode has been the principal origin of fatigue for the whole cell (Vetter et al. 2005). As there is a wide number of causes associated with it which occur in parallel, it is difficult to study them independently. A fraction of them has a mechanical origin in both positive and negative electrodes. On the one hand, they experience volume expansion upon lithiation which indicates that their immediate environment must accommodate with it. While the PVDF binder should act as an elastic buffer, irreversible electric contact loss can happen (Huggins and Nix 2000). On the other hand, lithium diffusion through the material create stresses which increase with increasing C-rates. This can drive to cracks (Wang 1999; Zhao et al. 2010) or structural change (Chan et al. 2007; Lin et al. 2011). The mechanism is simply described in the next section. Then a particular focus on spinel $LiMn_2O_4$ is brought in the last section of this chapter.

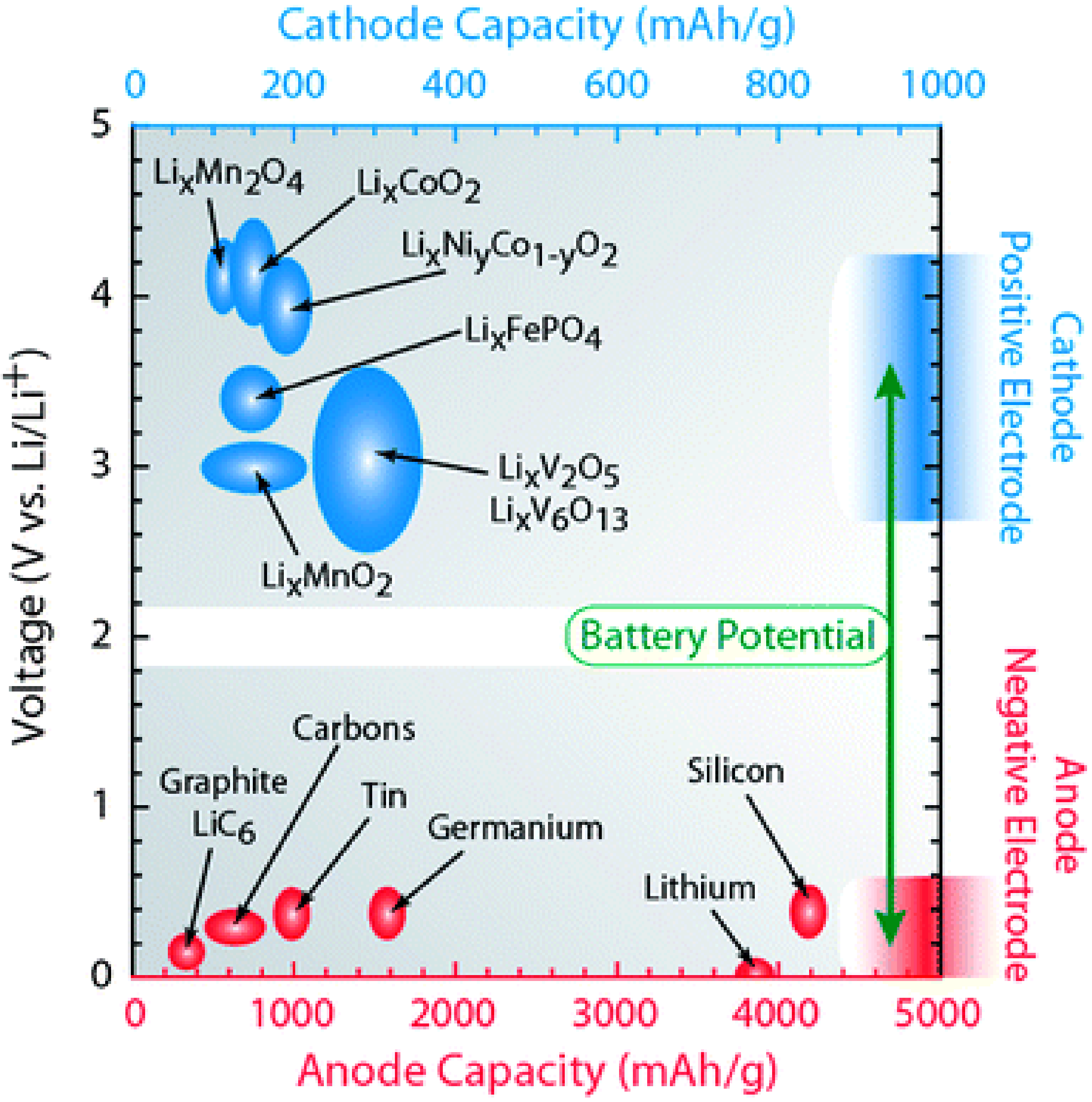

Figure 1.3: Various chemistries used as positive and negative electrodes in lithium-ion batteries. They are plotted in function of their chemical potential versus pure metallic lithium and in function of their specific capacity. From (Landi et al. 2009).

1.2 Origin of mechanical failure

This section gives an overview of the origin of mechanical fracture in active material. More importantly, it targets at demonstrating which are the fundamental material properties controlling failure, not at establishing a physical model.

Considering a uniaxial problem for simplicity, the stress σ originating from lithium intercalation can be understood as follows (readapted from Bohn et al. (2013)):

$$\sigma = E(\varepsilon - \Omega_{\mathrm{Li}}\left(c_{\mathrm{Li}} - c_0\right)), \tag{1.6}$$

where E is the isotropic Young's modulus, ε is the total strain, $\varepsilon_{\mathrm{Li}} = \Omega_{\mathrm{Li}}\left(c_{\mathrm{Li}} - c_0\right)$ is the strain induced by the lithium ions, $c_{\mathrm{Li}} = N/V_0$ is the concentration of lithium ions, with N being the number of lithium ions per unit volume V_0, and c_0 is the initial concentration. Ω_{Li} corresponds to the isotropic approximation of the partial molar volume: this is the parameter that controls lattice expansion upon insertion of lithium ions and is here constant. Without going further into the details, eq. (1.6) already shows that the stress is dependent on the lithium variation $(c_{\mathrm{Li}} - c_0)$.

The variation of c_{Li} is derived from Fick's law:

$$\begin{aligned} J_{\mathrm{Li}} &= -D_{\mathrm{Li}}\nabla c_{\mathrm{Li}} \\ \frac{\partial c_{\mathrm{Li}}}{\partial t} &= -\nabla J_{\mathrm{Li}}, \end{aligned} \tag{1.7}$$

where t is the time variable, D_{Li} is the diffusion coefficient binding the ionic flux J_{Li} to the gradient of concentration ∇c_{Li}. Equation (1.7) is a simplified version and a more complete version is described in chapter 11. As ionic diffusion in the solid is a relatively slow process as compared to in the electrolyte or mechanical equilibrium, gradient of c_{Li} builds up very quickly in the body at high C-rates(Zhao et al. 2010). Consequently compressive and tensile stresses are generated (see fig. 1.4).

For brittle materials such as ceramics, the total stress σ can increase only up to a critical stress σ_c where brittle fracture happens. This corresponds to the theoretical ultimate strength of the body, which is the same as the breaking strength for brittle materials, where creating new surfaces requires less energy than increasing elastic deformation. A typical strain-stress curve of linear elastic brittleness is plotted in fig. 1.5. Note that in the real case, plastic deformation occurs as well.

The work $W = \sigma_c/(2E)$ represented by the gray area under the strain-stress curve corresponds to the maximum strain energy per unit volume. The energy is then released by the fracture as there is no strain. A certain amount of energy is necessary to produce a new surface. It is expressed per unit surface area and is denoted γ_s. The critical energy release rate G_c is the double as two surfaces are formed, then $G_c = 2\gamma_s$. G_c is a material property which was first introduced by Griffith (1921). The link between G_c and σ_c depends on the boundary conditions (e.g. crack length, geometry of the body, etc.), not

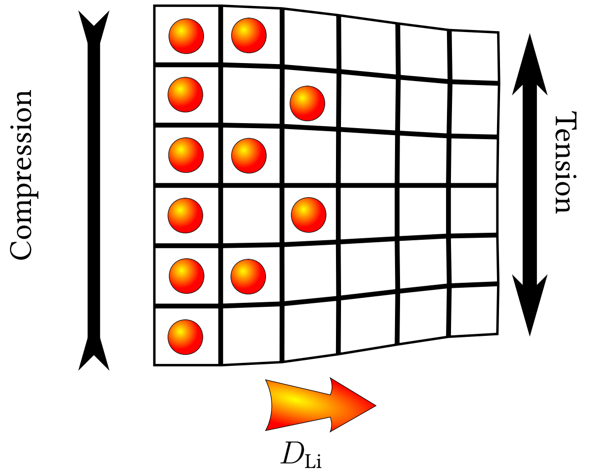

Figure 1.4: Compression and tensile stress induced by (de)lithiation. The grid represent interstitial sites and the red spheres represent Li$^+$.

further detailed here. Irwin's critical stress intensity factor K_C is commonly used to define the fracture toughness (Irwin 1957; Rice 1968) and is expressed as follows:

$$K_c = \sqrt{E^* G_c}, \tag{1.8}$$

where $E^* = E$ for plane stress conditions and $E* = E/(1 - \nu^2)$ for plane strain conditions. K_C is further detailed in section 2.2.1.

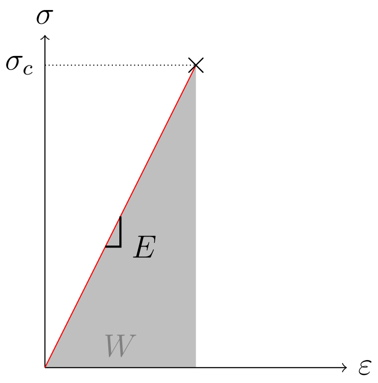

Figure 1.5: Schematics of the strain stress curve of a purely linear elastic brittle material in uniaxial loading.

To recapitulate, the elastic modulus E defines the relation between the strain induced by lithium intercalation $\varepsilon_{\mathrm{Li}}$ and the stress σ. The diffusion coefficient D_{Li} determines the amplitude of concentration gradients and hence $\varepsilon_{\mathrm{Li}}$. Failure happens when σ reaches σ_c which is determined by the fracture toughness K_C. E, D_{Li} and K_C are all intrinsic material properties which are particularly important for understanding mechanical failure upon cycling. As lithiation-induced stress is a microscopic problem, these parameters must be determined as well at the local scale.

1.3 Lithium Manganese(III,IV) Oxide

In this section, $LiMn_2O_4$ is first described, then its use and fatigue mechanisms in LiB are discussed and last the state-of-the-art concerning knowledge of its intrinsic properties is listed.

$LiMn_2O_4$ has a spinel cubic structure of space group $Fd\bar{3}m$ in its stoichiometric form. Oxygen ions are located in 32e sites, making a face-centered cubic closed pack frame, with the manganese cations in 16d sites (half of the octahedral sites). The building block of this structure are MnO_6 octahedron where the metal is located in the center. Lithium cations are located in tetrahedral interstitials 8a. The other half of octahedral sites (16c) are empty, which explains the 3 dimensional diffusion path opened to lithium ions as they can reach the next tetrahedral site through an empty 16c site (Xu and Meng 2010). Schematics of the structure can be seen in fig. 1.6.

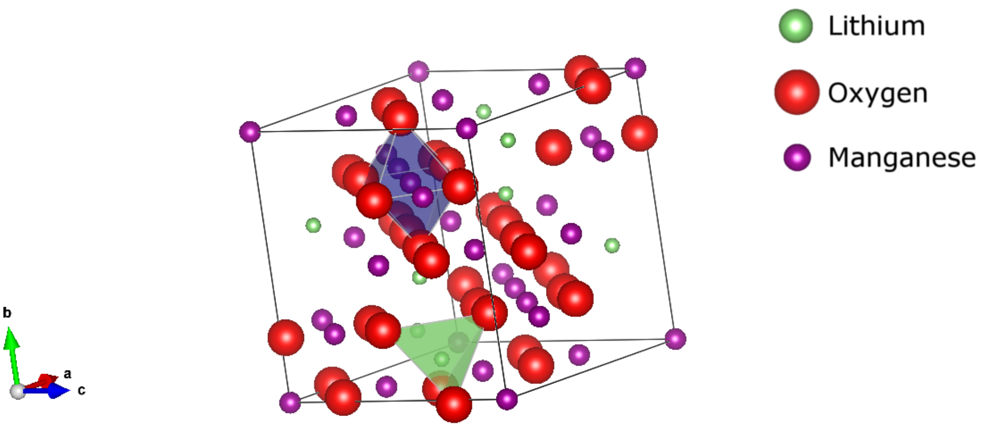

Figure 1.6: Crystal structure or $LiMn_2O_4$ spinel. One MnO_6 octahedron appears in purple and one Li-centered tetrahedron interstitial site appears in green. The image was build using Vesta (Momma and Izumi 2011)

One of the particularity of Lithium Manganese (III,IV) Oxide is its good stability, in the sense that there is little release of oxygen upon cycling, even at high voltages (delithiated state). This property has a structural origin as the bonds between manganese cations and oxygen anions are stronger than in other $LiMO_2$ materials (M = transition metal), yet not as much as in olivines.

In ideal operation of the electrochemical cell, the crystal $Li_xMn_2O_4$ keeps its spinel structure upon delithiation for $0 \leq x \leq 1$. The lattice parameter of stoichiometric $LiMn_2O_4$ is 8.24Å and reduces to about 8.03Å, reaching a cubic $\lambda{-}MnO_2$ phase where lithium atoms left the 8a sites (Berg and Thomas 1999). Figure 1.7 experimentally shows how the lattice parameter of the structure increases upon lithiation. The mea-

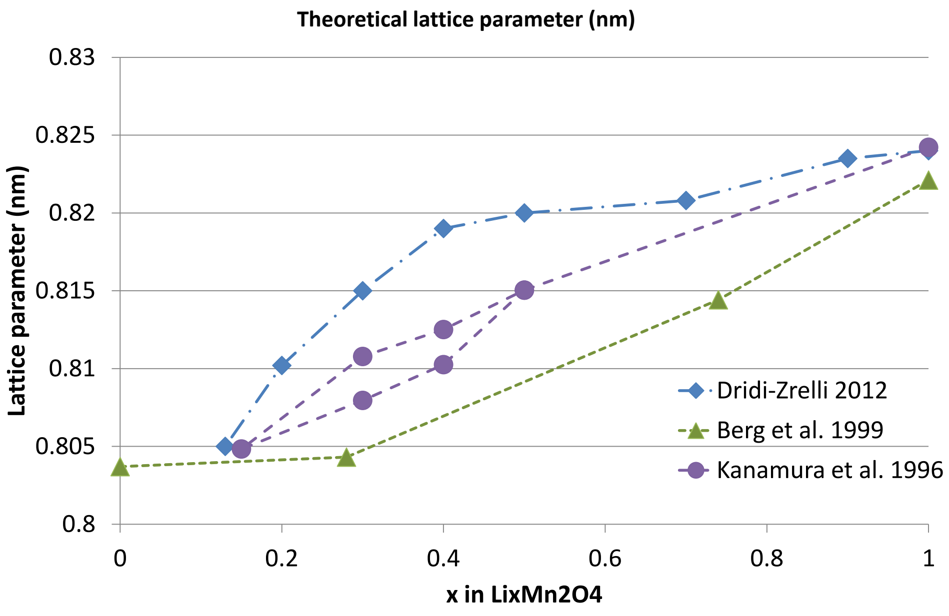

Figure 1.7: Lattice parameters versus x in $Li_xMn_2O_4$ calculated from X-Ray diffraction measurements (Kanamaru et al. 1996; Dridi-zrelli 2012) and ex-situ neutron diffraction measurements (Berg and Thomas 1999).

surements follow the same trend and the differences can be explained by the synthesis conditions, hence by different defects in the structure. The crystal experiences a volume expansion of about 7 % upon lithiation. The oxidation state of manganese ions is tightly connected to the lithiation of the crystal and the chemistry could be described as $Li_x^+Mn_x^{3+}Mn_{2-x}^{4+}O_4{}^{2-}$. It is thought that 3 stable phases intervene in the electrochemical process, the first one is lithium-rich and corresponds to the ordered stoichiometric $LiMn_2O_4$. The second one is $Li_{0.5}Mn_2O_4$ where the crystal reaches a new ordered phase with every other 8a site empty forming a superstructure which is more stable than random positioning of Li. The last one is $\lambda{-}MnO_2$ where all the interstitials are thought to be empty. Experimental measurements showed that there are remnant lithium ions and this phase contains about 25 % lithium in its delithiated state (Berg and Thomas 1999). It was observed that poorly lithiated $\lambda{-}MnO_2$ and $Li_{0.5}Mn_2O_4$ can be present in parallel in the low concentration range, where one phase would grow at the expense of the other (Yoshio and Noguchi 2009). This is a reason why two peaks can be detected in XRD measurements (Kanamaru et al. 1996; Xia and Yoshio 1996). In other cases, a single set of peaks are detected and could be attributed to non-stoichiometric (de)lithiation of single phases (Xia and Yoshio 1996; Berg and Thomas 1999; Dridi-zrelli 2012).

The 2 first-order phase transitions translate into plateaus in the OCV curves as plotted in fig. 1.8 (see fig. 1.2).

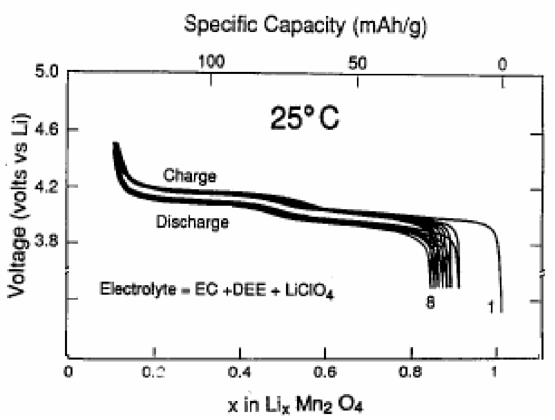

Figure 1.8: Potential evolution of $LiMn_2O_4$ vs metallic Li at 25°cycled at 1/22 C-rate. From (Dridi-zrelli 2012), readapted from (Guyomard and Tarascon 1992).

The different oxidation states of the manganese cations have important consequences on the crystal structure. Overlithiated $Li_xMn_2O_4$ ($x > 1$) experience a Jahn-Teller phase transition where additional Mn^{3+} ions induce a distortion of the MnO_6 octahedral, the crystal is no longer symmetric and becomes tetragonal along with lithium ions moving from 8a sites to the empty 16c sites, with a I41/amd symmetry (Berg et al. 1999). The material has poorer cycling performance as the transition can be irreversible if the battery is pushed too far in the low potentials. It is thought that inhomogeneities within cathode particles lead some particles to lithiate faster than others, creating Jahn-Teller distortions in some particles even though the full cell do not seem fully discharged. Reducing inhomogeneities, e.g. by using thin films where conditions are better controlled (Park et al. 2000), can increase the cycle life. Besides a Jahn-Teller deformation can also happen at temperatures just below room temperature between 270K and 300K where the structure becomes orthorhombic. Structural change can also have a third origin: Lin et al. (2011) found that for non-hydrostatic stresses as low as 0.4 GPa, irreversible phase transformation can occur even for manganese valence below 3.5. Upon lithiation at relatively high C-rate, non-hydrostatic conditions are met in non-spherical particles (Huggins and Nix 2000).

An equally important factor for capacity loss in $LiMn_2O_4$ at low potentials is manganese dissolution in the electrolyte (Vetter et al. 2005). This is due to disproportion of Mn^{3+} where 2 Mn(III) can lead to one Mn(II) and one Mn(IV). Mn^{2+} are soluble in the electrolyte which leads to an irreversible loss of material. Moreover Mn can be found in the graphite anode of cycled full cells which increases the total impedance and make the cell quickly unusable.

These two inter-related issues (Jahn-Teller and low potential dissolution of Mn) can be circumvent by the use of doping metallic impurities (Co, Ni, Cr, Cu, Fe, Mg or Al) with lower valence. This makes some manganese ions to stay in a tetravalent oxidation state and keep a ratio of Mn(III) versus Mn(IV) below one during the whole electrochemical cycle. Another way is to reduce the oxidation of Mn by cation vacancies (Kim et al. 2005).

Dissolution can also happen at higher potentials due to reaction with hydrofluoric acid which could be present because of hydrolysis of $LiPF_6$ (presence of water impurities in the electrolyte). Dissolution is very dependent on the surface to volume ratio of $LiMn_2O_4$ particles (Yoshio and Noguchi 2009). Fracture of the particles increases the specific area and hence increases this effect.

1.3.1 Electronic and ionic properties

Diffusivity of the ionic charge carrier is a key performance metric of active material in batteries. Diffusion coefficient of lithium ions in the material can be indirectly calculated from titration techniques at different states of charge (SoCs), such as potentiostatic intermittent titration technique (PITT) and galvanostatic intermittent titration technique (GITT). The titration techniques measure the time dependent response of half cells after each small incremental (dis)charge steps. These techniques are not local, in the sense that not only one particle is characterized but the whole system. They offer the advantage of being simple to set-up with a good resolution in terms of concentration.

Diffusivity in the spinel was measured between 10^{-16} $m^2.s^{-1}$ and 10^{-13} $m^2.s^{-1}$(Park et al. 2010; Chung et al. 2011b). This relatively large range can be explained by the use of different synthesis conditions. Within a single cell, a change of one order of magnitude can be experimentally measured as measurements from PITT demonstrate it (fig. 1.9). The two minima correspond to the plateaus in the OCV curves (fig. 1.8) as diffusivity and the chemical potential are related quantities (this will be further developed in part V). They hence correspond to the first-order phase transitions $LiMn_2O_4 \longleftrightarrow Li_{0.5}Mn_2O_4$ and $Li_{0.5}Mn_2O_4 \longleftrightarrow \lambda{-}Mn_2O_4$.

$LiMn_2O_4$ is not an insulator but a mixed ionic-electronic conductor with dominating ionic conduction. It was first thought that electronic conductivity is similar to semiconduction, i.e. following band conduction model. Temperature dependent conductivity measurements using ion-blocking electrodes dismissed it. From Arrhenius plots, an activation energy of $\approx$ 0.2 to 0.5 eV (Guan and Liu 1998; Marzec et al. 2002) was measured, which is smaller than the electronic band gap of the spinel as obtained from optical absorption (1.2 eV, Ouyang et al. (2006)) and from simulations (1.3 eV, Liu et al. (2009)). The mechanism which could explain the easier electron diffusion is hopping of small non-adiabatic polarons. Polarons are quasi-particles that describe the interaction between an electron and its self-induced polarization within the ionic lattice of dielectric crystals (Devreese 1996). The term “large polaron” is used when the electronic charge interacts in the long range and has a small activation energy (0.1 eV) (Maier 2005) . “Small polaron” refers to electronic charge which produces a polarization in a region of the order of magnitude of the lattice parameter. Its activation energy is bigger as is the case in the spinel (Maier 2005). In the spinel, properties of polarons is not completely understood and still many questions arise (Park et al. 2010). In particular ionic and electronic mobility are often decoupled for simplicity. Even though they are considered non-adiabatic, e.g. electrons do not follow automatically

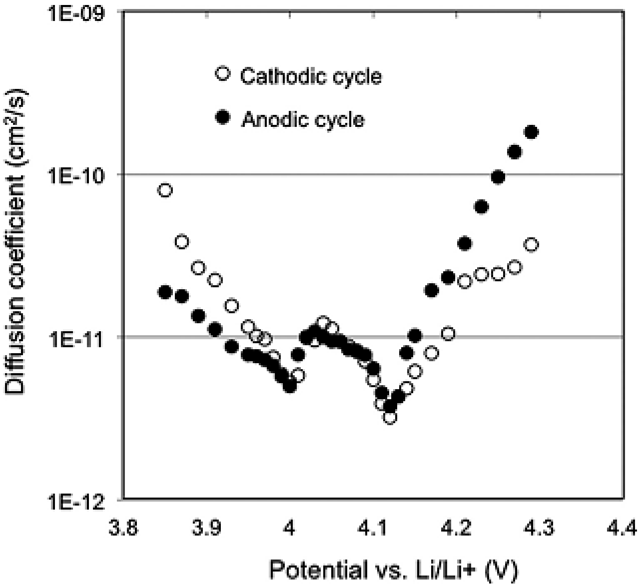

Figure 1.9: Li diffusion coefficient in $\mathrm{Li}_x\mathrm{Mn}_2\mathrm{O}_4$ $(0 < x < 0.85)$ as a function of cell potential vs. Li/Li+. Cathodic (upon lithiation) and anodic (upon delithiation) measurements are shown. From (Chung et al. 2011b)

the motion of ions, it is expected that they are dependent due to lattice distortion and Coulomb interaction (Maxisch et al. 2006). In the case of $\mathrm{LiMn_2O_4}$, the polaron is associated with the oxidation state of the manganese ions, where polaronic hoping can be described as a change of valence between two neighboring transition metals with different valences. It was showed by molecular dynamics simulations that Li ions experience self diffusion if electron hopping is modeled (tateishi et al. 2004), which could demonstrate that the polarons are *anti*-adiabatic, e.g. ions follow the motions of electrons. Charge transport mechanism is also by small non-adiabatic polaron hopping for other manganate spinels (with Ni, Ni/Zn or Ni/Mg in place of Li) (Watanabe et al. 2012; Schmidt et al. 2005), certainly without self-induced diffusion as these interstitial metals are bigger and cannot diffuse as easily. Quantitatively, electronic conductivity was measured to be between 10^{-6} to $10^{-3.6}$ S·m^{-1} at room temperature (Park et al. 2010).

1.3.2 Mechanical properties

As explained in section 1.2, lithium concentration gradient upon cycling produces internal stresses which can lead to fracture, phenomenon increasing for higher C-rates. Hence the intrinsic mechanical properties of the material are of interest in order to predict mechanical failure.

Growth of single crystals or poly crystals large enough to measure bulk properties using traditional methods is limited due to self-decomposition during synthesis (Iguchi

ET AL. 1998; KITTA ET AL. 2013). Bulk samples can be obtained only by sintering particles together. SUGIYAMA AND TAMURA (1995) is the first reference to the necessity of mechanical measurements of $LiMn_2O_4$. They sintered powder into thin pellets before running vibrating-reed measurements. Taking into account the porosity of the sample, an elastic modulus of 25 GPa was found. A value of 10 GPa was later reported using a similar technique. Other groups measured the bulk-modulus of powder by means of hydrostatic compression and found values between 120 and 140GPa (DARUL ET AL. 2012; LIN ET AL. 2011). This difference of one order of magnitude could be explained due to the porosities and a lack of knowledge of the real structure of $LiMn_2O_4$ in 1995. A value around 100 GPa seems more appropriate for such ceramics, particularly as Iron Manganate spinel shows values above 10^{11} GPa. ZHU AND ZENG (2012) used Instrumented Indentation Technique (IIT) to measure the E-modulus and the hardness of thin-film $Li_xMn_2O_4$, finding values of about 203 GPa and 11GPa for as-deposited electrode film and values of about 140 GPa (± 5 GPa) and 7 GPa (± 2 GPa) after 10 cycles, respectively. The elastic modulus would decrease further more to about 120 GPa after 100 cycles while the hardness would stay constant. They suggest that tensile stresses are stored within the delithiated cathode while internal compressive stresses could be present when fully lithiated. Residual tensile stresses decrease pile-up effect (BOLSHAKOV ET AL. 1996), hence decreasing the measured E-modulus and Hardness. The decrease of both values during the first 10 cycles could be explained by a release of internal stresses after surface topography change, reducing pile-up effect. Hence the 200 GPa E-modulus and 10 GPa Hardness might be over-evaluated.

Other groups(DARUL ET AL. 2012; LIN ET AL. 2011) measured Bulk-moduli of powder by means of hydrostatic compression. A small deviation from hydrostatic equilibrium lead to a Jahn-Teller distortion with an irreversible phase transition to a distorted tetragonal phase. It is an important information as lithium concentration gradient upon electrochemical cycling creates non-hydrostatic stress. It is again highly related to the valence of Mn where reducing the ratio of Mn(III) would decrease the chance of observing this irreversible transition. Quantitatively, bulk moduli between 120 and 140 GPa are found, which correspond to E-moduli between 140 and 170 GPa (for a Poisson's ratio of 0.3). They note that these values are much smaller than the ones obtained for other spinel chemistries. It is explained by the fact that the LiO_4 8a tetrahedras are responsible for most of the elastic compression, while with other metals (M) intercalated in 8a sites, the M$-$O bond is stronger. *Ab-initio* simulations were carried out for $\lambda{-}MnO_2$, $Li_{0.5}Mn_2O_4$ and $LiMn_2O_4$ (GRECHNEV ET AL. 2002). Similar bulk moduli around 200 GPa were found for all phases. It is surprising as experimental measurements show that lithium-centered tetrahedras are responsible for most of the elastic property of the material. Later (LEE ET AL. 2013), molecular dynamics calculation were done for $0 < x < 1$. A Young's modulus of 174.4 GPa is found for $x = 0$, which drops quickly to 142.2 GPa for $x = 0.25$ and re-increase to 155.1 GPa for $x = 0$. They explain that the two opposite trends are due to the competition of inter-atomic bonds: the ratio of very stiff $Mn^{4+}-O^{2-}$ tend to decrease upon lithiation explaining the first drop which is compensated at higher SoC with an increasing number of $Li^{+}-O^{2-}$. Until the present work, there were no experimental report on the dependence between the elastic properties and the lithiation state of the material.

Concerning fracture properties, cracks have long been reported as an important cause of capacity loss in batteries (MOON AND LEE 2003). Using acoustic measurements, cracking events were reported during lithium-ion insertion (OHZUKU ET AL. 1997). A work carried out on $LiMn_{1.95}Al_{0.05}O_4$, a spinel with higher average Mn valence, suggest two parallel mechanical failure of the particles: first a brittle crack during the first cycle, then fatigue leading to fracture (CHEN ET AL. 2011). A similar behavior was later reported for $LiMn_2O_4$ (HAO ET AL. 2014), where the authors indicate that failure happens at a higher frequency, when oxygen vacancies are present as is the case in commercial samples. For both spinels, the favorite cracking plane is {111}. It is expected as these planes have the lower solid-to-vapor surface energy (HUANG ET AL. 2001). Quantitative measurements of fracture toughness have never been reported before the present work to the best of our knowledge.

2 Chapter
Characterization

With the advent of device miniaturization lead in forefront by the semiconductor industry, characterization methods had to be developed in order to study their properties. The scope of this thesis is the study of micro-metric particles which lie in a matrix, the challenge is hence to study the properties of heterogeneous samples. Scanning electron microscopy (SEM) was an important tool in the advancement of the present work as it allows to quickly image the sample. On the other hand, two other techniques have been primarily used in order to study the properties of this type of sample *quantitatively*: instrumented indentation testing (IIT) and AFM, which will be the focus of this section.

2.1 Instrumented Indentation Testing (IIT)

2.1.1 Measuring device

IIT is a method used to measure the mechanical properties of volumes at the micro- or nano-scale. It is more commonly called *nanoindentation* when referring to the nano-scale and both terms will be used interchangeably in this manuscript. It is similar to traditional hardness testing insofar as a relatively stiff tip of known shape is pushed into the surface of the material of study. Two physical quantities are being measured during an indentation procedure: the load applied on the tip and its displacement into the sample surface. They are continuously controlled and monitored at high-resolution during the whole process, which is the main difference with the original hardness test where the print had to be imaged after each test and to be associated with a single load. The depth of indentation can range from several nanometers to several micrometers and the positioning precision is in the order of the micrometer. Hence mechanical properties of a surface can be mapped at a rather high resolution, which is suitable for heterogeneous materials, without requiring complex nanoscale imaging techniques.

Tip shapes used in this work are Berkovich's and cube corner. The Berkovich's indenter has a self-similar three-sided pyramidal shape with the same indentation depth-to-area ratio than Vicker's tip. The latter is used in traditional micro-hardness techniques and is four-sided. When indentation precision went from *micro* to *nano*, trigonal tips replaced tetragonal ones as it is technologically much simpler to manufacture

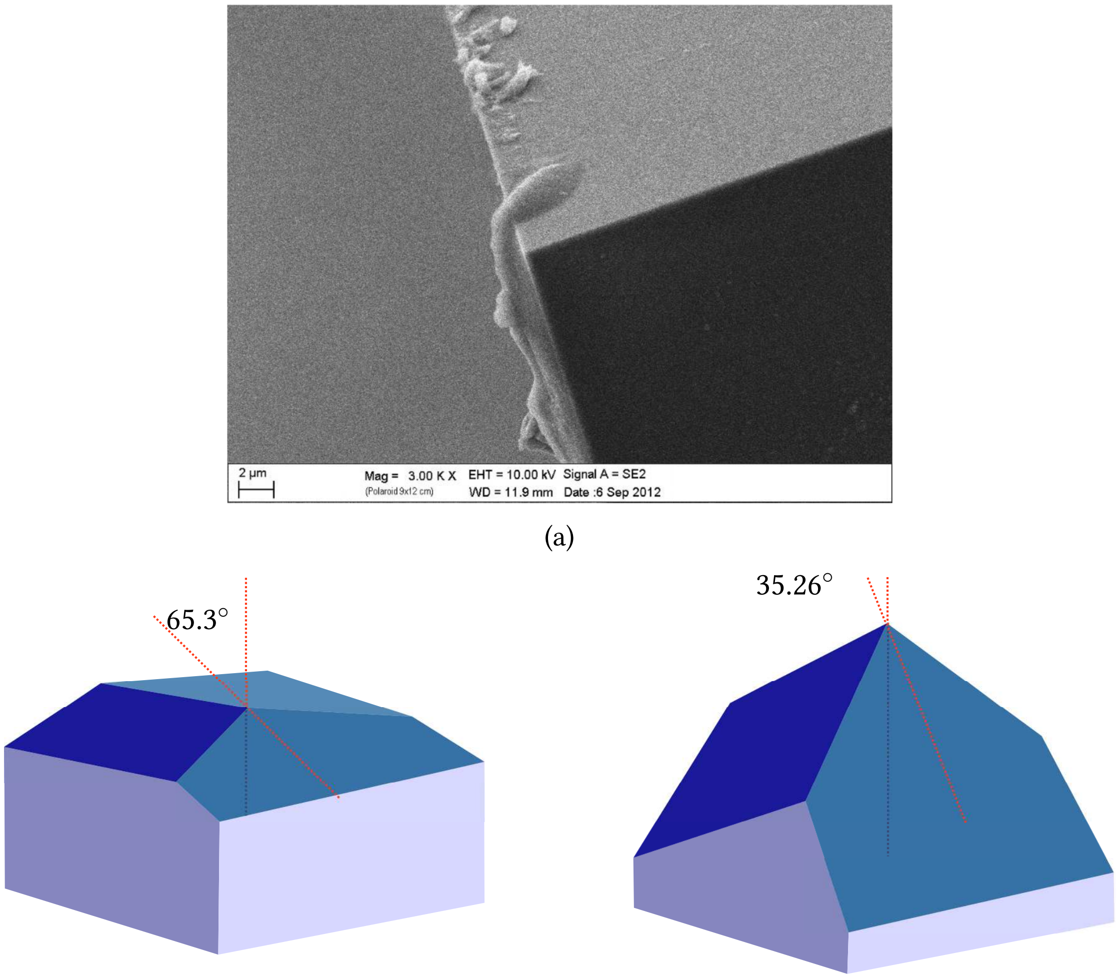

(b)

Figure 2.1: (a) SEM image of the cube corner tip used in this study. (b) Schematics of a Berkovich tip (left) and a cube corner tip (right).

a three-sided single-point tip. Berkovich are commonly used for indentation modulus and hardness measurements and have been extensively studied for this purpose(Oliver and Pharr 1992 2004). Cube corner tips are sharper and are favored for fracture testing as they require a much smaller load to produce cracks (PHARR 1998).

The favorite tip material is diamond as its high stiffness lets the measurements be mainly, if not only, influenced by the material of study rather than the tip itself. It can be changed to other chemistries in adverse environment, e.g. high temperature, like sapphire or tungsten.

Assuming that the surface is flat, the contact area can be deduced from the continuous measurement of the depth of penetration. Elastic modulus and hardness are the two main properties widely derived from IIT data which do not require imaging of the indent. The simplicity of the process made nanoindentation a widely used tool in the fields of thin films and micro electro-mechanical systems (MEMS). The theory behind it is however not as trivial as the measurement itself. The first reference to continuous recording of depth and load relates to indentation of magnesium oxide with a Vicker's tip (LOUBET ET AL. 1984), where Sneddon's solution for elastic deformation of a solid with a flat punch (SNEDDON 1965) was used to estimate the indentation modulus. Sneddon derived a law for the elastic recovery during unloading using solids of revolution as follows:

$$L = \alpha h^m, \tag{2.1}$$

where L refers to the indenter load, h to the elastic unloading displacement, α is a constant which depends on the materials of study and m is a constant which depends on the geometry of the indenter. Solutions for flat cylinders ($m = 1$), cones ($m = 2$) and spheres ($m = 1.5$) were given. DOERNER AND NIX (1986) used Sneddon's solution for a flat cylinder ($m = 1$) to generalize the unloading curve of Vicker's indentation to any isotropic material. It was only six years later that the formalism still used today was developed by Oliver and Pharr (1992) where they would not limit the power law to a flat punch but would determine m for each measurement. The method, generally called the Oliver and Pharr method, is further described in the next chapters.

Note that IIT can also be used to measure various quantities which are listed in table 2.1.

2.1.2 Oliver and Pharr method

Warren Oliver and George Pharr published in 1992 an article that describes a method to obtain *quantitative* measurements from nanoindentation without the need of imaging techniques (Oliver and Pharr 1992). It became a milestone in hardness testing with more than 9000 citations thanks to its simplicity and is referred to as the "Oliver and Pharr method". This paper had a follow up in 2004 (Oliver and Pharr 2004) that describes advances in understanding and fixed some key parameters. This subsection deals

Accuracy	Quantity	source
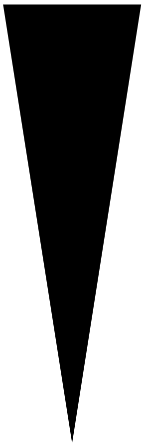	**Hardness**	**Oliver and Pharr (1992)**
	Elastic modulus	**Oliver and Pharr (1992)**
	Storage and loss modulus	Oliver and Pharr (1992)
	Yield stress	Shim et al. (2008)
	Work hardening	Shim et al. (2008)
	Fracture toughness	*Pharr (1998)*
	Residual stress	Swadener et al. (2001)
	Creep parameters	LaManna et al. (2004)

Table 2.1: List of quantities measurable by nanoindentation and ordered by accuracy. Each is associated with a paper describing the measurement procedure. Bold lines indicate methods explained in section 2.1.2. The italic line indicates a method briefly described in the Results part VI, section 15.1. The other methods were not used in this work and are only here for informative purpose. Table inspired by Pharr (2013).

with the state-of-the-art concerning this method and finishes with its adaptation to heterogeneous materials.

2.1.2.1 Load and displacement

In an indentation test, a stiff tip is driven into the sample surface as load L and depth h are continuously monitored. The penetration continues until reaching a set load L_{max} or a set depth h_{max}. The tip is optionally kept at this maximum for a certain duration (e.g. 1 s) in order to estimate creep. The tip is thereafter unloaded down to 10 % of the maximum load and held for a long duration (e.g. 10 s) to estimate the thermal drift. Last, the tip is completely unloaded from the surface.

Figure 2.2 shows a typical load versus displacement measurement made on SiO_2 (silica). It is important to note that the measuring procedure is calibrated to remove the machine compliance contribution as well as the thermal drift contribution from the data set. Several data are important: the maximum load, L_{max}, the depth reached at this load, h_{max}, and the residual depth, h_f. They can be directly deduced from the data set.

According to Oliver and Pharr (1992), the unloading is a purely elastic process. Hence the stiffness S at max load is calculated as being the derivative of the load with respect to the displacement during unloading:

$$S = \left.\frac{\mathrm{d}L}{\mathrm{d}h}\right|_{L=L_{max}}, \tag{2.2}$$

where L was defined in eq. (2.1). During loading, both plastic and elastic deformation

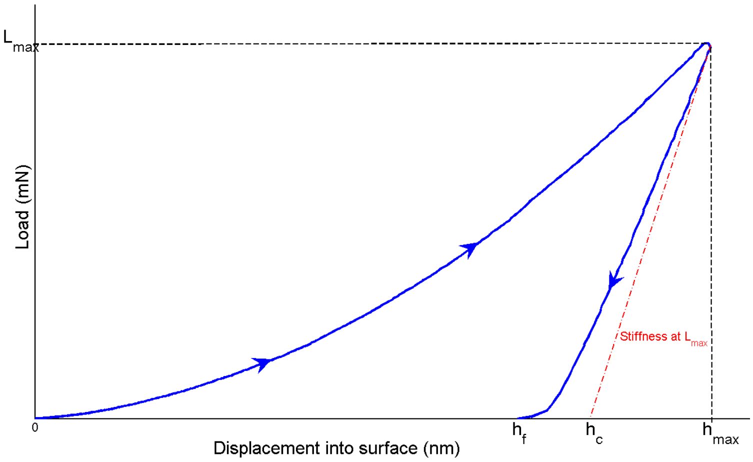

Figure 2.2: Typical load versus displacement curve on silica. L_{max} corresponds to the maximum load, h_{max} to the maximum depth, h_f to the residual depth after the indenter is withdrawn and h_c to the real depth of contact for $\epsilon = 1$.

processes occur which lead to the hardness impression. As the tip is driven into the material to a depth h_{max}, an elastic deformation occurs around the contact zone as shown schematically on fig. 2.3. This phenomenon is called sink-in. It leads the real contact depth h_c to be smaller than h_{max}. This sink-in is describe in the method by a simple elastic half space indented by a rigid material. The following equation describes this sink-in depth h_s:

$$h_s = \epsilon \frac{L_{max}}{S}, \tag{2.3}$$

where ϵ is a coefficient linked to the tip geometry and usually fixed to 0.75 (Oliver and Pharr 2004). Hence the depth of the real contact h_c is:

$$h_c = h_{max} - h_s = h_{max} - \epsilon \frac{L_{max}}{S}. \tag{2.4}$$

In modern set-ups, the stiffness can be continuously measured by adding a small dynamic load (usually around 40 kHz). This enables to have not only two but three quantities monitored during the whole procedure at good resolution: the penetration depth h, the load L and the stiffness S_{CSM}.

The method does not take into account potential plastic flow to the surface nor friction between the tip and the surface. The former is referred to as pile-up, where material is driven up by the plastic deformation towards the surface, physically increasing the contact area (see fig. 2.4). It occurs particularly in ductile materials (e.g. metals). Sharper tips such as cube-corners tend to increase both phenomena (Pharr 1998; Hay and Pharr 2000). The ratio $\frac{h_f}{h_{max}}$ gives an indication on the amount of pile-up. If this value is smaller than 0.7 (Berkovich's indenter) (Pharr 1998), the pile-up can be neglected as it is the case in the method. This can be easily understood as a high $\frac{h_f}{h_{max}}$ ratio indicates

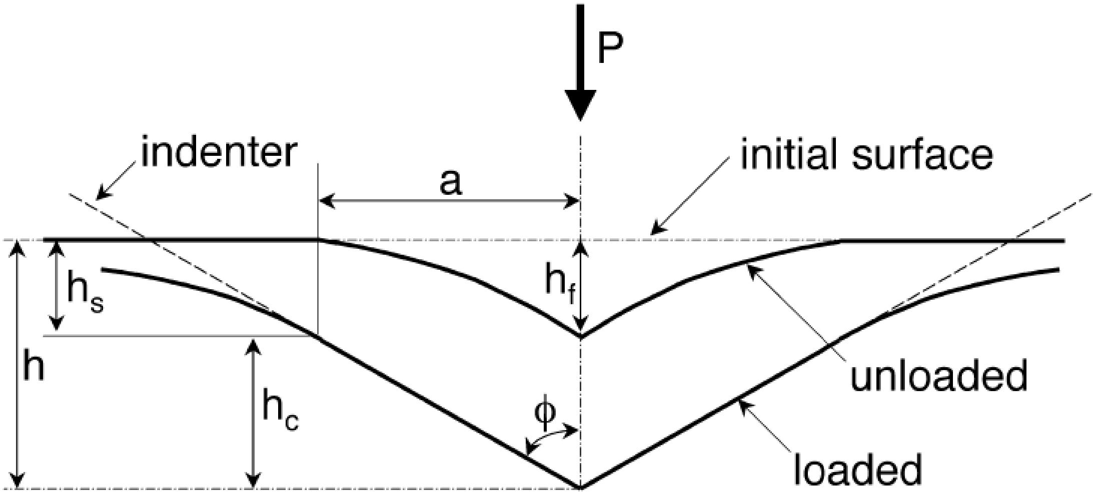

Figure 2.3: Schematic illustration of the contact geometry of an indentation under a load, here noted P, and its different depth values. h corresponds here to the maximum depth h_{max}, h_c to the real depth of contact, h_s to the depth of elastic sink-in and h_f to the residual depth after the indenter is withdrawn. a is the equivalent radius of contact and Φ the equivalent tip angle. From Oliver and Pharr (1992).

a very plastic deformation of the surface, while pile-up is a consequence of a low yield stress as compared to elastic modulus (Bolshakov and Pharr 1997), hence an easily plastically deformable material. In case of pile-up, the indented area must be imaged to know the real h_c.

2.1.2.2 Measurement of hardness

The hardness H is calculated as follows:

$$H = \frac{L_{max}}{A(h = h_c)}. \tag{2.5}$$

Here, A is the projected area of the impression at L_{max}, hence for $h = h_c$. It is important to note that the hardness calculation in IIT is *therefore not linked to the residual plastic impression* as it is in traditional hardness testing. The smaller the plastic deformation produced by nanoindentation, the higher is the discrepancy between these two values. H could be measured at any load but the method requires to know h_c which is computed from S, itself depending on the unloading behavior of the tip-surface system. A is determined by a function of penetration which is determined by a calibration procedure presented in section 2.1.2.4.

2.1.2.3 Measurement of the elastic modulus

The theoretical derivation starts with a set of hypotheses: the sample is defined as a perfectly flat, semi-infinite, isotropic, and homogeneous solid. Based on Hertz's

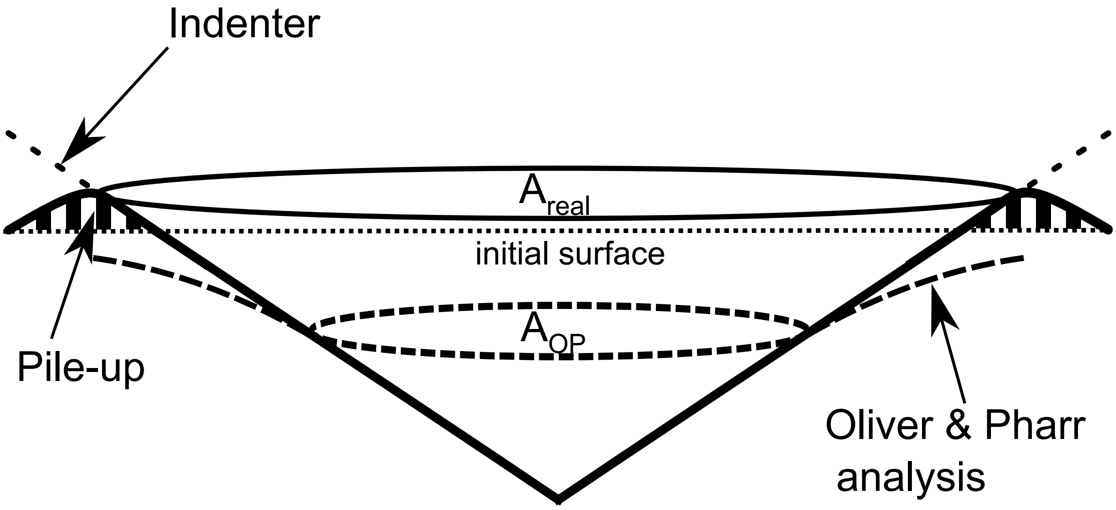

Figure 2.4: Schematic illustration of the consequences of pile-up deformation where A_{real} is the real projected surface area and A_{OP} is the projected surface area computed by the Oliver and Pharr method.

solution, the effective elastic modulus E_{eff} is calculated as follows from purely elastic unloading:

$$E_{eff} = \frac{S\pi^{1/2}}{2\beta A^{1/2}}. \tag{2.6}$$

Here β is a correction factor accounting for the geometrical features of the system. For a rigid axisymmetric punch of smooth profile, this factor is 1. Real indentation experiments involve the use of pyramidal shapes which can be elastically deformed with high strain, hence the factor can deviate from unity. Historically, it was set to 1.034 as derived empirically. It is the value used in this thesis. Thorough research has been undertaken with the help of both experiments and finite element simulations to find a more accurate value depending on the materials properties: all the solutions lie between 1.0226 and 1.085 (see OLIVER AND PHARR 2004). It should be noted that eq. (2.6) corresponds to the elastic unloading of a indenter on a *flat* surface. It is used as the authors consider that the elastic pressure distribution of a plastically deformed surface at maximum load can be assimilated to the one exerted onto a purely elastic flat surface indented by a tip with a different geometry: the *effective indenter shape*. This can also explain why m in eq. (2.1) is not fixed as it rather depends on this effective shape.

For isotropic materials, the sample Young's modulus can be derived as follows:

$$\frac{1}{E_{eff}} = \frac{1}{M} + \frac{1-\nu_d^2}{E_d} = \frac{1-\nu_s^2}{E_s} + \frac{1-\nu_d^2}{E_d}, \tag{2.7}$$

where E_s and E_d are respectively the elastic moduli of the sample and the tip and ν_s and ν_d are respectively the Poisson's ratios of the sample and the tip. M is the indentation modulus, computed when ν_s is unknown. For the case of anisotropic semi-infinite

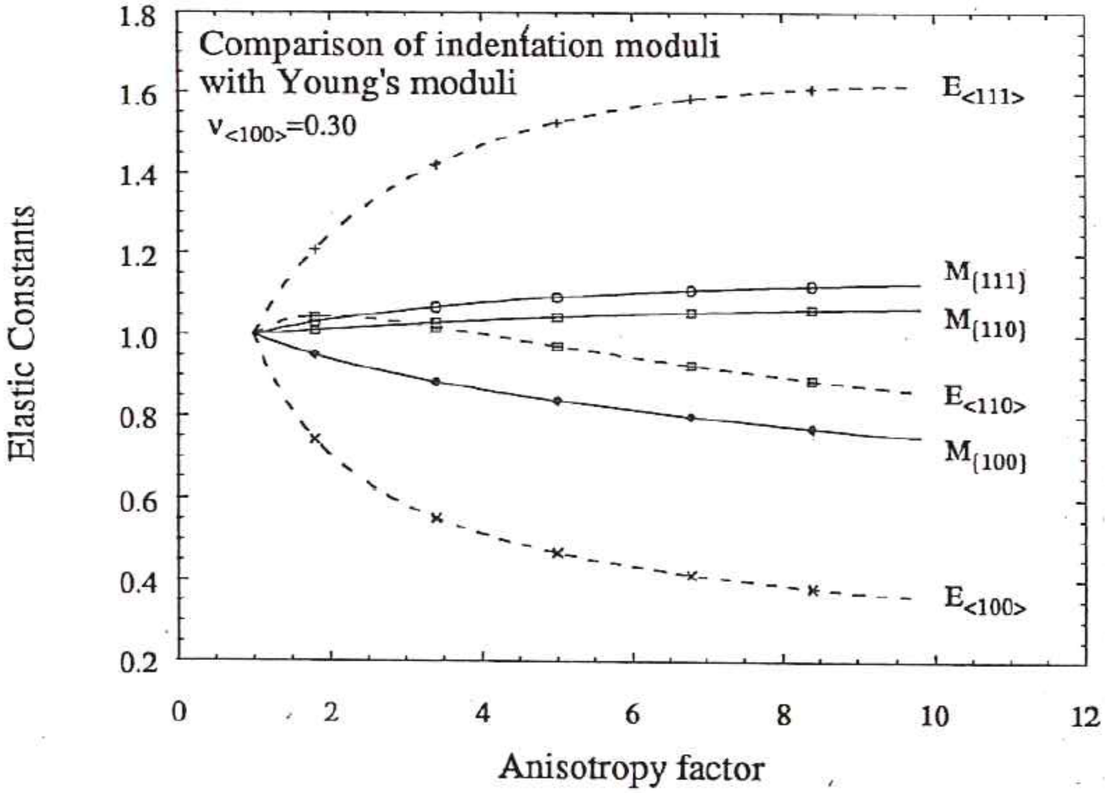

Figure 2.5: Normalized indentation moduli $M_{<hkl>}$ and normalized elastic moduli $E_{<hkl>}$ (Poisson's ratio $\nu_{<100>} = 0.3$) for the crystalline directions noted $< h\,k\,l >$ as a function of the anisotropy factor of crystals with cubic symmetry. From Vlassak and Nix (1993).

crystals, Vlassak and Nix (1993) calculated the deviation that would be observed between the indentation modulus and the real anisotropic Young's modulus of a flat punch unloading a crystal of cubic symmetry. Young's modulus in $< 1\ 1\ 1 >$ and $< 1\ 0\ 0 >$ directions have the greatest difference with this symmetry and the difference depends on the anisotropy factor. In fig. 2.5, Young's moduli of these two directions as well as the $< 1\ 1\ 0 >$ direction are compared to the indentation moduli that would be extracted from eq. (2.7) by indenting in a single crystal for the same three directions. The calculations are not trivial and require analytical simplifications or numerical methods. It should be noted that the indentation moduli for directions $< 1\ 1\ 1 >$ and $< 1\ 0\ 0 >$ deviate less than 20 % from the polycristalline modulus for an anisotropy factor of 5 while the equivalent Young's moduli deviate more than 50 %. This indicates that indentation cannot be used to describe quantitatively the anisotropy of a material.

2.1.2.4 Calibration

Calibration of the machine is done on known isotropic samples. Fused silicon oxide is usually used as it has other benefits, including the ease to produce flat samples by cleavage and low cost. It is routinely used before and after indentation tests. Using only one calibration material can be adequate when studying materials of similar properties but can have severe consequences otherwise (Fischer-Cripps 2006). International standards (ISO 14577-2) require the use of two different reference specimens. In this work, only SiO_2 was used on a daily basis for calibration as its properties approach the ones of common ceramics. Indentation of an aluminum single crystal was sometimes used to check the consistency of the measurement.

Machine compliance C_m

Equations (2.6) and (2.7) do not consider the deformation of the measurement device. The system can be calibrated by using the continuous stiffness measurement as described by Joslin and Oliver (1990):

$$\frac{1}{S_{CSM}} = C + C_m, \tag{2.8}$$

where S_{CSM} is the measured stiffness, C is the inverse of the tip/surface contact stiffness S and C_m is the machine compliance. Following Joslin and Oliver (1990), multiplying eq. (2.8) by $L^{1/2}$ yields:

$$\frac{L(h)^{1/2}}{S_{CSM}(h)} = L(h)^{1/2} C_m + J_0^{1/2}. \tag{2.9}$$

Here $J_0 = L/S^2 \propto H/E_{eff}^2$ is the Joslin-Oliver parameter which is constant for any depth. C_m can then be computed from the slope of $L^{1/2}/S_{CSM}$ versus h for large depths and its inverse can be subtracted to S_{CSM}. Note that this enables a calibration which does not require prior knowledge of A.

Area function A

The area function can be computed from eq. (2.6) as E_{eff} is known. For fused silica, E_{eff}=69.9 GPa with a diamond tip (E_d=1141, ν_d=0.07) as E_s= 72 GPa and ν_s=0.17. The measurement of $A(h_c)$ is fitted with the following function:

$$\begin{aligned} A(h_c) &= \sum_{n=0}^{8} C_n h_c^{2^{1-n}} \\ &= C_0 h^2 + \cdots + C_8 h^{1/128}, \end{aligned} \tag{2.10}$$

where C_n are constants determined by the fitting procedure. A perfect pyramid can be described with C_0 only which is equal to 2.598 for a cube-corner tip and 24.5 for Berkovich's (and Vicker's) tip. The second term refers to a paraboloid of revolution. This function has no physical meaning in its most extended forms and is used only for its ability to fit the curve. Due to roundness and other defects close to the tips, the function usually fits only for a certain depth range. For large depths, C_0 is often enough.

2.1.2.5 Indentation of heterogeneous materials

The method developed by Oliver and Pharr cannot directly work on heterogeneous materials as the load-displacement curve are the results of a composite response. Analysis of composites started with the study of thin films. The assumption of an infinite half space is respected when indentation depth does not exceed 10 % of the film thickness (empirical value). It is a condition which cannot be respected in many cases due to tip bluntness and surface roughness. Extrapolating the mechanical properties of a film with known thickness for indentation depth approaching zero has been proposed by MENČÍK (1997). This method requires also the mechanical properties of the substrate as inputs, measurements which can be separately conducted. It is hardly useable for particle-matrix composites like LiB materials as the geometry of the problem are not known in advance. Besides, strong differences in the mechanical properties of the two phases lead to significant sink-in or pile-up of the indented phase (YAN AND PUN 2011 2012; LEISEN ET AL. 2012). A statistical method was developed by CONSTANTINIDES ET AL. (2006); ULM AND VANDAMME (2007) to extract the mechanical properties of single phases composing nanocomposites such as bones and cement. It is based on making a large number of indentation measurements in a matrix, as to produce images from scanning techniques. If one indent produce an elastic zone with a volume much smaller than the typical volume of each feature, each data point is associated to a statistical event with a probability corresponding to the surface fraction of the phase. The unique properties of each phase can be obtained after deconvolution of the cumulative distribution function (CDF) of the indentation measurements. The CDF is built by defining the accumulation function $D(X_t)$ as follows:

$$D(X_t) = \frac{t}{T} - \frac{1}{2T}, \tag{2.11}$$

where X_t is the value of the measured material property (Hardness or elastic modulus) for the test t, where $t \in [1, T] \subset \mathbb{N}^*$ corresponds to the numbering of the sorted values of X_t and T is the total number of tests. As each phase produces a Gaussian distribution, then the experimental CDF $D(X_t)$ approaches the sum of each individual phase CDF, denoted $D_{\text{fit}}(x)$. $D(X_t)$ is fitted with the following equation:

$$D_{\mathrm{fit}}(x) = \sum_{i=1}^{N-1} \frac{1}{2} K_i \left(1 + \operatorname{erf}\left(\frac{x - m_i}{\sqrt{2}\,\sigma_i}\right)\right) + \frac{1}{2}\left(1 - \sum_{i=1}^{N-1} K_i\right) \left(1 + \operatorname{erf}\left(\frac{x - m_N}{\sqrt{2}\,\sigma_N}\right)\right) \tag{2.12}$$

where erf is the error function, x is any positive mechanical property value, m_i is the mean property value of the phase i, σ_i is the corresponding standard deviation, K_i is the surface fraction of each phase i and N is the number of material phases. As the total sum of surface fraction must be equal to 1 and to reduce fitting parameters, the surface fraction of the N-th phase is $K_N = 1 - \sum_{i=1}^{N-1} K_i$.

The method functions well for composites with similar elastic properties. There is a drawback for very heterogeneous samples like in the present work as most statistical events are a composite response. LEISEN ET AL. (2012) suggested to adapt an extrapolation formalism to such heterogeneous systems by following an empirical framework. Some shortcomings are present due to the complexity of the procedure, including systematic error when the used extrapolating equation overfits the curves. A different approach was proposed by JAKES ET AL. (2008 2009) and ZHU (2011) (see also ZHU AND ZENG 2012) where they use eq. (2.9) at their advantage as the additional phase induces a structural compliance C_s. The former suggests to calculate this compliance for each test as it is done for determining the machine compliance C_m, slope of $\sqrt{L}/S$ versus $\sqrt{L}$ also known as the SYS plot after Stone, Yoder, and Sproul (1991). However they make the hypothesis that C_s is depth-independent, which seems an over-simplification of a heterogeneous system. ZHU (2011), on the contrary, do not make assumptions but rather determine a range for which the measurements have no effect from the other phase, e.g. the range for which the $\sqrt{L}/S$ curve is constant.

2.2 Atomic Force Microscopy

AFM is a nano-scale scanning technique which rely on the interaction between a probe, usually a silicon tip with a nanometric radius, and a sample surface. The tip is located at the end of a cantilever. The lateral displacement are controlled by the system through a scanner located either below the sample or attached to the cantilever. The vertical displacement is controlled by a piezoelectric transducer. A laser beam reflects onto the cantilever to reach a 4-quadrant photodiode. By recording this signal, the cantilever deflection can be interpreted and with the help of a feedback loop to the piezoelectric controller, the deflection can be kept constant upon scanning. A schematic can be seen on fig. 2.6.

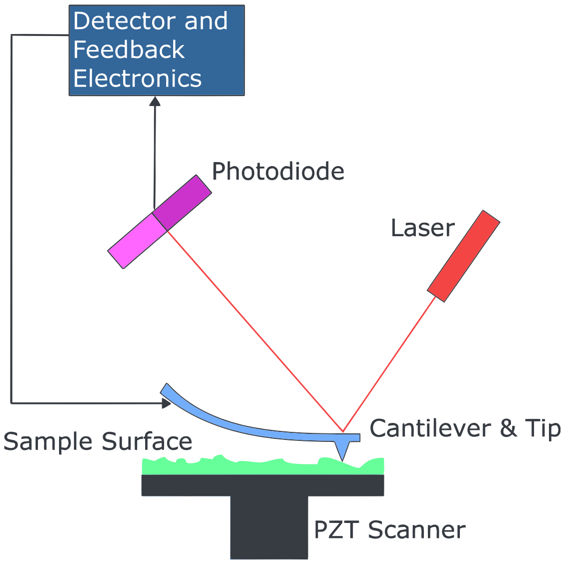

Figure 2.6: Block diagram of an AFM set-up. From Wikimedia Commons (2009)

It was first used to visualize the topography so as a constant force would be kept while the tip scans the surface, recording features in the Z-direction (Binnig et al. 1986). It is also used to measure other features with more complex set-ups, somewhat qualitatively so as it is difficult to know the exact configuration of the tip-sample contact. Due to its high resolution, AFM is the perfect tool to assess the intrinsic properties of micrometric particles. The present work used it as a measurement tool for three magnitudes. The first presented here is solely based on measuring topographical features in order to estimate the fracture property of the ceramic by using Irwin's near field method. The second technique revolves around the relationship between the dynamics of the cantilever vibration and the sample-tip contact. As the interaction is mainly elastic, it can be used to measure elastic properties. This measurement requires a special set-up and is called CR-AFM. The last method introduced here is electrochemical strain microscopy (ESM), where it is thought that ionic motions within the lithium host can excite the AFM probe and hence be measured when a voltage difference is applied between the tip and the sample.

2.2.1 Irwin's near field method

Significant plastic deformation normally occurs during fracturing in the vicinity of high stress concentration areas (Rice 1968, Chapter 3). Elastic fracture theories can however be adopted for cracks propagating beyond the plastic zone, where the apex of a crack (or a notch) produce a region with high stress distribution where plasticity is insignificant. Originally, fracture tests were done by four-point bending of a notched body. This can be also achieved by indenting brittle materials like metal oxides with sharp pyramidal tips, where the corners of the diamond produce high-stress zones from which cracks can grow past the plastically deformed zone. Theoretical fundamentals concerning elastic brittle fracture has been defined by G.R. Irwin, notably the introduction of the stress-intensity-factor noted K. The stress field has the highest value close to the crack tip. During loading, inplane tensile stress components increase until reaching a critical value called fracture toughness, denoted K_C. When it is reached ($K = K_C$), the energy is released by creating new traction-free surfaces, hence the crack is growing. This is schematically pictured in fig. 2.7.

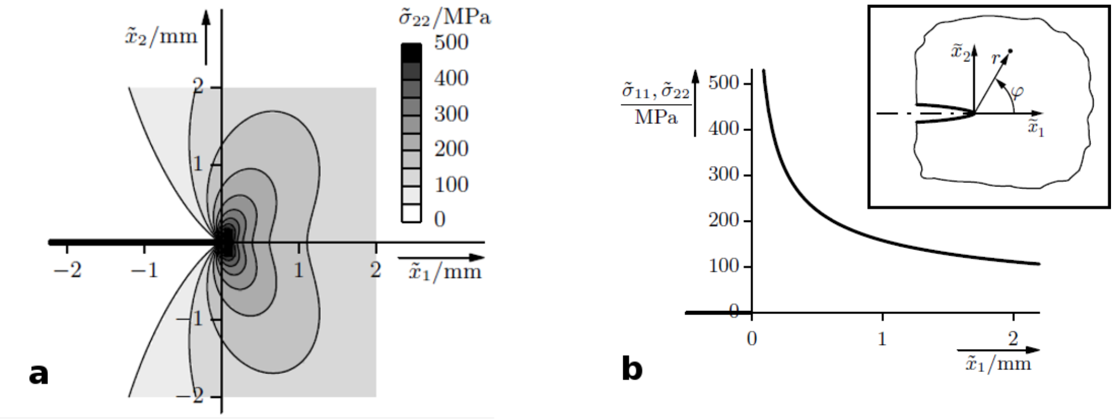

Figure 2.7: (a) Elastic stress field in mode I traction in the y-direction (here noted x_2) in the vicinity of a crack tip. (b) Same information along the crack direction (x-direction) ahead of the crack tip. Inset: coordinate system. Reproduced from Rösler et al. (2008, Chapter 5).

Cracks are classified by Irwin into three distinct groups (see fig. 2.8):

- mode I fracture where the stress fields induce an opening displacement,
- mode II fracture where the stress fields induce an in-plane shear,
- mode III fracture where the stress fields induce an out-of-plane shear.

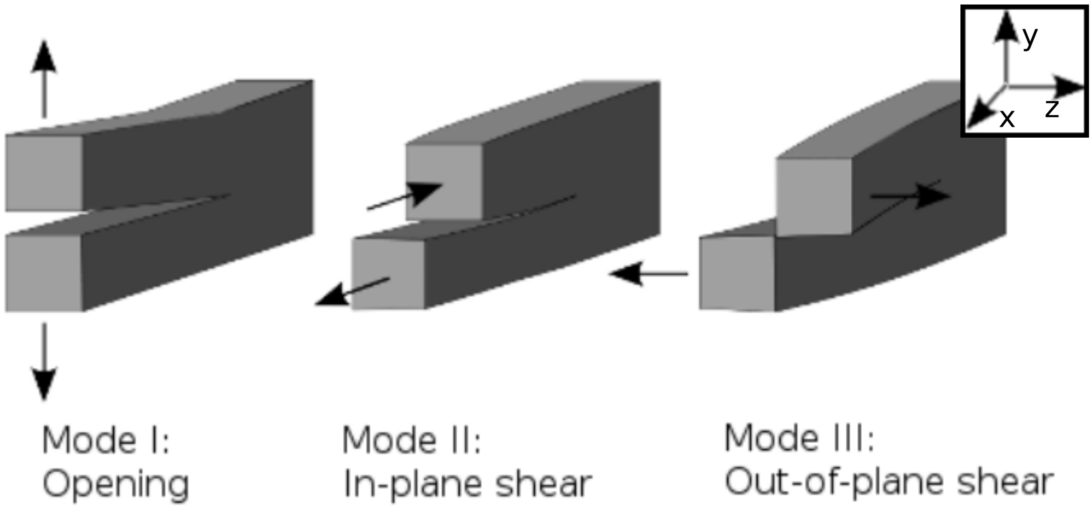

Figure 2.8: 3 fracture modes after Irwin. Reproduced from Rösler et al. (2008, Chapter 5). Inset shows the coordinate system system.

Using imaging techniques, it is difficult to identify mode II fracture. The two other modes can be identified with the opening width, called crack-opening displacement

(COD), and the Z-displacement of the crack walls. For a crack along the x-axis and its tip located at $(x = 0, y = 0)$, Irwin describes the *traction-free* crack displacements in plane strain as follows (Lawn 1993a):

$$u_y(X) = \begin{cases} \frac{(1-\nu^2)K_{IC}}{E}\sqrt{\frac{8X}{\pi}}, X \geq 0 \\ 0, X < 0 \end{cases} \tag{2.13}$$

$$u_z(X,Y) = \frac{(1+\nu)K_{IIIC}}{E}\sqrt{\frac{8\left\|\vec{r}\right\|}{\pi}}sin(\theta/2), \tag{2.14}$$

where $u_y(X)$ represents the near-tip crack opening displacement at position $(x = X, y = 0)$, u_z represents the mode III z-displacement in the near-tip surface for any (x, y), $\vec{r}$ is the position vector at coordinates $(x = X, y = Y)$, θ is the angle between the crack and the vector $\vec{r}$, E is the elastic modulus, ν represents Poisson's ratio, K_{IC} and K_{IIIC} are the mode I and the mode III fracture toughness, respectively. Equation (2.14) can be simplified as follows on the crack faces:

$$u_z(X) = \frac{(1+\nu)K_{IIIC}}{E}\sqrt{\frac{8X}{\pi}}, X \geq 0. \tag{2.15}$$

Evaluating the mode I crack tip toughness using imaging techniques was first introduced by Rödel et al. (1990). They used a Scanning Electron Microscope to image the near crack tip profile in alumina ceramics during four-point bending. Later, Meschke et al. (1997) started using AFM to make similar measurements. Ang et al. (2012) reused the AFM based technique for bovine teeth toughness where the topography measurement allowed not only for the mode I displacement to be measured but also the mode III. For this, they indented with a Vicker's tip to produce cracks several tens of micrometers long. A rule-of-thumb was suggested to have traction-free crack faces outside of the plastic zone: the crack length to indentation radius ratio should have a minimum of 1:3(Ang et al. 2012).

K_C is directly correlated with the energy release rate G, the energy per unit surface released when new surfaces are created (see eq. (1.8)). In the ideal case there is only mode I displacement, no bridging action and stress-free crack walls, we can assume that $K_C = K_{IC}$. The bridging condition is almost systematically respected for brittle ceramics, so as the crack needs to grow above a few nanometers as the bridging action of inter-ionic bounds does not extend the nanometric scale. However plastic deformation occurs at the micrometric scale and the plastic zone can produce residual tensile elastic stresses after the sample is unloaded. Moreover it is suspected that the grains of lithium manganese oxide crack under cleavage fracture. The crystal orientation plays a role as fracture does not solely depend on the stress-intensity-factor field but also on the energy release rate of the different cleavage planes. Hence it is possible that mixed-mode fracture occurs to accommodate for the crystal orientation.

To the best of our knowledge, this technique has been used only on polycrystalline bulk samples. It is proposed in the present work to extend its use to micro-metric particles as nanoindentation with cube-corner tips allows for crack initiation at just a few mN (Pharr 1998). Ultra sharp AFM tips were developed with an apex radius in the 2–5 nm range, allowing for COD measurements of narrower cracks.

2.2.2 Contact Resonance AFM

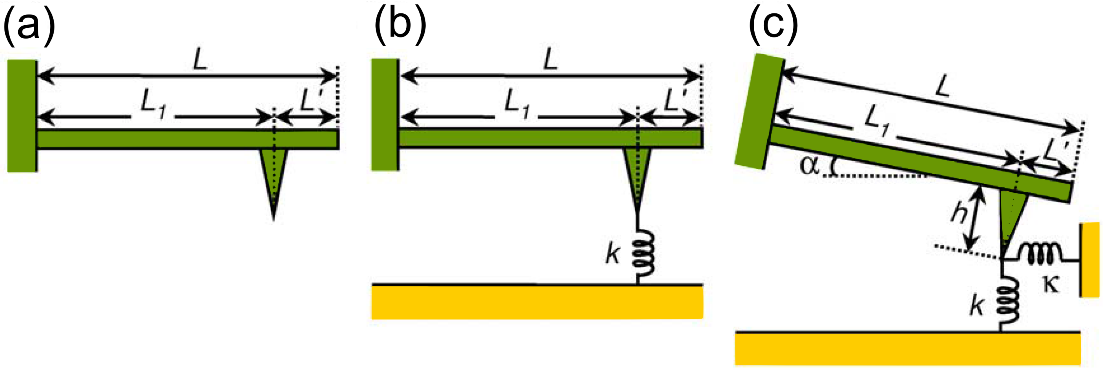

Figure 2.9: Schematics of the cantilever geometry for the models used in CR-AFM. The boundary conditions correspond to (a) tip out of contact (free) ; tip in contact considering (b) only an elastic vertical oscillator and (c) normal and tangential forces.

IIT has a few hindrances: it has a limited spatial resolution to study the intrinsic mechanical properties of micro-metric particles and it is destructive. AFM seems to be an attractive alternative as it is based on elastic interactions between a sensor tip and the sample. It can measure features down to the nano-meter scale without damaging the sample. If one can understand the mechanics of the tip-sample contact, nano-mechanical properties can be measured. IIT present the advantage of having a well defined geometry, enabling quantitative measurements more simply particularly since the birth of the Oliver and Pharr method. But several AFM-based techniques have been developed for the same purpose, yet the most appropriate for stiff materials such as ceramics is atomic force acoustic microscopy (AFAM) (Rabe and Arnold 1994; Yamanaka et al. 1994) which has recently also been called CR-AFM (Hurley 2009). An actuator is placed below the sample to transmit waves in the MHz range. Each AFM cantilever has a unique set of resonance frequencies depending on its spring constant k_{lever}, which depends on the shape, the geometrical dimensions and the material properties of the beam. If its geometry is simplified to a simple cuboid, its theoretical spring constant k_{lever} is:

$$k_{\text{lever}} = \frac{Eb^3w}{4L^3}, \tag{2.16}$$

where b, w and L are the thickness, the width and the length of the cuboid, respectively, and E is Young's modulus (Hurley 2009). The resonance frequencies f_n^0 can be calculated assuming a mass-distributed model with a beam of density ρ clamped at one end by solving the following eqs. (2.17) and (2.18) (Rabe 2006):

$$(x_n^0 L)^2 = 4\pi f_n^0 \frac{L^2}{E}\sqrt{\frac{3\rho}{E}} = f_n^0 (c_B L)^2 \tag{2.17}$$

and

$$1 + cos(x_n^0 L) cosh(x_n^0 L) = 0, \tag{2.18}$$

where f_n^0 and x_n^0 are the resonance frequency and the wave number of the nth free flexural mode, respectively, and c_B is a parameter depending on the cantilever properties. Solving eq. (2.18) to find the roots of the x_n^0s and re-arranging eq. (2.17), the ratios between the first three f_n^0 can be found:

$f_2^0 / f_1^0 = 6.27,$
$f_3^0 / f_1^0 = 17.55.$

These ratios can be compared to experimentally measured resonance frequencies for determining if the cantilever can be simplified to a simple cuboid. As soon as the tip is brought into contact with the sample surface, the mechanical boundary conditions of the cantilever are changed because of the tip-sample interaction. The frequencies of the resonant modes increase. This shift of resonance frequencies depends on the mechanical properties of the sample and the area of contact. The contact-resonance frequency shifts to higher values on stiffer materials. If a constant force is applied and if the resonance frequency is tracked, a qualitative stiffness map can be imaged. By calibrating the system on known samples and measuring more than one resonant vibrational mode, quantitative measurements can be achieved (Rabe et al. 2002). The models used to solve this problem are depicted in fig. 2.9. Figure (a) corresponds to the free-cantilever problem. Figure (b) corresponds to the simplest contact dynamics where the interaction is a simple elastic vertical oscillator of stiffness k. The objective of the measurement is hence to find k. In this configuration, a new variable must be added, L_1, which is the position of the tip on the cantilever. Its reciprocal is denoted $L' = L - L_1$ and the corresponding ratio $\gamma = L_1/L$. The solution of this problem can be found in textbooks (Hurley 2009):

$$\frac{k}{k_{\text{lever}}} = \frac{2}{3}(x_n L\gamma)^3 \frac{(1 + \cos(x_n L)\cosh(x_n L))}{D}, \tag{2.19}$$

where

$$\begin{aligned} D = \Big[&\sin\Big(x_nL(1-\gamma)\Big)\cosh\Big(x_nL(1-\gamma)\Big) \\ &\qquad - \cos\Big(x_nL(1-\gamma)\Big)\sinh\Big(x_nL(1-\gamma)\Big)\Big] \\ &\qquad \times \Big[1-\cos(x_nL\gamma)\cosh(x_nL\gamma)\Big] \\ - \Big[&sin(x_nL\gamma)\cosh(x_nL\gamma) - \cos(x_nL\gamma)\sinh(x_nL\gamma)\Big] \\ &\qquad \times \Big[1+\cos\Big(x_nL(1-\gamma)\Big)\cosh\Big(x_nL(1-\gamma)\Big)\Big]. \end{aligned}$$

In order to find k, x_nL needs to be first obtained from the resonance frequency measurements using eq. (2.18):

$$x_nL = c_BL\sqrt{f_n} = x_n^0L\sqrt{\frac{f_n}{f_n^0}}, \tag{2.20}$$

where f_n is the nth contact flexural mode resonance frequency. There are two unknown variables left, k and L_1, that can be found if at least two contact resonance frequencies are measured by solving eq. (2.19) twice.

If lateral forces κ are taken into account as depicted in fig. 2.9c, the tip height h and the cantilever angle α must also be added to the boundary conditions, significantly increasing the complexity of the problem. Solutions can be found in textbooks (RABE 2006; HURLEY 2009) and will not be included in this thesis because they were not used.

The next step consists of translating the qualitative information from the contact stiffness k into a quantitative material properties, e.g. Young's modulus E or indentation modulus M. Considering a Hertzian contact (sphere on flat surface), the tip-sample interaction force k is

$$k = 2aE_{eff}, \tag{2.21}$$

where E_{eff} was defined in eq. (2.7) and a is the contact radius of the Hertzian contact given by

$$a = \sqrt[3]{\frac{3RL}{4E_{eff}}}, \tag{2.22}$$

where L is the static load applied to the tip and R the curvature radius of the tip. The approach developed by RABE ET AL. (2002) consists of eliminating a (and hence L and R_{tip}) by calibrating the tip on a known reference sample. Experimentally this is done by applying the same sets of deflection force onto the cantilever alternatively on the reference sample(s) and the sample of study to find the corresponding contact stiffnesses k_{ref} and k. E_{eff} can be deduced from E_{eff}^{ref} as follows:

$$E_{eff} = E_{eff}^{ref} \left(\frac{\frac{k}{k_{\text{lever}}}}{\frac{k_{ref}}{k_{\text{lever}}}} \right)^{1.5} . \tag{2.23}$$

The exponent (1.5) corresponds to m in eq. (2.1) for the elastic recovery upon unloading of an indenting spherical tip. E or M can now be deduced from eq. (2.7). The principles of elastic property measurement in section 2.1.2.3 also hold for this section, notably concerning elastic anisotropy of the sample of study.

2.2.3 Electrochemical Strain Microscopy AFM

Application of Piezoresponse Force Microscopy (PFM) to non-ferroelectric ionic conductors by Morozovska et al. (2010) initiated ESM in 2010. Using a conductive AFM cantilever, the user can apply an alternative current (AC) between the tip (in contact) and the sample that induces an alternating mechanical strain which in return excites the cantilever and hence can be measured. Ideally, this signal is induced solely by an ionic-mechanical coupling, enabling characterization of the ionic properties of the sample at the grain level. This would contrast with other electrochemical characterization methods such as impedance spectroscopy and titration techniques which are non-local. In reality however, several mechanisms are taking place simultaneously besides ionic motion (Kalinin and Morozovska 2014): space charge, flexoelectricity, dipolar contributions and other mechanisms depending on the sample and tip properties. As it is thought that ionic motion is much slower than the different other processes, a different approach was suggested (Guo et al. 2011) called *time spectroscopy*. The building block of this experiment consists of applying a direct current (DC) voltage pulse followed by an AC excitation. After releasing a positive (negative) DC pulse, ions are moving towards (outwards) from the tip. Consequently the ESM signal increases (decreases), respectively. Therefore, the variation of the ESM response after the DC pulse is predominantly governed by ionic diffusion. The technique is illustrated in fig. 2.10. Local space charge relaxation also occurs but at very different length scales. Considering the current material of study, $LiMn_2O_4$, with a static dielectric permittivity of about 10 (Hoang 2014) , an electrical conductivity of 10^{-4}–10^{-2} S·m^{-1} (Guan and Liu 1998; Park et al. 2010) and a lithium diffusion coefficient of 10^{-16}–10^{-13} m^2·s^{-1} (Park et al. 2010),the space charge relaxation time is 10^{-8}–10^{-6} s while the diffusion relaxation time for the ESM probed volume is 10^{-3}–10^{2}s (Jesse et al. 2011).

To sum up, while the total ESM response is the sum of several mechanisms, the *variation* of the signal after a DC excitation lies in the order of the second and has an ionic origin. Monitoring the timely evolution of the signal allows for *time spectroscopy* measurements. By applying successive blocks with different DC voltages, a *voltage* *spectroscopy* measurement is carried out. Plotting the voltage dependence of the ESM signal can also give some information on the material. The methods are also illustrated in the experimental part, section 4.3.2.3 (see figs. 4.2 and 4.3).

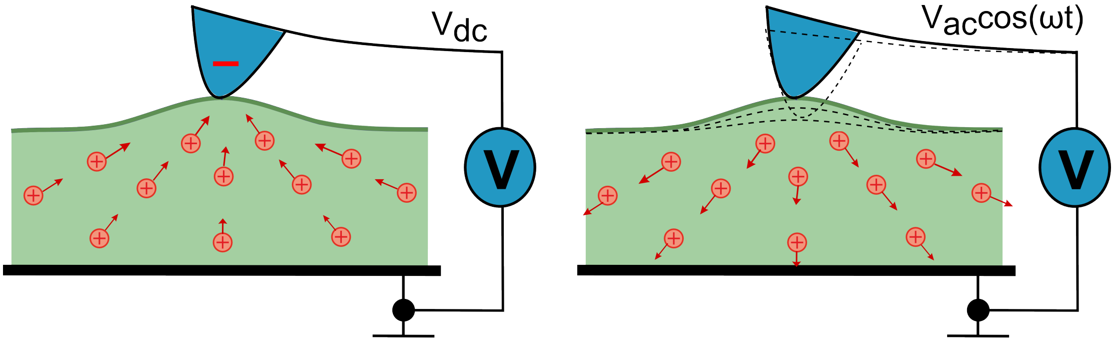

(a) DC ON (b) DC OFF

Figure 2.10: Schematics of time spectroscopy measurement: (a) first a DC pulse is applied and a reversible local change of ion concentration occurs. Then (b) the DC is turned off and the concentration field returns to its original state during which an AC is applied to monitor this evolution. Credits: Sergey Yu. Luchkin

To explain the origin of the signal, two phenomena should be carefully distinguished: one occurring because of the DC pulses in the time domain and an other one because of the AC excitation in the frequency domain. Most of the models so far derive from the first one proposed by MOROZOVSKA ET AL. (2010) where a diffusion-based mechanism is considered for both cases. Considering this hypothesis, the surface moves below the tip because lithium ions (or other mobile ions) diffuse within the solid and change locally the volume of the crystal through Vegard's tensor denoted here in its molar form Ω_{Li} in mol·m^{-3}.

Time domain

The analytical description of MOROZOVSKA ET AL. (2010) considers two scenarios where the boundary conditions at the tip are either concentration-determined, i.e. the tip is ion-blocking and there is only exchange of electrons at the tip-sample boundary ; or are flux-determined, i.e. there is a constant ionic exchange at the interface. Only considering the former case, the out-of-plane strain (denoted u_z) relaxation centered at the tip-sample contact in the DC off state after a square pulse is described as:

$$u_z(t \gg t_0) \approx -(1+\nu)\frac{\Omega_{Li}\bar{\phi}_0 R_{tip}^2 t_0}{6\eta\sqrt{\pi D_0}t^{3/2}}, \tag{2.24}$$

where R_{tip} is the tip contact radius, $\bar{\phi}_0$ is the applied voltage, t_0 indicates the end time of a DC pulse starting at $t = 0$, D_0 is the diffusion coefficient of Li and η is a coefficient related to the ohmic behavior of the tip contact. A power law follows with an exponent equal to -3/2. If u_z can be measured, the ratio $R_{tip}^2/\sqrt{D_0}$ could be derived while all other parameters can be determined with other methods. However measuring the strain in a static regime by AFM is challenging due to pink (1/f) noise (Guo et al. 2011). The ESM signal is a strain measured in the high frequency regime with proper lock-in amplification and the origin of the signal is discussed presently.

Frequency domain

Considering the same boundary conditions with an ion-blocking tip and with the same diffusion-driven process, the frequency dependent strain at the center of the contact becomes (Morozovska et al. 2010):

$$u_z(\omega) = \frac{-(1+\nu)\Omega V(\omega)}{\eta}\frac{2D_0}{i\omega R_{tip}}\left[\exp\left(-(1+i)\sqrt{\frac{\omega R_{tip}^2}{2D_0}}\right) - 1 \right. \\ \left. + (1+i)\sqrt{\frac{\omega R_{tip}^2}{2D_0}}\right]. \quad (2.25)$$

One important feature here is that it is linearly dependent on Vegard's tensor, hence it is intrinsically related to ions diffusing and locally changing the lattice volume at high speed. Later, the same group developed an analytical model using the same approach only for the special case of a mixed electronic-ionic conductor with the ion-blocking boundary condition (Morozovska et al. 2012b). This model added a layer of complexity as compared to the previous one as they considered the fact that non-electroneutrality can arise at the local scale at high frequency depending on the electronic and ionic behavior of some ceramics. They quantitatively calculated the frequency dependent response of the system for $LiMn_2O_4$ and $LiCoO_2$. An important result from this study is an out-of-plane displacement well below 1 pm for frequencies above 10 kHZ. Using the same diffusion-driven hypothesis, a finite element model was developed to study the time and length scales of the dynamic response more thoroughly (Tselev et al. 2014), confirming the previous result. They also calculated the mean oscillation path of an ion for several frequencies with a diffusion parameter $D_0 = 10^{-15}$ $m^2 \cdot s^{-1}$, a tip contact radius $R_{tip} = 5$ nm and an applied AC voltage $V_{ac} = 0.1$ V listed in table 2.2. Comparing this values to the lattice parameter of $LiMn_2O_4$ (8.24Å) or any other similar material raises doubt concerning the significance of Vegard's contribution to the ESM signal at high frequencies.

This could be suspected as it is known that measurements by impedance spectroscopy, which is a common tool used in electrochemistry, do not give information on the ionic transport properties of a material at high frequencies, but rather at frequencies below 1 kHz, as ionic diffusion mechanisms are relatively slow (Huggins 2009, chapter 17). However it was experimentally demonstrated that there is an ionic contribution to the signal with typical relaxation processes in time spectroscopy measurements at

Frequency f (Hz)	mean oscillation path length (nm)
100	0.32
10^4	3.2×10^{-3}
10^6	3.2×10^{-5}

Table 2.2: Mean oscillation path lengths of lithium ions in a material of diffusion parameter $D_0 = 10^{-15}$ $\mathrm{m}^2 \cdot \mathrm{s}^{-1}$ under an AFM tip applying an AC excitation of amplitude $V_{ac} = 0.1$ V with a tip contact radius $R_{tip} = 5$ nm. Source: Tselev et al. (2014)

frequencies above 200 kHz (Balke et al. 2010; Jesse et al. 2011; Luchkin et al. 2015). Hence the origin of the signal in the frequency regime is still an open question.

Part II

Objectives

Electrodes used in LiBs consist often of highly heterogeneous composites of which the active material are solid micro-metric particles. Mechanical failure is commonly induced by lithium concentration gradient building up upon cycling. The intrinsic micro-structural properties of the ceramics are the parameters influencing its mechanical behavior, i.e. the elastic modulus, the fracture toughness and the lithium diffusivity as detailed in section 1.2. Hence measuring these properties at the local scale is necessary to better design battery components.

The primary goal of this work is to design new characterization methods to measure the intrinsic mechanical properties of micro-metric particles, in particular the elastic modulus and the fracture toughness. The first approach is to implement the statistical analysis developed by ULM AND VANDAMME (2010) for nanoindentation and improve it for highly heterogeneous composites. Then techniques based on Atomic Force Microscopy will be used in order to measure qualitatively and whenever possible quantitatively both the elastic properties and the fracture toughness. The accuracy and the easiness of the methods will be discussed.

The second goal of this work is to better comprehend Electrochemical Strain Microscopy as it can be used to measure the intrinsic ionic properties of micro-metric particles. As experimental measurements are done elsewhere, this thesis focuses on the theoretical aspect of the machine. In particular, as it seems unlikely that the ESM signal originates from a diffusion-driven process, a different mechanism will be suggested and implemented in a finite element model. Consequently, the results from the model will be directly compared to experimental measurements.

Spinel lithium manganese (III,IV) oxide ($LiMn_2O_4$) is the material of study. It is the perfect candidate as it is commercially available on the battery market while estimates for its elastic modulus ranges over 1 order of magnitude (from 10 GPa to 200 GPa) and for its diffusion parameter ranges over several orders of magnitude (from 10^{-16} $m^2 \cdot s^{-1}$ to 10^{-13} $m^2 \cdot s^{-1}$) and was never locally characterized. Moreover, no previous mention of its fracture toughness could be found. Hence, as a parallel objective, the properties of this material will be characterized more thoroughly using the aforementioned techniques and discussed.

Part III

Experimental

3 Chapter
Sample preparation

3.1 Commercial batteries

$LiMn_2O_4$-cathode samples were obtained from commercially available 18650 cells pictured in fig. 3.1. The manufacturer's data are listed in table 3.1.

Figure 3.1: Commercial cell

Typical capacity	1200 mAh
Minimum capacity	1100 mAh
Nominal Voltage	3.8 V
Charge Voltage	4.2 V
Discharge cut-off voltage	2.5 V
Charge current (max)	2 A ($<$ 1.7 C-Rate)
Discharge current(max)	20 A ($<$ 17 C-Rate)
Volumetric energy density	286 Wh/l
Gravimetric energy density	101 Wh/kg

Table 3.1: Cell specifications

Cycling
Cells were cycled in 3 different ways using constant current (CC) / constant current constant voltage (CCCV) protocols with a Cell Test System (Basytec, Germany). Eight cells were cycled 3 times at 0.2 C-Rate following protocol 1 in order to measure their real capacity. Then six of them were charged until reaching the desired SoC: 0 %, 25 %, 50 %, 75 % or 100 % while two of them were discharged down to 50 % depth of discharge (DoD). This was done to see if there is a difference in the properties between

charging or discharging.

```
input  : fresh cell
         charge/discharge current $I_{cyc}$;                  // 0.2 or 1 C-Rate
         number of cycles $N_{end}$;                           // 3 or 100 cycles
         end state of charge $SoC_d$;   // 0, 25, 50, 75 or 100 % SoC
output : cell ready for opening
         Real cell capacity $C_{real}$
/* cycling                                                              */
while $N < N_{end}$ do
    discharge at $I_{cyc}$ C-Rate until 2.5 V;
    wait 15 s;
    charge at $I_{cyc}$ C-Rate until 4.2 V ;                          // CC
    charge at 4.2 V until $< I_{cyc}/5$ C-Rate;                        // CV
    wait 15 s;
    N = N+1;
end
/* finalizing                                                           */
if $SoC_d == 0\ \%$ then                                 /* deep discharge */
    discharge at 0.2 C-Rate until 2.3 V;                               // CC
    discharge at 2.3 V until <0.04 C-Rate;                             // CV
else if $SoC_d == 100\ \%$ then                           /* normal charge */
    discharge at 0.2 C-Rate until 2.5 V;
    charge at 0.2 C-Rate until 4.2 V ;                                 // CC
    charge at 4.2 V until <0.04 C-Rate;                                // CV
else
    discharge at 0.2 C-Rate until 2.5 V;
    charge at 0.2 C-Rate until $SoC_{current} == SoC_d$ ;
end
```

Protocol 1: Normal CC/CCCV cycling procedure. N is the current cycle. SoC_d is the desired State of Charge to reach after cycling. $SoC_{current}$ is the current state of charge and equal to $C_{current}/C_{real}$ with $C_{current}$ the current capacity (in Ah) and C_{real} the real total capacity measured during the first `while` loop.

Three cells were cycled harshly at the maximum C-rate (see table 3.1) following protocol 2. This conditioning could not be done in our laboratory as the cycling system could not reach high currents but was carried out by the “Zentrum für Sonnenenergie- und Wasserstoff-Forschung” in Ulm (ZSW) (see Waldmann et al. (2014)). The first protocol 1 was then used in order to reach the following SoCs: 0 %, 50 % and 100 % SoC. Two cells were cycled 100 times at 1 C-Rate following protocol 1 before opening at 0 % and 50 % SoC. All the samples are listed in table 3.2.

Opening

For each cell, the case has been carefully opened in an argon-filled glove box in such a

```
input  : fresh cell
         end State of Health 80 %
         end state of charge $SoC_d$;          // 0, 50 or 100 % SoC
output : fast aged cell
/* cycling                                                        */
while $SoH > 80\,\%$ do
    discharge at 16 C-Rate until 2.5 V;                     // CC
    wait 15 s;
    charge at 1.6 C-Rate until 4.2 V ;                      // CC
    charge at 4.2 V until <0.2 C-Rate;                      // CV
    wait 15 s;
    N = N+1;
end
/* finalizing                                                     */
discharge at 1 C-Rate until 3 V;
```

Protocol 2: fast CC/CCCV cycling procedure. SoH is the current state of health measured at each cycle. In the finalizing procedure, the cells were brought back to their original voltage. Courtesy of ZSW (Waldmann et al. 2014).

way that no short circuit occurs with the following procedure:

1. The negative side of the case is cut off with a metallic wheel opener (⚠ possible shortcuts).
2. The positive side is cut off following the notch (see fig. 3.1).
3. Some drops of dimethyl carbonate (DMC) is poured from one end to wet the system and ease the uncoiling.
4. The rest of the case is peeled off with pliers and a ceramic knife.
5. The layers are uncoiled then the cathode and the separator are separated from each other. Particles falling off from the cathode were gathered and put in a first bottle. **Note:** the anode strongly sticks to the separator.
6. Some pieces (about 0.5×1 cm^2) are cut out and put in another bottle.
7. The anode is removed from the separator, cut into pieces of the same size and put into a third bottle.
8. The contents are throughly washed with DMC twice, left overnight in DMC and washed again twice.

9. The bottles are brought outside the glovebox and were left under an outlet until dried. **Note:** while the anode material is sensitive to air as lithium oxidizes or reacts with water, the cathode particles are relatively stable. It is however possible that some electrolyte salt is left and reacts with air.

The fallen out $LiMn_2O_4$ powder is used for XRD and ICP-OES characterization. The cathode pieces are embedded for SEM imaging, nanoindentation, and AFM measurements. Anodes were not studied.

Embedding

The sample sections were embedded in a commercial epoxy for mechanical stability during both polishing and indentation. The epoxy infiltrates the PVDF mesh. Thus the studied specimen consists of a composite of $LiMn_2O_4$ active particles embedded in a matrix which turns to be a mixture of PVDF, carbon black, and epoxy. For this reason the measured matrix properties do not correspond to the ones of PVDF. The properties of the epoxy, and at some extend of the carbon black, will make up for most of the matrix mechanical properties. After the epoxy has hardened, the sample is polished on a Struers rotoforce. First, wet grinding is carried out with subsequent 1200 to 4000 silicon carbide foils. Then 3 µm and 1 µm diamond suspensions are used to polish followed by Struers OP-S abrasive solution. Last, Argon-based Ion-Beam Polishing was carried out: a 15 minute-long step of cleaning at a 10° angle followed by a 30 minute-long step of polishing at a 4° angle. Figure 3.2 shows a cross-section of this sample. The dark areas correspond to epoxy, the brighter particles are $LiMn_2O_4$ and the very bright band is the aluminum current collector.

Additionally reference powders were embedded and polished with the same protocol: A commercial powder of lithium manganese(III, IV) oxide (CAS 12057-17-9), a commercial powder of manganese(IV) oxide (CAS 1313-13-9) and amorphous silica particles. The latter was specifically prepared to mimic an electrode and was prepared before this work [1]. 14 µm big amorphous silica particles were milled with PVDF 6020 (Solvay Solexis) and carbon black to obtain a homogeneous mixture similar to the ones used in batteries. The whole was hot pressed at 300 bars and 217° Celsius and coated onto an aluminum sheet. The sample thickness is about 170 µm. A cross-section of the sample was then prepared with the same above mentioned method without Ion-Beam Polishing, see fig. 3.3. As the silica particles are less reflective than the cathode material particles, a higher brightness was used. For this reason carbon black powder induces very bright areas in the epoxy. A commercial powder of lithium manganese(III, IV) oxide (CAS 12057-17-9) and a commercial powder of manganese(IV) oxide (CAS 1313-13-9) were also embedded.

---

[1] courtesy of Daniel Leisen, see LEISEN ET AL. (2012)

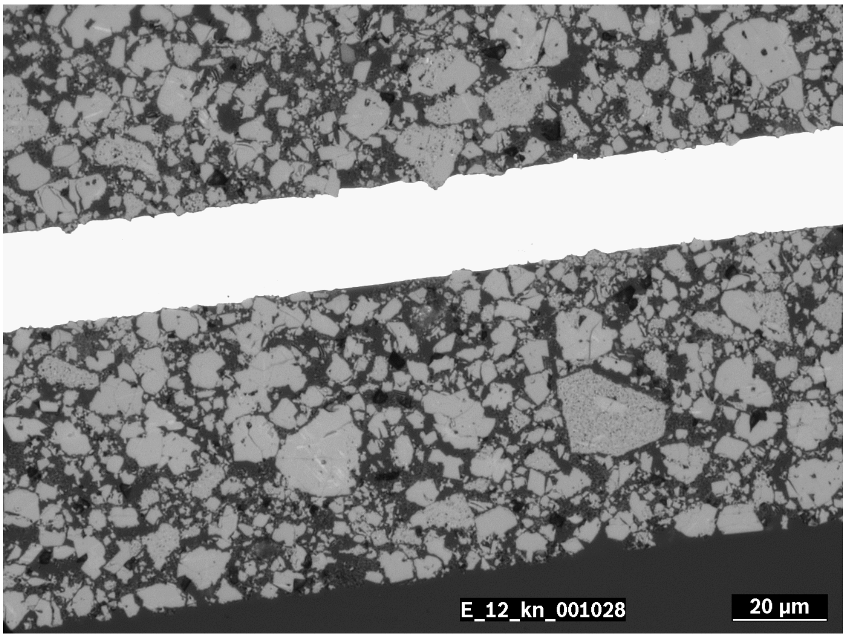

Figure 3.2: Optical image of the $LiMn_2O_4$ electrode cross-section. The dark area is the matrix consisting of a mix of epoxy, carbon black and PVDF. The bright particles correspond to the lithium manganese oxide active material and the very bright band corresponds to the aluminium current collector.

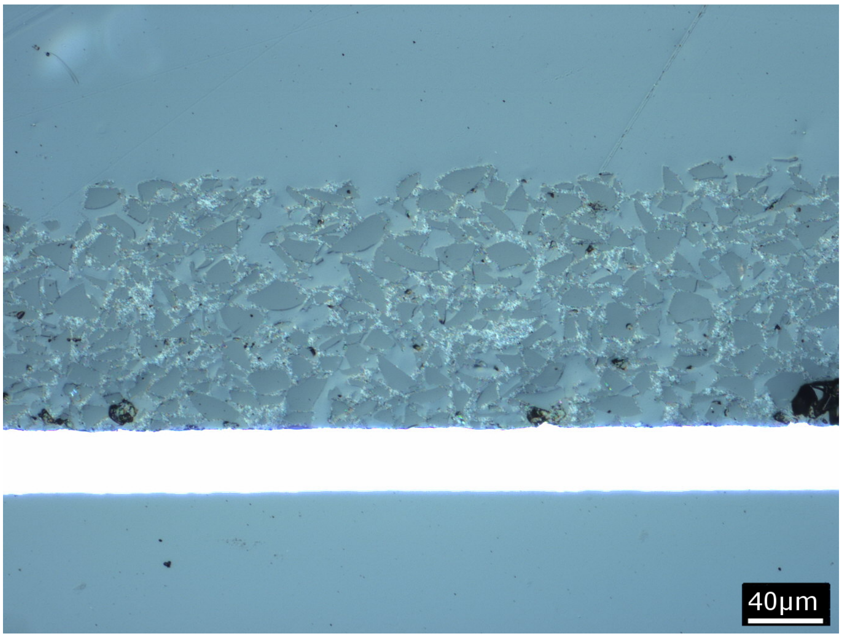

Figure 3.3: Optical image of the SiO_2 battery like sample cross-section. The light blue area corresponds to the epoxy/PVDF matrix, the dark blue particles correspond to the silica particles, the very bright band to the aluminum sheet, the dark areas to holes. The very bright dots between the silica particles are due to carbon black particles.

3.2 Wafers

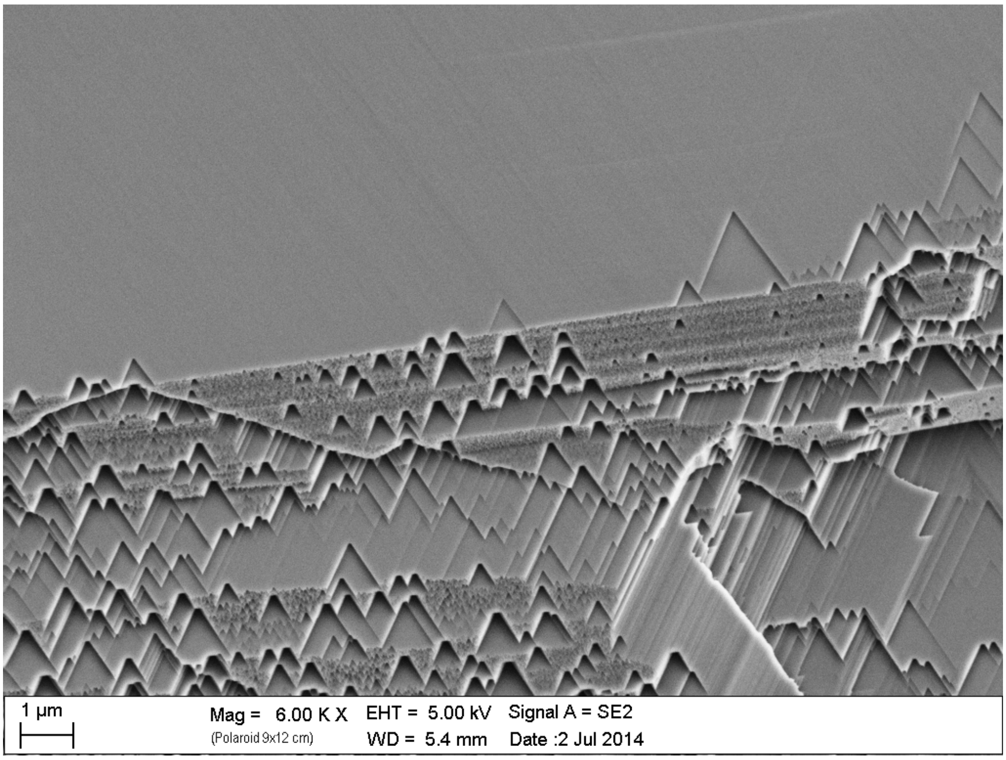

Figure 3.4: SEM image of a spinel $LiMn_2O_4$ (111) wafer synthesized on top of a (111) MnO wafer.

Kitta et al. (2013) developed a unique procedure to make single grains of spinel $LiMn_2O_4$ on a wafer with a single out-of-plane orientation: (111), (101) or (100). As the former was reported as the most stable, the procedure was repeated for this one only. A $10 \times 10 \times 0.5$ mm^3 precursor wafer of (111)-oriented manganese (II) monoxide MnO (SurfaceNet GmbH, Rheine, Germany) was acquired. It was cut into 16 identical smaller wafers with a diamond saw. Three wafers were then prepared. Each was cleaned in an ultrasonic acetone bath and then placed on a gold sheet inside a magnesium oxide crucible together with 10 mg of lithium hydroxide ($LiOH \cdot H_2O$) powder. The crucible is placed in an oven where the temperature is ramped up to 900°C at a 3K/min rate, then kept constant for 15 hours and finally slowly ramped down to room temperature at a 0.1 K/min rate (6 days). Figure 3.4 shows the final result of one of the wafers. Like for Kitta et al. (2013), typical triangular patterns can be recognized.

3.3 Sample review chart

Table 3.2 lists all the samples used in the thesis.

Sample name	State of charge	Aged	comments
Extracted from batteries			
C0SoC_1	0 %	✗	
C0SoC_2	0 %	✗	
C0SoC_100	0 %	✓ 100 cycles	
C0SoC_aged	0 %	✓ 80 % SoH	
C25SoC	25 %	✗	
C50SoC	50 %	✗	
C50DoD	50 % DoD	✗	
C50DoD_2	50 % DoD	✗	
C50SoC_100	50 %	✓ 100 cycles	
C50SoC_aged	50 %	✓ 78 % SoH	
C75SoC	75 %	✗	
C100SoC	100 %	✗	
C100SoC_aged	~~100 %~~	✓ 78 % SoH	cell dead at 4.08 V
Reference samples			
SiO2s	N/A	N/A	courtesy of LEISEN ET AL. (2012)
MnO2p	N/A	N/A	CAS 1313-13-9
LiMn2O4p	N/A	N/A	CAS 12057-17-9
Wafer	N/A	N/A	see KITTA ET AL. (2013) for synthesis

Table 3.2: List of samples. N/A means not applicable.

4 Chapter Characterization

This chapter relates to all the techniques used to study the material. The first section deals with composition characterization, the second section deals with nanoindentation — in other words mechanical characterization — and the last section deals with different imaging techniques which can also be used at some extend to characterize the composition and the mechanics.

4.1 Chemical Analysis

Powders from the cathode and the wafers were characterized by X-ray diffraction (XRD) (Bruker-AXS D8advance, Bruker, Germany) with Cobalt Kα radiation, Bragg-Brentano-optics, a 1 mm aperture slit, secondary monochromator and scintillation counter. The sample is irradiated over an surface area of about 7×20 mm^2 with a penetration depth of about 3 µm. It was used to determine the crystal structure by comparing the signal with the one obtained for spinel $LiMn_2O_4$. The lattice parameter was also calculated with the Rietveld fit program TOPAS by Bruker. Lithium atoms are so small that they are "invisible" to X-rays, making the lattice parameter change for different SoCs an indirect indication of lithium concentration. Results are shown in section 13.1.

The same batch of powder was dissolved in a mixture of chloric- and nitric acid. The solution was thereafter filtered and deposited onto a Pt-crucible, glown and dissolved by fusion with Lithiumtetra/-metaborate. inductively coupled plasma optical emission spectrometry (ICP-OES) (ICAP 6300 Spectrometer, EA-G-22-002 SOP, Thermo) scanned the different solutions. It was calibrated with certified standards of each respective element. This analysis was specifically targeted at determining the ratio of Li versus Mn or other metals, thence the lithium content was determined with the first solution as the second solvent contains lithium. Results are shown in section 13.3.

Raman spectroscopy with a confocal LabRAM Aramis Raman spectrometer (Horiba Jobin Yvon) was used on some battery samples (*C0SoC*, *C100SoC*) to characterize their composition qualitatively and locally. Results are shown in section 14.2.

4.2 Nanoindentation

A Nano Indenter XP by MTS Systems Corporation (now owned by Agilent Technologies recently renamed Keysight Technologies) has been used. A calibrated coil magnet drives the indenter tip, whose current-to-force relationship is known. A triple-capacitor-based gauge is used to measure the displacement. The resolutions of each are 50nN and $<$ 0.01nm respectively. The continuous stiffness measurement (CSM) option was used.

Elastic and hardness measurements

Samples have been indented by either cube-corner or Berkovich tips (indicated in the Results section). The former was originally used as it has the advantage of having a depth-to-area ratio 10 times smaller making the probed volume much smaller for equal depth, hence improving the lateral resolution and reducing the probability of composite response from the particle/matrix system. However Berkovich tips have a well known behavior with a smaller range for β (see Eq. (2.6) and HAY AND G.M. (1999)), produce significantly less or no pile up. Besides, friction between the tip and the sample can be disregarded. It was thenceforth used. When cube-corner tips were used, a penetration depth of 250 nm was set ; with Berkovich, the depth was fixed to 100 nm. These depths were assumed small enough as compared to the typical size of a particle (see fig. 3.2) while deep enough to avoid tip rounding inaccuracies in the first 10s of nm. Each sample has been indented several hundreds of times following the same procedure. Only one batch of indentation was carried out during a night in order to avoid noise caused by daytime activities. A batch always consisted of one small 3×3 indentation matrix on a reference fused silica sample and one indentation matrix with a size ranging from 10×10 to 20×30 indents on the sample of interest with a step size of 2 to 3 µm. Each following morning the tip area function was checked with data from the indents on silica and recalibrated if necessary. The Nanosuite software (Keysight Technologies) controlling the nanoindenter was used to make rough verifications of the measurements. Then the measurements were exported in coma-separated value files (`*.csv`) before being processed on Matlab. The indented area was then imaged by SEM and later analyzed. Due to the large amount of data and the complexity of measurements on composites, a specific procedure was developed to process them which is described in part IV. Nanoindentation results are shown in section 14.1.

Crack topography

Cube corner tips were used for an indentation depth of 400 nm, leaving a print of about 600 nm wide. Several grids of 5×5 indents with a spacing of 5 µm were done overnight. The areas were subsequently imaged by SEM to find cracks which are long enough to be mapped by AFM and did not grow too close to a particle edge or a defect (see fig. 4.1).

4.3 Imaging techniques

4.3.1 Scanning Electron Microscopes

SEM imaging was carried out on each sample with a Supra 35 VP (Carl Zeiss, Germany). Platinum palladium thin films are deposited on the cross-sections beforehand so as the top surface is conductive and can be grounded, epoxy being an insulator. SEM images can be found throughout parts IV and VI.

Electron backscatter diffraction (EBSD) was carried out with a Supra 55 VP (Carl Zeiss) on some of the reference samples (*LiMn2O4p*, *Wafer*) in order to determine the crystal orientations using as input the crystal structure determined by XRD. These data were used in sections 14.1.1 and 15.2.

Energy dispersive X-ray analysis (EDX) was occasionally carried out on the two aforementioned SEMs and results can be found in section 13.2 and appendix B.

4.3.2 Atomic Force Microscopes

Three different AFMs were used in this work depending on the application.

4.3.2.1 General topography imaging

A Dimension 3100 NanoScope (Digital Instruments, Santa Barbara, CA, USA) was used to image topography features of the particles in the laboratories of the Corporate Research unit of Robert Bosch GmbH (Gerlingen-Schillerhöhe, Germany).

Indent and pile up topography
Scans were carried out in tapping mode with OTESPA tips (Bruker, Germany) with a free resonance frequency of about 300 kHz and a spring constant around 42 N/m. This tip is relatively resistant and offers the advantage that its apex is visible from the optical microscope of the AFM. The scanning frequency was set to 1 Hz or less. Results are shown in section 14.1.1.

Crack topography
Figure 4.1 represents the workflow of COD measurements. Suitable cracks are first sought by means of SEM (see fig. 4.1a). Then they are imaged with the AFM using very sharp tips (TESP-SS, Bruker, 42N/m, 320kHz, 5 nm max radius). These tips are more fragile than OTESPA. For this reason the approach and the scan are done using a very small initial force setpoint (2 %) in order to find the cracks without damaging the tip. Large 20×20 μm^2 scans are carried out to find the crack at a frequency of about 0.1 Hz using a very low resolution (32 or 64 lines per image). Once a crack is found, the scan area is decreased to 1×1 μm^2 or less, the scan frequency increased to 1 Hz

or less, the image resolution is increased to 512 lines $\times$ 512 points and the force is regularly increased until trace and retrace lines are similar (see fig. 4.1c). TGX1 test grating samples (NT-MDT) are used before and after measurements to characterize the AFM tip sharpness using the same procedure.

For each crack image, u_y (COD) and u_z (tearing displacement) are measured on 12 cross-sections perpendicular to the crack for different distances X to the crack tip with the help of a semi-automated Matlab application (see fig. 4.1c). Care is given to take into account reverse tip imaging at the crack walls. K_{IC} and K_{IIIC} are calculated by measuring the slopes of $\sqrt{X}$ vs u_y and $\sqrt{X}$ vs u_z and putting them into eqs. (2.13) and (2.15). The reliability of the measurements is estimated by the coefficient of determination R^2 of the linear regression. Results are shown in section 15.1. A simulation of this procedure was also built and described in chapter 5.

4.3.2.2 Contact-Resonance Atomic Force Microscopy

The preparation of three specimens (0, 25 and 100 % SoC) were specifically changed for CR-AFM, as it requires a good transmission of the sound waves through the sample. They are first embedded in a metallic alloy composed of tin, copper and antimony (Balver Zinn Josef Jost GmbH & Co. KG, Germany) before being embedded in epoxy. The rest of the preparation is the same as in section 3.1. The samples are glued onto the actuator with silver paste.

A Dimension 3000 NanoScope (Digital Instruments, Santa Barbara, CA, USA) was employed for this study in the laboratories of Fraunhofer Institute for Nondestructive Testing (IZFP). As the detection electronics of this AFM have a sufficient bandwidth, the resonance frequencies are measured directly from the instrument. An in-house LabView application was used to control the actuator, the X-Y table, and gather the data from the detection system. The data are then exported in ASCII and processed with another LabView application.

Two types of AFM tips were used. The major part of the work was carried out with Point Probe Plus Non-Contact /Tapping Mode - Long Cantilever (PPP–NCL, NANOSENSORS, Switzerland) with a first free resonance frequency of about 190 kHz and a spring constant of 48 N/m. Some quantitative measurements were done with all-diamond tips: ND-SSCRL (NaDiaProbes series, Advanced Diamond Technologies, Romeoville, Illinois, USA), with an average first free resonance frequency of 80 kHz and a force constant of about 5.5 N/m.

Qualitative measurements were done with the PPP-NCL tips. Two types of image can be built:

Resonance frequency map For each pixel, the excitation frequency of the actuator was varied continuously over a fixed time interval to a maximum cut-off frequency while the force is kept constant. The contact resonance of the system is detected

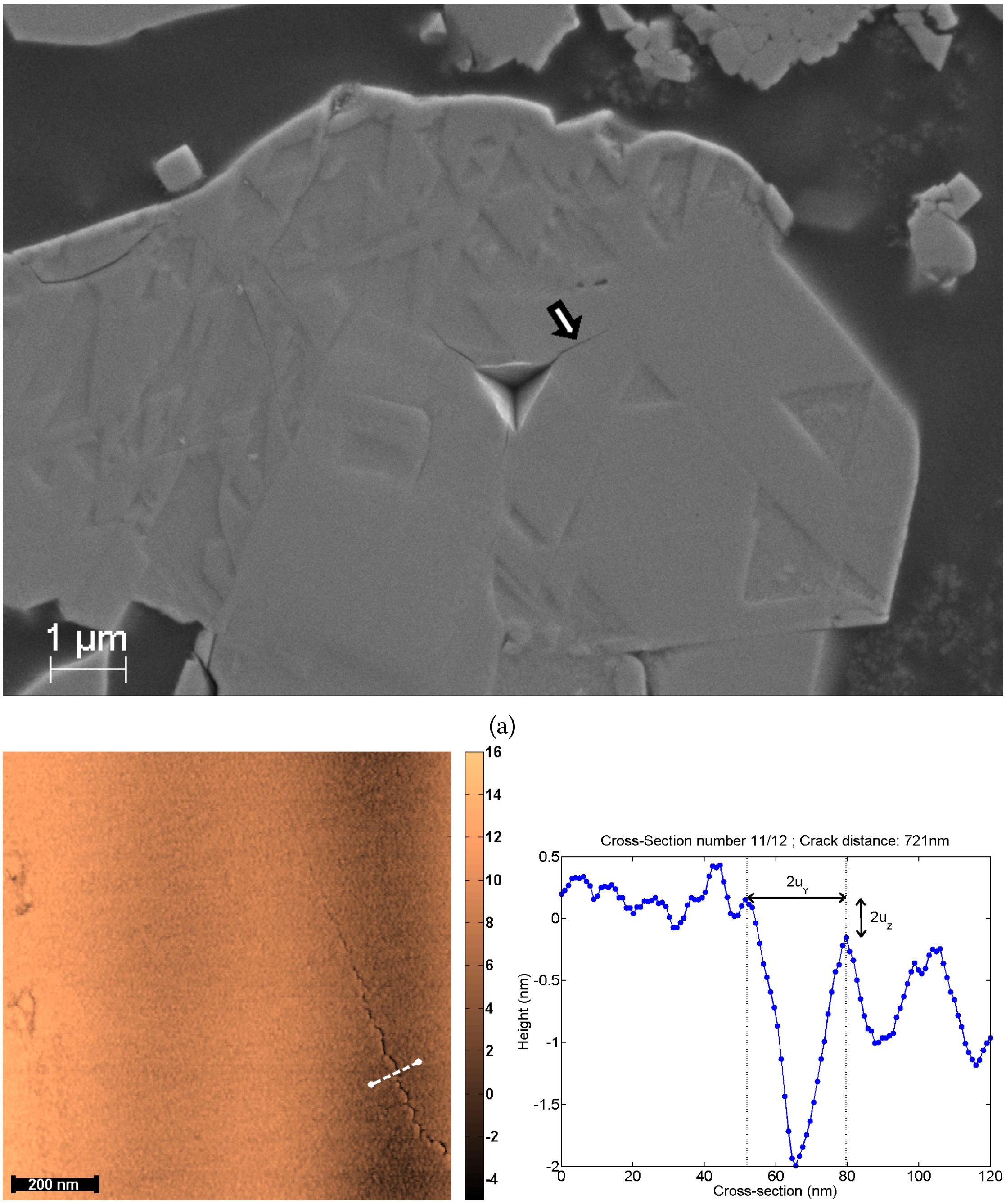

(a)

(b)

(c)

Figure 4.1: (a) SEM micrograph of a cube-corner indent in a $LiMn_2O_4$ particle. The cracks do not propagate straight from the corners of the indent. They are also not much longer than the indent. The arrow indicates the crack mapped by means of AFM and visible on (b). (c) is the cross-section indicated by a white line in (b) used to estimate u_y and u_z for X=721 nm.

by the center of the Gaussian distribution of the peak around the maximum cantilever vibration amplitude. The resonance frequency (in kHz) then gives the color of the associated pixel (in gray scale). This technique is relatively slow.

Amplitude map Upon scanning, both the applied force and the excitation frequency are kept constant. Each pixel gives the amplitude of the cantilever vibration (in Volt). High amplitudes indicate that the applied frequency is close or equal to the contact resonance frequency. Several maps at different frequencies are necessary to qualitatively differentiate the phases.

Quantitative measurements require reference samples in order to find k_{ref} in eq. (2.23) (see section 2.2.2). Fused Silica and Zerodur (Schott AG, Germany) were used as reference samples: they have well known elastic properties, their properties are close to the ones of $LiMn_2O_4$ and they are isotropic. Fused silica has an elastic modulus of 72 GPa and a Poisson's ratio of 0.18 ; Zerodur has an elastic modulus of 91 GPa and a Poisson's ratio of 0.24. Each time, one reference sample and one sample of study were glued onto an actuator and placed on the X-Y table. The measurements were repeated on each sample, one after the other, following the same procedure:

1. Scan the surface in contact mode with a low force to find a relatively flat area.
2. Immobilize the tip (scan size = 0 nm) and find the cantilever deflection force. Set the deflection to 10 nm.
3. Find at least two of the the first three contact resonance frequencies.
4. Redo item number 3 with a different deflection: 20, 30, 40 or 50 nm.
5. Go to the next sample and repeat the procedure.

Ideally, the procedure starts with the sample of study as the tip is more prone to being damaged on them during the first step (scanning) than on the reference samples, as the latter ones are large (radius > cm) and flat (cleaved surface).

Results are shown in section 14.2.

4.3.2.3 Electrochemical Strain Microscopy

ESM measurements were performed using a Solver Next (NT-MDT, Zelenograd, Russia) working at room temperature under ambient conditions in the laboratories of the University of Aveiro, Portugal. $LiMn_2O_4$ cathode samples were grounded via the Al current collector serving as a back electrode. Voltage was applied to a Pt/Ir coated cantilever with a stiffness of about 5 N/m and 105 kHz resonance frequency. Probing AC-voltage was 3 V in amplitude and 0.6 to 1 MHz frequency. The latter was selected outside of contact resonance as a change of the tip/surface mechanics could be interpreted as a change of material properties. The response was measured by the internal lock-in amplifier of the microscope. Time spectroscopy ESM measurements (Jesse et al. 2011) were performed after application of a 10 ms short rectangular 10 V DC pulse (see fig. 4.2). Voltage spectroscopy ESM measurements (Kumar et al. 2011) were performed by applying 10 ms DC pulses of increasing and decreasing amplitude with 100 pulses per cycle (see fig. 4.3). ESM response was acquired between the pulses in the DC-off state. This system was modeled (see part V). Results are shown in chapter 16.

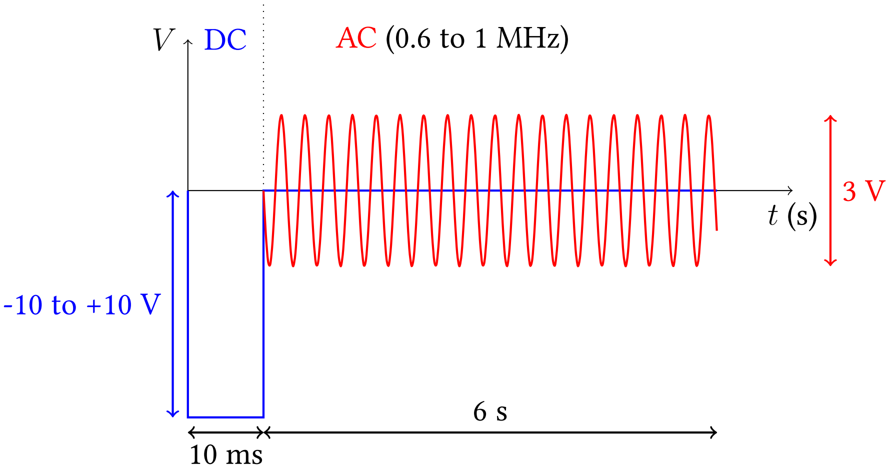

Figure 4.2: Schematics of time spectroscopy experiment: a short 10 ms DC pulse is followed by a 3V AC excitation with a frequency of 0.6 to 1 MHz.

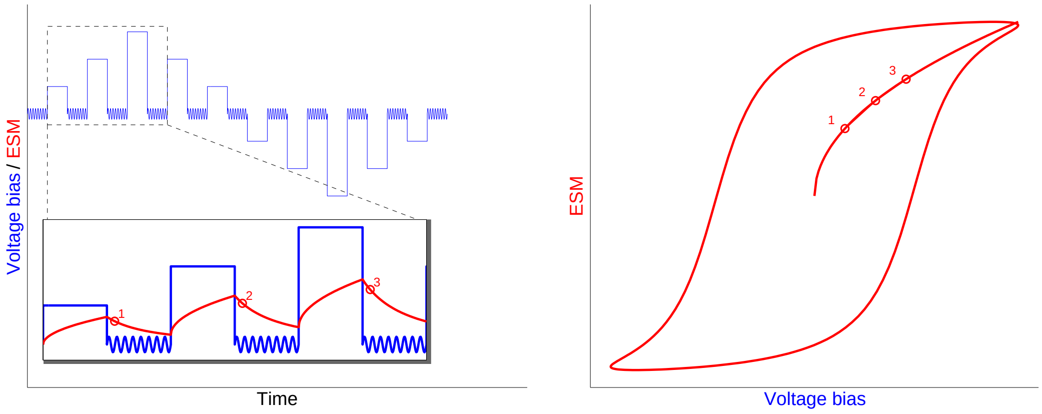

Figure 4.3: Simplified schematics of voltage spectroscopy measurement. Successive voltage pulses of different amplitudes are applied with AC excitation between the DC pulses (blue curves). The ESM signal is measured (red curve). Only one data point per pulse is recorded (numbers) and placed onto the hysteresis plot (right). In reality, one spectrogram consists of 100 pulses, not 10.

5 Chapter
Crack topography simulation

Section 2.2.1 related to the theoretical background of Irwin's near field method. This method infers that experimental AFM measurements of the crack topography are reliable. There is always an uncertainty present in topography measurement because the exact shape of the tip is unknown. It is indeed difficult to decipher inverse AFM tip imaging from crack wall imaging. Experimentally, mode III tearing displacement is in the same order of magnitude of typical sample roughness.

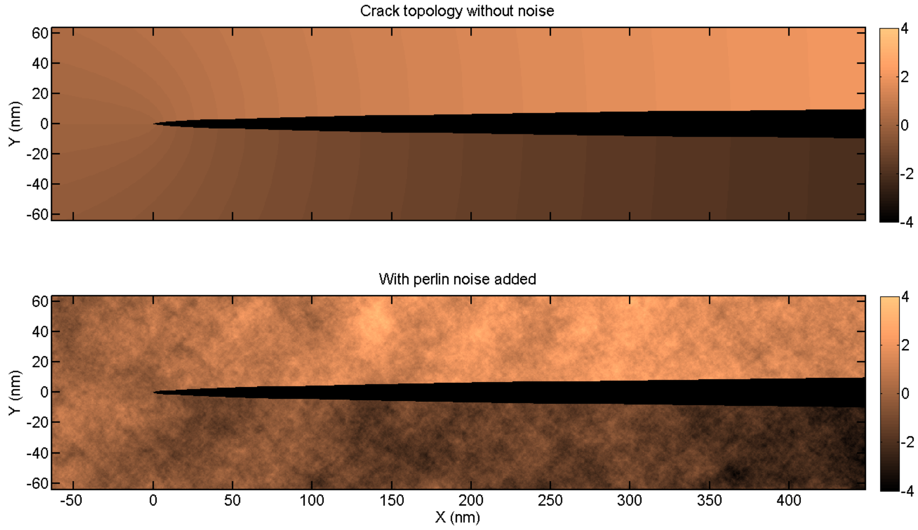

Figure 5.1: Simulated topography of a crack tip in a material with the following parameters: $K_{IC} = 10^6$ Pa·m$^{1/2}$, $K_{IIIC} = 1.5 \cdot 10^5$ Pa·m$^{1/2}$, $E = 10^{11}$ Pa and $\nu = 0.3$. (top) perfect surface. (bottom) Same surface with fractional Brownian motion noise added. Note: on the top image, the "stepping" effect of the color patches creates an optical illusion at their borders. The slopes in the x-direction are monotonic in reality.

Artificially cracked surfaces were created with Matlab (2013b). A surface was described with 3 matrix (X,Y,Z) of 5120*1280 points each, where X defines the x-position on [-64nm,448nm], Y defines the y-position on [-128 nm,128 nm] and Z is the topography defined by eq. (5.1). X and Y represent a surface of 512*256 nm^2 with a resolution of 0.1 nm. Z was computed in such a way that the crack is parallel to the x-axis and the crack tip is located at 1/8 of the left border. The border of the crack was computed using Irwin's near field theory as follow:

$$Z_{ij} = \begin{cases} -50\text{ nm} & \text{if } |Y_{ij}| < u_y(X_{ij}) \\ u_z(X_{ij}, Y_{ij}) & \text{if } |Y_{ij}| \geq u_y(X_{ij}), \end{cases} \tag{5.1}$$

where the ij couple represents one data point of a matrix for line i and column j, and where u_y and u_z are defined in eqs. (2.13) and (2.14). A depth of -50 nm was used as it is "infinitely" deep in regard to AFM measurements of such a narrow hole. In order to generate a more realistic surface, a noise based on fractional Brownian motion was added on the surface with an amplitude of 3 nm (see appendix A.1). The root-mean square approximates 1 nm. A sample surface with and without noise can be seen in fig. 5.1. AFM scans were simulated using a tip with a radius of 7 nm, a front angle of 25°, a back angle of 15°and a side angle of 22.5°. Angles are the same as in the specifications for TESP-SS tips. The tip radius is however a worst-case scenario, as Bruker specifies it should be between 2 and 5 nm. A cantilever angle of 10° was added (subtracted) to the front (back) angle. A 3D image of the tip is visualized in fig. 5.2. Two types of simulated scans were done (see fig. 5.3):

Simulation 1: scan step size of 1 nm on a material with a K_{IC} of 10^6 Pa·m$^{1/2}$ and a K_{IIIC} of $1.5 * 10^5$ Pa·m$^{1/2}$

Simulation 2: scan step size of 2.5 nm on a material with a K_{IC} of $0.6 * 10^6$ Pa·m$^{1/2}$ and a K_{IIIC} of $1.5 * 10^5$ Pa·m$^{1/2}$

The former is easier to interpret as the image resolution is better and the COD is wider. The other parameters are the same as specified in fig. 5.1. Cross sections from such scans can be seen in fig. 5.4. One scan with a tip radius of 2 nm is added: it can be noticed how the tip radius smooths the profile of the crack. More importantly, it is difficult to pinpoint where the crack walls are located even as we reduce the step size or the tip radius due to surface roughness.

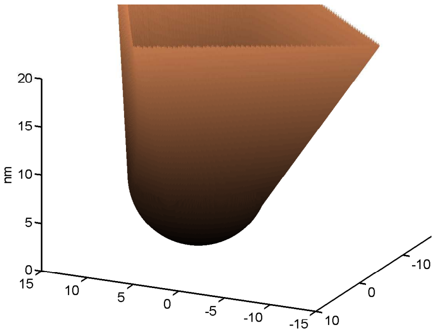

Figure 5.2: Simulated shape of an TESP-SS AFM tip with a radius of 7 nm.

Thence the accuracy often depends on the user's interpretation of the position of the crack walls. An experiment was designed with nine persons. The two simulated scans were mixed with two real scans with different tearing (Z) displacements. The four scans were submitted to the nine persons for COD measurements as described in section 4.3.2.1. They were previously introduced to the method and all had a university degree related to mechanics and/or materials science.

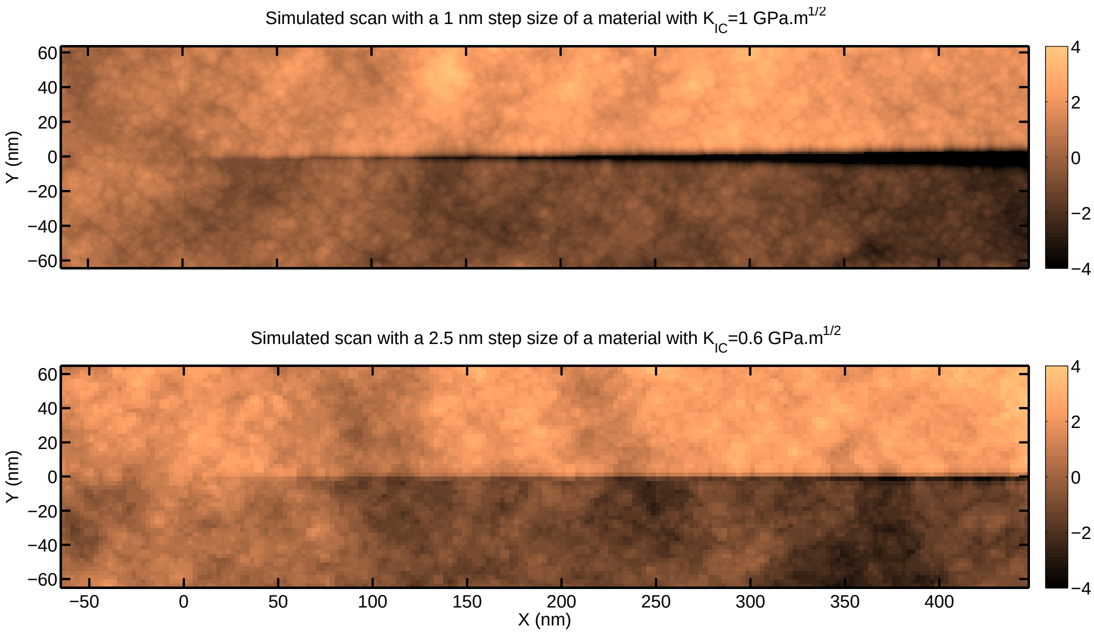

Figure 5.3: Simulated scans of a crack tip. (top) $K_{IC} = 10^6 \mathrm{Pa} \cdot \mathrm{m}^{1/2}$ and step size of 1 nm. (bottom) $K_{IC} = 0.6 * 10^6 \mathrm{Pa} \cdot \mathrm{m}^{1/2}$ and step size of 2.5 nm.

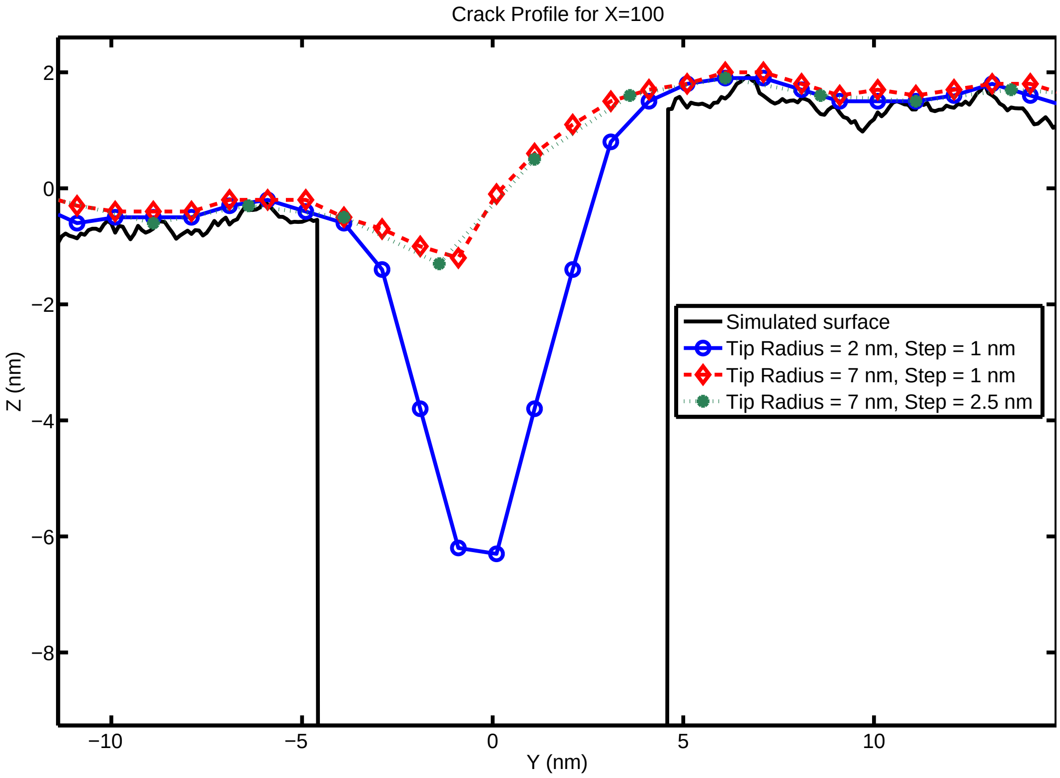

Figure 5.4: Cross-sections of simulated scans of a crack at a distance of 100 nm from the crack tip. It is difficult to determine the exact position of the wall. The differences between the two curves from the 7-nm tip radius are due to interpolations with neighboring data points in the X direction.

Part IV

Selective nanoindentation

Measuring the elastic modulus and hardness of the different phases of a composite is challenging. In this part, we will consider measurements on one battery sample (*C0SoC_1* in table 3.2), which is deemed unknown, and the silica-based composite (*SiO2s* in table 3.2), which is a known reference. The properties of the silica bulk were previously measured by means of Berkovich indentation: 70.5 (± 1.5) GPa and 6.5 (± 0.2) GPa for the elastic modulus and the indentation hardness, respectively.

It will be first demonstrated that applying the Oliver and Pharr method to the measurements (see section 2.1.2) and then applying the statistical deconvolution suggested by Ulm and Vandamme (see section 2.1.2.5) is not sufficient for this data set. A new method was developed of which the essence is to select the one measurement that correctly fits into the Oliver and Pharr set of hypotheses, giving it its name "selective nanoindentation". Last the method will be applied to the considered data set and quantitative measurements will be statistically deconvoluted. Using the object-oriented programming ability of Matlab, a graphical user interface toolbox was built to do what is described in this section. This work was peer-reviewed and published in Materials Science and Engineering: A (see Amanieu et al. 2014). Portions of the text and the figures used here are similar if not the same as in the corresponding scientific article.

6 Chapter
Procedure

The cathode cross-section was indented at three different locations for a total of 820 indents. Two of them, denoted *M1* and *M2*, are pictured in fig. 6.1 before indentation. They were specifically targeted at particles. A third, blindly selected, bigger area *M3* was also indented to increase the number of statistical events. The sample was indented over a 10 × 10 point matrix for *M1* a 16 × 20 point matrix for *M2* and a 20 × 20 matrix for *M3* following the protocol described in section 4.2.

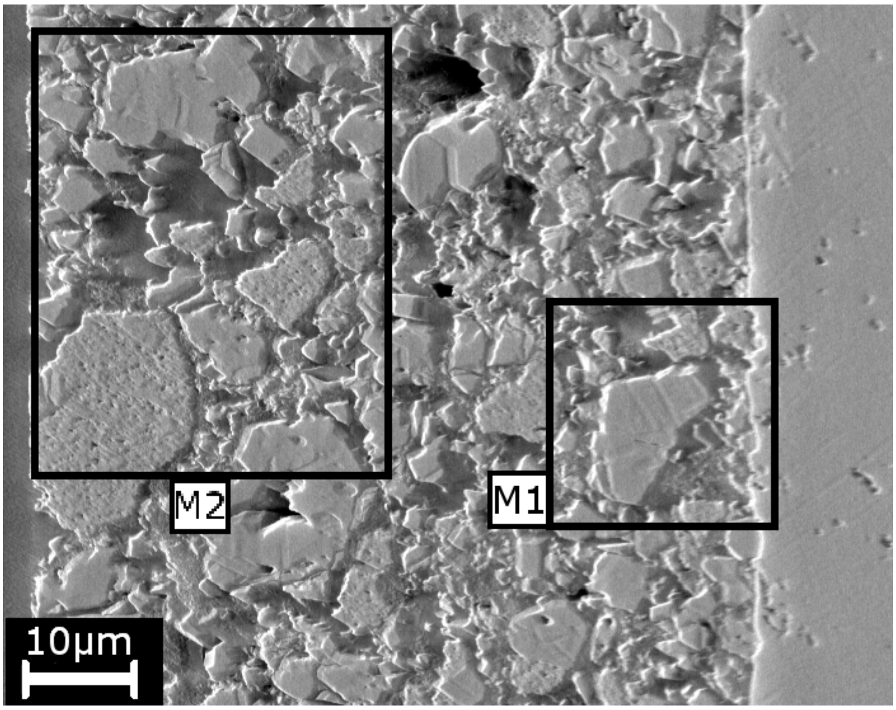

Figure 6.1: SEM image of the areas of interest *M1* and *M2* of the $LiMn_2O_4$ cross-section before indentation.

The cathode samples are of commercial origin. Due to the cheap manufacturing process of the batteries, the particles are not homogeneously similar. In fig. 6.1, a mix of porous particles and compact particles can be observed. The pores are small relative to the indents, about 10 nm^3. To understand at which extend the sample is complex, FIB cross-sections were taken from a similar sample in Roma Tre University. SEM images of these FIB cuts are shown in fig. 6.2. A compact particle (figs. 6.2c and 6.2d) stays compact also in depth but can be relatively thin, with a porous particle or epoxy just below it. This normally hidden information has an impact on the indentation measurements. A porous particle (figs. 6.2a and 6.2b) shows pores over the whole particle, with an apparent random scatter.

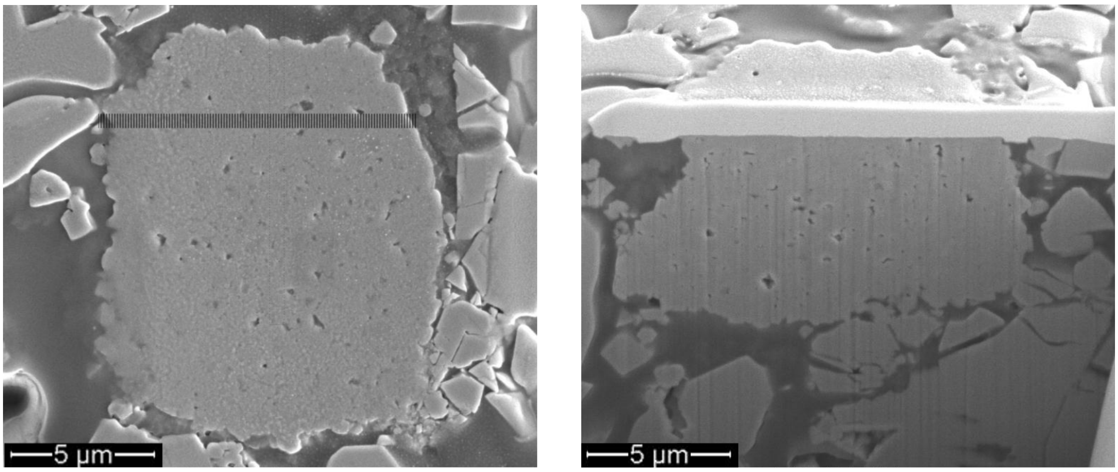

(a) Porous particle

(b) FIB cross section of fig. 6.2a

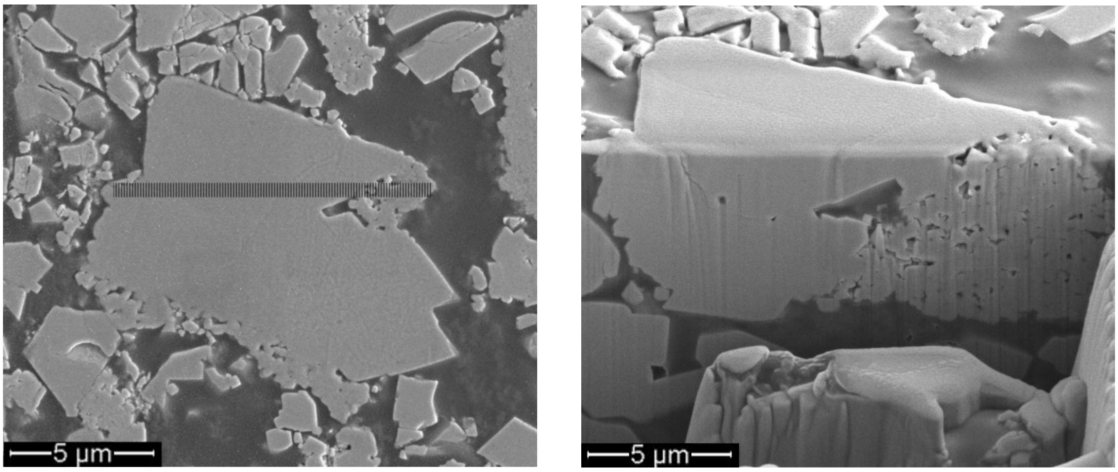

(c) Compact particle

(d) FIB cross section of fig. 6.2c

Figure 6.2: SEM pictures of $LiMn_2O_4$ particles. (a) shows a porous particle and (b) shows a FIB cross section of the same particle. (c) shows a compact particle and (d) a FIB cross section of it. Location of the cross-sections are indicated by dashed lines in (a) and (c). Courtesy of Roma Tre University.

7 Chapter

Raw experimental data

After applying the Oliver and Pharr method to extract the elastic modulus on the whole batch, the measurement data can be plotted like probability distribution functions. Histograms with a bin size of 2 GPa can be seen on figs. 7.1 and 7.2 for *C0SoC_1* and *SiO2s*, respectively. The large number of spurious peaks demonstrates the inconsistency of many measurements. Two or three gaussian distributions are expected, corresponding to the different phases present in each specimen. Figure 7.1 has a peak in the middle, around 40 GPa, and a succession of single bars with high frequency counts which do not correspond to any phase. The phases of the silica-based sample are known: we expect a distribution around 4 GPa for the epoxy and one around 70 GPa for the silica particles. In fig. 7.2, there are high peaks around these values, but the distribution in the higher end of the elastic modulus range seems to be the sum of several Gaussians between 50 and 70 GPa with a large standard deviation. There are also several smaller peaks: around 15 GPa, 20 GPa, 30 GPa and 46 GPa. From these observations, we can make the hypothesis that the results obtained from the other sample are also not correctly distributed. The composites studied by Ulm et al. (Constantinides et al. 2006; Ulm and Vandamme 2007 2010), e.g. bones, cement and metallic alloys, are made of phases with similar chemical and mechanical properties. The samples studied in this work have howbeit phases with distinctive chemical properties and are hence weakly bound, but also mechanical properties with at least one order of magnitude difference. For these two reasons, there can be significant composite responses associated with substract and edge effects. Hence directly deconvulating the original data set is not sufficient.

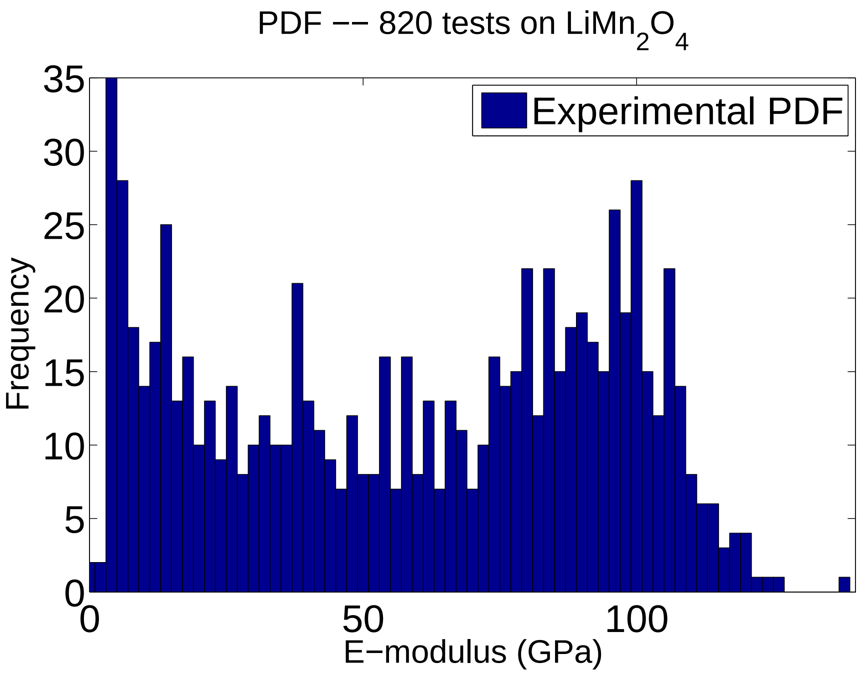

Figure 7.1: Probability distribution function of E-modulus measured by a batch of 820 indents on a $LiMn_2O_4$ electrode cross-section from sample *C0SoC_1*. Bin size=2GPa.

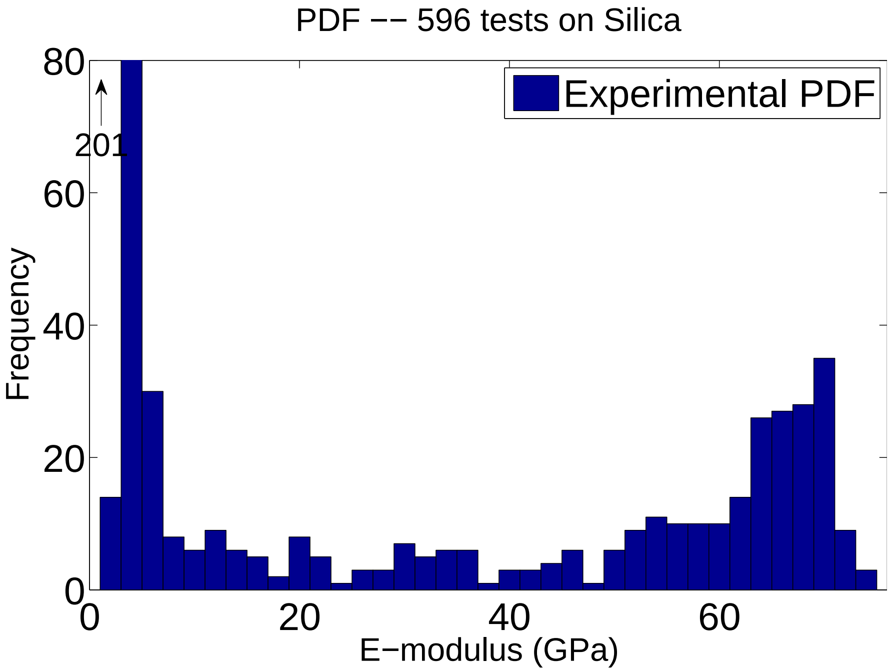

Figure 7.2: Probability distribution function of E-modulus measured by a batch of 596 indents on the SiO_2 ersatz electrode cross-section. Bin size=2GPa.

8 Chapter
Origin of discrepancies

8.1 Load displacement curves

Load versus displacement ($L(h)$) curves are expected to approach a quadratic function during loading with conical tips (Oliver and Pharr 1992). If they do not follow this rule, it can be assumed that the intrinsic hypotheses used by the O-P method, notably an isotropic semi-infinite sample, are not respected and it is common to manually withdraw the erroneous tests from the batch. Figure 8.1a is a SEM image showing a portion of the *M2* area shown in fig. 6.1. It can be seen that some indents are close to the inter-phase borders or produce significant cracks. Cracks appear when an indent is close to a border or when the crystal already has structural defects. These phenomena can be visible on the load versus displacement curve as cracks produce significant steps, also known as pop-in events (Mukhopadhyay and Paufler 2006) (see the two non-solid lines of fig. 8.1b). The primary problem with crack-induced steps is that the contact area might be underestimated and that the sample does not correspond to a semi-infinite bulk any more. The red solid line in fig. 8.1b shows a typical load versus displacement curve. It can be assumed that the corresponding indent accurately measurs the sample property. We can see micro-cracks around the solid-line circled indent in fig. 8.1a. This phenomenon is expected to be occurring more frequently with cube corners than with a Berkovich indenter but has a limited effect on the measurement (Chudoba et al. 2006) and happens mainly during unloading, see Mukhopadhyay and Paufler (2006). This also shows that lithium manganese oxide is a brittle material. In our paper, micro-cracks should not be confused with cracks. While the former was formed during unloading on the corner of the indent print (Lawn et al. 1980), the latter is a failure which significantly deformed the loading curve and split or broke the particles. When close to a particle/matrix interface, composed responses show irregular non-quadratic curves (dotted curve of fig. 8.1b). This indicates that the volume under study is not isotropic, hence the Oliver and Pharr method is not usable either.

The calculated E-moduli of these erroneous tests do not correspond to real material properties and contribute to the noise in the probability distribution functions plotted in fig. 7.1.

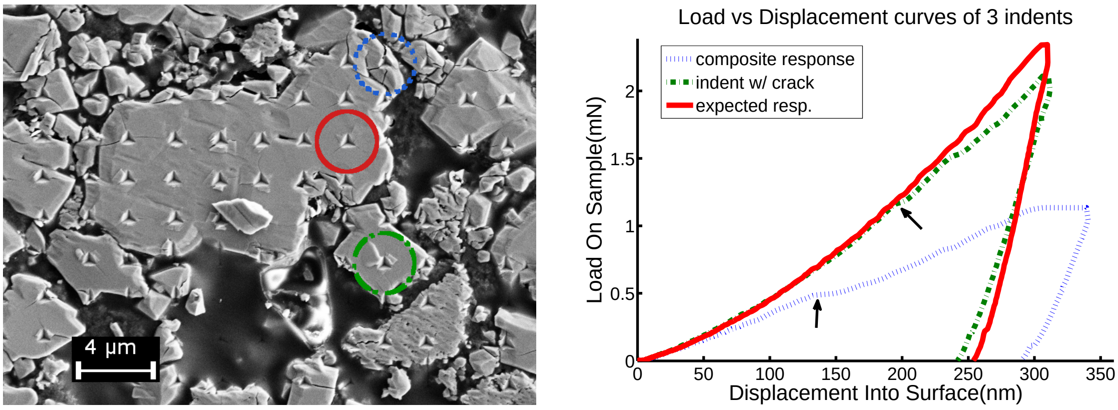

(a) SEM image

(b) Load vs displacement curves

Figure 8.1: (a) is an SEM image of a portion of *M2*. (b) shows the three load versus displacement curves measured for the circled indents of (a). Line styles are corresponding. The two arrows point at the inflections where the load versus displacement curves stop following a quadratic function. The red solid line corresponds to the expected response from nanoindentation, the green dot/dash line corresponds to a test which cracked the particle, inducing pop-in events, and the dotted line corresponds to a composed response. The two latter are not analyzable by the Oliver and Pharr method.

8.2 Structural compliance

As introduced in section 2.1.2.5, indentation in a single phase of a composite can activate a composite response as the other phase(s) induce a structural compliance C_s. This new compliance has a double impact on the measurement: on the one hand, full body sink-in of a stiff particle into the compliant matrix generates an underestimation of the indentation depth h, hence eq. (2.4) cannot be used. On the other hand, C_s will have an impact when plotting eq. (2.9) as it is the case for the machine compliance C_m, i.e. $\frac{L_{max}^{1/2}}{S_{CSM}}$ is constant if there is no structural compliance, otherwise the slope is equal to the structural compliance C_s (Jakes et al. 2008). Figure 8.2 shows the $\frac{L_{max}^{1/2}}{S_{CSM}}$ plots for two measurements on the stiff particles of the silica based sample that produced normal quadratic-like loading curves. The green solid line, closer to a constant, correspond to a measurement that extracted an elastic modulus value very close to the bulk value: 69.5 GPa. Per contra, the blue dashed line has a relatively high slope and consequently produces a value for the elastic modulus which is induced by the more compliant epoxy phase: 63.4 GPa.

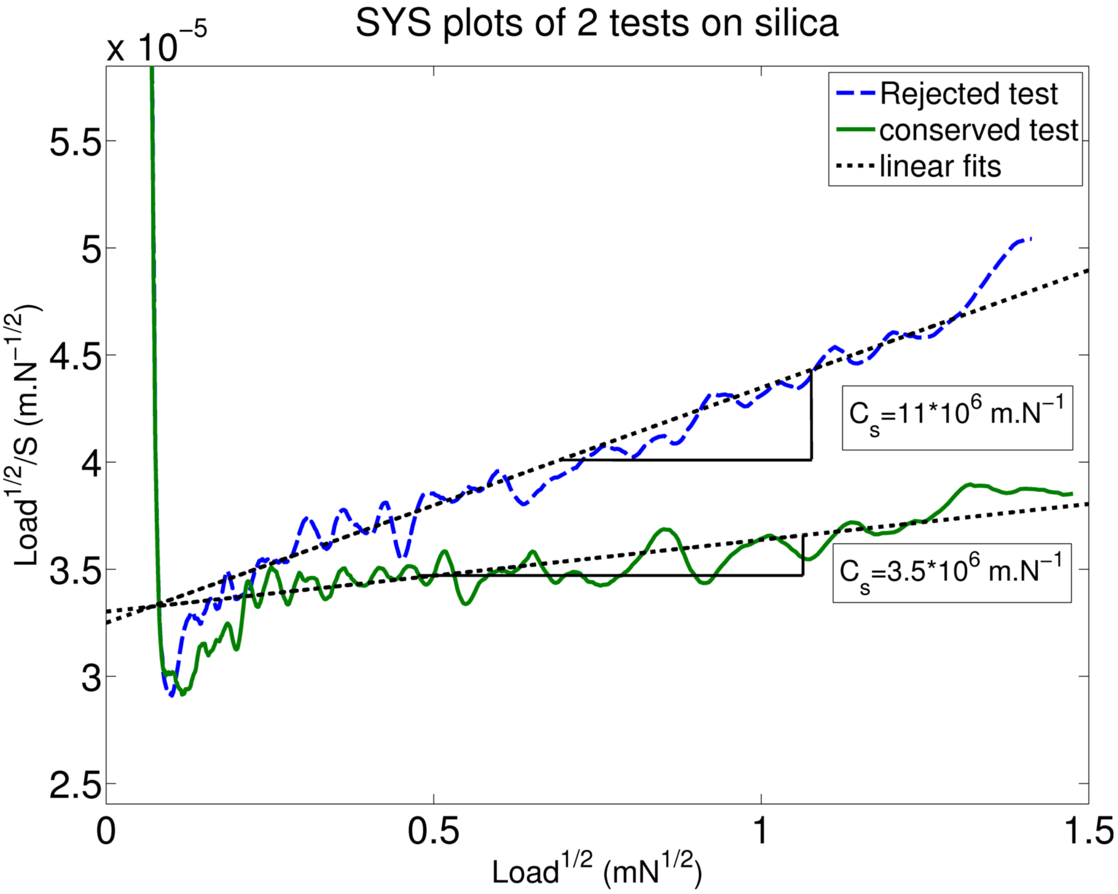

Figure 8.2: $L_{max}^{1/2}/S_{CSM}$ versus $L_{max}^{1/2}$ plots of two tests made on the silica-based sample. The broken line has a relatively high slope, or structural compliance. The measured E-modulus was 63.4 GPa. The solid line represents a good test as it is fairly constant with a measured E-modulus of 69.5 GPa. The two dotted lines represent linear fits calculated for depth above 45 nm.

9 Chapter Filtering method

Following the previous observations, a 2-step method has been developed to select non-erroneous tests. It is based on a post processing of the raw data of each test by using procedures implemented in Matlab. The processed raw data regard load, displacement, and continuous stiffness. The method is influenced by threshold parameters which are empirically chosen with the help of tests on calibration materials, imaging technique data and literature. In short, the first step consists of filtering tests with a consistent ($L(h)$) curve as showed in fig. 8.1. The second step consists of checking how the compliant matrix impacts the stiffness measurements in order to keep the tests which are not dominated by composite response. Last, the statistical method developed by Ulm et al. (Constantinides et al. 2006) is used only on the selected tests to extract the mechanical properties of the different phases.

9.1 Step 1: Load curve filter

The surface quality can be assessed by the shape of the $L(h)$ curve. Curves which are close to what they should theoretically look like to apply the Oliver and Pharr method are sought. Load versus displacement curves induced by the loading of three-sided pyramid tips theoretically follow a quadratic function with null 1st and 0th order constants.

The area function of a perfect cube-corner tip is $A(h) = 2.598 * h^2$ and of a perfect Berkovich's tip is $A(h) = 24.5 * h^2$ where A is the projected area and h the indented depth. Without taking into account size-effect, the hardness in eq. (2.5) is expected to stay constant for any indentation depth (Pelletier 2005). The load is hence expected to be linearly proportional to the area function. This is why the $L(h)$ curve is also expected to follow a quadratic function. Using Kick's law, the 1st and 0th order parameters are expected to vanish for a perfect tip geometry indenting a homogeneous surface. But due to the real tip shape, the 1st or both of the parameters are expected to be non-null (Pelletier 2005). Experimentally, at very low load, tip rounding and hertzian nature of the contact induce a different load versus displacement relationship, where the beginning of the curve seems linear with a very low slope over a few nm on stiff materials. When h reaches a threshold value (around 6 nm in our case), the load drastically increases and takes the above mentioned particular quadratic shape. This can be observed in fig. 8.1b if one takes a closer look to the start of the loading curve. Hence, the quadratic law is experimentally seen only for depth where tip rounding becomes insignificant. As measurements on heterogeneous materials require shallow depths, it is advised to use a very sharp tip. The tip used in our case has a tip radius of about 25 nm over a distance from the tip end of 6 nm.

For the derived conclusions in the following, it is important to note that the fitting is not meant to derive quantitative values. For that the Oliver-Pharr method is used. It is only meant to detect tests with consistent $L(h)$ curves.

The $L(h)$ curve above 6 nm is fitted by a quadratic function, see eq. (9.1), using the implemented 2nd order polyfit function of Matlab based on the least-squared method. According to PELLETIER (2005), himself inspired by the work of CHENG AND CHENG (1998), the 2nd order constant depends on the sample properties while the 1st and 0th order constants are functions of the tip shape and the material properties. It is shown in these papers that the 2nd and 1st order constants should be positive. The n fitted values $\widehat{L_j}$ corresponding to the n observed load values L_j is defined as follows:

$$\begin{cases} \widehat{L_j} = a_2 * h^2 + a_1 * h + a_0 \\ L_j = a_2 * h^2 + a_1 * h + a_0 + \epsilon_j, \end{cases} \tag{9.1}$$

where a_1, a_2 and a_3 correspond to the 3 fitting parameters, h to the indentation depth and ϵ_j is the error to be minimized. If a_2 or a_1 are negative, the test is removed. Tests which cracked the particle show pop-in events on the $L(h)$ curve and tests with composite response show an irregular (non-quadratic) shape. Hence, it is expected that the area between the experimental curve and the quadratic fit is relatively bigger. This area is numerically calculated by trapezoidal numerical integration. Load data and depth data are beforehand divided by the maximum load and the maximum depth, respectively, in order to have a dimensionless value. The dimensionless property of the area is important to be able to compare tests on different materials with a single threshold. The threshold is picked empirically and equals $4 * 10^{-3}$ for both samples. All tests with a relative area above the threshold are filtered out.

It was found out that this filter was not sufficient. Due to the larger elastically deformed zone under indentation as compared to the plastically deformed zone, the stiffness measured by the indenter can be influenced by other phases, even if the $L(h)$ curve seems proper. Another step was necessary to account for this effect.

9.2 Step 2: Joslin-Oliver parameter based filter

The aim is to filter out tests on particles which induced a contribution from the matrix. The hypothesis is the following: if the SYS function (see section 2.1.2.5 and Stone, Yoder, and Sproul (1991)) is constant for all h, there is no composed response at all loads, hence only the single phase contributed at lower loads. The filtering is done by checking this ratio for depths above 45 nm. 45 nm was as well picked empirically, as SYS plot tends towards infinity for depth below this value for all nanoindentation tests due to uncertainties at low indentation depth. The function $L_{max}^{1/2}/S_{CSM}({L_{max}}^{1/2}(h > 45nm))$ is fitted by a first order polynomial. The slope of the curve corresponds to C_s. These slopes C_s are reported on the Y-axis of fig. 9.1 for all the tests which passed the first filter for both of our samples. Each of them is correlated with the measured E-modulus, on the X-axis. The blue diamonds correspond to tests made on the silica-based sample while the green crosses represent the battery sample. One can see that C_s is close to zero around the expected E-modulus of the silica particles (70.5GPa) and it tends to increase for lower E-moduli until about 50GPa. This can be explained as follow: the bigger the contribution of the elastic properties of the matrix on the measurement, the bigger is the structural compliance C_s. As the matrix is more compliant than the particles, the measured E-modulus appears smaller as it is a convolution of the elastic properties of the two phases. When there is no contribution from the compliant matrix, the structural compliance C_s approaches zero and the measured E-modulus corresponds to the single stiff phase. The phenomenon is assumed to be the same for the other sample. Inspired by the results on the silica-based sample, an upper threshold of $4 * 10^{-6}\mathrm{m} \cdot \mathrm{N}^{-1}$ is empirically chosen. If the slope C_s is found to be above this threshold, the test is rejected.

Like many polymers, epoxy has a strong size-effect when indented, hence the Joslin-Oliver analysis cannot be used and the slope does not physically correspond to a structural compliance, but is rather due to the intrinsic properties of the matrix. It can be seen in fig. 9.1 for lower E-moduli, where the SYS slope reaches values down to $-2 * 10^{-4}\mathrm{m} \cdot \mathrm{N}^{-1}$. Separated indentation executed solely on epoxy with the same tip showed that J_0 from eq. (2.9) tends to be constant only for penetration depth above 700 nm. The calculated E-modulus was in the range of 3∼4 GPa. This second filter is meant to sort out tests which produced a full body sink-in of the particle into the epoxy (positive calculated C_s) and not to filter all tests in epoxy [2](negative calculated C_s). For the sake of this example, no lower negative threshold was set for these samples. For SoC dependent measurements, a different approach was however used as we were interested in the properties of the ceramic particles only.

---

[2] We could have used it to extract tests on particles only, but this would have withdrawn the interest of using multi-phase characterization by Ulm's statistical method.

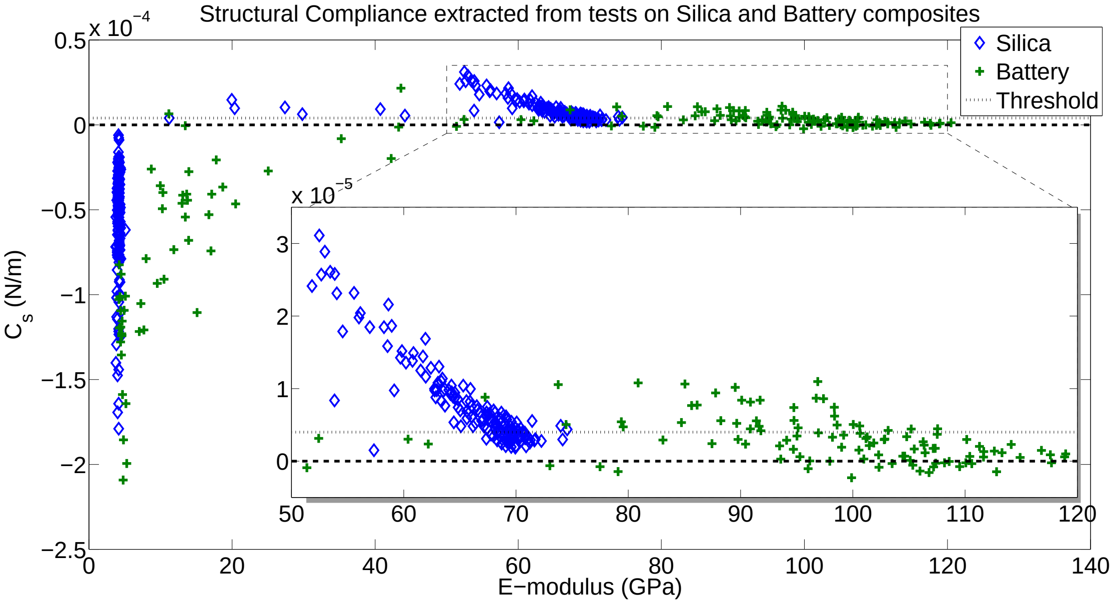

Figure 9.1: Structural compliance extracted from tests on the Silica-based sample (blue diamonds) and on the battery sample (green crosses) versus measured E-modulus. The threshold is a constant line at $C_s = 4 * 10^{-6}\mathrm{m} \cdot \mathrm{N}^{-1}$. Note how close the calculated E-modulus of silica is to the expected value of 70.5GPa for small values of C_s.

9.3 Oliver & Pharr method and statistical deconvolution

The E-modulus and the hardness are calculated by averaging (eqs. (2.5) and (2.6)) over a certain range of indentation depths h. From the method used by Zhu (2011), we search h for which $\frac{L_{max}^{1/2}}{S_{CSM}}(h)$ is constant. As previously done, 45 nm was picked as minimum depth. While we gave an answer in section 9.2 to find which tests are not dominated by composite responses, Yan and Pun (2012) theoretically investigated which depths are particle dominated. Their work gives a parameter, h_p/R, depending on the particle E-modulus E_p, the particle yield strength Y_p and the matrix E-modulus E_m. h_p is the maximum depth where indentation is particle dominated and R is the particle radius. This parameter h_p/R is a threshold below which the error of calculation using the O-P method stays under 10 %, assuming the real $A(L_{max})$ is accounted for. Our particular case was not investigated as the ratio Y_p/E_m is much higher and E_p/E_m is much smaller than the ones investigated by Yan and Pun (2012). It could nevertheless give us an insight of the parameter, and it was decided to pick a value below $h_p/R = 0.01$. As our particle radius is of an order of magnitude of 10 μm, 75 nm seemed to be a good compromise as maximum depth. Hence both hardness and E-modulus were measured between 45 nm and 75 nm before and after filtering.

Figures 7.1, 7.2, 9.2 and 9.3 are histograms of measured elastic modulus for the

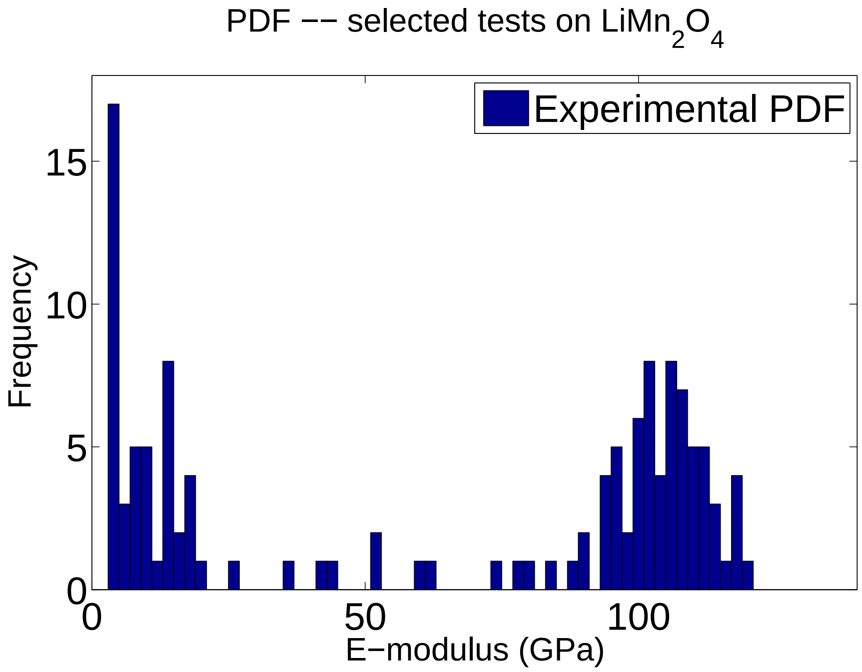

Figure 9.2: PDF of the 131 selected tests E-moduli on LiM_2O_4.

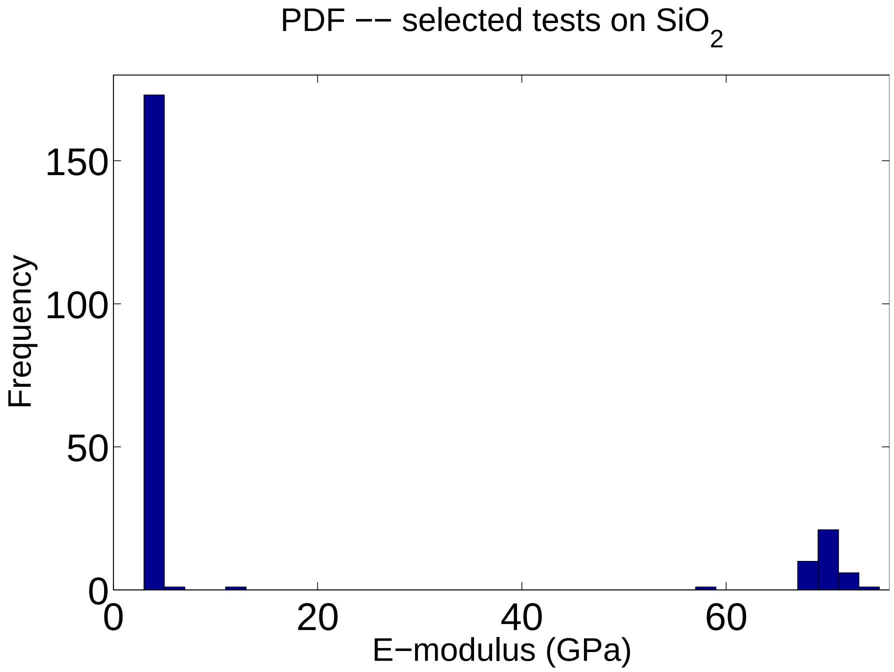

Figure 9.3: PDF of the 242 selected tests E-moduli on SiO_2.

battery sample after filtering, the silica-based sample after filtering, the battery sample before filtering and the silica-based sample before filtering, respectively. It can be observed that there are almost no spurious peaks left in the case of sample *SiO2s* and only two centered gaussians with a small standard deviation are present around the expected values. For the other sample, the PDF seems cleaner and dominated by two groups of measurements as well,but there is still a significant number of spurious peaks, translating the complexity of the sample. Data deconvolution was done on the cumulative measurements as described in section 2.1.2.5. The set of successful indentation tests t is denoted by T. The subset of T corresponding to the phase i is denoted by T_i. Each test t was sorted in each subset T_i depending on K_i from eq. (2.12) and their position in the sorted values of T. The filtering method presented in this paper significantly reduces the number of indents, crippling the regularly ordered structure of the indentation grid. Hence the surface fraction parameters K_i are not consistent with the real surface density of each phase.

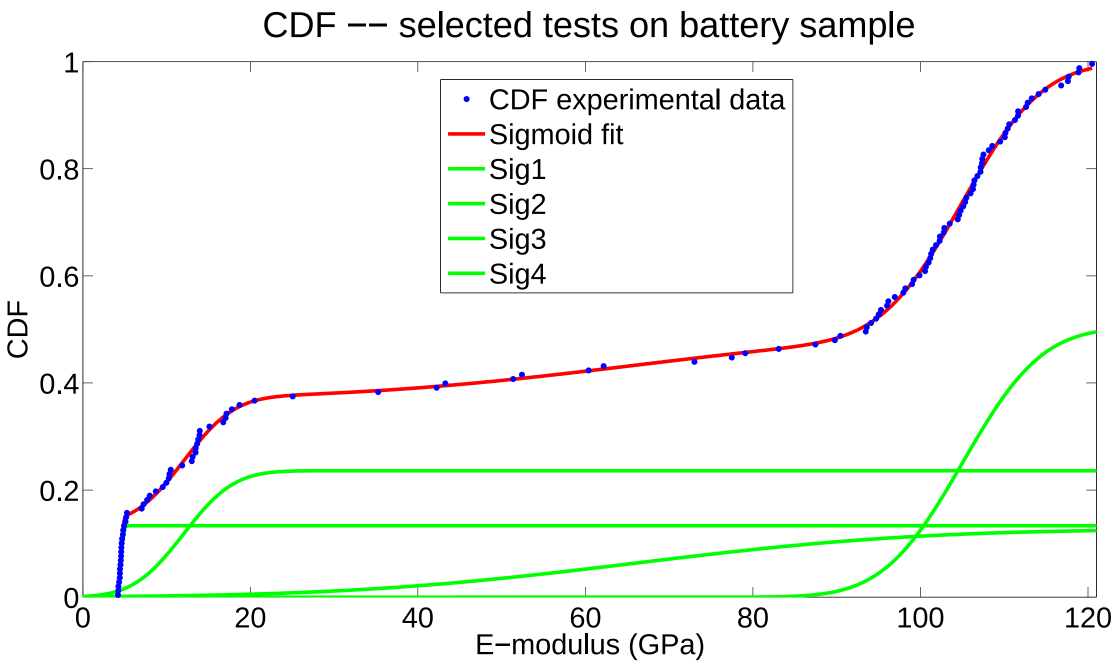

Figure 9.4: CDF of the 131 selected tests E-moduli on LiM_2O_4 (blue dots), sigmoid fit (red solid line) and the four elementary sigmoids from the sigmoid fit (green solid lines).

While 2 phases were expected for $LiMn_2O_4$, one for compact particles and one for the matrix, two other Gaussian functions had to be added in the fitting procedure to reach a consistent adjusted coefficient of determination $R^2 > 0.99$. Results are shown in fig. 9.4 and table 9.1. Each "phase" i result is related to the position of the indentation prints as shown in figs. 9.5 and 9.6. Some tests are not included in the same subset T_i for E-modulus and hardness due to different K_i values. This effect seems of minor

i	K	m (GPa)	σ (GPa)
		E-modulus battery sample	
1	0.13	4.59	0.22
2	0.24	12.04	4.73
3	0.13	65.92	26.88
4	0.50	105.06	7.45
		Hardness battery sample	
1	0.15	0.52	0.03
2	0.26	2.76	1.47
3	0.21	9.90	1.73
4	0.39	11.33	0.53
		E-modulus silica sample	
1	0.82	4.17	0.37
2	0.18	69.78	1.18
		Hardness silica sample	
1	0.82	0.34	0.01
2	0.18	7.27	0.24

Table 9.1: Result summary of fit parameters found for the battery sample and the silica sample. i, K, m and σ correspond to the parameters in eq. (2.12).

importance in the interpretation of the data and can be explained by the fact that elastic and plastic deformation by indentation have different volumes of interaction. It is clear from the SEM images that the subsets T_1 and T_4 correspond to tests located on the epoxy and tests located on compact particles, respectively. T_3 is associated with tests on particles closed to borders, pores, or other surface defects. Last, T_2 seems to correspond to tests on epoxy either close to a particle edge or with a higher concentration of carbon black. σ_2 and σ_3 are relatively big as compared to their corresponding m-s, indicating that they do not correspond to uniform physical phases. It also means that the filters are not sufficient to get rid of all fallacious tests and a visual verification must be done. This verification was semi-automated on the Matlab application where the tests that passed the filters are marked on the associated SEM image in a similar fashion as on figs. 9.5 and 9.6.

Concerning silica, the noise was significantly reduced to fit with a 2-phase CDF. The results are summarized in table 9.1. It can be noticed that the K_i were consistent for both hardness and elastic measurements. In appendix B, fig. B.1 representing a SEM picture of one of the indentation grid can be found.

E-modulus and hardness of the epoxy in both cases correspond to T_1 and approach 4 GPa and 0.5 GPa, respectively. As already discussed, the E-modulus of epoxy has a strong size-effect and is over evaluated. In the case of silica we could retrieve mechanical properties close to soda lime glass. An E-modulus of 69.8 GPa was measured, 1 % below the bulk value, and a hardness of 7.27 GPa was measured, about 10 % above the bulk value. Indenter of smaller angles induce a higher nanoindentation hardness (SHIM ET AL. 2008). The fact that a cube corner tip (angle of 35.3°) was used rather than a Berkovich tip (angle of 65.3°) might explain this 10 % overestimate. In the case of $LiMn_2O_4$, a modulus of about 105 GPa ($\pm$6 GPa) and a hardness of 11 GPa ($\pm$0.5 GPa) corresponding to T_4 were measured. There is formation of pile-up which induces an overestimate of these values and will be discussed in the Result part (see chapter 14). The industrial particle synthesis is not homogeneous as there is formation of porous and non-porous particles. It is a source of potential error for our measurements. One of the two spurious "phases", T_3, might be induced by this inhomogeneity. It might also induce the relatively bigger standard deviation between $T_4^{Battery}$ and T_2^{Silica} ($\sigma_4^{Battery}/m_4^{Battery} > \sigma_2^{Silica}/m_2^{Silica}$). Last the concentration and the distribution of carbon Black and PVDF is certainly different between the two samples. It could explain the presence of the other spurious phase $T_2^{Battery}$, absent in the case of the reference silica-based sample.

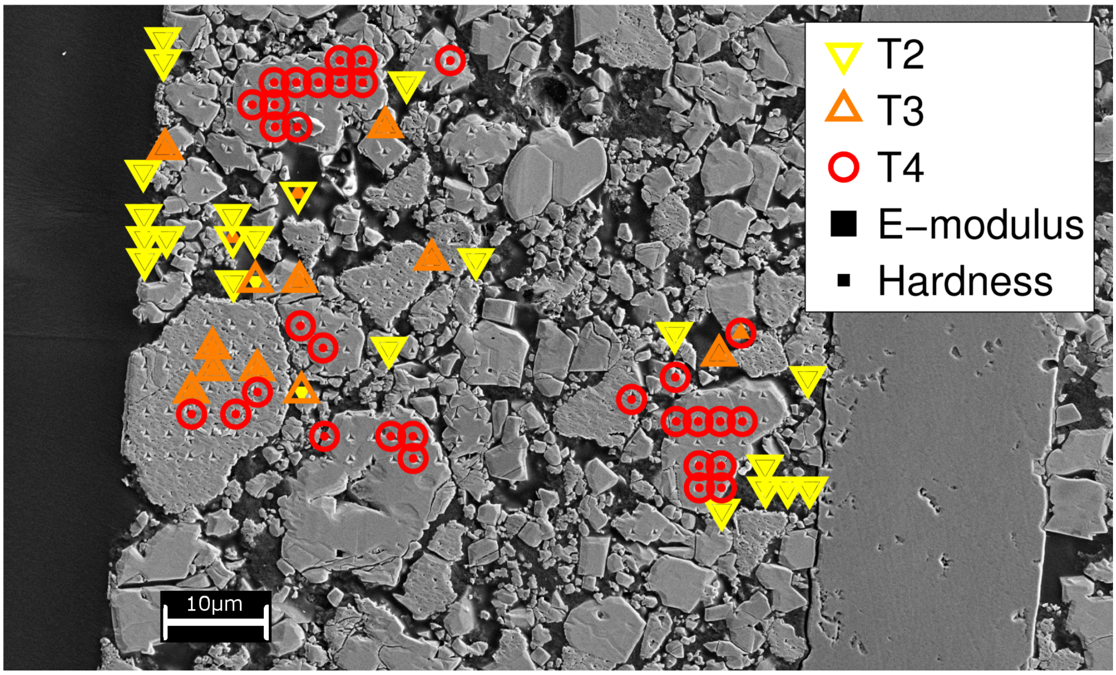

Figure 9.5: SEM images of *M1* and *M2* after indentation. The selected tests are marked as well as their related E-modulus (outer marker) and hardness (inner marker) test sets T_i.

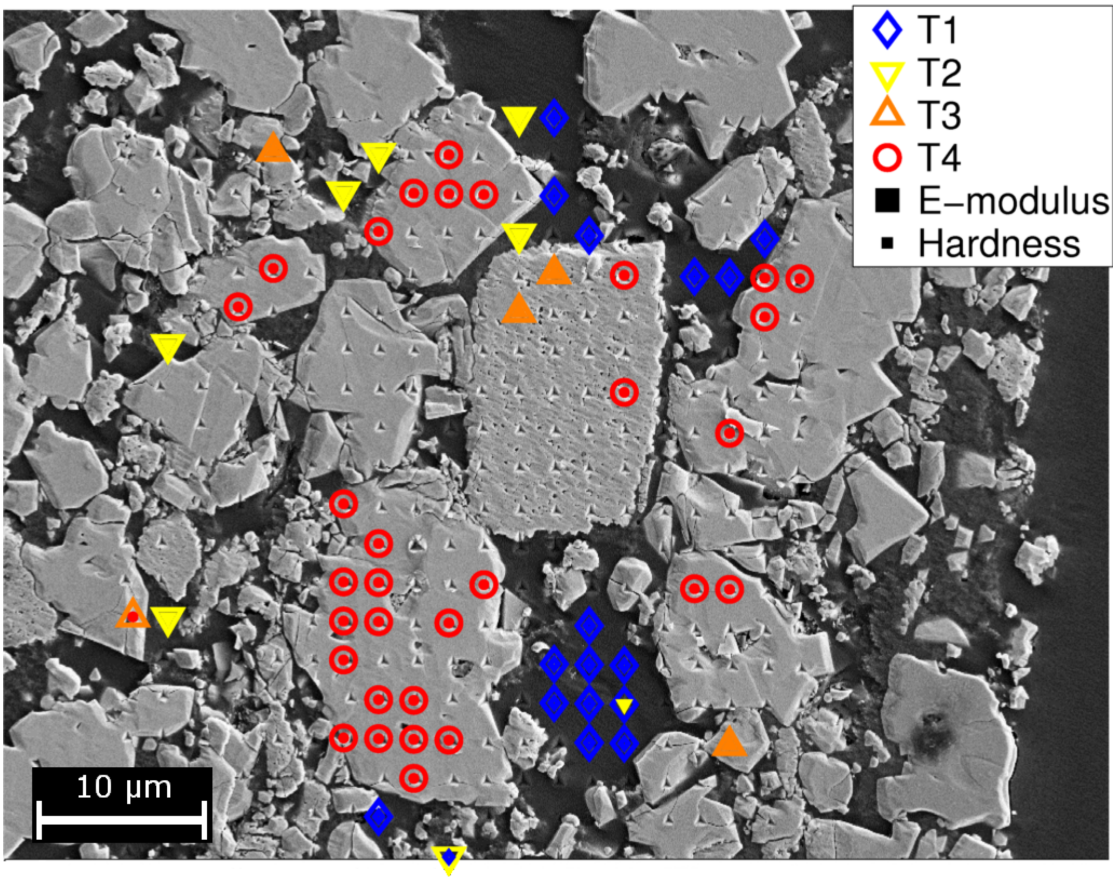

Figure 9.6: SEM images of *M3* after indentation. The selected tests are marked as well as their related E-modulus (outer marker) and hardness (inner marker) test sets T_i.

10 Chapter
Method summary and remarks

The procedure can be summarized as follows:

Step 1 Make several grids of 100s of indentations per sample.

Step 2 Filter the measurements by finding the ones with quadratic-like loading curves. This is done by normalizing the loading portion of each $L(h)$, fitting each with a second order polynomial and calculating the surface between the experimental curve and the fit. This surface must not exceed an empirical threshold for the measurement to be accepted.

Step 3 Filter the measurements by finding the ones with little or no structural compliance C_s, which can be measured from the slope of the SYS plots. If there are enough statistical events left, continue to the next step ; otherwise, return to **Step 1**.

Step 4 Either:

4.a Deconvolve the data set by fitting the experimental CDF by a sum of sigmoid functions.
(fast, for simple composites) (Constantinides et al. 2006)

OR

4.b Compare the filtered measurements to SEM images of the indented areas and group them according to their position
(slow, for complex composites)

Selective nanoindentation can highly increase the signal to noise ratio. It was particularly powerful to extract the material properties of the simple silica-based reference material. It was however not sufficient to delete all fallacious tests from the initial batch in the case of the $LiMn_2O_4$ sample. This could be explained by the complex structure of the commercial $LiMn_2O_4$ cathode which can not be simply modeled by a mix of two homogeneous phases. When characterizing micro-mechanics of complex composite materials by statistical nanoindentation, it is important to understand the origin of each statistically extracted mechanical parameter (see **Step 4.b**). The Joslin-Oliver parameter based filter is also limited to materials with little or no size-effect but was demonstrated to be powerful for tests on hard particles embedded in a compliant matrix as shown by fig. 9.1.

Part V

Electrochemical Strain Microscopy: Model

In this part, the ESM experimental set-up described in section 4.3.2.3 is simplified and modeled with COMSOL. The formal description of Bohn et al. (2013), which is very similar to previous works done on ESM modeling (Morozovska et al. 2010; Chung et al. 2011a; Morozovska et al. 2012b), will be used. The objective is to model the time evolution of lithium concentration, surface displacement and the ESM signal below the tip during and after DC pulses. Our model will approach the philosophy of Morozovska et al. (2012b) in that sense that ion-blocking electrodes will be considered only. However, local electroneutrality will be preserved for simplicity. As introduced in section 2.2.3, the ESM signal was determined at frequencies as high as 400 kHz , with a typical relaxation process that can be probed using time spectroscopy (Balke et al. 2010; Jesse et al. 2011; Luchkin et al. 2015). Previous models showed that these high frequencies are too quick to drive ionic diffusion and provoke a mechanical excitation through Vegard's deformation. Also, a constant diffusion coefficient was used. The present work is innovative in two aspects:

1. the calculation of the ESM signal is done differently. Instead of modeling Vegard's deformation in the frequency domain (Chung et al. 2011a; Morozovska et al. 2012b), we suggest to calculate the mean Lorentz electric field applied to the ions by the AC excitation.

2. An effective diffusion coefficient is used which takes into account irregularities in the Gibbs free energy of $LiMn_2O_4$ during lithiation (see section 1.1). The formalism of Bohn et al. (2013) will be used.

Time domain response will be examined and compared to previous analytical work of Morozovska et al. (2010)) and experiment done in the University of Aveiro. It is proposed to study ionic transport from the relaxation of the ESM signal in the time domain.

This work is currently being peer-reviewed and was submitted to the Journal of Applied Physics (Amanieu et al. 2015c). It was carried out in close collaboration with two PhD candidates from the *Nanomotion* project, Mr Huy Thai from the University of Duisburg-Essen and Dr Sergey Luchkin from the University of Aveiro, and their respective supervisors. Portions of the text and the figures used here are similar if not the same as in the corresponding scientific article.

11 Chapter
Constitutive equations

11.1 Primary variables

In order to simulate the mechanisms acting onto a $\mathrm{LiMn_2O_4}$ body by the application of a DC pulse during ESM time spectroscopy, the following primary variables need to be taken into consideration:

- the lithium concentration c_{Li},
- the displacement $\boldsymbol{u}$,
- and the electric potential ϕ.

Considering small-strain theory, the total strain $\boldsymbol{\varepsilon}$ can be computed

$$\boldsymbol{\varepsilon} = \mathrm{sym}[\nabla \boldsymbol{u}], \tag{11.1}$$

where it is considered that the strains are small enough to stay in the elastic regime and where tensile and compressive strains are symmetrical. The electric field $\boldsymbol{E}$ can also be derived from the electric potential:

$$\boldsymbol{E} = \nabla \phi. \tag{11.2}$$

11.2 Energy description

The Gibbs free energy per unit volume of $\mathrm{LiMn_2O_4}$ is defined as

$$\psi = \hat{\psi}(\boldsymbol{\varepsilon}, c_{\mathrm{Li}}, \phi) = \psi^{\mathrm{mech}} + \psi^{\mathrm{chem}} + \psi^{elec}, \tag{11.3}$$

which depends on the total strain $\boldsymbol{\varepsilon}$, the electric potential ϕ and the concentration of lithium ions $c_{\mathrm{Li}} = N/V_0$, with N being the number of lithium ions per unit volume V_0. The free energy is subdivided into mechanical energy ψ^{mech}, chemical energy ψ^{chem}, and electric energy ψ^{elec}. The mechanical component is defined as follows

$$\psi^{\mathrm{mech}} = \frac{1}{2}\big(\boldsymbol{\varepsilon} - \frac{1}{3}\Omega_{\mathrm{Li}}\left(c_{\mathrm{Li}} - c_0\right)\boldsymbol{1}\big)\mathbb{C}\big(\boldsymbol{\varepsilon} - \frac{1}{3}\Omega_{\mathrm{Li}}\left(c_{\mathrm{Li}} - c_0\right)\boldsymbol{1}\big), \tag{11.4}$$

where **1** is the second-order identity tensor (Kronecker delta) and $\mathbb{C}$ is the fourth-order elasticity tensor. Here we assume that lithium causes an expansion of the system in proportion to the partial molar volume of lithium Ω_{Li}, which is constant over the range of the intercalation and which is small enough in $\mathrm{LiMn_2O_4}$ to consider small-strain theory (contrary to e.g. silicon anodes (Dal and Miehe 2015)). $\Omega_{\mathrm{Li}}/3$ is the isotropic approximation of the partial molar volume (Bohn et al. 2013) and is directly related to the isotropic Vegard tensor. In its simple form, the chemical energy per unit volume is defined as

$$\psi^{\mathrm{chem}} = \mu_0 c_{\mathrm{Li}} + RT\left[\left(1-\frac{c_{\mathrm{Li}}}{c_{max}}\right)\ln\left(1-\frac{c_{\mathrm{Li}}}{c_{max}}\right)+\frac{c_{\mathrm{Li}}}{c_{max}}\ln\frac{c_{\mathrm{Li}}}{c_{max}}\right], \tag{11.5}$$

where μ_0 is the reference chemical potential in the system, R is the ideal gas constant, T is the absolute temperature and c_{max} is the stoichiometric maximum lithium concentration. In this case, we assume that the temperature is constant in the whole system, therefore the chemical energy only depends on the concentration of lithium c_{Li}. Note that $\mu_0 c_{\mathrm{Li}}$ corresponds to the internal energy due to the presence of lithium ions in their stable sites, not interacting with each other. Following Bohn et al. (2013), a contribution of the inter-ionic interaction $\Delta U_{\mathrm{interac}}$ can be added to the internal energy with eq. (11.5) which becomes

$$\psi^{\mathrm{chem}*} = \psi^{\mathrm{chem}} + \Delta U_{\mathrm{interac}}, \tag{11.6}$$

with

$$\left.\frac{\partial \Delta U_{\mathrm{interac}}}{\partial c_{\mathrm{Li}}}\right|_{p,T} = gRT\frac{c_{\mathrm{Li}}}{c_{max}},$$

where p is the pressure, g is the dimensionless parameter characterizing the inter-ionic interactions and dependent on the lithium concentration c_{Li}. Two models were used for the simulations, a simplistic one where the contribution of $\Delta U_{\mathrm{interac}}$ is ignored ($g = 0$) and an extended one, where it is taken into account.

Further, we introduce the electric energy

$$\psi^{\mathrm{elec}} = \rho F \phi = (z_{\mathrm{Li}}\, c_{\mathrm{Li}} + z_e\, c_e) F\, \phi, \tag{11.7}$$

where F is the Faraday constant and ρ is the charge density. The latter can be defined as the sum of the concentration of lithium ion charges $z_{\mathrm{Li}}\, c_{\mathrm{Li}}$ and electron charges $z_e\, c_e$, with $z_{\mathrm{Li}} = +1$ the number of charges per one ion lithium, $z_e = -1$ the number of charges per electron and c_e the concentration of electrons.

11.3 Constitutive equations

From Gibbs free energy we obtain the mechanical stress as

$$\boldsymbol{\sigma} = \frac{\partial \psi}{\partial \boldsymbol{\varepsilon}} = \mathbb{C}\big(\boldsymbol{\varepsilon} - \frac{1}{3}\Omega_{\mathrm{Li}}\,(c_{\mathrm{Li}} - c_0)\,\mathbf{1}\big), \tag{11.8}$$

the electrochemical potential of lithium ions as

$$\begin{aligned}\eta_{\mathrm{Li}} &= \frac{\partial \psi}{\partial c_{\mathrm{Li}}}\\ &= \mu_0 + gRT\frac{c_{\mathrm{Li}}}{c_{max}} + RT\ln\frac{c_{\mathrm{Li}}}{c_{max}-c_{\mathrm{Li}}} - \Omega_{\mathrm{Li}}\sigma_h + z_{\mathrm{Li}}F\phi,\end{aligned} \tag{11.9}$$

with $\sigma_h = \frac{1}{3}\boldsymbol{\sigma} : \mathbf{1}$ the hydrostatic stress. The electrochemical potential of electrons is

$$\eta_e = \frac{\partial \psi}{\partial c_e} = z_e F\phi. \tag{11.10}$$

From eq. (11.9) the flux of lithium ions for single phase concentrations can be defined as

$$\begin{aligned}\boldsymbol{J}_{\mathrm{Li}} &= -c_{\mathrm{Li}}M_{\mathrm{Li}}\nabla\eta_{\mathrm{Li}}\\ &= -c_{\mathrm{Li}}M_{\mathrm{Li}}\left\{\frac{1}{c_{\mathrm{Li}}}RT\left(1+\frac{c_{\mathrm{Li}}}{c_{max}-c_{\mathrm{Li}}}+g\frac{c_{\mathrm{Li}}}{c_{max}}+\frac{\mathrm{d}g}{\mathrm{d}c_{\mathrm{Li}}}\frac{c_{\mathrm{Li}}^2}{c_{max}}\right)\nabla c_{\mathrm{Li}}\right.\\ &\qquad\left. - \Omega_{\mathrm{Li}}\nabla\sigma_h + z_{\mathrm{Li}}F\nabla\phi\right\},\end{aligned} \tag{11.11}$$

with the mobility of lithium ions M_{Li}

$$M_{\mathrm{Li}} = \frac{D_0}{RT}\left(1-\frac{c_{\mathrm{Li}}}{c_{max}}\right). \tag{11.12}$$

Solid solutions of two phases are introduced later and thoroughly detailed by Bohn et al. (2013). From eq. (11.10) the flux of electrons can be defined as

$$\boldsymbol{J}_e = -M_e\nabla\eta_e = -M_e z_e F\nabla\phi, \tag{11.13}$$

with the mobility of electrons M_e

$$M_e = \frac{\kappa_e}{z_e^2F^2} \tag{11.14}$$

where D_0 is the diffusion coefficient of Li and κ_e is the electric conductivity of $LiMn_2O_4$. The definition implies that the mobility of lithium ions depends on the lithium concentration, and that the lithium mobility tends to zero when its concentration reaches the maximum c_{max}. A hypothesis from these two flux definitions is that there is no coupling between electrons and ions, where the electrochemical potential of one charge carrier influences the flux of the other one (Allnatt and Lidiard 1993). As introduced in section 1.3.1, it was however shown that electron conduction in this spinel is mediated by hopping of small non-adiabatic polarons (Iguchi et al. 1998 2002; tateishi et al.

2004; Park et al. 2010). It was theoretically shown that the polaron hopping can impact lithium ion movements (tateishi et al. 2004) and experimentally deduced that lithium diffusivity is intrinsically related to the polaronic properties (Marzec et al. 2002). As this coupling is little understood and hard to quantify, it will be reserved to future studies.

Replacing the mobility of lithium ions from eq. (11.12) to eq. (11.11) gives

$$\boldsymbol{J}_{\mathrm{Li}} = -D_0 D_{eff} \nabla c_{\mathrm{Li}} + \frac{D_0 \Omega_{\mathrm{Li}} c_{\mathrm{Li}}}{RT}(1-\frac{c_{\mathrm{Li}}}{c_{max}})\nabla\sigma_h - \frac{D_0 z_{\mathrm{Li}} F c_{\mathrm{Li}}}{RT}(1-\frac{c_{\mathrm{Li}}}{c_{max}})\nabla\phi, \quad (11.15)$$

which depends on the lithium concentration and its gradient ∇c_{Li}, hydrostatic stress $\nabla\sigma_h$ and electric potential $\nabla\phi$. D_{eff} is the normalized effective diffusivity that translates the irregularity in the Gibbs free energy. It impacts the diffusivity and depends on g . Multiplying D_{eff} by D_0 yields the total effective diffusion coefficient. It has been already derived for $\mathrm{LiMn_2O_4}$ by Bohn (2011) and is defined as a piecewise function for the range $0 < c_{\mathrm{Li}} < c_{max}$.

D_{eff} is a factor that translates the irregularity in the Gibbs free energy that impacts the diffusivity and depends on g. In the case of single phase, it is equal to:

$$D_{eff} = 1 + \frac{c_{\mathrm{Li}}}{c_{max}}(1-\frac{c_{\mathrm{Li}}}{c_{max}})(g + c_{\mathrm{Li}}\frac{\mathrm{d}g}{\mathrm{d}c_{\mathrm{Li}}}). \quad (11.16)$$

When $g = 0$, we find the simple case scenario where $D_{eff} = 1$ and the gradient of concentration is only factorized with the constant diffusion parameter D_0. Otherwise, D_{eff} can be derived from the open-circuit voltage (OCV) measurements of a $\mathrm{LiMn_2O_4}$/Li(m) half-cell as explained by Bohn et al. (2013) and Van Der Ven et al. (2013). In the presence of a solid solution of two $\mathrm{Li}_x\mathrm{Mn_2O_4}$ phases, the OCV is constant which induces $D_{eff} = 0$: lithium diffusion is only driven by the gradient of hydrostatic stress and the electric field. g is an unknown thermodynamical parameter, but D_{eff} can be estimated from experiment. D_{eff} for $\mathrm{LiMn_2O_4}$ has been already derived by Bohn (2011) and is defined as a piecewise function for the range $0 < c_{\mathrm{Li}} < c_{max}$. It is plotted in fig. 11.1 and represents both single phase and solid solutions of two phases.

Two models were implemented in the current work:

simple model where the diffusivity is kept constant ($D_{\mathrm{eff}} = 1$) as it is the case in previous models of ESM.

extended model where the effective diffusivity $D_{\mathrm{eff}}\ D_0$ is used ($D_{\mathrm{eff}} =$ fig. 11.1). Here, the phase transition is taken into account.

The reason for exploiting both models is to leave the ability to compare with previous work (Morozovska et al. 2010).

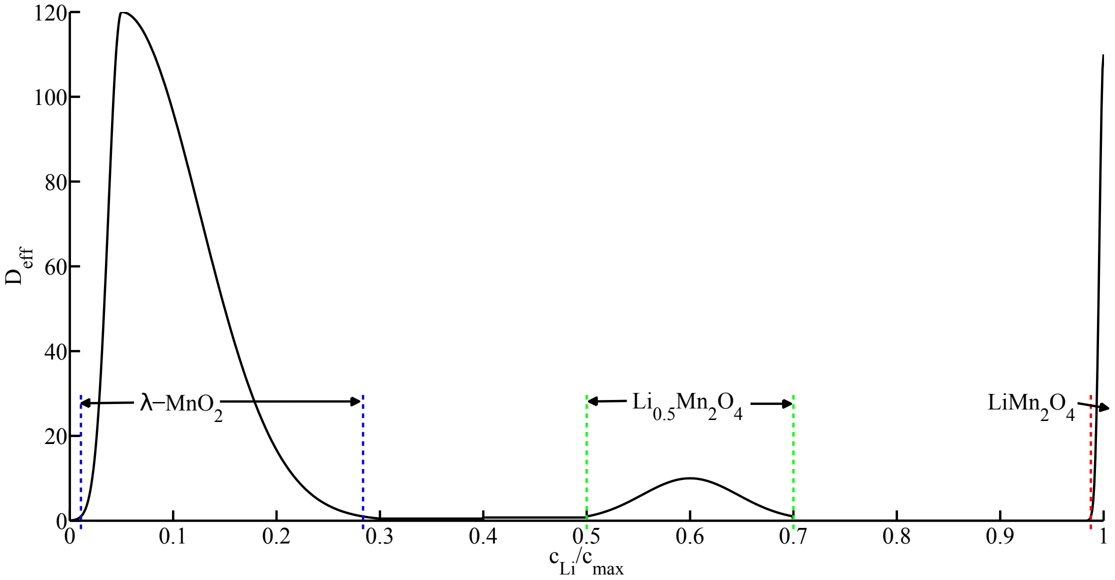

Figure 11.1: D_{eff} as function of c_{Li}/c_{max}. The three phases of spinel $\text{Li}_x\text{Mn}_2\text{O}_4$ are marked on the plot. Colored bars are used in fig. 16.5.

Based on the Nernst-Einstein relation, the electric current is defined as

$$\begin{aligned}\boldsymbol{I} = \boldsymbol{I}_e + \boldsymbol{I}_{\text{Li}} = z_e F \boldsymbol{J}_e + z_{\text{Li}} F \boldsymbol{J}_{\text{Li}} = -\kappa_e \nabla\phi + z_{\text{Li}} F \boldsymbol{J}_{\text{Li}} \\ = -D_0 D_{eff} z_{\text{Li}} F \nabla c_{\text{Li}} + \frac{D_0 z_{\text{Li}} F \Omega_{\text{Li}} c_{\text{Li}}}{RT}\left(1 - \frac{c_{\text{Li}}}{c_{max}}\right)\nabla\sigma_h \\ - \left\{\kappa_e + \frac{D_0 z_{\text{Li}}^2 F^2 c_{\text{Li}}}{RT}\left(1 - \frac{c_{\text{Li}}}{c_{max}}\right)\right\}\nabla\phi. \quad (11.17)\end{aligned}$$

11.4 Balance equations

In order to model the system, we need to use balance laws such as balance of momentum for the mechanical stress

$$\nabla \cdot \boldsymbol{\sigma} = \boldsymbol{0}, \quad (11.18)$$

the conservation of mass

$$\frac{\partial c_{\text{Li}}}{\partial t} + \nabla \cdot \boldsymbol{J}_{\text{Li}} = 0, \quad (11.19)$$

and the conservation of charge

$$\frac{\partial \rho}{\partial t} + \nabla \cdot \boldsymbol{I} = 0. \quad (11.20)$$

The LiMn_2O_4 particle is connected to a closed circuit, thus the electron influx and electron outflux are the same. Following GARCÍA ET AL. (2005), we assume that there is no local charge accumulation ($\partial\rho/\partial t = 0$), so that eq. (11.20) simplifies to

$$\nabla \cdot \boldsymbol{I} = 0. \tag{11.21}$$

As polaron/ion coupling is an important and poorly known mechanism, local charge accumulation seemed to be not significant enough to be implemented, but this actually remains an open question.

11.5 Mean electric force

In this section, we outline how the ESM signal is estimated from the output of the model. The AC excitation (frequency domain) is not directly modeled but only suggested through a mean electric force.

As explained in the Introduction, we consider that the ESM signal does not originate from diffusion of lithium as the excitation frequency is too high for allowing hopping significant enough to be detected through Vegard's deformation (Tselev et al. 2014). Instead, we consider the signal to be driven by ionic polarization mechanisms where the lithium ions are vibrating within their interstitial sites without long-range hopping. The ionic vibration is induced by the electric force and in return induces the ESM signal. An alternative electric potential $\bar{\phi}_{AC}(t)$ of frequency ω is applied without interruption during experiment. Here, the electric potential is given as follows:

$$\bar{\phi}_{AC}(t) = \sqrt{2}\bar{\phi}_{AC}^{rms} cos(\omega t), \tag{11.22}$$

where $\bar{\phi}_{AC}^{rms}$ is the root mean square (RMS) voltage. Considering quasi-static motions, the magnetic field produced by the alternating electric field is ignored (Bolotovskii 1994). The mean electric force $\mathfrak{F}_{AC}(t)$ applied onto the ions is

$$\mathfrak{F}_{AC}(t) = \int_V z_{\mathrm{Li}} c_{\mathrm{Li}}(x, y, z, t) F \boldsymbol{E}_{AC}(x, y, z) \mathrm{d}V, \tag{11.23}$$

where V is the volume of the body and $\boldsymbol{E}_{AC}(x, y, z) = -\nabla\phi_{AC}(x, y, z)$ is the mean electric field, with $\phi_{AC}(x, y, z)$ the local RMS electric potential. ϕ_{AC} is equal to $\bar{\phi}_{AC}^{rms}$ at the tip contact and is calculated by COMSOL in the rest of the body. It is constant in time, consequently $\boldsymbol{E}_{AC}$ is also constant in time and $\mathfrak{F}_{AC}$ varies in time only with the concentration field ($c_{\mathrm{Li}}(x, y, z, t)$). This force is the static part of Lorentz' force. The ESM signal $S_{\mathrm{Total}}(t)$ measured after the release of the DC voltage is considered to be the sum of a constant background noise $S_{\mathrm{background}}$ and a time-dependent signal originating from the lithium ions $S_{\mathrm{Li}}(t)$. In a first approximation, the latter is considered linearly proportional to $\mathfrak{F}_{AC}(t)$:

$$S_{\mathrm{Li}}(t) \propto \mathfrak{F}_{AC}(t). \tag{11.24}$$

Since the real underlying mechanism is unknown, $\mathfrak{F}_{AC}$ should be understood as a mathematical tool to probe the concentration of lithium just under the tip. Equation (11.23) is in fact a weighted sum of c_{Li} where the weight is given by the amplitude of the electric field $\boldsymbol{E}_{AC}$. $S_{\mathrm{Li}}(t)$ consequently probes c_{Li} within a small volume.

12 Chapter Boundary conditions and implementation

The system is reduced to a simple Li$_x$Mn$_2$O$_4$ single crystal particle with a half spherical shape. Only the spinel material as described in chapter 11 will be implemented. This implies that neither the air, the water meniscus around the tip, the carbon black around the particle, nor the tip materials are implemented in the model. The tip is implicitly conveyed through the applied voltage onto a small disk of the top particle surface. As there is a voltage drop at the contact, the experimental applied voltage and the model applied voltage cannot be quantitatively compared. The carbon black is similarly conveyed by grounding the bottom surface of the particle to act as if the carbon black particles produce a thin layer homogeneously and perfectly in contact with the crystal and perfectly connected to the AFM electronics.

12.1 Boundary conditions

The modeled body consists of a spinel Li$_x$Mn$_2$O$_4$ single crystal particle with an initial arbitrary normalized concentration of lithium ions $\hat{c}_{ini} = c_0/c_{max}$. It is a half-spherical particle of radius R_{part}. A top view of the particle with the mechanical boundaries is schematically shown in fig. 12.1a. These boundaries do not allow rigid body motion but there is no counter mechanical forces on the particle, hence it is free to swell. Lithium ions can freely move within the particle if enough vacancies are available ($c_{\text{Li}} < c_{max}$). There is no flux of lithium across the boundaries, i.e. the total amount of lithium ions stays the same within the particle

$$\begin{aligned}\frac{\int_V \hat{c}\,\mathrm{d}V}{V} &= \hat{c}_{ini}\\ \boldsymbol{J}_{\text{Li}} \cdot \boldsymbol{n} &= 0,\end{aligned}$$

where $\hat{c} = c_{\text{Li}}/c_{max}$ is the normalized lithium concentration and $\boldsymbol{n}$ is the surface unit vector. The electric potential applied by the AFM tip $\bar{\phi}_{DC}$ is defined as:

$$\bar{\phi}_{DC} = \bar{\phi}_0(t)\frac{R_{tip}^2}{((x-x_0)^2 + (y-y_0)^2 + R_{tip}^2)}, \tag{12.1}$$

where $\bar{\phi}_0(t)$ is the time dependent applied voltage and R_{tip} is the tip radius centered at position (x_0,y_0). $\bar{\phi}_{DC}$ is applied over the whole top flat surface but is locally distributed within a circle of radius R_{tip} with smooth edges following a 2D Lorentz-like function (Choudhury et al. 2008). The remainder of the surface is grounded to mimic a perfect ohmic contact with carbon black. Note that the dimensions of the particle are big enough as compared to R_{tip} so that most of the electric field is concentrated in the vicinity of the tip. The electric and chemical boundaries are shown in fig. B.6.

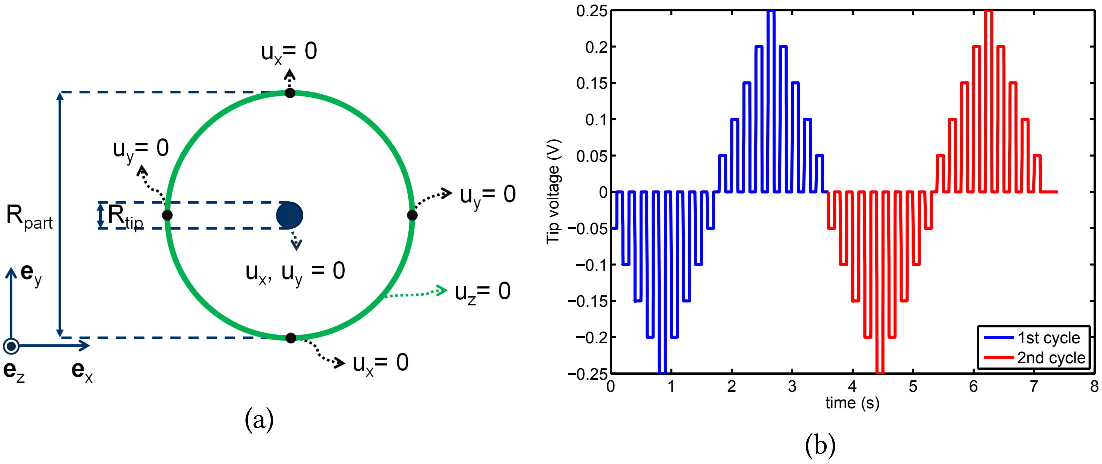

Figure 12.1: (a) Displacement boundary condition. Conditions on displacements are indicated by the letter u with the direction in subscript. (b) Voltage steps used in the simulation of voltage spectroscopy measurements.

12.2 COMSOL implementation

The model is implemented in COMSOL Multiphysics 4.4 with a segregated (or iterative) solver for time dependent problems, where two coefficient form partial differential equation modules are used for eqs. (11.19) and (11.21). Equation (11.18) is put in the solid mechanics module. For modeling time-spectroscopy measurements as explained in the experimental section 4.3.2.3, $\bar{\phi}_0(t)$ is described by a gate function where

$$\bar{\phi}_0(t) = \begin{cases} \Phi_0 \text{ for } 0 < t < 10\text{ms} \\ 0 \text{ otherwise,} \end{cases}$$

where Φ_0 is the applied voltage. The gate function is gradually increased over a period of 0.1 ms. Concerning simulation of the voltage spectroscopy, the voltage is plotted versus time in fig. 12.1b (pulse time of 100 ms smoothed over a period of 1 ms).

In order to simulate the ESM signal, a supplementary electrostatics physics module was used with no coupling with any variable used in the other modules. It is merely aimed at describing the AC electric field $-\nabla\phi_{AC}$ within the body when the AC voltage $\bar{\phi}_{AC}$ is applied. $\bar{\phi}_{AC}^{rms}$ is applied in the same way as $\bar{\phi}_{DC}$ (see eq. (12.1)).

The mesh consists of 10920 elements with a high refinement in the vicinity of the AFM tip (see fig. 12.2). Default parameters are listed in table 12.1.

Results from the model and experiments are given in chapter 16.

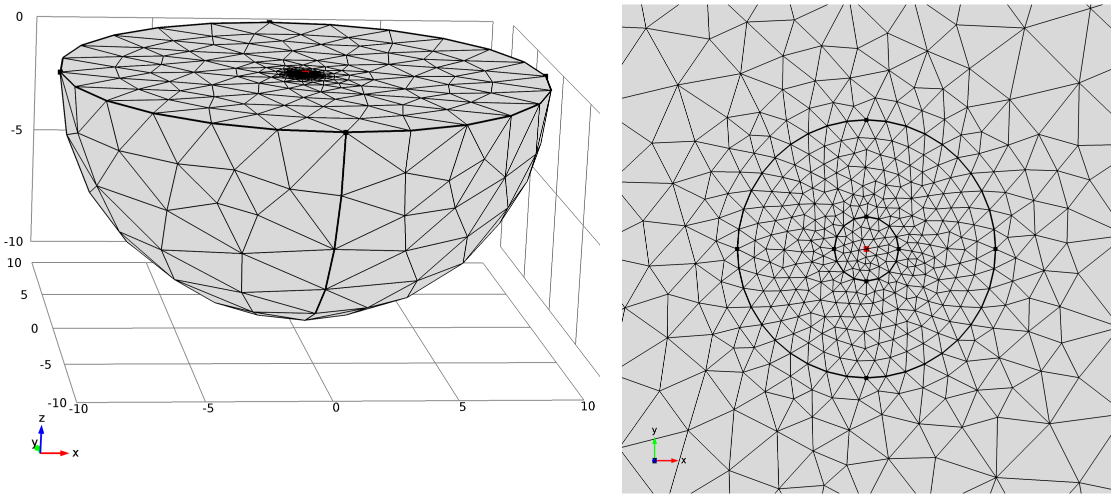

Figure 12.2: FE mesh of the simulation as generated by COMSOL.

Property	Symbol	Value	Unit
Electrical conductivity	κ_e	10^{-2}	$\mathrm{S.m}^-1$
Lithium diffusion	D_0	10^{-14}	$\mathrm{m}^2.\mathrm{s}^-1$
Molar volume expansion	Ω_{Li}	3.5×10^{-6}	$\mathrm{m}^3.\mathrm{mol}^{-1}$
Maximum concentration	c_{max}	22900	$\mathrm{mol.m}^{-3}$
Initial concentration	c_{ini}	0.5	[1]
Elastic modulus	E	100	GPa
Poisson's ratio	ν	0.3	[1]
Temperature	T	293.15	K
Tip radius	R_{tip}	0.05	µm
Particle radius	R_{part}	10	µm
Applied voltage	$\bar{\phi}_0$	-0.1	V

Table 12.1: Default parameters.

Part VI

Results

In this part, results from the different studies are listed.

First structure analyses of each sample are presented: crystal structure by XRD, then the geometry and the content of the particles are qualitatively imaged by SEM and EDX and last their chemical composition is quantified by ICP-OES. Subsequently, the results obtained by applying the selective nanoindentation method described in part IV are shown for most samples and further analysis is carried out by means of micro-Raman spectroscopy and CR-AFM. The latter was done in the laboratories of Fraunhofer Institute IZFP under the supervision of Dr. Rabe and Dr. Batista. These data were peer-reviewed and published in Acta Materialia (see AMANIEU ET AL. 2015a), portions of the text and the figures used here are similar if not the same as in the corresponding scientific article.

The following chapter introduces fracture properties of $LiMn_2O_4$. Quantitative measurements at the microscale are challenging as it is difficult to obtain experimental conditions with well-defined geometries, unlike on bulk samples where more traditional techniques can be used (e.g. single edge notch bend) as the samples can be machined. Few data were obtained from crack opening displacement measured by AFM. On the other hand, qualitative observations supported by focused-ion beam were made on a {111} wafer to determine cleavage planes. This work has been submitted to Acta Materialia for peer-review (AMANIEU ET AL. 2015b), portions of the text and the figures used here are similar if not the same as in the corresponding scientific article.

The last chapter of this part deals with data obtained from the simulation described in part V. The data are also compared with experimental measurements (described in section 4.3.2.3). As already said in part V, this work has been submitted to Journal of Applied Physics for peer-review (AMANIEU ET AL. 2015c) and was carried out in close collaboration with Mr. Huy Thai and Dr. Sergey Luchkin. Portions of the text and the figures used here are similar if not the same as in the corresponding scientific article.

13 Chapter
Chemical characterization

13.1 X-Ray Diffraction

Diffractograms for 4 samples are shown in fig. 13.1a. Similar spectra were obtained for all the samples. They show a single phase of spinel-like $\lambda-MnO_2$. The diffraction peaks are sharp, indicating a homogeneous structure for all of them while two phases could have been expected for 50 and/or 75 % SoC (Kanamaru et al. 1996). No other phase could be detected for all the battery samples. However, 2 % (wt) of a $LiCoO_2$ phase was found in the reference sample *LiMn2O4p*.

Calculated lattice parameters from these diffractograms are shown in table 13.1. They decrease regularly upon delithiation as expected (Kanamaru et al. 1996; Berg and Thomas 1999; Dridi-zrelli 2012), except for *C50DoD* which has a value similar to delithiated material like *C100SoC*. Another cell was opened in the same conditions, called C50DoD_2, where X-Ray diffraction shows more reasonable data. This discrepancy might be due to a laboratory error rather than an effect from discharging (DoD) versus charging (SoC) and was also reported for ICP-OES data (see section 13.3). There was almost no difference between the two samples obtained from 0 % SoC batteries. Note that the samples from discharged batteries have a lattice parameter smaller than the one expected for pristine lithiated spinel ([0.822–0.824] nm (Kanamaru et al. 1996; Berg and Thomas 1999)) like sample *LiMn2O4p*. This might be due to the fact that the cathode does not fully relithiate from the first cycle, as previously reported in literature (Dridi-zrelli 2012), because the electrochemical exchange is not perfectly reversible when full cells are cycled at relatively high currents like 1 C-Rate (ohmic drop) and the anode/cathode ratio is not correctly balanced. An observation can be done for the fast aged samples: their lattice parameters seem all to be above the ones from the less cycled cells. This should be considered carefully: *C100SoC_aged* could not be charged above 4.08 V and *C50SoC_aged* is not much different from *C50SoC*. Concerning the specimen from cell *C75SoC*, powder obtained from cell disassembly (as described in section 3.1) and powder obtained from scratching the current collector where studied separately in order to check the reliability of the analysis methods. The second powder batch was obtained later and its origin as not disclosed before all the analysis was run. As can be seen from table 13.1, there is a difference which is not substantial but significant enough regarding the precision of the Rietveld method. This could indicate that there can be differences within the same cell, either because the first set of particles is close to the separator in the cell and the second set is close to the current collector or because they originated from different areas.

When compared with literature data,the lattice parameter obtained for 0 % SoC corresponds to an x in $Li_xMn_2O_4$ between 0.4 (Dridi-zrelli 2012) and 0.9 (Berg and Thomas 1999). On the other end of the electrochemical cycle, the lattice parameter obtained for 100 % SoC corresponds to an x between 0.2 (Dridi-zrelli 2012) and 0.5 (Berg and Thomas 1999). Note that impurities substituting the relatively big manganese ions, such as nickel or cobalt, can help with reducing the lattice parameters, while intercalation impurities would have the opposite effect.

On the wafer, two phases were detected (fig. 13.1b). The main phase was a strongly {111}-textured, polycrystalline spinel phase. The second one, which showed less intensity, was a {100}-textured, polycrystalline cubic phase of Bixbyite Mn_2O_3. No MnO phase from the original wafer was detected. SEM images show a similar triangular pattern as reported by Kitta et al. (2013) in the outer ring of the top surface (see fig. 3.4). A very different structure was observed in the central area, which might be associated with the Bixbyite phase. EBSD showed that the outer ring of the surface was only composed of spinel phase with very clear diffraction patterns (see fig. B.2 in appendix B). Only this area was studied by nanoindentation.

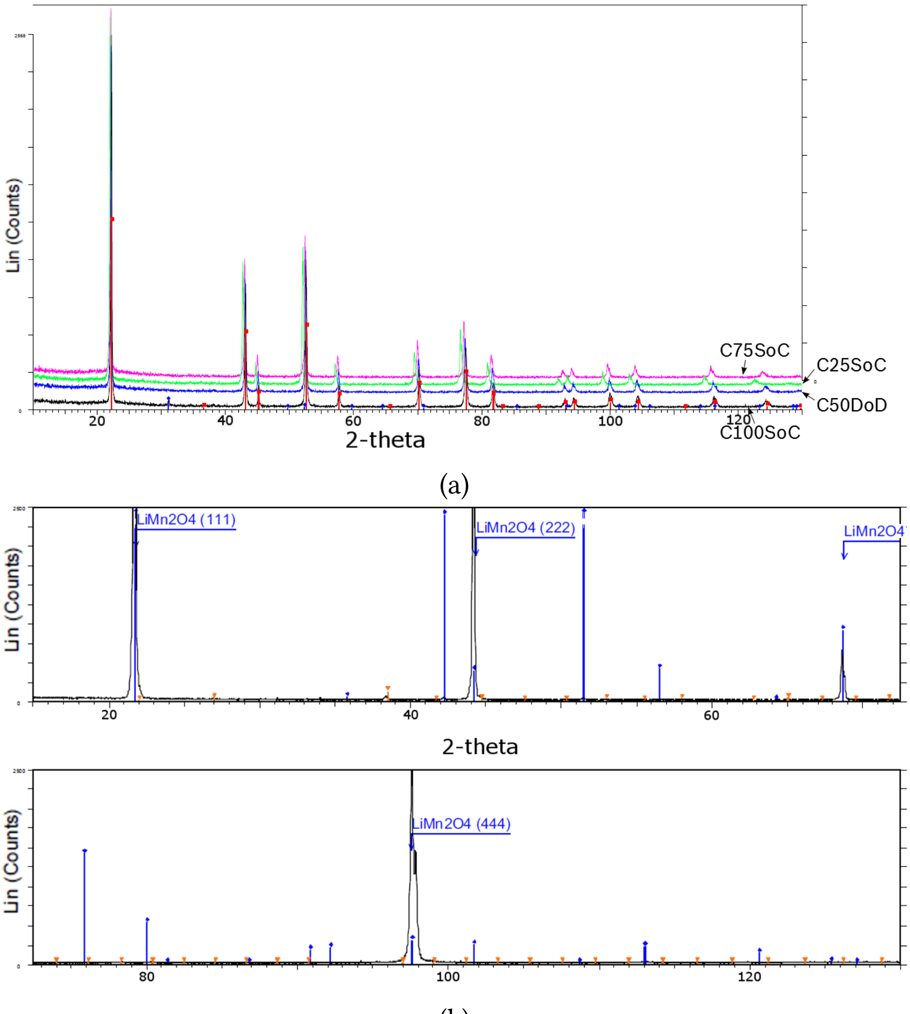

(a)

(b)

Figure 13.1: (a) XRD diffractograms of *C25SoC*, *C75SoC*, *C100SoC*, *C50DoD*. A single spinel phase was detected for all samples. (b) XRD diffractogram of the *Wafer*. A spinel phase with a strong {111} orientation was detected (blue lines). With less intensity, a cubic phase of Mn_2O_3 Bixbyite was also detected (orange lines).

Sample name	SoC (%)	lattice parameter a (nm)	GoF (χ^2)
C0SoC_2	0	0.81779	1.26
C0SoC_100	0	0.81791	1.08
C0SoC_aged	0	0.81888	N/C
C25SoC	25	0.8158	1.12
C50SoC	50	0.8141	1.25
C50DoD	50	0.80952	N/C
C50DoD_2	50	0.81352	1.13
C50SoC_100	50	0.81333	N/C
C50SoC_aged	50	0.81413	N/C
C75SoC (powder)	75	0.8112	1.15
C75SoC (scratch)	75	0.81144	N/C
C100SoC	100	0.8092	1.16
C100SoC_aged	100	0.81104	N/C
LiMn2O4p	0	0.82355	1.31

Table 13.1: Lattice parameters a obtained from Rietveld fitting of X-Ray diffraction measurements with their respective goodness of fit (GoF). N/C indicate GoF that were not communicated by the analysis department. These data are plotted in fig. 13.2. Note: for *LiMn2O4p*, 2 % (wt) of a $LiCoO_2$ phase was found.

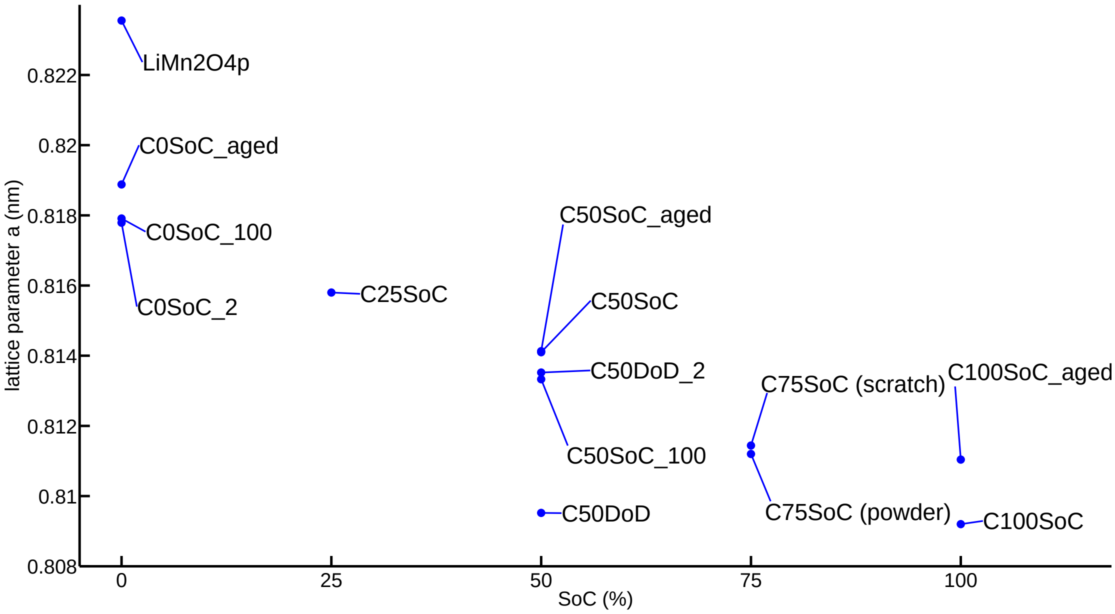

Figure 13.2: Data from table 13.1: states of charge versus lattice parameters a measured for each sample.

13.2 Scanning Electron Microscopy

Scanning electron micrographs of cross-sections were reported in part IV (see figs. 6.1 and 6.2). Porous and solid particles were detected. Figure 13.3 is an SEM micrograph of a cathode. Some particles approach an octahedral shape as reported for pristine $LiMn_2O_4$ grains (Akimoto et al. 2000; Tang et al. 2001; Takahashi et al. 2006). Various sizes can be seen where what was thought as porous particles seems to be in fact several $\sim$ 100 nm particles sintered together. All of them have polyhedron-like sharp edges which could indicate incomplete octahedrons. In rare cases, some particles have smooth edges as can be seen on a cross-section of sample *C0SoC_1* in fig. 13.4a. Energy dispersive x-ray analysis (EDX) indicates that these particles contain cobalt (see fig. 13.4b). They could be metal oxides containing mainly cobalt and less or no manganese. These particles could hypothetically come from factory dust as different types of cells are made by the same assembly-lines. Round shapes were previously reported for manganese cobalt oxides (Lavela et al. 2007). The amount of such particles was below the detection level of XRD but can be detected from ICP–OES as seen in the next section. A large area surrounding the particle from fig. 13.4a was also scanned by EDX and is reported in appendix B.

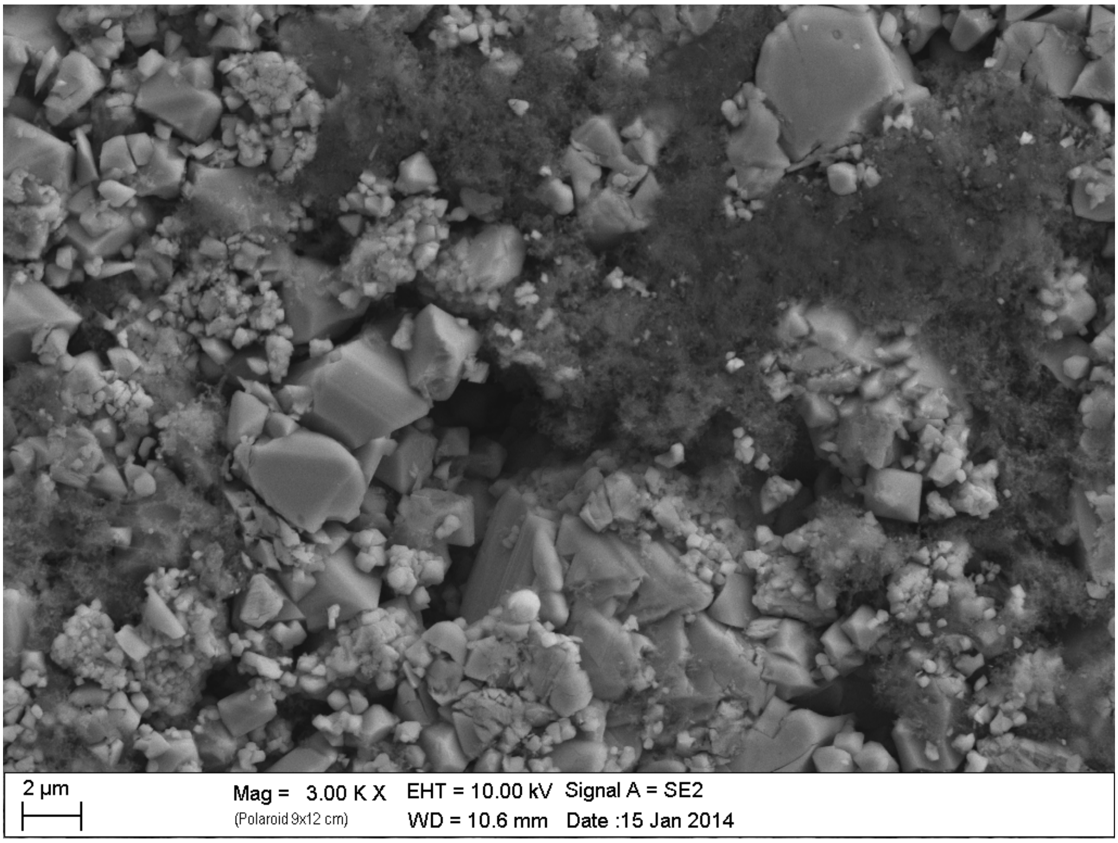

Figure 13.3: SEM picture of a cathode material after extraction from the cell denoted *C0SoC_2*.

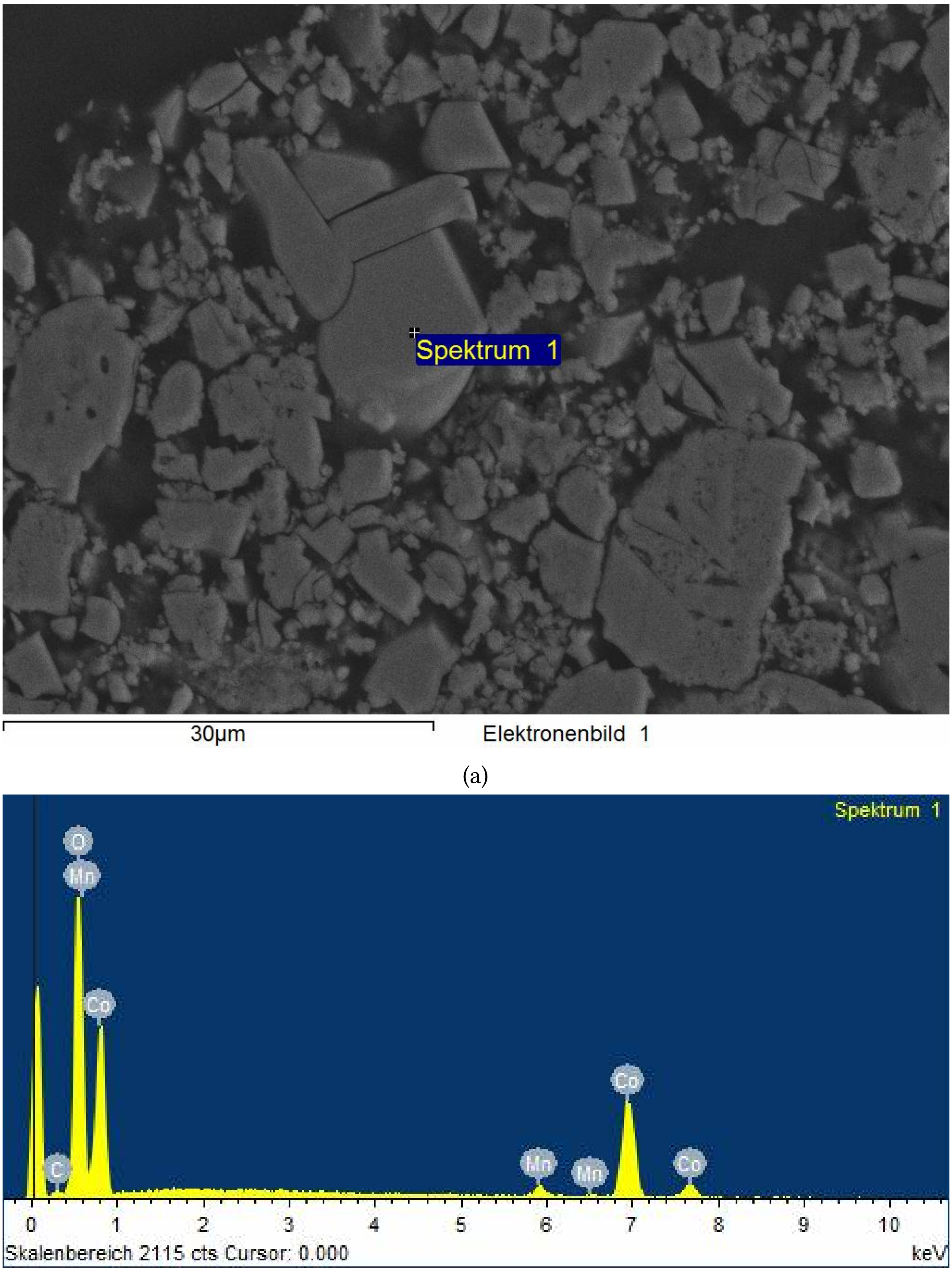

(a)

(b)

Figure 13.4: (a) SEM image of a cathode cross section. (b) EDX spectrum measured in the middle of a cobalt-based particle.

13.3 ICP-OES

Table 13.3 lists the most important results from the ICP–OES measurements with content of Li, Mn and Co. Traces of Al, Na, Ni and K were also found and their exact quantities are not reported here. The original data are weight ratios of each species as compared to the total weight of each specimen. In order to have more intelligible data, they were changed to molar ratios as compared to 1 mole of Mn, as listed in the third column. A triple determination was systematically done except for one sample to determine a standard deviation, reported in table 13.3 as a percentage. It is believed that all the cobalt found is due to the cobalt-based particle reported by SEM in the previous section. For simplicity[3], if it is considered that the same amount of lithium x is present per Mn_2O_4 unit cell as per CoO_2 unit cell, then x can be calculated as follows:

$$x = \frac{n_{\mathrm{Li}}}{0.5 n_{\mathrm{Mn}} + n_{\mathrm{Co}}}, \tag{13.1}$$

where n_{Mn}, n_{Co} and n_{Li} are the unit-less ratios of moles of Mn, Co and Li, respectively, per unit mole of Mn (i.e. $n_{\mathrm{Mn}} = 1$). The standard deviation σ is subsequently calculated as follows according to error propagation rules (Harvard University 2007):

$$\frac{\sigma}{|x|} = \sqrt{\left(\frac{\sigma_{\mathrm{Li}}}{n_{\mathrm{Li}}}\right)^2 + \left(\frac{\sqrt{(0.5\sigma_{\mathrm{Mn}})^2 + \sigma_{\mathrm{Co}}^2}}{0.5 n_{\mathrm{Mn}} + n_{\mathrm{Co}}}\right)^2}, \tag{13.2}$$

where σ_{Mn}, σ_{Co} and σ_{Li} are the standard deviations obtained from the experimental triple determination of n_{Mn}, n_{Co} and n_{Li}, respectively. x and the standard deviation percentages ($\sigma/|x|$) are reported in the fourth column. When x is compared with the molar ratio of Li:Mn, it can be noticed that the influence of the cobalt particles on lithium content is not so significant. If no cobalt is present, x is equal to the double of Li:Mn (see eq. (13.1)).

Previously, the lattice parameters were reported smaller than expected, all of them being under 0.819 nm, indicating potentially less lithium concentration. The ICP–OES shows opposite results, where it seems that the ratio of Li for each Mn is bigger than expected: all of them are above 0.5, even at 0 % SoC. Some of the triple determinations show significant standard deviations, above 10 % for two samples (*C50SoC_100* and *C100SoC*). Concerning sample *C75SoC*, the two tests have a difference of more than 10 % while the triple determinations resulted in small standard deviation. The XRD results show very similar results with fine peaks comparatively for the same specimen powders. This indicates that lithium ions are present outside of the particles in non-crystalline agglomerates, undetectable by XRD: solid electrolyte interfaces, $LiPF_6$ leftovers, etc.

---

[3] A more realistic model would balance the electrochemical potentials of both species versus metallic lithium: x could then have different values in $Li_xMn_2O_4$ and Li_xCoO_2.

ICP-OES data were considered qualitatively only in this study, as quantification seems to be unreliable for these specific samples.

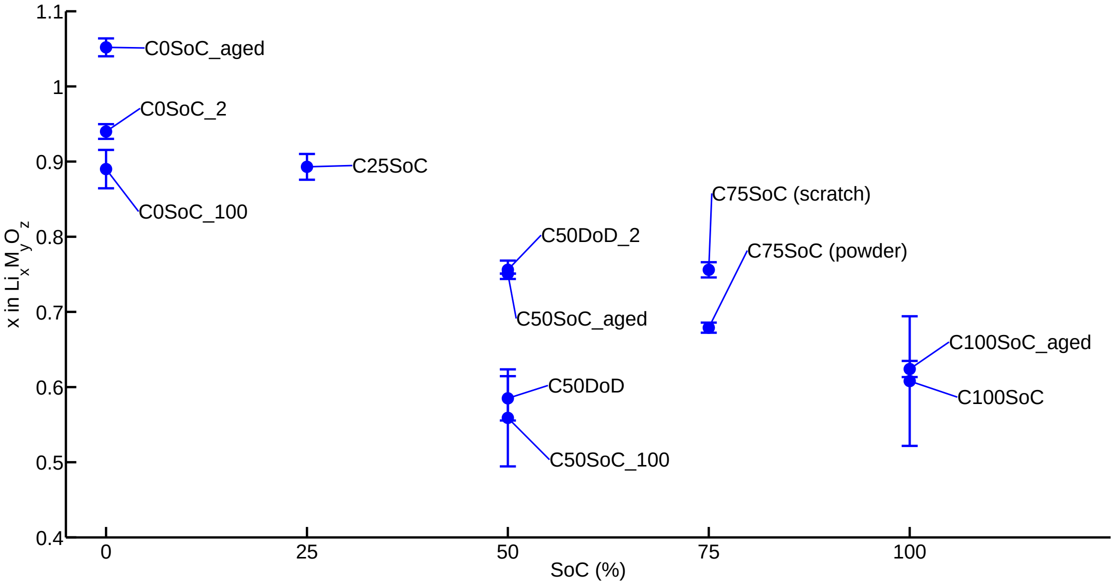

Figure 13.5: x in $\mathrm{Li}_x\mathrm{M}_y\mathrm{O}_z$, y=2 for M=Mn and 1 for M=Co, versus states of charge of the samples. The error bars represent standard deviations. Data from table 13.3.

Sample names (SoC)	Metal (M)	$M^{\dagger}$:Mn ± st. dev.	x in $Li_xM^{\dagger}_yO_z$	± st. dev.
C0SoC_2 (0 %)	Li	0.485 ± 0.58 %	0.940	± 1.0 %
	Mn	1.000 ± 0.90 %		
	Co	0.016 ± 1.0 %		
C0SoC_100 (0 %)	Li	0.462 ± 0.56 %	0.890	± 2.9 %
	Mn	1.000 ± 2.9 %		
	Co	0.019 ± 0.81 %		
C0SoC_aged (0 %)	Li	0.526 ± 0.85 %	1.052	± 1.1 %
	Mn	1.000 ± 0.75 %		
	Co	N/C		
C25SoC (25 %)	Li	0.465 ± 1.9 %	0.893	± 1.9 %
	Mn	1.000 ± 0.37 %		
	Co	0.021 ± 0.81 %		
C50DoD (50 %)	Li	0.302 ± 2.4 %	0.585	± 5.1 %
	Mn	1.000 ± 4.6 %		
	Co	0.017 ± 3.1 %		
C50DoD_2 (50 %)	Li	0.390 ± 1.1 %	0.756	± 1.6 %
	Mn	1.000 ± 1.2 %		
	Co	0.017 ± 1.0 %		
C50SoC_100 (50 %)	Li	0.289 ± 5.3 %	0.559	± 12 %
	Mn	1.000 ± 11 %		
	Co	0.017 ± 0.40 %		
C50SoC_aged (50 %)	Li	0.388 ± N/A	0.751	± N/A
	Mn	1.000 ± N/A		
	Co	0.017 ± N/A		
C75SoC (powder) (75 %)	Li	0.351 ± 0.83 %	0.679	± 0.99 %
	Mn	1.000 ± 0.56 %		
	Co	0.017 ± 1.0 %		
C75SoC (scratch) (75 %)	Li	0.395 ± 1.1 %	0.756	± 1.3 %
	Mn	1.000 ± 0.75 %		
	Co	0.022 ± 4.7 %		
C100SoC (100 %)	Li	0.315 ± 14 %	0.608	± 14 %
	Mn	1.000 ± 3.8 %		
	Co	0.018 ± 17 %		
C100SoC_aged (100 %)	Li	0.325 ± 1.3 %	0.624	± 1.7 %
	Mn	1.000 ± 1.2 %		
	Co	0.021 ± 1.5 %		

† M=Mn or Co, y= 2 for Mn and 1 for Co

Table 13.3: Results from ICP-OES for each sample for lithium, manganese and cobalt. Original data are weight percentage, they were re-arranged in order to have a molar ratio with respect to 1 mole of manganese. The fourth column corresponds to what would be the amount of lithium if it was allocated equally between $Li_xMn_2O_4$ and Li_xCoO_2. Standard deviations are calculated from triple determination. N/A indicates single determination. N/C indicates that cobalt was not reported, yet there could still be traces. Traces of Al, Na, Ni and K were also found.

14 Chapter Elastic properties and hardness

14.1 Nanoindentation

14.1.1 Observation and Pile-up correction

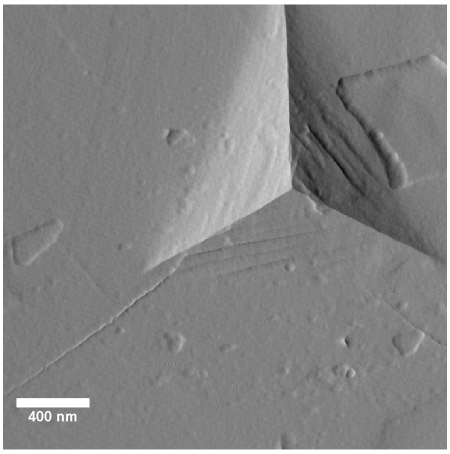

Figure 14.1: AFM error image of a 250 nm deep indent produced by a Berkovich tip on a particle from sample *C0SoC_1*.

An AFM image of a 250 nm indent made by a Berkovich tip in a particle from sample *C0SoC_1* can be seen in fig. 14.1. A small pile-up can be noticed on the top right hand edge. There is no pile up on the other edges. Cracks can be seen but they are not growing from the corners, where the stress is expected to be the highest. Two AFM images of 250 nm deep cube corner indents made by cube-corner tips can be seen in fig. 14.2, associated with the EBSD data of the same particle. Pile-up is significantly bigger for the same depth and is present on all the edges. Additionally, they present geometrical features: a rectangle is present on the bottom image on the bottom-right hand edge which is 55 nm higher than the pile-ups on the opposite edges. The top image represents however a triangular shape on the left hand edge which is as high as the other pile-ups. These features are due to chipping, which are induced by some fracture mechanisms. Furthermore, they present also different cracking behaviors: on the top image, 2 radial cracks grow from the indent corners as expected, but there is no crack for the third corner. The bottom image also shows 2 cracks which do not directly originate from the corners, hence it cannot be testified that they are radial. These 2 different behaviors (pile-up+fracture) were in fact observed on two other indents from each grain, indicating that they depend on crystal orientation.

Two important conclusions can be made: Berkovich tips produce significantly less pile-up and the crystal orientation plays an important role in the plastic deformation and the cracking behavior. Concerning the latter, it seems also unlikely to measure the

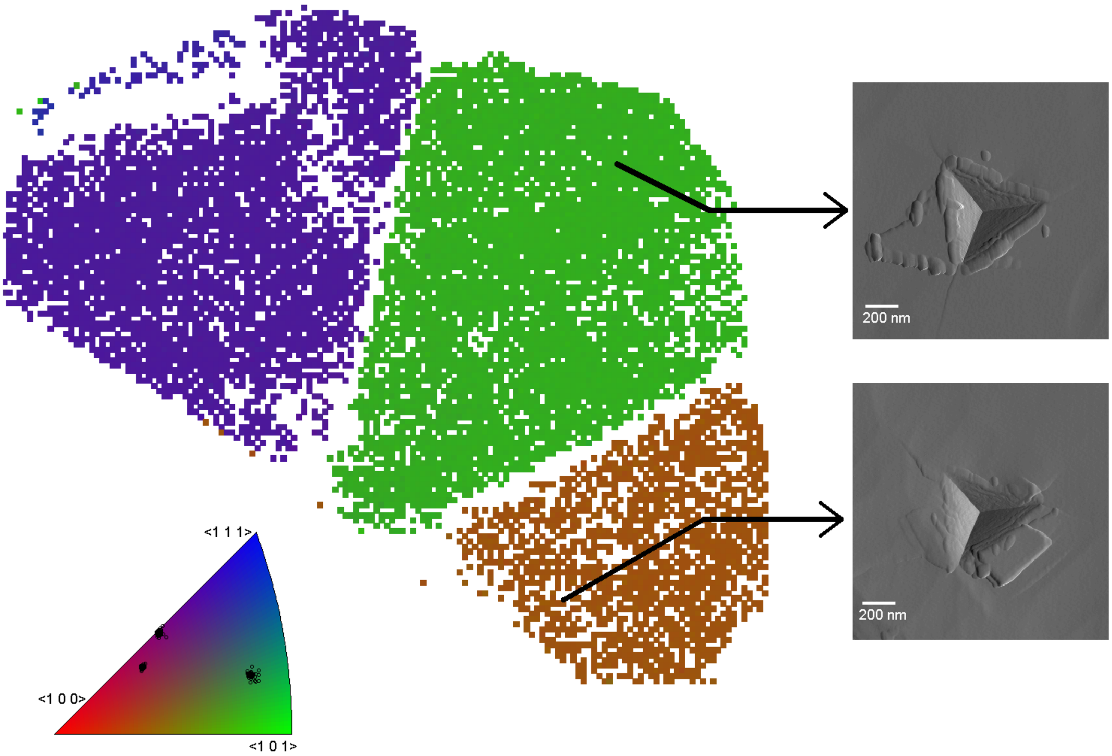

Figure 14.2: EBSD image of a particle from sample *C0SoC_1* associated with error AFM images of two indents corresponding to the middle and the top grain.

fracture toughness by crack length measurements, this will be discussed in section 15.1.

Samples *C0SoC_1* and *C0SoC50* were indented with a cube-corner tip following the protocol described in part IV. Cube corner was selected for the first samples as it was thought to yield better results due to its smaller depth-to-area ratio as explained in section 4.2. However this posed the problem of pile-up as explained previously. Besides, experimental data showed that the ratio of final depth over maximum depth (h_f/h_{max}) is above 0.7, hence pile-up was expected (Bolshakov and Pharr 1997). Pile-up induces an over-estimate of the elastic modulus and the hardness. In order to balance it, small 75-nm deep indents were made in the particles to quantify the error. The hypothesis is that the pile-up is in relation as big for 75 nm indentation depth as it is for the range of measurement (45–75 nm). At this depth, the three pile-ups seem semi-elliptical and less crystal-orientation dependent as for higher depths (see fig. 14.3a). The solution of Kese and Li (2005) seemed adapted to our case while still relatively simple. AFM topography measurements were carried out on each edge of two 75-nm deep indents for samples *C0SoC_1* and *C0SoC50*. Kese's solution simplifies the contact between the pile-up and the tip to 3 semi-ellipses. The distances a_i $(i = 1, 2, 3)$ between each edge center and the top of each pile-up can be obtained by AFM (see fig. 14.3b) and converted to a total

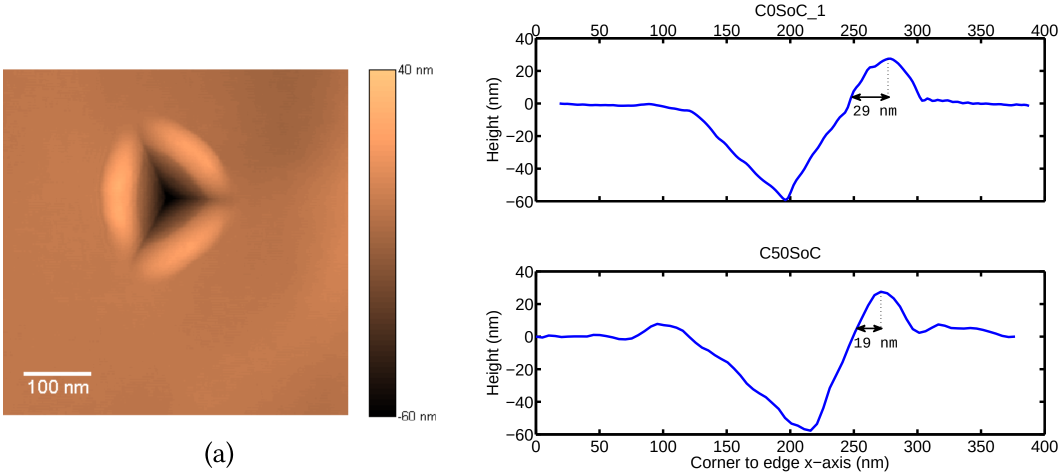

(a)

(b)

Figure 14.3: (a) AFM topology of one 75-nm deep indent located in *C0SoC*. Pile-ups are at this depth similar on the three sides and have a semi-elliptic shape. (b) Topography of two pile-ups of 75-nm deep indents in (top) sample *C0SoC_1* and (bottom) sample *C50SoC*.

pile-up area A_{PU}:

$$A_{PU} = \frac{\pi b}{4}(a_1 + a_2 + a_3), \tag{14.1}$$

where b is the edge length expected by the Oliver and Pharr method (see section 2.1 and Kese and Li (2005)).

The real area of contact was found to be 27 % and 21 % bigger than the one calculated by the Oliver and Pharr method for samples *C0SoC_1* and *C50SoC*, respectively. This induces the same overestimation of the hardness and an overestimation of 13 % and 10 % of the E-modulus for samples *C0SoC_1* and *C50SoC*, respectively. Note that these estimates are not particularly accurate because the semi-ellipse model does not take into account elastic recovery of the pile-up nor can it be assured that all the selected indents produced similar pile-ups. It gives nonetheless a good order of magnitude of the error induced by pile-up.

14.1.2 Indentation results

Several hundred indents per commercial sample were applied until at least 50 selected indents were obtained. Less indents were introduced on the reference samples. The results are reported in table 14.1. Selective nanoindentation was applied as explained in part IV. The success rate was between 2 % and 12 % for the commercial samples and up to 60 % for the wafer. The procedure, described in chapter 10, including step 4.b (visual inspection) was applied to all the samples except for sample *C0SoC_1*, where step 4.a

Sample name	E-mod (GPa)	Hardness (GPa)	selected/total indents
Cube Corner (after pile-up correction)			
C0SoC_1 * †	93 ± 5	8.9 ± 0.4	75/820
C50SoC ‡	98.0 ± 7	8.5 ± 0.7	68/536
Si02 †	69.7 ± 1	7.3 ± 0.2	242/596
Berkovich			
C0SoC_2	86.7 ± 11	7.0 ± 0.8	66/3743
C0SoC_100	86.7 ± 8	6.8 ± 0.6	62/1068
C25SoC	89.7 ± 6	6.5 ± 0.4	54/968
C50DoD	97.5 ± 12	7.4 ± 0.9	71/1405
C75SoC	102.8 ± 7	7.6 ± 0.6	74/1694
C100SoC	104.2 ± 10	8.0 ± 0.8	85/2235
MnO2p	176.3 ± 26	13.5 ± 3.7	3/84
LiMn2O4p	128.9 ± 14	10.7 ± 0.8	36/400
Wafer	95.7 ± 4	6.7 ± 0.4	76/121

* pile-up correction: 27 %.

† Note: step 4.a from chapter 10 was applied to these samples.

‡ pile-up correction: 21 %.

Table 14.1: Elastic modulus and hardness (± standard deviation) measured by selective nanoindentation.

was used instead (statistical deconvolution). For the former case, the measurements correspond to a mean of all the selected indents. A CDF could also be of interest as they can show the heterogeneity among the particles but would only add in complexity.

The pristine powder *LiMn2O4p* is unexpectedly much stiffer and harder than its battery counterparts. This might originate from a much better level of purity (99.9 % according to the manufacturer) than for factory-made particles. For the latter, impurities could contribute to reducing its hardness. The wafer is also stiffer, but has a similar hardness as *C0SoC_aged* and *C0SoC*. Last, despite the small number of selected indents (3), the MnO_2 particles are almost twice stiffer and harder than the battery particles. The different reference samples cannot be directly compared with the battery materials due to the different synthesis conditions. However, they give a good hint on the order of magnitude, which lies around 100 GPa.

Concerning the battery samples, there is a clear trend of increasing elastic modulus upon delithiation (see fig. 14.5a). For decreasing lithium concentration, the ratio of Mn^{4+}/Mn^{3+} increases. $Mn^{4+}-O$ bonds are stronger than the $Mn^{3+}-O$ ones (Xu AND MENG 2010), inducing a stiffer material. This can be seen also by the fact that the bond length is shorter, giving rise to a lower lattice parameter as reported by XRD measurements. There is a difference between the elastic modulus measured in the previous work and the two samples from 0 % SoC batteries due to the statistical extraction of the values. In the former case, deconvolution of the data from the mixed measurements was done (step 4a). The different Gaussian function centers were later associated with the positions of the indents. For all the other samples, the indents were visually filtered beforehand: only indents falling on compact particles are used. On account of this, the latter measurements are more trustworthy despite the higher standard deviation. The use of different tips does not seem to be the cause, because it can be assessed by the similar results for samples *C50SoC* & *C50DoD* and *C0SoC_1* & *C0SoC_2*. It seems that charging versus discharging the cell has a negligible influence that the methods used here cannot quantify. Note how important the standard deviations are for each of them, in the order of 10 %, except for the wafer. Because of this, it is difficult to fit a function as some of the values overlap. These high standard deviations are certainly due to the particle/matrix structure. But it was also observed that different E-moduli were measured on different particles of the same commercial cells. Micro-Raman spectroscopy was used in order to understand this behavior (see section 14.2).

Concerning hardness measurements, it could be expected from brittle metal oxides that there is little plastic deformation and mainly fracture. While it is true for microhardness testing with Vickers tips, 100 nm indents are produced here with a force below 1.5mN. For such low loads, mainly plastic deformation occurs associated with geometrically necessary dislocations (NIX AND GAO 1998; GHOSH ET AL. 2010). The hardness seems to follow a similar trend as the elastic modulus except for 0 % SoC (see fig. 14.5b). There is also a clear drop for 25 % SoC before a sharp increase to 0 % SoC. The general trend could also be explained by stiffer and stronger bonds for a higher ratio of Mn^{4+} but it can not explain the deviation at lower States of Charge. In order to circumvent this coupling between hardness and elastic modulus, the resistance to plastic deformation, H^3/E^2, is plotted in fig. 14.5c. This ratio is proportional to the necessary load to initiate plastic deformation (TSUI ET AL. 1995) and helps to increase the signal from inelastic deformation. Three maxima can be seen for 0, 50 and 100 % SoC. The value for 75 % SoC is not far below and within the uncertainty of the three maxima. However the resistance is significantly lower for 25 % SoC. There are three phases reported for spinel cathodes: $\lambda{-}MnO_2$, $Li_{0.5}Mn_2O_4$, $LiMn_2O_4$ (JULIEN ET AL. 2014; DRIDI-ZRELLI 2012; BERG AND THOMAS 1999; JULIEN AND MASSOT 2003). These three phases might correspond to the three maxima of the resistance plot. It is usually thought that there is an alternance between 1 and 2 phases during charging or discharging (JULIEN ET AL. 2014), but XRD measurements indicate that only one phase is present. We could suspect to have one of these 3 phases in non-stoichiometry. When decreasing the amount of lithium ions from $LiMn_2O_4$, there is an increasing number of lithium vacancies. These point defects could act as steps allowing for plastic flow in the structure. But it is difficult to imagine that lithium ions alone could contribute to the plastic behavior of the system as they diffuse easily within the lattice, as demonstrated by their application in Li-ion batteries. If the same mechanisms as in $MgAl_2O_4$ spinel at low temperature (VEYSSIÉRE, P. ET AL. 1980) is imagined for lithium manganese oxide, {110}<110>is expected to be the easy glide system rather than the $\{111\}$ plane, where mixed $\{110\}$ planes of Li-Mn-O and Mn-O would glide on each other in the packed anion (or cation) <110>direction (see fig. 1.6). In the case of 25 %SoC, it could be imagined that lithium vacancies facilitate the glide because of disordering of the lattice and random positioning of Mn^{3+}. When the concentration of lithium is halved, like in the case of 50 % SoC, every other tetrahedral site is empty and the lattice reaches an ordered $Li_{0.5}Mn_2O_4$ phase with a higher hardness. This hypothesis could be checked if bigger single crystals could be grown or by in-situ mechanical testing in High Resolution Transmission Electron Microscopy.

Overall, almost no difference was observed between the two samples at 0 % SoC. This result could have been expected regarding the stable capacity rate of sample *C0SoC_100* plotted in fig. 14.4. There is almost no change of capacity for 100 cycles, the state of health was at 100 %. The increase of capacity can be explained by activation of some host particles: here initial fatigue has a positive effect as it makes the material more permeable to lithium ions.

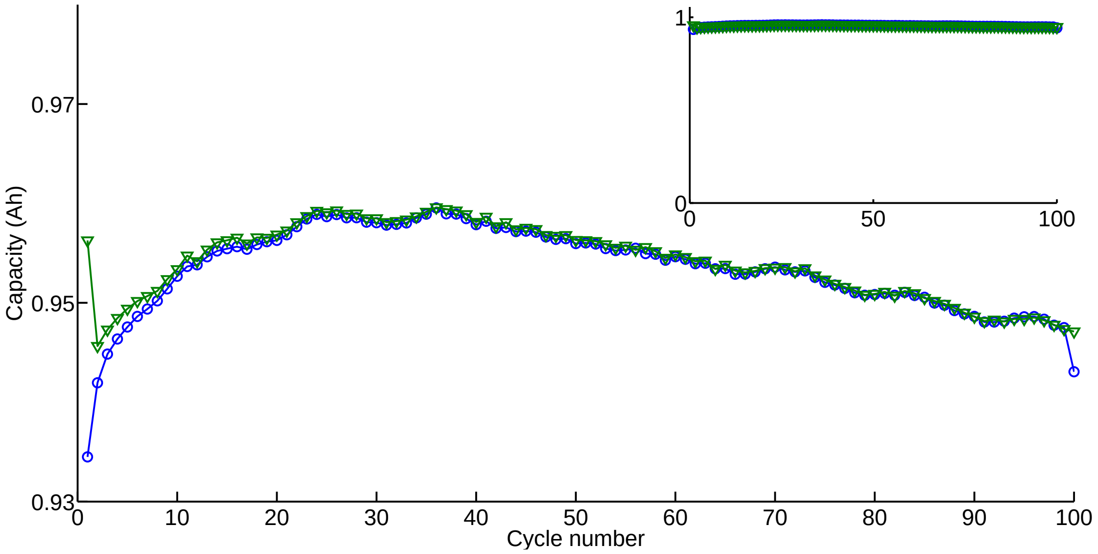

Figure 14.4: Capacity of sample *C0SoC_100* upon cycling. A slight capacity rise can be observed for the first 30 cycles due to the activation of the cell followed by a slow capacity decrease. In the inset, it can be seen that it is relatively stable during the whole process.

Indentation was also carried out on the intensively cycled samples. The success rate of the indentation test selection was much lower than for the other samples due to surface imperfections. This rendered no statistical study possible within an appropriate time frame, explaining the lack of comparative data for aged cells. It can however be concluded that the integrity of the grains is not kept for high C-Rate cycling.

The measured elastic moduli and hardness seem still quite below the ones reported by ZHU AND ZENG (2012) for all the samples: {203 GPa, 10 GPa} ({elastic modulus, hardness}) for as-deposited electrode, {140 GPa, 7 GPa} after 10 cycles and around {120 GPa, 7 GPa} after 100 cycles. As explained in section 1.3.2, they did not take into account pile-up in their calculation. The particles lying in a compliant matrix are certainly residual stress-free as compared to thin films. Upon cycling, internal stresses are released explaining why the value tends towards our measured values.

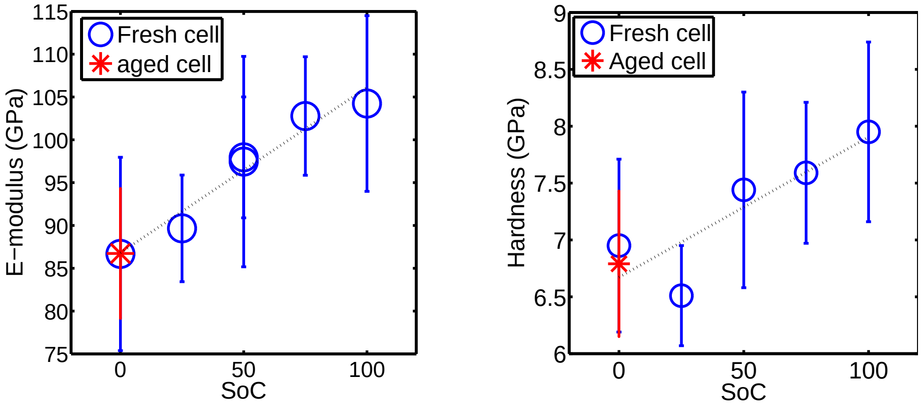

(a) *SoC vs elastic modulus* (b) *SoC vs hardness*

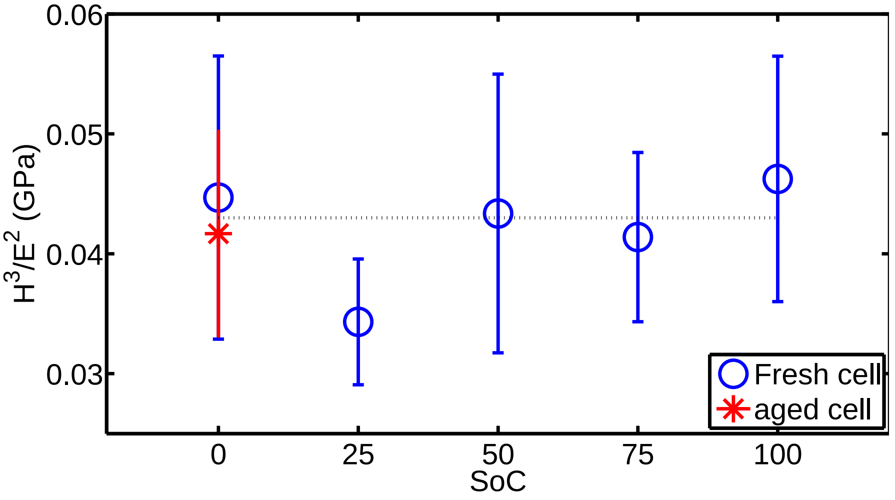

(c) SoC vs H^3/E^2

Figure 14.5: Elastic modulus (a) and hardness (b) measured by selective nanoindentation plotted versus different States of Charge for the samples extracted from the commercial cells. (c) plots the resistance to plastic deformation H^3/E^2 versus SoC. The dotted lines should only be used as a guide to the eye. Measurements with a cube corner tip do not appear on (b) and (c) as the tip shape has an influence on hardness measurement (Shim et al. 2008).

14.2 Local properties: a micro-Raman and contact-Resonance AFM study

14.2.1 Micro-Raman spectroscopy

Inspecting the nanoindentation and ESM data with scrutiny, it was observed that some particles were stiffer than nearby particles. Figures 14.6a and 14.6b show two cross-sections of samples *C0SoC* and *C100SoC* where such observations were made. The elastic moduli associated with each particle were obtained from two to four selected indents: As nanoindentation has a limited lateral resolution, it is difficult only with this analysis to draw definitive conclusions. These sets of particles were analyzed by micro-Raman spectroscopy and the results are shown in fig. 14.6c and compared to results from Dridi-zrelli (2012) and Julien and Massot (2003). Both samples present a peak at around 150 cm^{-1} of different intensities which is attributed to the lithium sublattice vibrations. As expected, *C0SoC* presents the biggest intensity at this shift as it has the highest amount of lithium. However, different intensities can be noticed for *C100SoC*, with the biggest peak for particle number 4 and almost non-existent peaks for particles number 1 and 3. In the case of *C100SoC*, a strong peak at around 592 cm^{-1} is found for all particles which corresponds to $\lambda{-}\mathrm{MnO}_2$. Another peak of different intensity can be seen at around 658 cm^{-1} which seems to correspond to different levels of lithiation. Again the biggest is found for particle number 4. Then come, in this order, particles number 2, 3 and 1. When compared to their elastic modulus, we find that the higher the amount of lithium in the particle, the lower is its stiffness. This local trend corresponds to the general trend depicted in fig. 14.5a. The Raman shifts obtained for *C100SoC* correspond to the ones measured by Dridi-zrelli (2012) for x≈0.3 in $Li_xMn_2O_4$, both after charging and discharging. On the other hand, the *C0SoC* Raman spectrogram seems to correspond to the one measured for x=0.73 in $Li_xMn_2O_4$ after one charge-discharge cycle. She reported peaks at 490 cm^{-1}, 565 cm^{-1}, 575 cm^{-1}, 596 cm^{-1}, 625 cm^{-1} and 652 cm^{-1} which well fit the spectra measured for the two particles in fig. 14.6c. This demonstrates that the crystal was not fully lithiated, as reported by XRD measurements. However, spectrograms for *C0SoC* seem almost identical despite a difference of 13 GPa, which indicates that it is not due to its composition but hypothetically to its structure.

14.2.2 Contact-resonance atomic force microscopy

CR-AFM was used to obtain information on the elastic isotropy of spinel $\mathrm{LiMn_2O_4}$, information on the elastic homogeneity within single grains, and in general to image elastic properties with a better resolution.

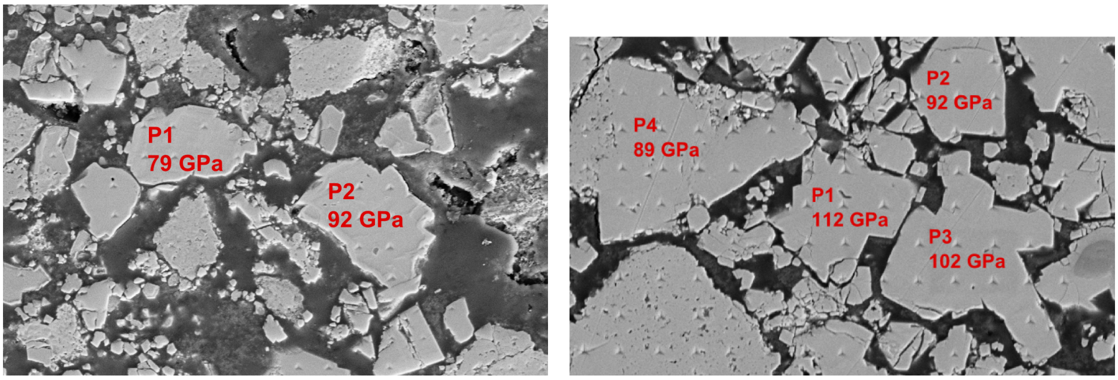

(a) *C0SoC* (b) *C100SoC*

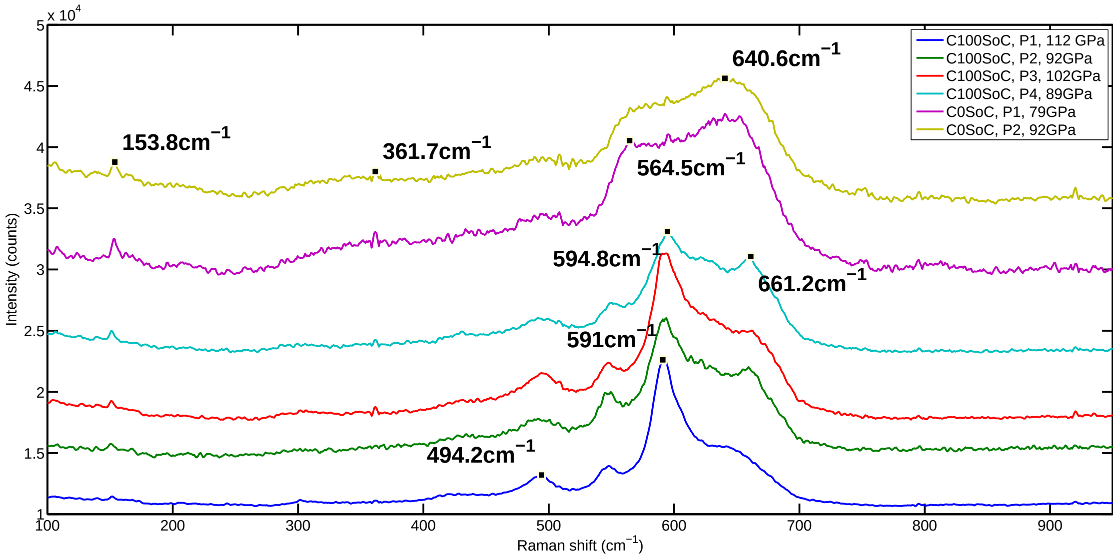

(c) Raman spectra

Figure 14.6: (a) shows a micrograph of 2 particles from sample *C0SoC* and (b) of 4 particles from sample *C100SoC*. The particles are numbered and associated with their measured elastic modulus. (c) shows the 6 obtained Raman Spectra.

14.2.2.1 Qualitative maps: reference sample

In order to check for elastic isotropy, *LiMn2O4p* was studied. Using a pristine powder helped discarding side effects from electro-chemical cycling and impurities. Additionally, a large and fairly flat polycrystalline particle could be imaged. Figure 14.7a shows the topography of the particle. Four holes can be noticed and can be used as landmarks. While the root mean square topography of the particle surface is below 1 nm, the edges fall off to the sides by at least 200 nm. The EBSD map (fig. 14.7b) reveals that the particle observed in the topography image (fig. 14.7a) is not a single crystal, rather a polycrystalline structure with different grain orientations. The four holes are all located at grain boundaries, as if each grain could not grow completely during the sintering process. Figure 14.7c shows the resonance frequencies of the cantilever while scanning in contact mode with a constant force. For each pixel, the excitation frequency of the output signal was varied continuously over a fixed time interval to a maximum cut-off frequency, whereby the contact resonance of the system was detected and displayed in a gray scale image. The four holes are marked with blue dots. The darker spot (marked by a blue arrow) not visible in the topography image is due to a hole located below the surface. It is visible by SEM when operated at high voltage (20kV, see fig. B.4 in appendix B). It is at a grain boundary, like the four other holes. Upon reversing the scan direction, the AFM tip can be damaged or the tip-sample contact area can be slightly changed as it reaches the edges of the particle. Such a variation of contact mechanics results in different resonance frequencies between two scans or, in other words, in lines of different colors in the image. The focus of the reader should therefore be brought to the frequency change within single lines. The frequency stays stable even as the tip runs from one grain to another. In particular as it goes from any of the two {111} oriented grains (in blue) to the {001} one (in red). When analyzing spinel (cubic) crystal symmetries, it turns out that anisotropy of the elastic properties is maximized between these two orientations. Our measurement here demonstrates that $LiMn_2O_4$ spinel has an anisotropy ratio close to 1. It should be however specified that the indentation modulus is less dependent on crystal orientation than the elastic modulus. The elasticity tensor components (C_{ij}) of $LiMn_2O_4$ and Mn_2O_4 were calculated by Qi et al. (2014). $LiMn_2O_4$ was computed as an orthorhombic structure at 0 Kelvin, hence the elastic properties are highly anisotropic. Considering only the elasticity tensor of spinel Mn_2O_4, an anisotropy factor of 1.6 was computed. Using this factor, the maximum indentation modulus difference calculated by Vlassak and Nix (1993) (flat punch) is $(M_{\{111\}} - M_{\{100\}})/E_p < 8\ \%$ while $(E_{\{111\}} - E_{\{100\}})/E_p = 42\ \%$, where E_p is the polycrystalline elastic modulus. A difference of 8 % could be detected by CR-AFM, but the real indentation modulus ratio might be even lower even though the anisotropy factor stays significant. Hence the isotropy of the material is shown only within the detection limits of CR-AFM.

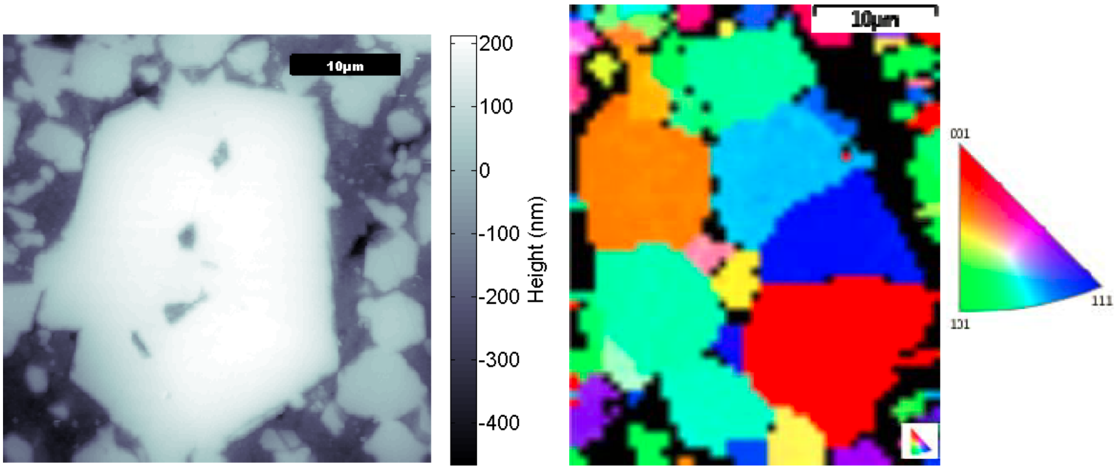

(a) Topography (b) EBSD

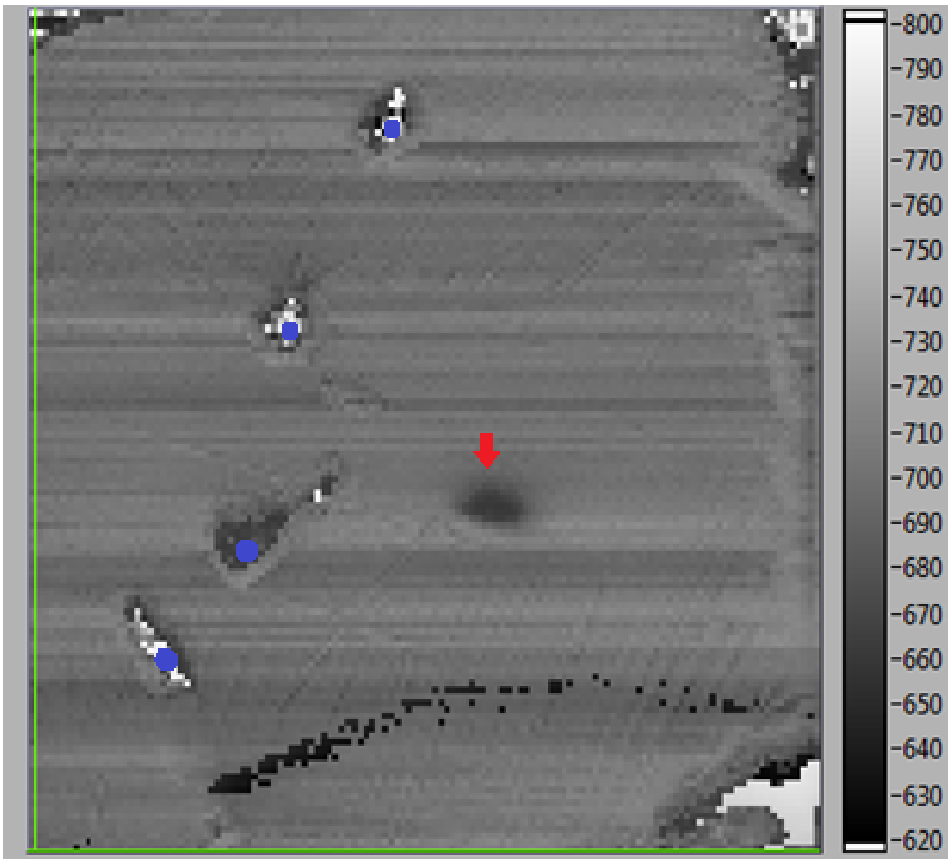

(c) Resonance frequency map (kHz)

Figure 14.7: (a) Topography of the particle of interest from sample *LiMn2O4p*. (b) EBSD map of the same particle in the Z-direction (out of plane). (c) Contact-resonance frequency image measured by means of CR-AFM. It can be noticed how each fast-scan line keeps the same contact-resonance frequency, even when the sensor tip scans grains having different crystalline orientations. Differences between the lines might be induced by wear of the sensor tip.

14.2.2.2 Qualitative maps: commercial samples

Unfortunately, the samples used in the previous study could not be applied to CR-AFM as the signal-to-noise ratio of the sound waves was much too low. New thinner samples had to be made with a partial embedding in a metallic alloy as explained in section 4.3.2.2.

Figure 14.8a is a topography image of a polished area from specimen *C25SoC*. The particles and the epoxy matrix can be clearly distinguished, because they present different heights after the polishing process (fig. 14.8a). The topography height variation is about 150 nm. Figure 14.8b shows an CR-AFM amplitude image under an excitation frequency of 570 kHz. The cantilever vibration amplitude is at the highest when the tip is in contact with the more compliant phase, here the epoxy matrix. Scanning again at a higher excitation frequency so that it is at or close to the higher contact resonance frequency (figs. 14.8c and 14.8d), the amplitude of the cantilever decreases on the more compliant phase and increases on the stiffer one. Hence, the stiffer phase, here the particles, appears brighter now. A contrast inversion is observed by varying the excitation frequency. When comparing the particles distributed in the matrix it can be observed that they do not present the same elastic properties. At an excitation frequency of 677 kHz, the vibration amplitude of the cantilever is particularly high for contacts on the top left hand particle, the middle particle and the bottom left hand particle (indicated by arrows in fig. 14.8c). After increasing the frequency by 20 kHz (now at 697 kHz, see fig. 14.8d) the cantilever vibration amplitude reduces for these particles while increasing for the one on the top right hand corner (indicated by an arrow in fig. 14.8d). Apart from topology convolution, each particle seems to have a homogeneous response to CR-AFM. Different particles can have different stiffnesses. As shown in fig. 14.8, there are particles of different lithiation levels inducing different stiffnesses. A similar behavior was observed in the samples *C0SoC* and *C100SoC*. Additional images can be found in appendix B.

14.2.2.3 Quantitative measurements

Figure 14.9 is an AFM topography image of the $LiMn_2O_4$ wafer. The typical triangular patterns can be readily recognized. Besides, they are almost perfectly flat, which is the reason why they were first studied quantitatively by CR-AFM. Figures 14.10a and 14.10b show CR-AFM amplitude images acquired at excitation frequencies of 355 kHz and 357 kHz. By increasing by just 2 kHz, the resonance peak was found and is the same across the whole image but the edges of the patterns. As the resonance frequency depends on the tip/surface contact, it indicates that the surface is very flat and that the sample has homogeneous elastic properties.

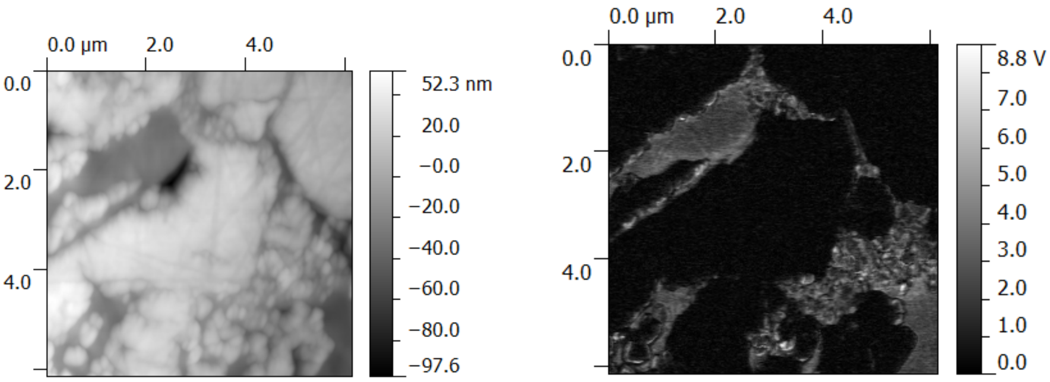

(a) Topography (b) 570 kHz

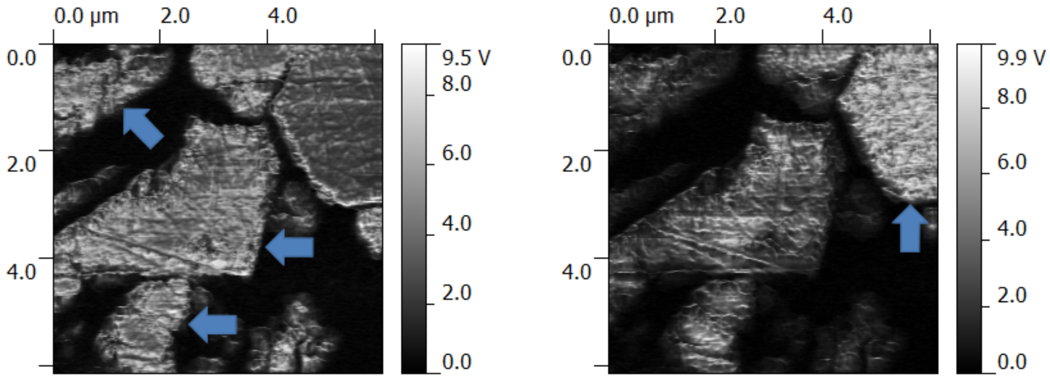

(c) 677 kHz (d) 697 kHz

Figure 14.8: AFM images of a set of particles from *C25SoC*. (a) Topography image. CR-AFM amplitude images acquired at different excitation frequencies: (b) 570 kHz, (c) 677 kHz and (d)697 kHz. Arrows in (c) and (d) indicate particles for which the biggest amplitudes were obtained. The first free flexural resonance frequency of the cantilever is f_0=151.9 kHz.

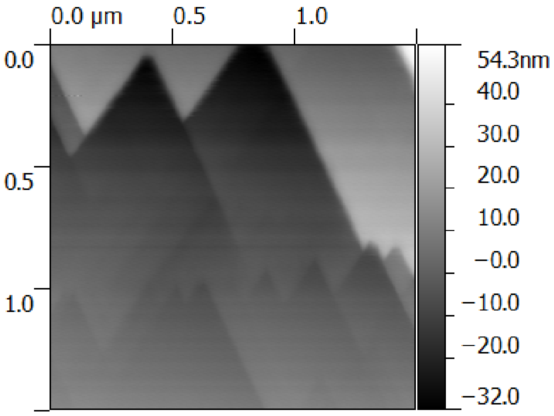

Figure 14.9: AFM topography image of the wafer reference sample.

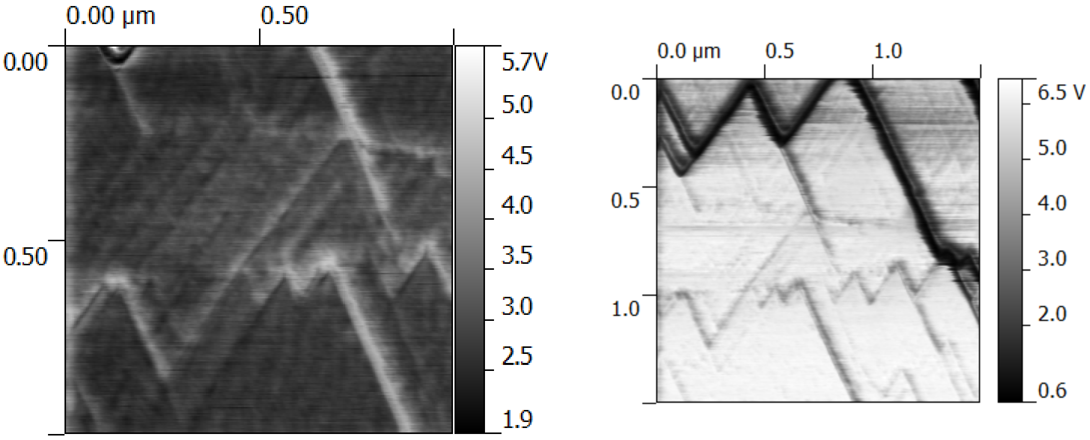

(a) 355 kHz

(b) 357 kHz

Figure 14.10: Contact resonance AFM images of the wafer reference sample at different excitation frequencies: (a) 355 kHz and (b) 357 kHz.

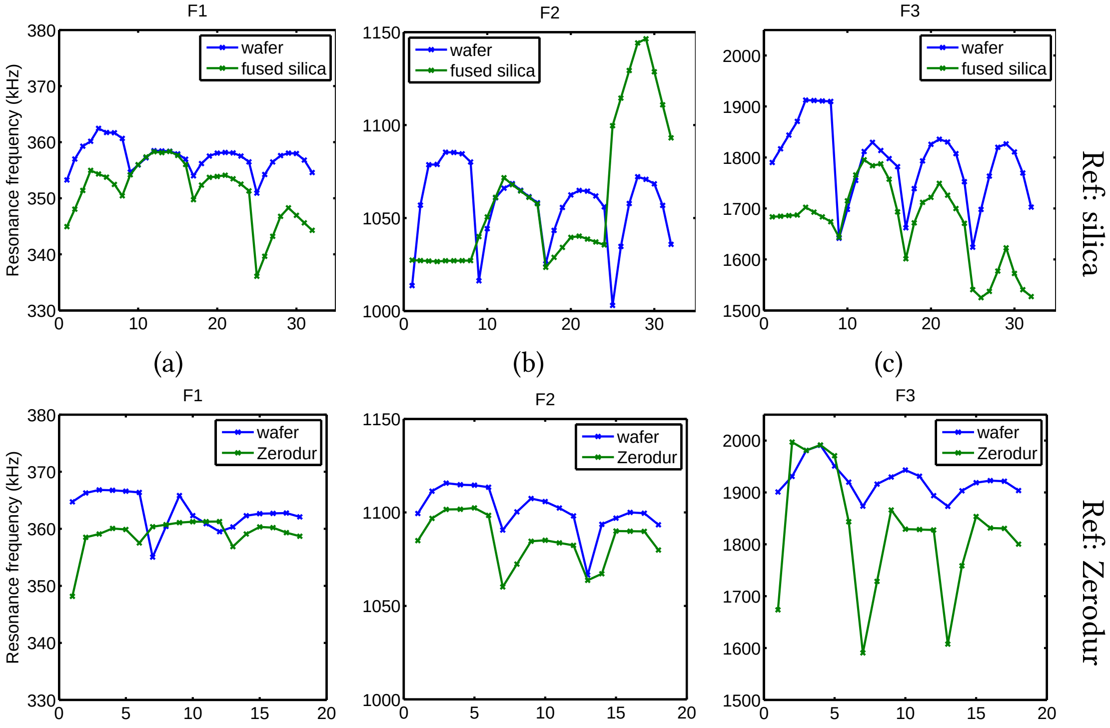

(a) (b) (c)

(d) (e) (f)

Figure 14.11: First (a,d), second (b,e) and third (c,f) contact resonance frequencies measured alternatively on the $LiMn_2O_4$ wafer and a reference sample with known mechanical properties: (a-c) fused silica and (d-f) ZERODUR©. The x-axes represent the measurement numbers. Refer to the text or section 4.3.2.2 for further explanation on these plots.

ZERODUR© has an elastic modulus of 91 GPa while fused silica has an elastic modulus of 72 GPa. Regarding previous measurements by nanoindentation, the $LiMn_2O_4$ wafer is expected to have elastic properties closer to ZERODUR©. Quantitative CR-AFM, as explained in section 4.3.2.2, is used and the results are reported on fig. 14.11. First, the three first contact resonance frequencies on the wafer were determined eight times for the following cantilever deflections: 10, 20, 30, 40, 50, 40, 30 and 20 nm, in this order. The eight measurements are reported by blue crosses on the plots for measurement numbers 1 to 8. Then the same measurements were repeated for the reference sample (silica or ZERODUR©), also reported for measurements numbers 1 to 8 but by green crosses. The procedure was repeated four times with the fused silica and three times with ZERODUR©. As it is not necessary to carefully image the reference samples to find appropriate areas, the wafer was always measured first for each loop as the tip would be less damaged between the two sets of measurements.

As seen in section 2.2.3, quantitative measurement on indentation modulus M requires at least 2 contact resonance frequencies in order to determine k without full knowledge of the cantilever geometry. The condition is however that the tip is not damaged between two successive sets of measurements between the reference sample and the sample of study. For each loop step, it is expected that the resonance frequency shift stays the same for the same deflection force. However results reported on fig. 14.11 show large scatter. For example, when one looks at the first contact resonance frequency measured on fused silica and the wafer (fig. 14.11a), the first step shows that the fused silica is softer, then it is almost identical, then softer again and the last step it seems much softer. Regarding the same data for the second and third resonance frequencies (figs. 14.11b and 14.11c), a similar trend is found for the first 3 steps, but the last one seems to diverge greatly in fig. 14.11b. Observing the comparative data with ZERODUR©, there is less scattering and most of the frequencies measured for both samples seem relatively similar.

If the theoretical equations from section 2.2.3 were applied to all these data, an elastic modulus varying from 70 to 100 GPa would be extracted. This shows much less precision than nanoindentation for a sample which is very flat. Several weeks of quantitative measurements on the commercial particles were unsuccessful as the obtained data were even less reliable.

15 Chapter Fracture

15.1 Toughness

Traditionally, fracture toughness is estimated after indentation by “simply” measuring the length of each crack growing from the 4 or 3 corners of the indent, with a Vicker’s tip or a cube-corner tip, respectively. This method is referred to in literature by either the “crack length method” or the “LEM model” after Lawn, Evans, and Marshall (1980) (see also ANSTIS ET AL. 1981; PHARR 1998; CUADRADOA ET AL. 2012). It consists of measuring the average length of the 3 (or 4) cracks, denoted c, as a simple relationship exist between K_{IC}, P and c:

$$K_{IC} = \xi_R \left(\frac{E}{H}\right)^{1/2} \frac{P}{c^{3/2}}, \tag{15.1}$$

where ξ_R is a constant depending on the tip geometry and set to 0.040 for cube corners (PHARR 1998). On fig. 14.2, it can be observed that it is impossible to use this particular method on the particles as the cracking mechanism does not follow the 3-fold rotational symmetry required to determine c.

However, the cracking pattern of the *wafer* sample pictured in fig. 15.1 seems to allow such measurement. Using eq. (15.1), a fracture toughness of 0.23 ± 0.07 MPa·m$^{1/2}$ was calculated. The value was determined by averaging the crack length of the 4 indents imaged in fig. 15.1. The crack patterns are all similar but yet the crack lengths are not consistent, this value can be used as a benchmark for the rest of this chapter.

The COD and the height difference versus the distance to the crack tips of 7 cracks from battery samples are plotted in fig. 15.2. It can be seen that not all measurements present the same quality: some are relatively linear for both plots while others are very irregular. This is due to the roughness of the particles, such as scratches from polishing, leading to imprecisions. Experimental measurements were fitted with linear functions forced to zero. The crack tips were previously positioned from the AFM error images. The slopes were inserted in eqs. (2.13) and (2.15) in order to find K$_{IC}$ and K$_{IIIC}$ using an elastic modulus of 90 GPa and a Poisson ratio of 0.3. The quality of the measurements was determined from the coefficient of determination R^2. The weighted means are applied to obtain a quantitative value, the weighs being the R^2 of each fit.

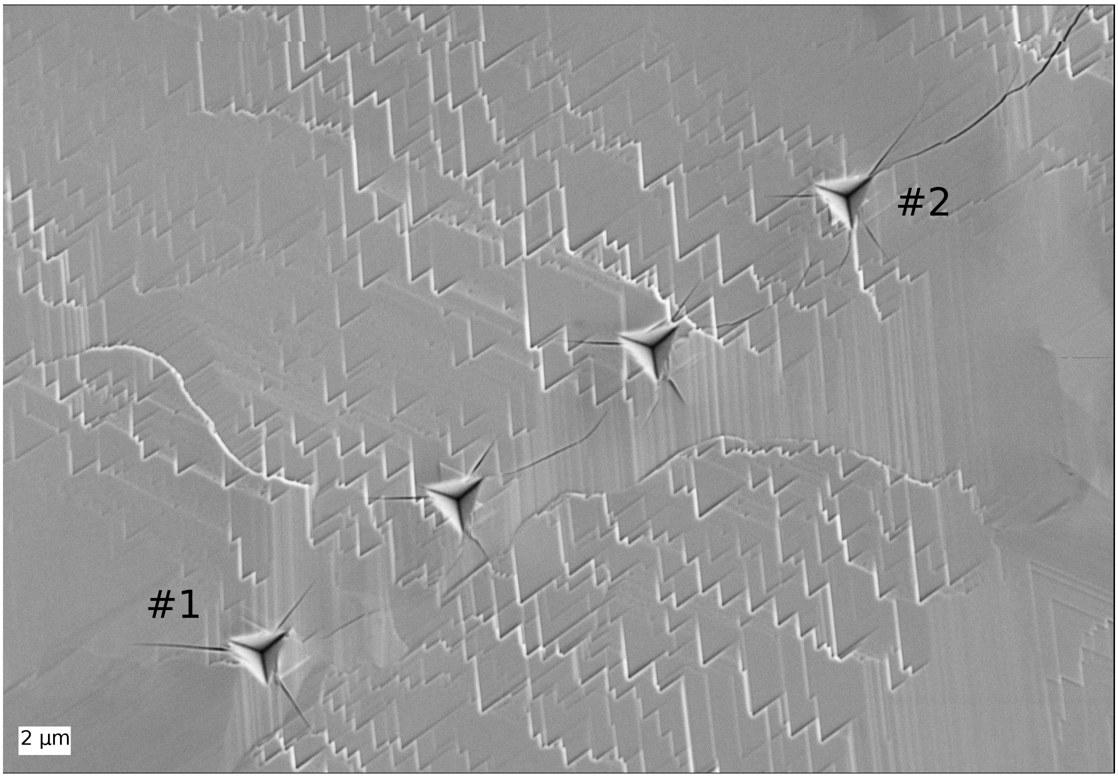

Figure 15.1: SEM micrograph of four 400-nm deep indents performed by depth control. Fracture induced by indents labeled #1 and #2 were investigated by FIB cross-sections.

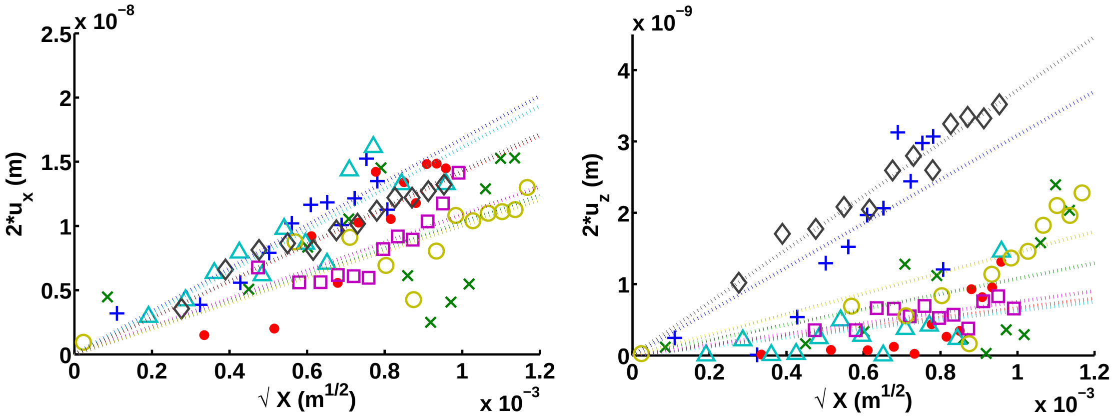

(a) (b)

Figure 15.2: (a) Crack Opening Displacement (2^*u_y) versus square root of distance to crack tip ($\sqrt{X}$) for 7 different cracks. (b) Mode III crack Displacement (2^*u_z) versus square root of distance to crack tip ($\sqrt{X}$) for the same cracks. Each plot is fitted with a linear function forced to zero (dotted lines). Colors of markers from the experimental measurements correspond to colors of fitting lines.

The overall results can be seen in table 15.1. For reference, the same method was used on cracks of the wafer (see fig. 15.1) and a crack-tip toughness of about 0.76 MPa·m$^{1/2}$ ($R^2 = 0.72$) was found, hence three times more than with the LEM method. This result seems debatable and the reliability of the method is discussed in section 17.3.

Sample	K_{IC}	R^2	K_{IIIC}	R^2
+	1.0 MPa·m$^{1/2}$	0.84	0.13 MPa·m$^{1/2}$	0.60
◇	0.89 MPa·m$^{1/2}$	0.95	0.16 MPa·m$^{1/2}$	0.96
○	0.62 MPa·m$^{1/2}$	0.69	0.063 MPa·m$^{1/2}$	0.62
□	0.67 MPa·m$^{1/2}$	0.66	0.033 MPa·m$^{1/2}$	0.30
△	0.99 MPa·m$^{1/2}$	0.77	0.027 MPa·m$^{1/2}$	0.34
●	0.88 MPa·m$^{1/2}$	0.70	0.029 MPa·m$^{1/2}$	0.35
×	0.64 MPa·m$^{1/2}$	0.13	0.047 MPa·m$^{1/2}$	0.28
Weighted means	0.85 MPa·m$^{1/2}$ ±17 %	N/A	0.091 MPa·m$^{1/2}$ ±60 %	N/A

Table 15.1: results summary from crack opening displacement measurements on $LiMn_2O_4$ particles.

15.2 Cleavage planes

As the fracture mechanisms depend on the crystal orientation, crack propagation in the wafer was studied with the support of focused-ion beam milling (courtesy of Roma

Tre University). Figure 15.1 is a SEM image of the home-made wafer after indentation. The 60° facet edges indicate the highly-oriented crystal as previously obtained (see Kitta et al. (2013)). It is not a single crystal as can be seen from EBSD measurements (fig. 15.3) but all the grains have their top surface parallel to the {111} plane and have only little misorientation. The edges of the triangular pattern are perpendicular to the <121> direction. All the indents formed cracks growing along the <121> direction (fig. 15.1), hence forming {101} planes if perpendicular to the top surface. It was observed that the cracks grow always perpendicularly to the edges of the triangular pattern regardless of the orientation of the indenting diamond tip. This phenomena is depicted in the schematics of fig. 15.4. FIB cross-sections were milled in order to see how the cracks develop below the surface (see fig. 15.5). They indicate that the cracks grew first perpendicular to the top surface, opening a {101} plane within a depth of 100 nm. Then they deviate at an angle of 30 to 40°. There are two possible explanations for this deviation. Another material could be present below the spinel material. X-Ray diffraction measurements showed that bixbyite Mn_2O_3 could be present and it is possible that there is a deficit of Oxygen ions between the cubic MnO substrate and the spinel $LiMn_2O_4$ top surface. Otherwise, only the spinel material could be present and the propagation deviates because surface formation is easier in this new plane. It is difficult to assess what is the plane in question only from the EBSD data. This question could be solved by analyzing a cross-section of the wafer by means of High Resolution Transmission Scanning Microscope.

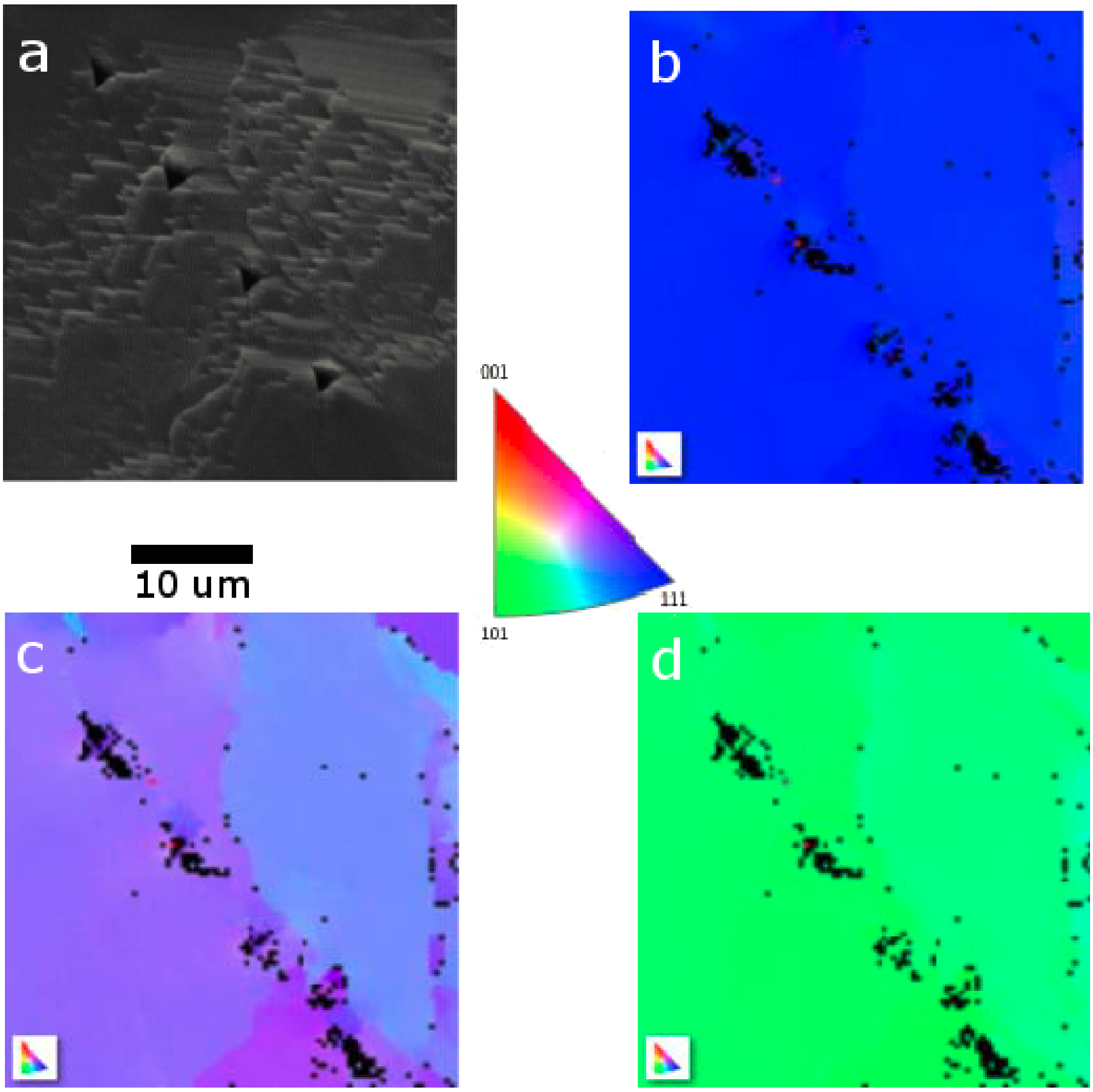

Figure 15.3: (a) Secondary electron image of the mapped area. (b) Z direction. (c) Y direction. (d) X direction. Color coding indicated in the center.

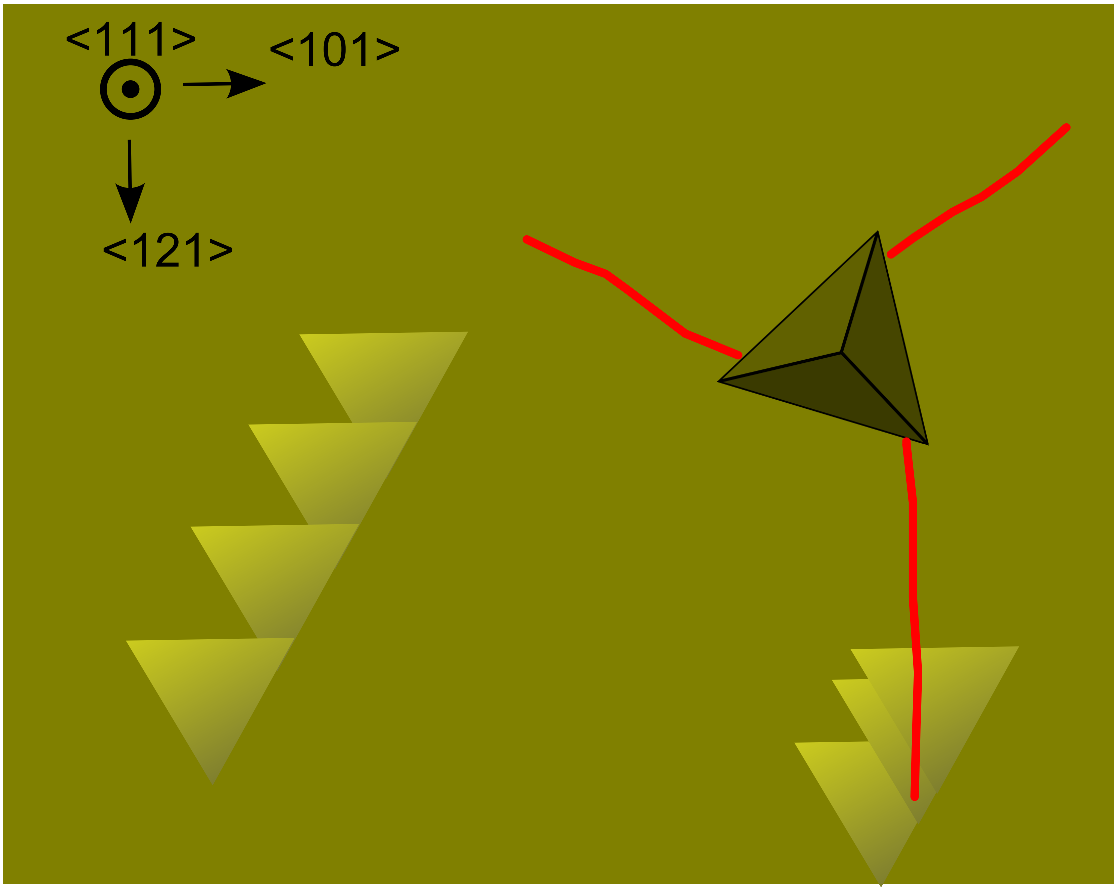

Figure 15.4: Schematics of the wafer. Yellow areas correspond to the wafer materials where the triangles represent the patterns observed on fig. 15.1, the darker triangle represents an indent print with a "random" rotation and the red lines represent typical cracks, growing perpendicular to the edge of the pattern triangles.

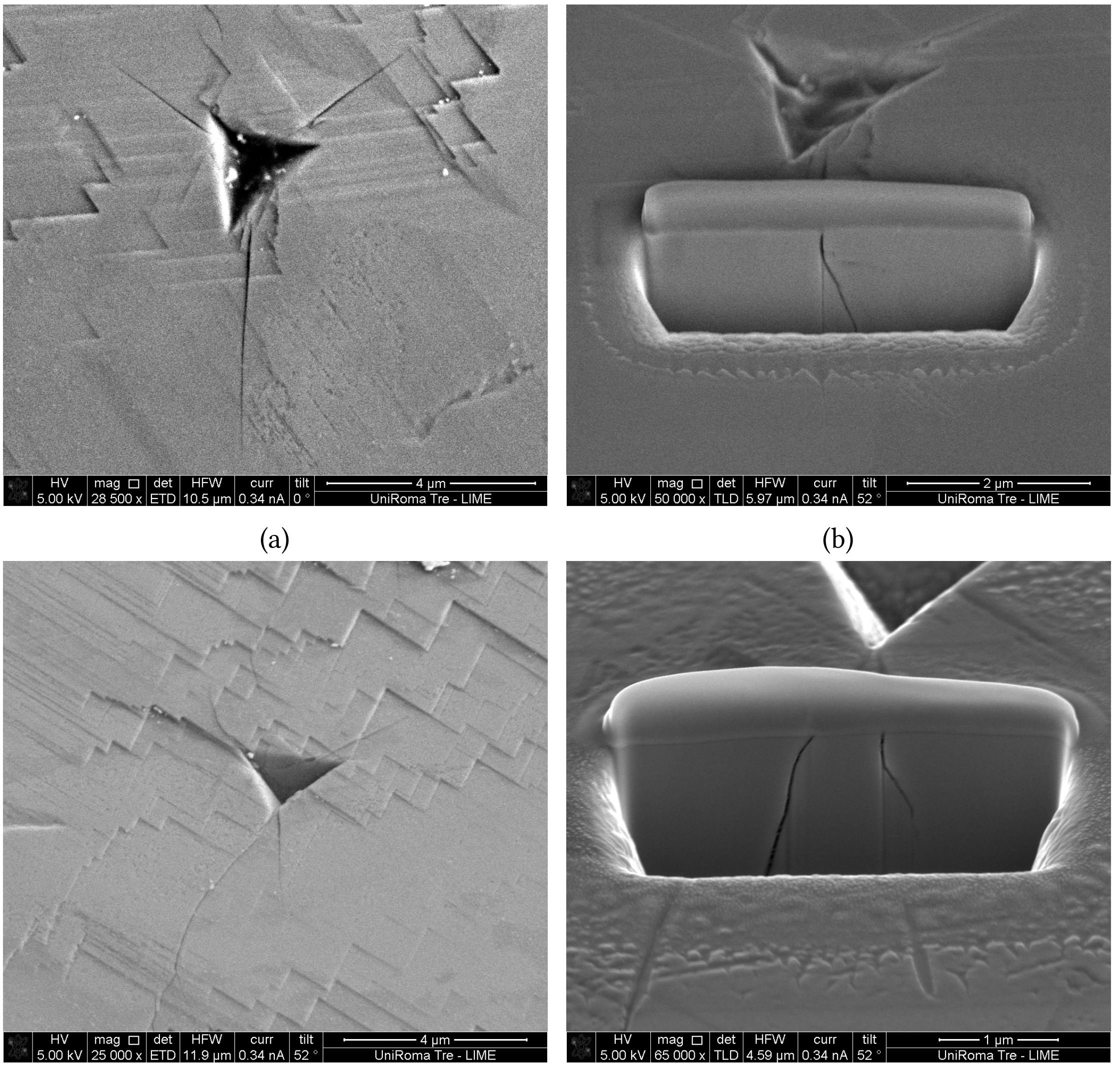

(a) (b)

(c) (d)

Figure 15.5: SEM images of two 400-nm deep indents before (a-c) and after (b-d) FIB milling. The first indent (a-b), labeled #1 in fig. 15.1, produced a reproducible crack pattern where 3 cracks forming perpendicular (or 30°) to the edges of the triangular pattern formed during crystal growth, regardless of the indenting tip rotation. The second indent (c-d), labeled #2 in fig. 15.1, produced two cracks at its corner, one similar to the previous one and another one which is much longer and certainly due to defects. Under the surface (b-d), the cracks grew perpendicular to the top surface for about 100nm before deviating by an angle of 30–40°. (courtesy of Roma Tre University).

16

Chapter

Electrochemical Strain Microscopy

16.1 Experiment

16.1.1 Voltage spectroscopy

Figure 16.1 shows hysteresis loops taken on the samples obtained from the fresh and aged batteries with 0 % SoC. Typical concentration-controlled loops are measured (Chen et al. 2014). Negative DC voltages applied to the tip attract mobile Li ions to the tip-sample contact point and increase the local Li concentration, thus increasing the ESM response. Positive DC voltages repulse Li ions and reduce local Li concentration, thereby decreasing the ESM response. Ideal ESM response is attributed to surface vibrations caused by lithium ions. However, the lock-in detection system of the microscope can measure other AC-mediated responses as explained in section 2.2.3. Taking into account that $LiMn_2O_4$ is a small polaron semiconductor (Iguchi et al. 2002), an additional contribution can emerge from AC mediated dipoles. Chen et al. (2014) suggested that voltage spectroscopy hysteresis loops can be used to distinguish between polar and non-polar contributions. Polar contribution would give rise to butterfly-like amplitude loops while concentration-dependent contributions would result in simple hysteresis loops. The loops in fig. 16.1 refer to the most common measurement on our samples but butterfly-like loops were also obtained (see Appendix of Amanieu et al. 2015c). It can be noticed that the fresh sample produces a more symmetrical loop than the aged sample, for which the loop is also more opened.

ESM loops are a too complex type of measurement to extract qualitative data with a clear physical meaning. Each data point depends on the length of the pulse, the history of the measurement (the accumulation of all the previous pulses in the spectroscopy) and the time lap between the release of the DC pulse and the data point (longer time laps give narrower loops). Nevertheless, voltage spectroscopy has the advantage of giving a qualitative overview within seconds of voltage dependencies in the ESM signal and the reversibility of the measurement. Time spectroscopy is a more appropriate measurement to quantitatively study diffusion processes.

It is important to note that voltage spectroscopy was also carried out on pure epoxy and the aluminum current collector and they exhibited no loops.

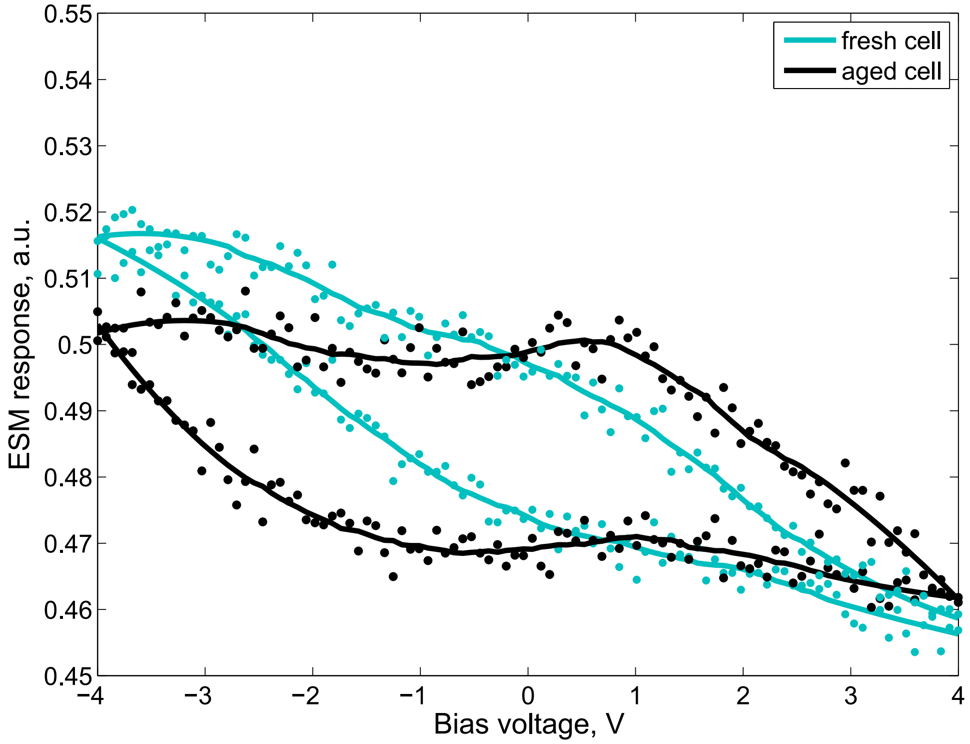

Figure 16.1: Experimental amplitude hysteresis loops measured on aged $LiMn_2O_4$ particles (black curves) and fresh $LiMn_2O_4$ particles (turquoise curves). The dots represent the average of 3 loops, the solid lines are smoothed versions.

16.1.2 Time spectroscopy

Figure 16.2 shows typical relaxation of the ESM response after DC pulses of different magnitudes on the same location. A higher DC voltage pulse results in a larger change of local Li concentration below the tip and, hence, in higher initial ESM response. Relaxation time of about 1 s is in agreement with the diffusion relaxation time estimated in the Introduction. It is much slower than the space charge relaxation time. Figure 16.3 shows two of the same measurements after normalization (gray and black lines). They were normalized by first subtracting the average signal before the DC pulse (background) and then by dividing by the first value when DC is off (extremum). They show the same relaxation time. Besides, the same measurements were carried out on the other fresh samples opened at 50 % and 100 % SoC. They also show the same speed of relaxation even though different diffusion coefficients are expected for different lithium concentrations as experimentally measured by macroscopic titration techniques (Deiss 2002; Tang et al. 2005) and as described in fig. 11.1. Experimental measurements show a non-linear change within a range of one order of magnitude (Deiss 2002; Tang et al. 2005), hence it is possible that these three samples with different SoCs exhibit similar diffusion coefficients. Additionally, the time spectroscopy signal has more complex underlying mechanisms than titration techniques due to the significant concentration change below the tip, where the whole range of diffusion parameters could act in parallel. Per contra, time spectroscopy done on the aged sample produces a much slower relaxation compared to the initial state. Being fitted with an appropriate physical model, the relaxation of the normalized ESM response can be thus used to estimate the local Li diffusion coefficient.

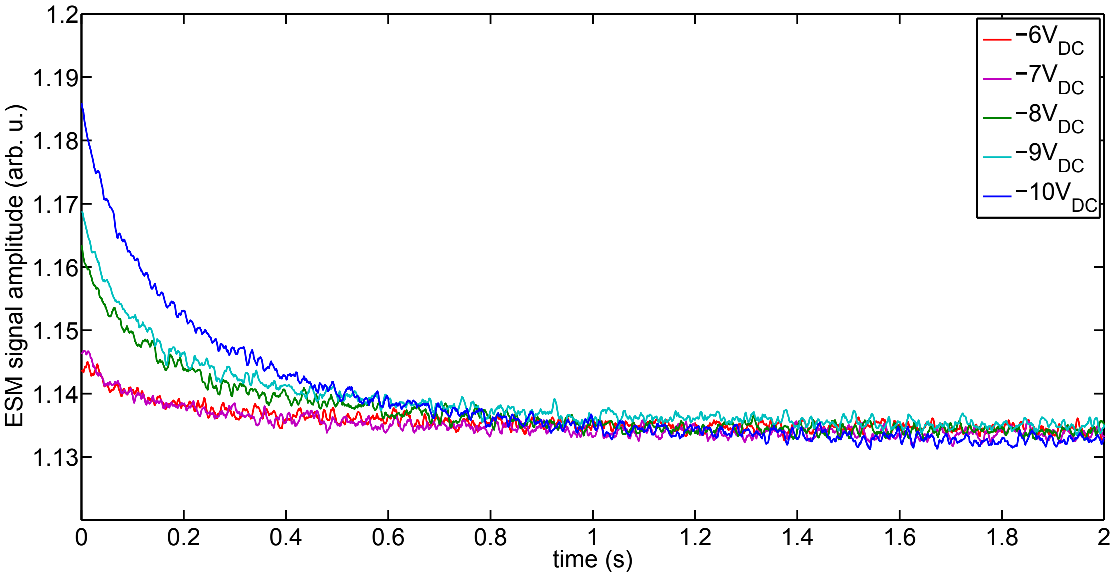

Figure 16.2: Relaxation curves after application of rectangular 10 ms DC pulses of -6, -7, -8, -9 and -10 V to the tip. Each curve represents an average of 5 reproducible consecutive measurements.

Note that similar measurements with longer, 100 ms, 10V DC pulses induced irreversible processes (unreproducible measurements). Irreversible processes such as Li extraction and its reaction with absorbed water and atmosphere gases could emerge and contribute to the response as well when the applied DC pulse is higher or longer than a certain threshold value (in voltage or time). These contributions are difficult to assess numerically because they depend on the sample properties and experimental conditions (humidity, temperature, gases, etc.). Nevertheless, they lead to irreversible changes of the topography and thus can be detected. Similar measurements were also done on epoxy and with the AFM tip lifted. Relaxation response was not detected for any applied DC voltages (up to 10 V).

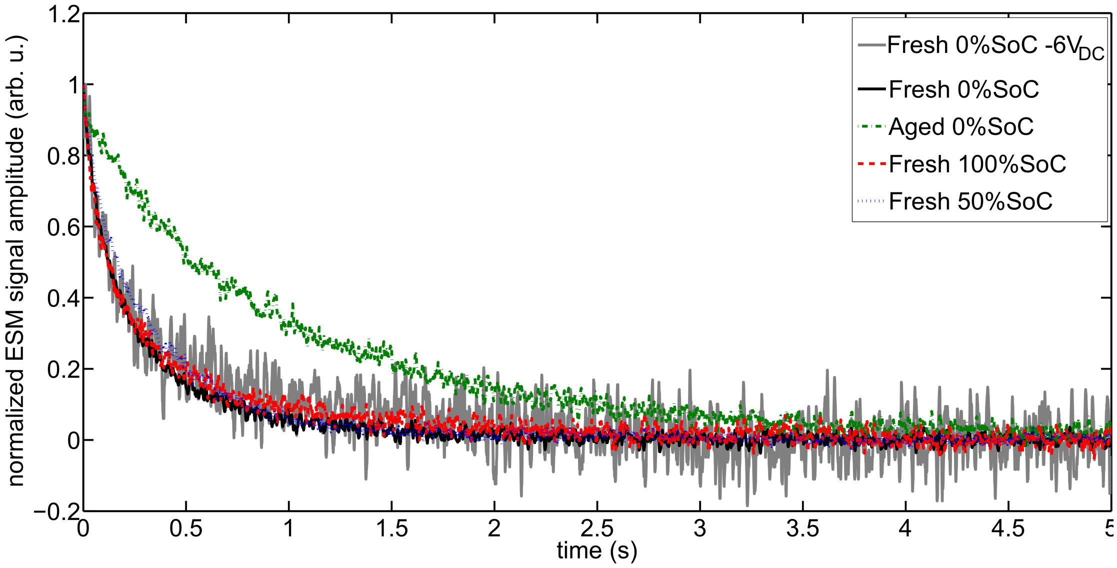

Figure 16.3: Normalized relaxation curves after application of rectangular 10 ms DC pulses of -10 V (unless otherwise stated) to the tip on three fresh samples of different states of charge (SoC) and one aged sample of 0 %SoC.

16.2 Model

16.2.1 Voltage spectroscopy

Two loops per model were calculated by producing a data point with the first value of $\mathfrak{F}_{AC}$ after each voltage drop with the default parameters from table 12.1. They can be seen in fig. 16.4. It can be noticed how the simple model (fig. 16.4a) yields a relatively symmetrical hysteresis loop while the other one (extended model) is flattened towards the negative potentials (fig. 16.4b). As $\mathfrak{F}_{AC}$ is directly connected to the local concentration of ions just below the tip, there is a direct relation to the dependence depicted in fig. 11.1 , in which $LiMn_2O_4$ would avoid local concentration associated with $D_{\text{eff}} << 1$, i.e. for concentrations between 0.7 and 0.98. This phenomenon is illustrated in fig. 16.5. When the positive pulses are applied (right hand side of the plot), the local concentration would jump from $c_{ini} = 0.5$ to the low concentration phase below 0.3 as the diffusivity tends to 0 between these two values. However, the system would not leave the 0.5−0.7 concentration range for the negative pulses (left hand side) easily, explaining why the loops do not extend to higher $\mathfrak{F}_{AC}$ values. In the simple case (see fig. 16.6), it can be seen how the concentration regularly increases when approaching the surface while there is an abrupt and thin boundary between the two phases $Li_{0.5}Mn_2O_4$ and $LiMn_2O_4$ with the extended model. It can also be seen how the system would slowly delithiate in the simple case while it would immediately come back to 0.5 with the extended model, trying to minimize the presence of this phase boundary. These different processes induced by phase transitions could explain the apparent asymmetry in the experimental loops of fig. 16.1.

16.2.2 Time spectroscopy

Figure 16.7 shows the evolution of $\mathfrak{F}_{AC}$ using the extended model for an initial concentration of 0.7. This value was picked as it is an extreme case just at the boundary between the two phases. When applying a positive voltage pulse, the concentration below the tip first reduces and then slowly returns to its initial state (red dot). For a negative voltage pulse, the concentration below the tip increases and a small volume experiences an irreversible phase transition to $LiMn_2O_4$ and does not return to the initial concentration, hence the measured $\mathfrak{F}_{AC}$ converges to a higher value than the initial one (red dot). This effect can be reversed by applying a pulse of opposite sign as was shown experimentally by Luchkin et al. (2015) (see fig. 16.8). Animations of the particle deformation using the extended model can be found in Appendix D of the article corresponding to this work (Amanieu et al. 2015c).

A parametric study was done only using the simple simulation model ($g = 0$ or $D_{\text{eff}} = 1$) in order to obtain simplistic time dependent responses that can be equated.

Normalized time spectroscopy ESM signal and normalized $\hat{\mathfrak{F}}_{AC}$ for different applied voltages are plotted in fig. 16.9. Both the experimental measurements and the simulation outputs are independent of the applied voltage once normalized. $\hat{\mathfrak{F}}_{AC}$ was calculated by setting the maximum value of $\mathfrak{F}_{AC}$ to 1 and the value before applying the DC pulse to 0. If not normalized, a higher applied voltage would induce a higher $\mathfrak{F}_{AC}$ as for the experimental results plotted in fig. 16.2.

Normalized time spectroscopy responses for different D_0 can be seen on fig. 16.10a. They reproduce a typical relaxation process similar to that in real measurements (black dotted line) where the speed at which it returns to equilibrium depends on D_0.

If divided by their own time derivative (see fig. 16.10b), they present a linear response. This behavior starts deviating for low D_0 and low t. Such behavior can be described by power laws of the form:

$$\begin{cases} \dfrac{\hat{\mathfrak{F}}_{AC}(t)}{\mathrm{d}\hat{\mathfrak{F}}_{AC}(t)/\mathrm{d}t} = (pt + p') \\ \hat{\mathfrak{F}}_{AC}(0) = 1 \end{cases}$$

$$\Leftrightarrow \hat{\mathfrak{F}}_{AC}(t) = (at + 1)^{1/p}, \tag{16.1}$$

where p is the negative first-order coefficient of the linear function and $a = p/p'$ is positive. The curve described by a power law is made of two parts. The initial decay is controlled by a/p, which describes at which speed the signal drops from 1. The second part of the curve is controlled by p and describes how low is the shoulder.

A parametric study was done where one parameter would be varied while the other ones would be equal to the default values (see table 12.1). The results are plotted in

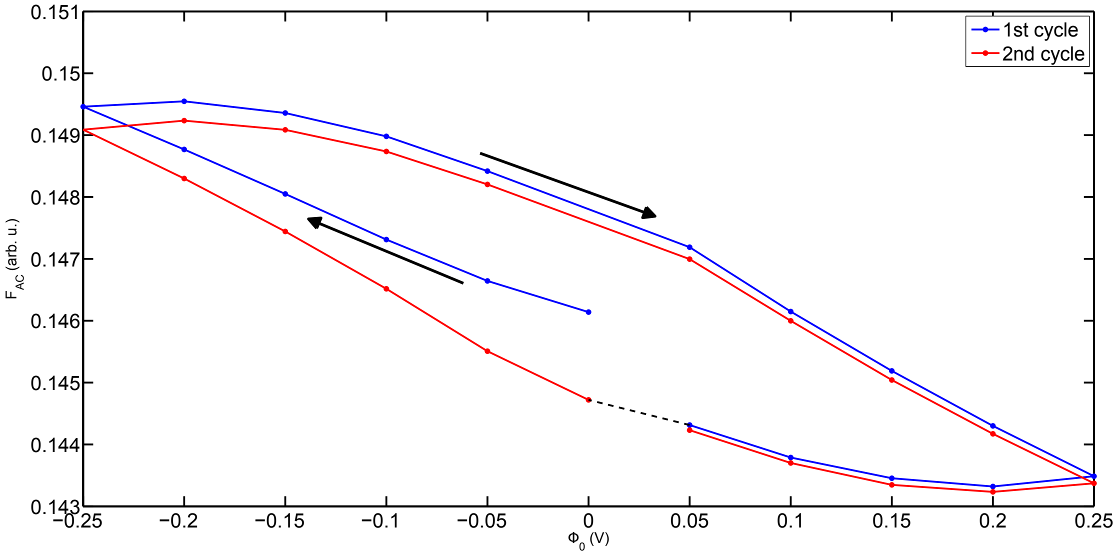

(a)

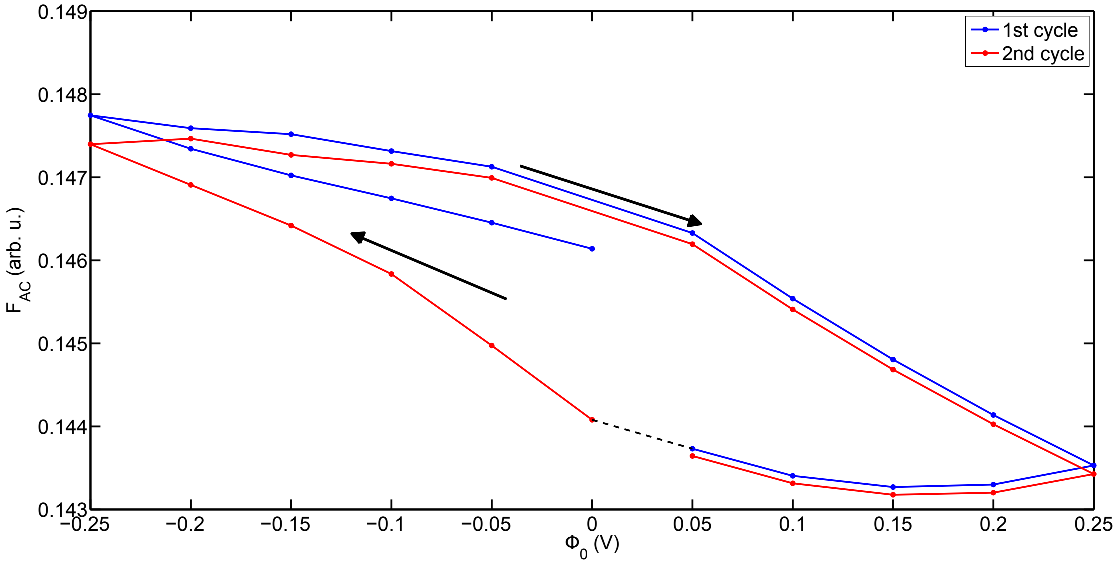

(b)

Figure 16.4: Simulated ESM hysteresis loops for the two models: (a) Simple model ($D_{\text{eff}} = 1$), (b) extended model (D_{eff} from fig. 11.1). Data points are constructed by associating each voltage pulse with the first $\mathfrak{F}_{AC}$ value obtained when DC returns to 0.

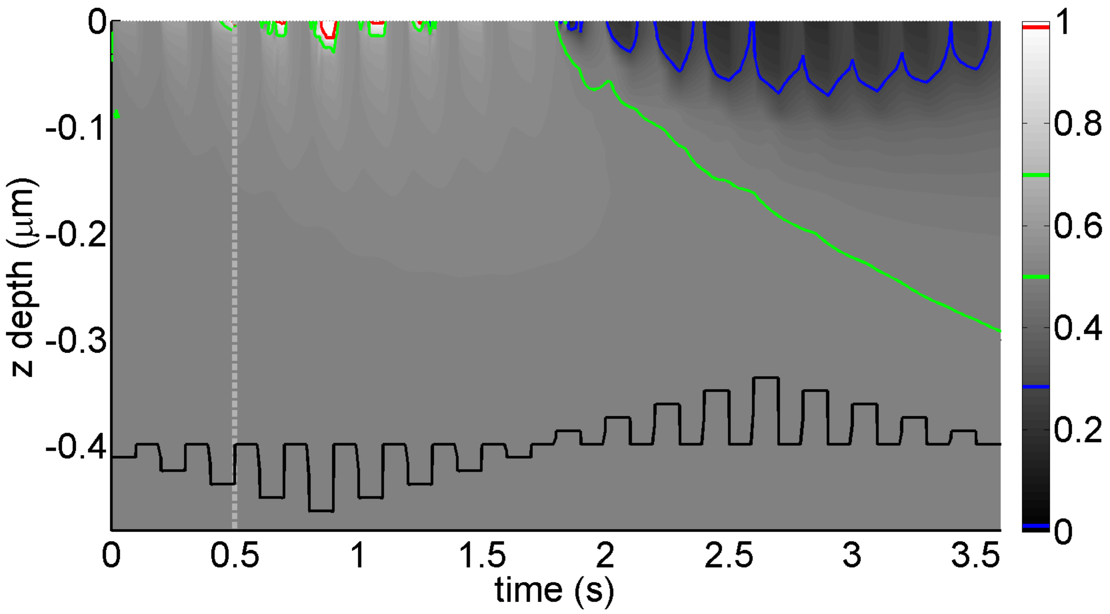

Figure 16.5: Evolution of the concentration of lithium ions below the tip down to a depth of 0.5μm during the first loop taking into account D_{eff}. The brightness is correlated with the concentration of lithium c_{Li} as indicated by the color bar. Colored contours represent each phase of spinel $\text{Li}_x\text{Mn}_2\text{O}_4$, with blue for poorly lithiated spinel, green for the middle phase and red for lithiated spinel as marked in fig. 11.1. These boundaries are located where $D_{\text{eff}}(c_{\text{Li}}) \sim 1$. The black line represents the applied voltage versus time. The same plot for the simple model can be found in fig. B.7, appendix B. The gray dashed line indicates the position of data plotted in fig. 16.6.

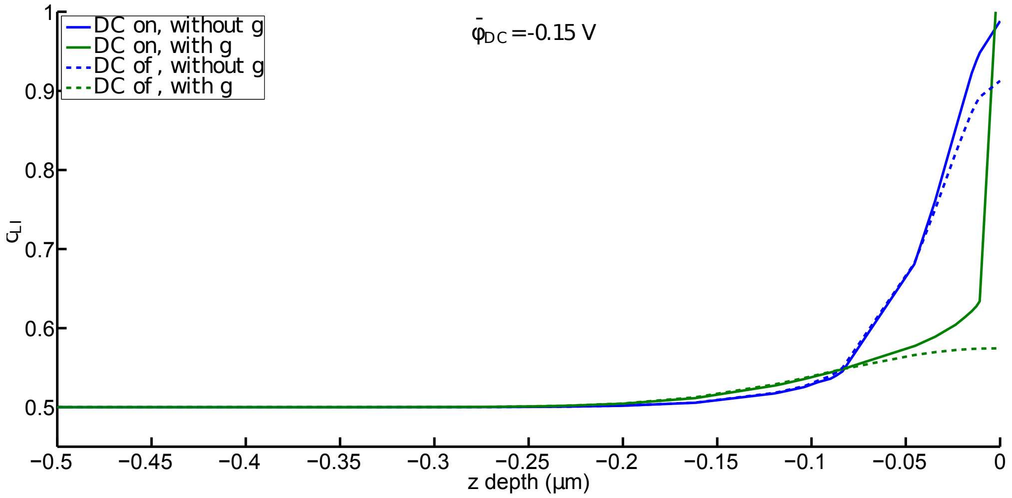

Figure 16.6: Same information as in fig. 16.5 with (green curves) and without (blue curves) using the extended model for $V_{DC} = -0.15$ V just before switching the DC voltage off (solid curves) and after switching it off (dashed curves).

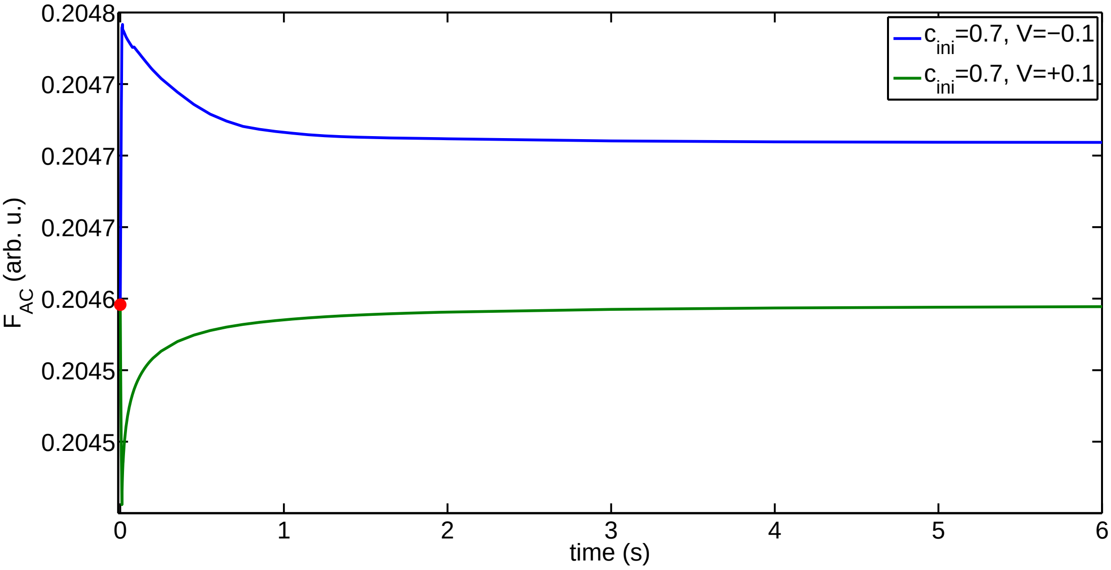

Figure 16.7: Time Spectroscopy modeled on a particle with an initial concentration of 0.7. A positive bias produces a reversible signal (green curve) while a negative bias produces an irreversible signal (blue curve). The initial signal for $t = 0$ s is represented by a red dot.

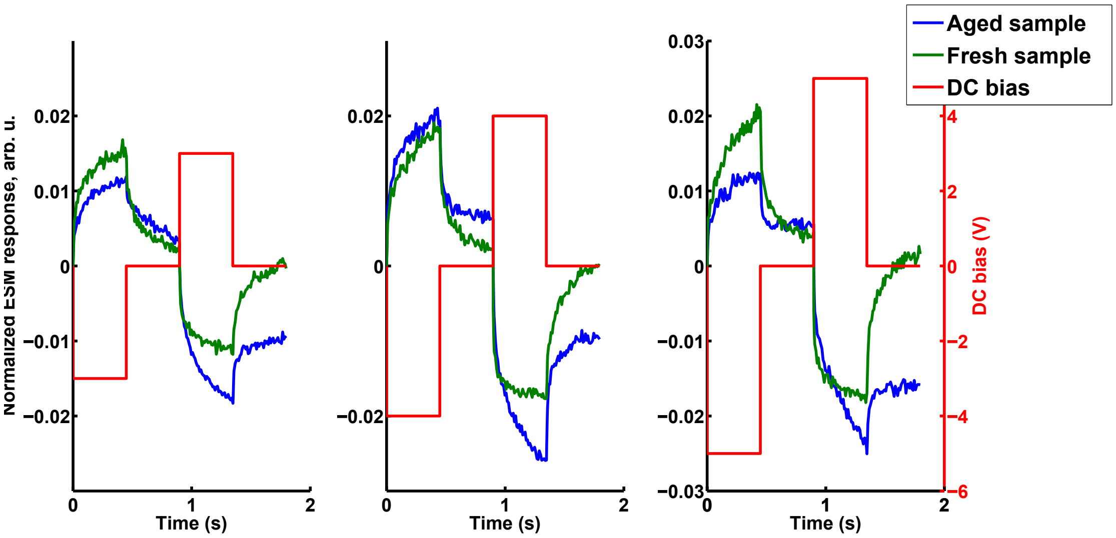

Figure 16.8: Time spectroscopy measurements on fresh (green curve) and aged (blue curve) samples. Plot re-adapted from figure 8 of Luchkin et al. (2015).

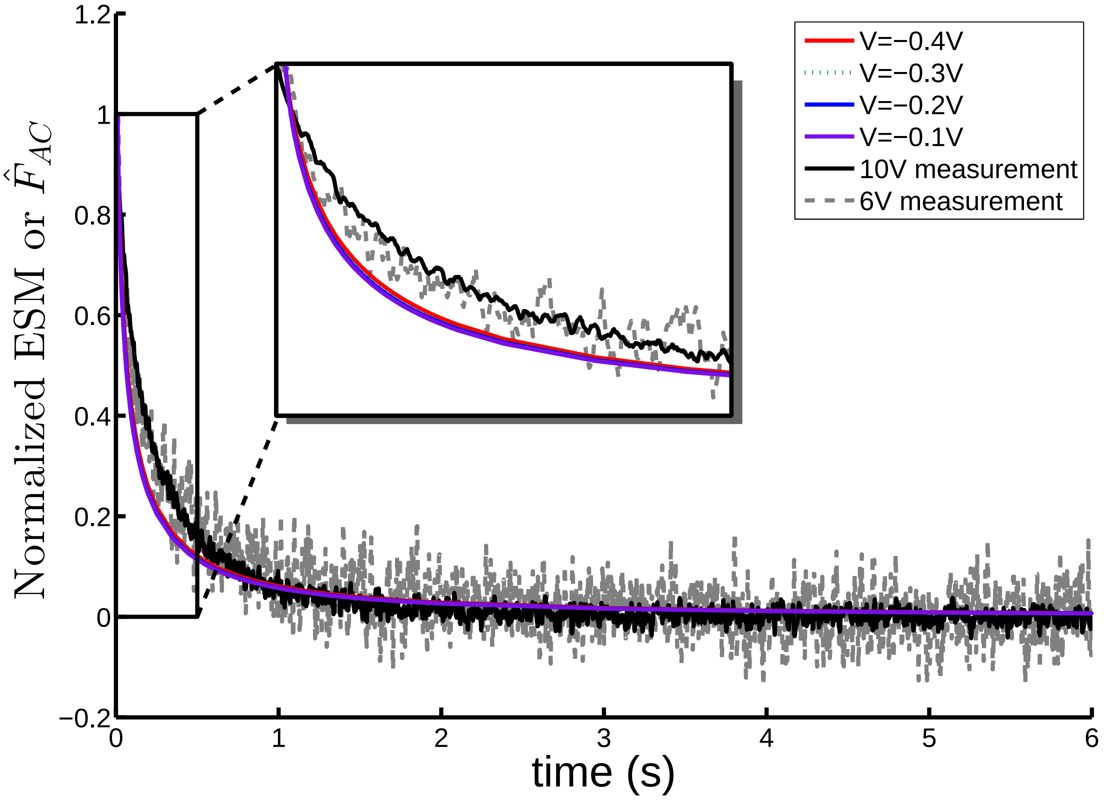

Figure 16.9: Normalized ESM signal after a 10ms, -10V DC pulse (solid black line) and after a 10ms, -6V DC pulse (dotted gray line). Normalized $\mathfrak{F}_{AC}$ from time spectroscopy simulations using the default parameters and different applied voltages $\bar{\phi}_0$ (solid colored lines, voltages indicated in the legend). Normalization procedure explained in the text.

figs. 16.11 and 16.12. p only slightly depends on the parameters and is around -1 as shown in fig. 16.11. It is strongly correlated to the tip radius. The parametric study for a is plotted in fig. 16.12. a is correlated with D_0 and R_{tip}. The other parameters seem to have a limited impact for the ranges of study. Even the initial concentration has a limited impact on the normalized signal. The thickness study would be done by modeling a half oblate spheroid particle of equatorial radius R_{part} and of different short radii (or thicknesses). The behavior strongly deviates from the one described in eq. (16.1) for thicknesses approaching the order of magnitude of R_{tip}. For all other cases the adjusted R-square is above 0.99 when fitted with eq. (16.1).

The power law resembles the analytical solution found by Morozovska et al. (2010) from eq. (2.24). The exponent is not always equal to $-3/2$ ($p = -2/3$) but is somewhat close ($p = [-0.8, -1.4]$). The parameter a had the following proportionality with R_{tip} and D_0:

$$a \propto \frac{D_0^{1/2}}{R_{\text{tip}}}. \tag{16.2}$$

The same power law was found for the tip displacement $u_z(t)$ in our case with differences in the exponents of eq. (16.2). As $u_z(t)$ is not a measurable quantity, further investigation on this matter is not published here.

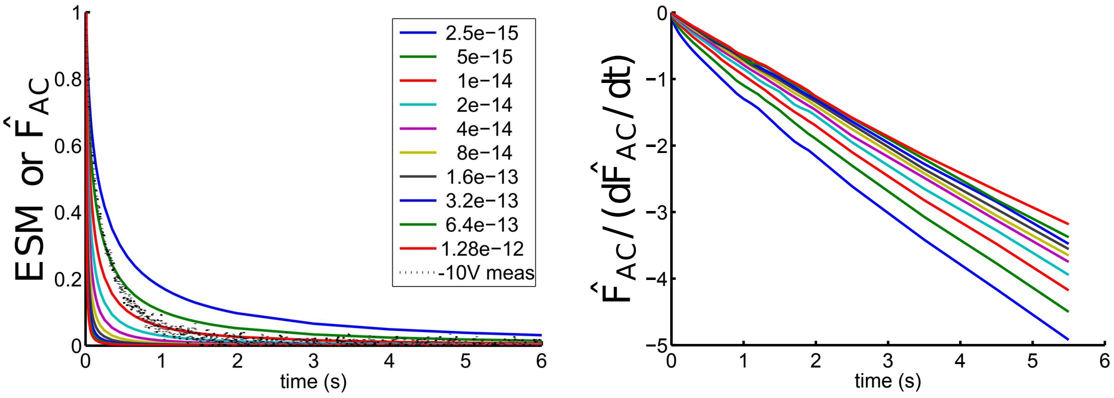

(a) (b)

Figure 16.10: (a) Normalized ESM signal after a 10 ms, 10 V DC pulse (dotted black line) in comparison with normalized $\mathfrak{F}_{AC}$ simulated using the default parameters and different diffusion coefficients (solid colored lines, coefficient values in the legend). (b) $\mathfrak{F}_{AC}$ divided by its time derivative (same legend).

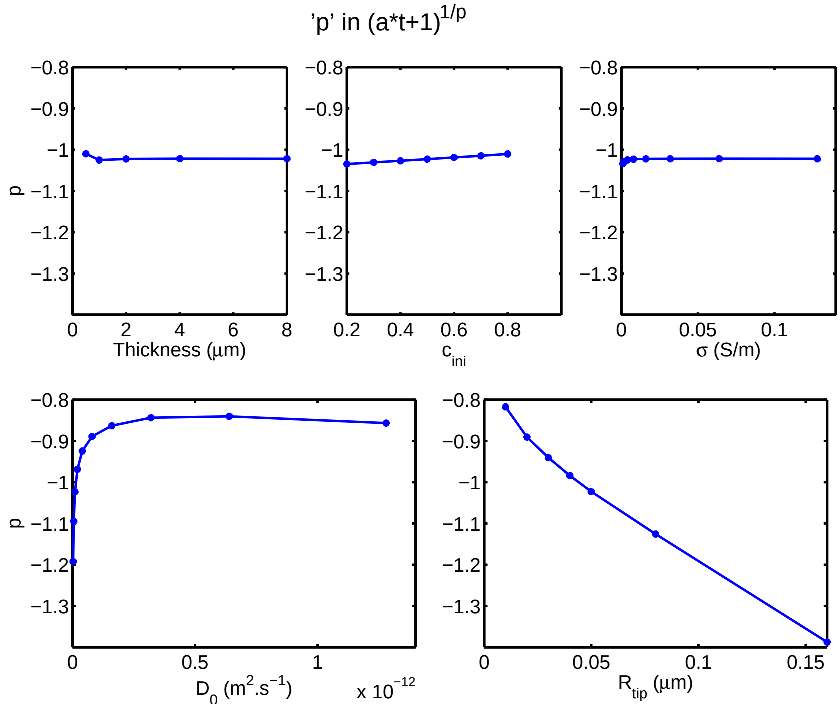

Figure 16.11: Parameter study for p with respect to the default state.

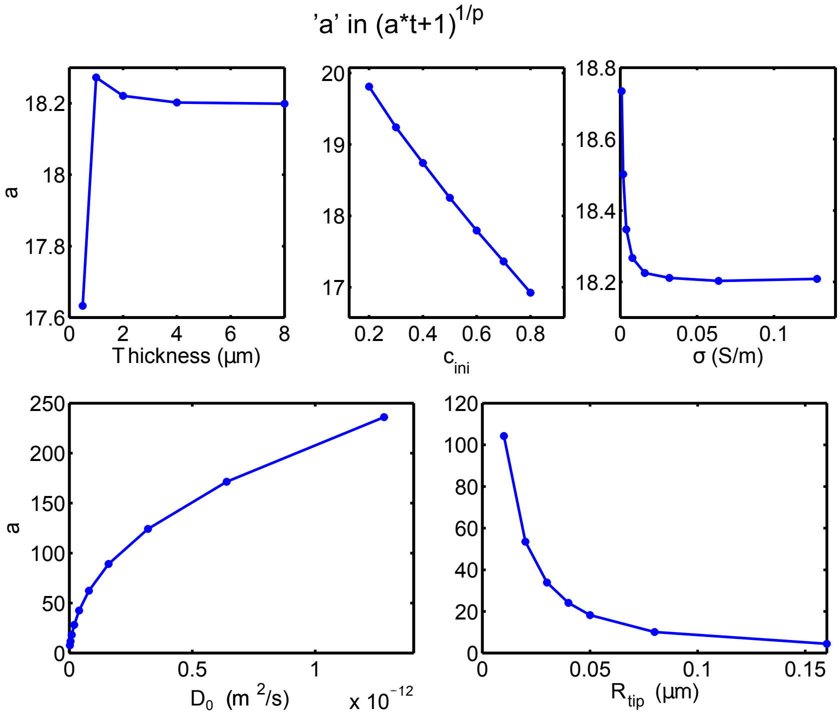

Figure 16.12: parameter study for a with respect to the default state. Note that the y-axis range is different for each plot for better visibility. A significant variation is only observed for D_0 and R_{tip}.

16.3 Equation fitting

Fitting eq. (16.1) to experimental measurements from fig. 16.3 yields the fitting coefficients shown in table 16.1. The first striking observation is that the exponent p seems off the range previously computed even though the 95 % confidence bounds provided by Matlab curve fitting toolbox are good (within 5 % of the fitted values). Based on eq. (16.2), the coefficient a of the aged sample is one order of magnitude smaller than the other ones, which could be interpreted as a diffusion coefficient which is two orders of magnitude smaller (for all other parameters fixed), if the hypothesis of eq. (11.24) stands. It is nevertheless not sufficient to obtain quantitative information without more rigorous description of eq. (16.2) and without knowing the value of the other parameters in advance.

Besides, the current model is relatively simplistic. A better experimental/model comparison could be obtained if polaron-ion coupling is better understood, phase descriptions of spinel $Li_xMn_2O_4$ are taken into account and if experimental conditions are better controlled, e.g. no humidity is present and the temperature is constant.

Sample	a	p	coefficient of determination
Fresh 0 %SoC	2.69	-0.45	0.9775
Fresh 50 %SoC	1.419	-0.3234	0.9964
Fresh 100 %SoC	4.515	-0.6846	0.9548
Aged 0 %SoC	0.3366	-0.257	0.9862

Table 16.1: Fitting parameters of experimental measurements.

Part VII

Discussions

17

Chapter

Mechanical characterization of heterogeneous materials

The structure of active particles obtained from commercial LiBs makes mechanical characterization of them laborious: they have different sizes, some are porous, there are impurities (e.g. cobalt oxide) and more than two phases make up for the composite. It was shown in the previous part that using already available methods is not straight forward. The fundamental problem revealed for all measurements is to obtain statistically relevant data.

17.1 Indentation

Statistical deconvolution using Ulm's method (Constantinides et al. 2006) requirs proper filtering of the measurements. One observation from the raw data plotted in figs. 7.1 and 7.2 is that several spurious peaks are obtained in-between the expected values. This problem was already raised by Pavel Trtik et al. (2009) with the help of a mechanical model of hardened cement pastes. They first simplified it to a biphasic checkboard composite and their main conclusion is as follows:

> "The results based on the image of an idealized two-phase material show that the linear size of the nanoindentation interaction volume has to be at least three times smaller than the homogeneous isotropic domains of a single phase, in order for the histograms of elastic modulus to show a bimodal distribution. If this requirement is not met, a spurious single peak appears at an elastic modulus corresponding roughly to the average of the moduli of the phases."
>
> (Pavel Trtik et al. 2009)

A critique ensues by Ulm and Vandamme (2010) where they demonstrate by means of simulation that the spurious peak is due to the 3-D checkboard microstructure: a composite with a matrix/inclusion microstructure shows no middle spurious peak for small indentation depths and would induce homogenization around a single peak upon increasing the depth. On the other hand, they reproduce Trtik's results with the checkboard structure, where a spurious peak that could be wrongly associated with a third phase is present at low depths.

It could be expected that our results correspond to the hypothesis of a matrix/inclusion microstructure. Our samples differ greatly because of the gap between the properties of the two phases: the elastic modulus of epoxy is one order of magnitude smaller, not a few percent less. Careful observation of the origin of our own spurious peaks revealed that the issue comes from composite response inducing load, displacement, and stiffness curves that do not fit the Oliver and Pharr hypotheses, hence wrongly calculated by the instrument.

Introducing a filtering method greatly increases the signal-to-noise ratio of the distribution functions. However, with a success rate below 10 % for *complex* composites, reaching a statistical significant sampling requires several hundred, if not thousands, of indentations and microscopic imaging. For future prospect, IIT is improving towards ultra-fast methods where the rate of indentation approach 1 Hz, allowing frequency counts as high as in XRD experiments in just a few hours (e.g. Express Test by Keysight Technologies). If this new hardware could be associated with proper software statistical and image analysis, selective nanoindentation could prove to be a reliable technique where measurements could be done in an appropriate time frame: from months, like for this work, to days.

17.2 Contact-resonance atomic force microscopy

Qualitative mapping was relatively fast and valuable as the measured magnitude, the cantilever amplitude, is directly obtained from the machine. Differences among the particles could be mapped within minutes and reveal which phases are stiffer. This is the fundamental benefit of an AFM-based technique as compared to nanoindentation.

However quantitative measurements were unsuccessful although most of the laboratory time was allocated to it (two times two weeks). The difficulties arose mainly from the set-up and the instrument itself: going back-and-forth between the reference sample and the sample of study consumed time and tips. The electronics was catching a lot of noise but it could be deciphered from the proper signal by changing the cantilever deflection force, as the peak should shift to higher frequencies for higher forces. The data-recording software was also limited as the peak detection script was not properly calibrated for complex peak shapes: it can be observed for example on fig. 14.11b where the first set of measurements on the fused silica seems identical for all cantilever deflections (flat green curve for tests 1 to 8). The signal was in reality shifting but the application could not decipher the constant noise at 1 MHz from it. A last issue is more theoretical: the cantilever shape and contact mechanisms are simplified to a horizontal cantilever with no lateral force (see section 2.2.2) but it seems to be minor as compared to instrumental issues. As is often the case in research, this hides in fact a lack of funding for this particular technique, even though scientific expertise exists.

17.3 Crack opening displacement

17.3.1 User interpretation

It is difficult to decipher inverse AFM tip imaging from crack wall imaging as the measured vertical displacements u_z have the same order of magnitude as the surface roughness. This can be observed from real measurements in fig. 4.1c. This behavior was simulated as shown in fig. 5.4. Mode I fracture toughnesses and mode III fracture toughnesses obtained from the group experiment described in chapter 5 are plotted in figs. 17.1a and 17.1b, respectively. It can be noticed how close the computed values are to the input values in the case of the simulated cracks. Yet user interpretation can drastically change the measurement from simple to double as is the case for Sample 1. Overall the averaged values from the group approach the author's measurements, which shows that most users interpreted the COD the same way.

17.3.2 Boundary conditions

High loads could not be applied without destroying the particles, rendering measurements impossible. Inevitably, the crack lengths come close to the typical size of an indent as shown in fig. 4.1a at lower loads. It is possible that the COD were determined within the plastic zone. A strong hypothesis of Irwin's near-field solution is that the crack walls are traction free (LAWN 1993a). There could be a systematic error in COD measurements where the fracture toughness is over-estimated due to residual tensile stresses induced by plastic deformation (LAWN 1993b). This could explain the discrepancy between the values extracted with this method, $\sim$ 0.9 MPa·m$^{1/2}$, and the value obtained on the wafer by crack-length measurement, $\sim$ 0.23 MPa·m$^{1/2}$.

COD measurements using Irwin's near field theory do not seem to be an appropriate method to quantify fracture properties of micrometric particles particularly because of the systematic error associated with the plastic zone. Besides, it takes time to obtain consistent data, as shown here, as only seven cracks were adequate for measurement which cripples statistical significance.

17.3.3 Additional techniques

As presented in the article related to this work (AMANIEU ET AL. 2015b), the pillar splitting method developed by M. Sebastiani and G. Pharr (SEBASTIANI ET AL. 2014) seems more adapted to the problem. Focused ion beam is used to mill a pillar out of the particles in a semi-automated fashion, which allows well defined boundary conditions.

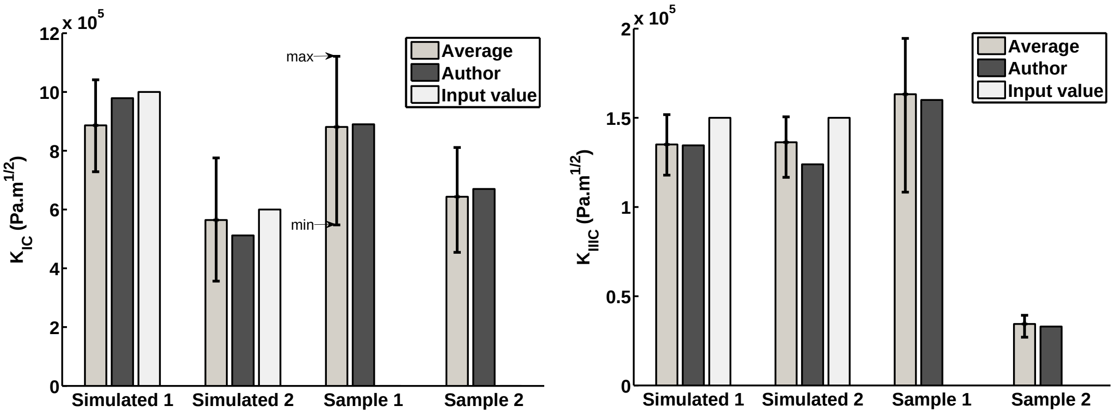

(a) (b)

Figure 17.1: Values obtained from the group experiment: (a) mode I fracture toughness and (b) mode III fracture toughness. The first set of bars show the average toughnesses measured by the group. The error bars associated with it indicate the highest and lowest values obtained from the group. The darker set of bars shows the values obtained by the first author. The lighter set of bars shows the values inputted to simulate the surfaces. Sample 1 and sample 2 correspond to ◊ and □ in table 15.1 and fig. 15.2.

The pillar is subsequently split by Berkovich indentation. If the pillar experiences brittle failure, its fracture toughness can be calculated as follows:

$$K_c = \gamma \frac{P_c}{r^{3/2}}, \tag{17.1}$$

where K_C is the fracture toughness (MPa·m$^{1/2}$), P_c is the critical load at failure (mN) and R the pillar radius (µm). γ is a dimensionless coefficient that is calculated by a finite element method and depends on the material properties (Sebastiani et al. 2014 2015). The benefit of this method lies in its simplicity as can be seen in eq. (17.1), as both the critical load and pillar radius are straightforwardly measured quantities. This method is also more repeatable as the inventors made a software platform to make pillar-milling an automatic procedure. The compliant matrix below the particles could falsify P_c but the γ factor is corrected for it. The correction is regardless well within experimental scatter (Sebastiani et al. 2015).

Other techniques based on the FIB milling try to reproduce macro-scale traditional conditions but at the micro-scale: notably by milling a single notched cantilever (Iqbal et al. 2012). These techniques present two important drawbacks that made them impracticable on the battery specimens. First, the samples must be prepared with two perpendicular polished surfaces in order to make a cantilever with controlled geometry. This drastically reduces the probability to find a good testing site, i.e. a relatively big and compact particle located at the 90° edge. Furthermore, FIB milling of the notch introduces defects in the cantilever leading to an underestimation of the toughness (Sebastiani et al. 2015).

A fracture toughness of 0.35 ± 0.05 MPa·m$^{1/2}$ for sample *C0SoC* and 0.29 ± 0.08 MPa·m$^{1/2}$ for the wafer were obtained with this method by Roma Tre university (see (Amanieu et al. 2015b)). Both of these values are closer to the toughness found by crack-length measurement. They also confirm that COD measurements overestimate the toughness value.

18

Chapter

Origin of the signal in electrochemical strain microscopy

$\mathfrak{F}_{AC}$ is used here as a mathematical tool rather than a real physical quantity to probe the concentration of lithium ions within a small volume below the tip. While it is believed that the normalized ESM signal is mainly driven by the change of concentration of ions below the tip, the Vegard contribution cannot be the origin of the signal under AC excitation. Other electromechanical couplings should be considered, including but not limited to converse flexoelectricy or electrostriction. Unlike $\mathfrak{F}_{AC}$ which is linearly dependent on $\boldsymbol{E}$, the former would be dependent on $\nabla \boldsymbol{E}$ and the latter on $\boldsymbol{E}^2$ (Morozovska et al. 2012a; Nguyen et al. 2013). The butterfly-like loops could originate from an electrostrictive effect (Chen et al. 2014). It is possible that the same effect is present even in the case of diamond-like loops, hence the first and second harmonic responses should be measured in future studies (see Chen et al. (2014)). Other potential mechanisms are given in Appendix C from the corresponding article (Amanieu et al. 2015c), credited to Dr. S. Luchkin .

With better knowledge of the underlying mechanisms, future work on ESM should focus on improving the definition of S_{Li} in eq. (11.24). In any case, the coupling should increase for higher lithium concentration as seen experimentally (see e.g. fig. 16.2 or Jesse et al. (2011)). The physical origin is not necessarily directly related to lithium concentration: it could depend on the valence of the transition metals, i.e. the local ratio of Mn^{3+} versus Mn^{4+}, or it could be coupled to polarons.

It should be additionally noted that even if S_{Li} is fully understood, measuring c_0 (initial concentration) quantitatively by ESM would not be possible due to the omnipresent background signal $S_{\mathrm{background}}$ which is a composite response depending on c_0 and other effects as discussed in section 2.2.3. Hence ESM-TS can only probe the diffusivity, i.e. the speed of concentration change.

19 Chapter

Properties of lithium manganese(III,IV) oxide

$LiMn_2O_4$ particles found in commercial batteries have slightly different properties than laboratory grade particles often found in literature. XRD data showed how the lattice parameter never extends above 0.82 nm. ICP-OES results were generally not quantitatively convincing but a certain trend of lower lithium concentration for higher SoC is shown, as expected. However a lot of impurities was found, most importantly cobalt which was also confirmed by EDX. Concerning other impurities, aluminum can originate from the current collector. Note that no copper from the negative electrode was found in the positive electrode, even with aged cells. Nickel could also be a product from the production line as other cathode chemistries contain it. However the traces of potassium and sodium can not be explained as simply because they are neither contained in the electrolyte nor any other part of the battery. They could have arrived after opening the battery (e.g. manipulators' fingers).

The nanoindentation results confirmed that the elastic modulus should lie around 90 GPa with a Berkovich hardness of about 7 GPa, which is the order of magnitude also found by Zhu and Zeng (2012). It was already explained in section 14.1 that they find twice as much for as-deposited cathode due to potential pile-up. The fracture toughness was found to be well below 1 MPa·m$^{1/2}$, down to about 0.3 MPa·m$^{1/2}$ using the pillar splitting method. The material is in general in the lower range of stiffness and toughness of ceramics.

For comparison, spinel $MgAl_2O_4$ has a fracture toughness one order of magnitude higher (Dericioglu et al. 2005) and an elastic modulus of about 270 Gpa (Roy and Gay G. Martin 1992). Compared to battery materials, the elastic modulus of $LiCoO_2$ was unavailable in the literature until 2012 where it was determined to be of 174 ± 14 GPa for polycrystalline $LiCoO_2$ pellets (Qu et al. 2012). It is also much stiffer than found here for $LiMn_2O_4$. A follow-up paper by Swallow et al. (2014) showed similar data for the same kind of specimen with an elastic modulus of 178 ± 5 GPa. They also charged pellets at very low current ($\sim$ 1/1000 C-Rate) and noticed a sharp drop of elastic modulus just after 50 hours charge (corresponding to 5 % SoC if the sample is homogeneously charged) as it falls to 100 ± 3 GPa and keeps this order of magnitude for all the charged specimens (maximum charging time was 500 hours, ~ 50 %SoC) without a monotonous trend. They find that, unlike the lattice parameter of $LiMn_2O_4$, the bond length in the c-axis increases upon delithiation ($LiCoO_2$ is a layered structure, see chapter 1) and it is expected that the elastic properties decrease. The same behavior was reported by Cho et al. (2014) for thin films at somehow much higher moduli: they range from 323 to 225 GPa for x in Li_xCoO_2 ranging between 1.0 and 0.6. Their article focuses on thermal properties of the material and they do not develop on the origin of the discrepancy between their values and the values of Qu et al. (2012) and Swallow et al. (2014), but this could be due to their measuring instrument which is not designed for it (time-domain thermoreflectance), so this measurement should be taken qualitatively. A computational simulation reports a similar trend (Qi et al. 2014).

An increase of stiffness upon lithiation was reported for another layered structure: $0.5Li_2MnO_3{\cdot}0.5LiNi_{1/3}Co_{1/3}Mn_{1/3}O_2$ or lithium-rich layer oxide. It consists of alternating lithium manganese oxide and lithium nickel cobalt manganese oxide layers (Li et al. 2015).

These data validate the hypothesis that *longer bond lengths lead to a more compliant material, whether it is induced by increasing or decreasing lithium concentration.*

The fracture toughness of $LiCoO_2$ is also reported by Qu et al. (2012) and Swallow et al. (2014), where the latter corrects the value of the former group and find in both cases about 1 MPa·$m^{1/2}$ for the as-obtained pellet. The latter also reports a significant decrease in the toughness upon electrochemical charging as K_{IC} falls down to 0.25 MPa·$m^{1/2}$ for all the samples (5 to 50 % SoC). This demonstrates that pristine materials become more fragile as soon as they are electrochemically activated, as it is the case for our commercial particles. As for the elastic modulus, there is no significant difference among the charged $LiCoO_2$ samples, so no correlation with lithium concentration was found. To the best of our knowledge, no quantitative measurements were carried out on real-life application particles unlike in this thesis.

No significant results could be obtained from the ESM model to characterize the commercial particles. The results have mainly been fruitful for understanding the instrument itself. We could however notice that time spectroscopy relaxation was slower on the aged particles, which indicates that lithium diffusivity was impaired due to the electrochemical fatigue. No significant differences were detected on the fresh samples with different SoC.

Conclusion

$LiMn_2O_4$ is reported in this work to be more compliant than other cathode ceramics with an elastic modulus of around 90 GPa and more brittle than expected, with a fracture toughness of about 0.3 MPa·$m^{1/2}$. Upon indentation, chipping, a brittle mechanism, seemed also more significant than piling-up. The hardness to elastic modulus ratio is above 0.1, another indication that the material is fragile and not ductile. We also reported that crystal orientation plays a crucial role in the fracture mechanisms, as shown by the different chipping and also by FIB cross-sections of indented wafers. The elastic modulus increases by about 10 % between charged and discharged cells, which does not seem significant and might be irrelevant to implement in simulations. Numerical simulations of mechanical fatigue can keep constant parameters upon lithiation and disregard ductility, but it seems more crucial to take into account the grain dimensions and the crystal orientation. This conclusion can be extended to most metal oxides such as $LiCoO_2$ but not for alloys, like silicon-based or tin-based anodes, which are very ductile and for which the mechanical properties change significantly upon lithiation. Further investigations should focus on the cleavage planes.

In this work, we showed that several methods must be combined to have a proper picture of the elastic properties of heterogeneous specimens. Selective nanoindentation must be associated with imaging techniques to obtain reliable quantitative results and with CR-AFM to obtain nanoscale characterization. Concerning fracture, the AFM-based method was not convincing due to the Ssystematic error and the slow speed. Pillar-splitting methods based on FIB milling should be favored despite its bigger investment cost.

We also showed that the ESM signal does not originate from Vegard's deformation but rather from an interaction between the alternating electric field and the crystal which depends on the lithium concentration c_{Li}, perhaps due to the transition metals as their valence states depend on c_{Li}. It is not yet fully understood to obtain quantitative measurements and further investigation must be done. However comparative studies can be carried out by using time spectroscopy.

Appendices

A Chapter Algorithm

A.1 Fractional Brownian motion

The following code is a Matlab implementation of an algorithm to produce fractional Brownian motion, allowing more realistic surfaces. It was reinterpreted from the following sources: Generate procedural perlin noise in matlab[4] (first visited on June 23rd, 2014) & Noise Fractals and Clouds[5] (first visited on June 23rd, 2014).

```
function im = fBm_noise(im)

    [n, m] = size(im);
    i = 0;
    w = sqrt(n*m);

    while w > 3
        i = i + 1;
        d = interp2(randn(...
            ceil((n-1)/(2^(i-1))+1),...
            ceil((m-1)/(2^(i-1))+1)),...
            i-1, 'spline');
        im = im + i * d(1:n, 1:m);
        w = w - ceil(w/2 - 1);
    end
end
```

---

[4] http://stackoverflow.com/questions/7347111/generate-procedural-perlin-noise-in-matlab

[5] http://nullprogram.com/blog/2007/11/20/

B Chapter Additional images

B.1 SEM images

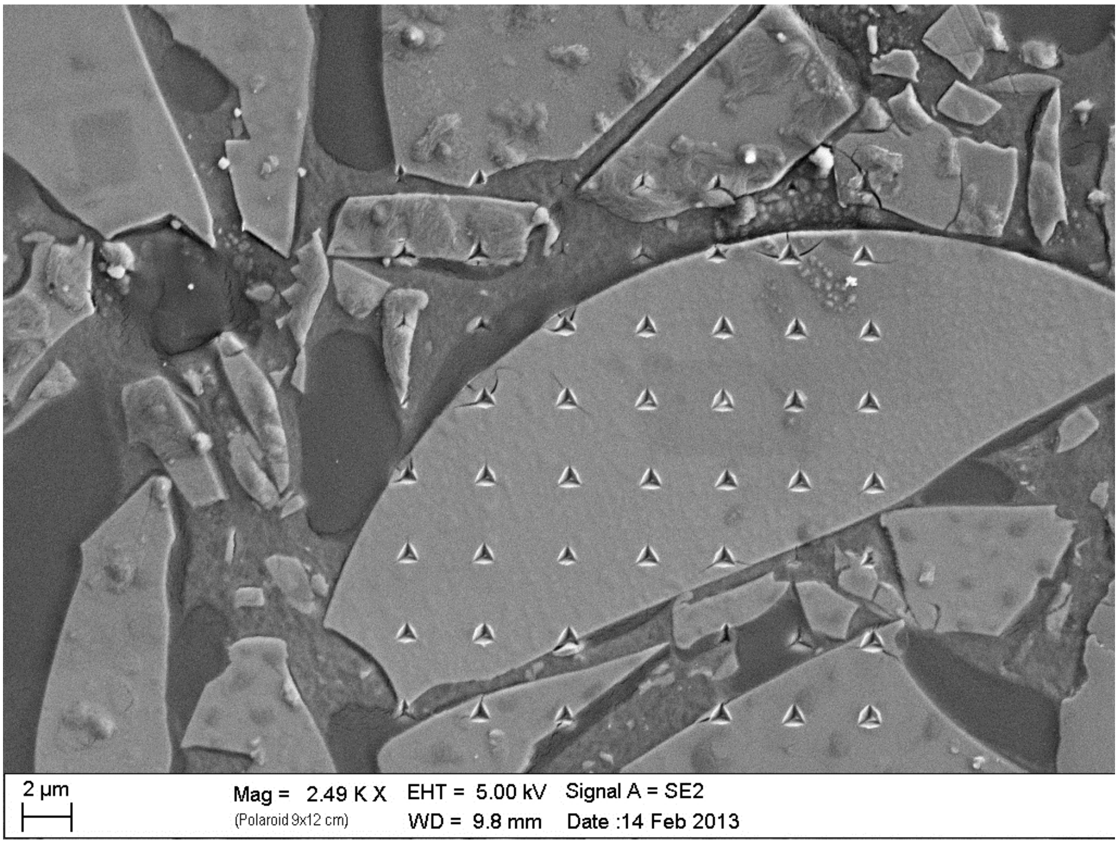

Figure B.1: SEM micrograph of an indentation grid on the silica-based sample. Used to establish the reliability of selective nanoindentation.

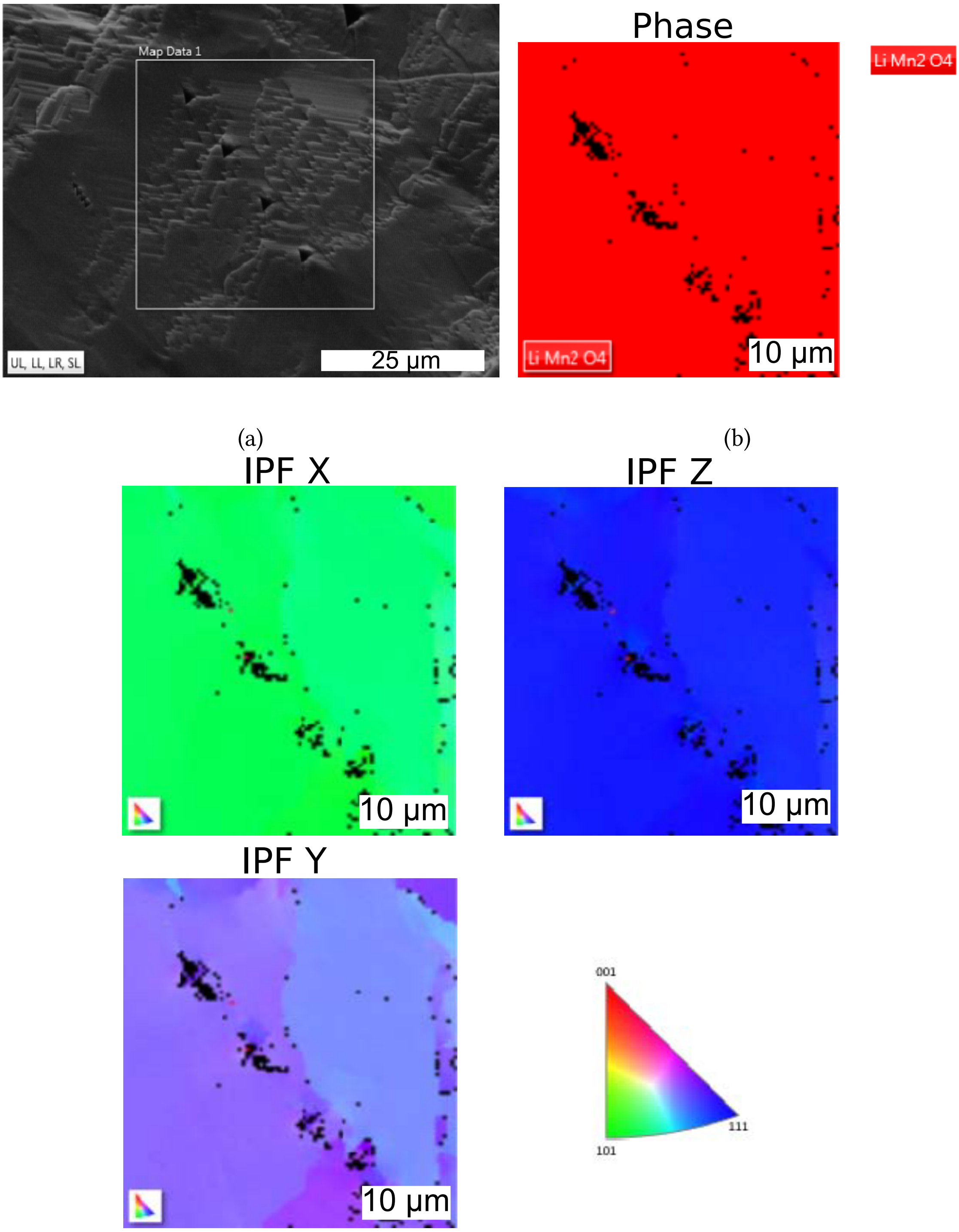

(a)

(b)

(c)

Figure B.2: (a) SEM image of the studied area from sample *wafer.* (b) Phase detected by EBSD. (c) Crystal orientation measured by EBSD.

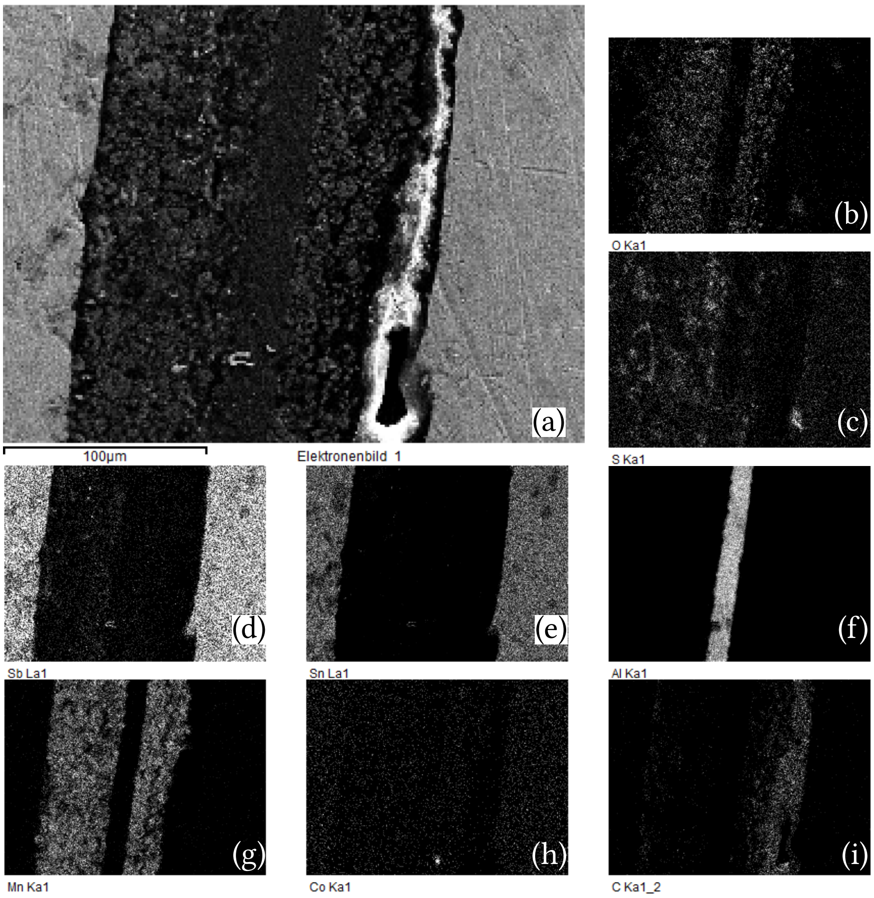

Figure B.3: (a) SEM picture of a cathode section from sample *S0SoC_2* embedded in a metallic alloy. (b),(c),(d),(e),(f),(g), (h) and (i) EDX signal obtained on the same area for the following emission lines: Kα1 of oxygen, Kα1 of sulfur, Lα1 of antimony, Lα1 of tin, Kα1 of aluminum, Kα1 of manganese, Kα1 of cobalt and Kα1 and 2 of carbon, respectively. Note how bright is the signal in (h) for a single spot corresponding to a cobalt particle.

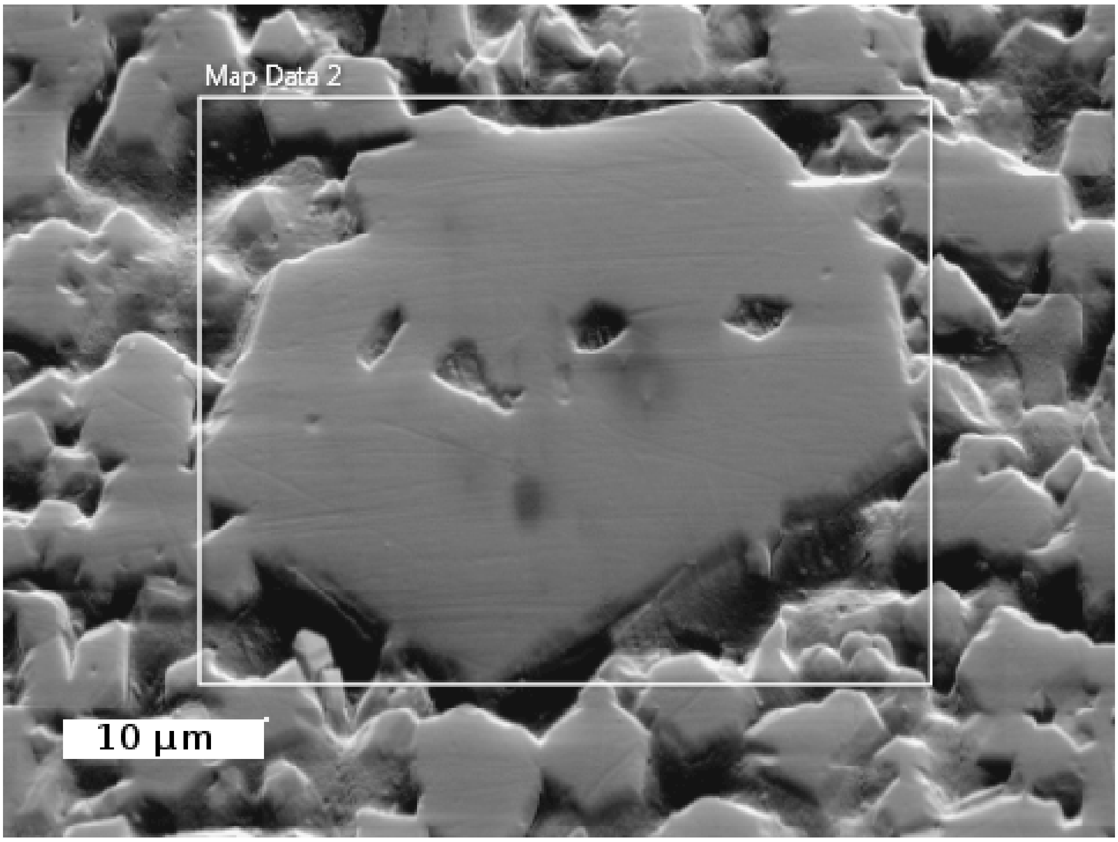

Figure B.4: SEM micrograph of the particle studied by CRAFM. The white square indicates the area imaged by EBSD. A dark spot referring to the arrow in fig. 14.7 can be observed and indicates a hole below the surface.

B.2 Contact resonance atomic force microscopy

Figure B.5a depicts AFM topography of a particle from sample *C0SoC*. The circular shapes are instrumental artifacts induced by the tip wear. Figure B.5b is an AFAM amplitude image of the same area at 691 kHz. There is a clear convolution between topography and the AFAM signal except for a small area invisible on fig. B.5a (red square). A close up was done on this area (fig. B.5c), then the transducer frequency was increased by 23kHz before being imaged again (fig. B.5d). A contrast reversal occurred. The frequency resonance was reached for the previously darker area. This is due to a higher stiffness of this area. This phenomenon could not be observed in other areas, from this sample or the other samples, indicating the rarity of the event. One hypothesis came out from this measurement: lithiation of a small volume within this particle can be blocked, leaving a delithiated and stiffer part. This difference might be caused by the presence of two different phases with one of them being electrochemically passive. Due to the inability to reproduce the measurement a second time, it could also be an instrumental problem and so is relegated to the appendix.

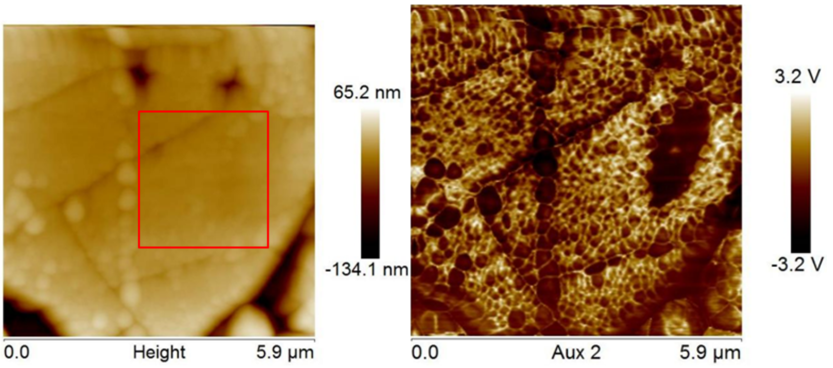

(a) Topography (b) 691kHz

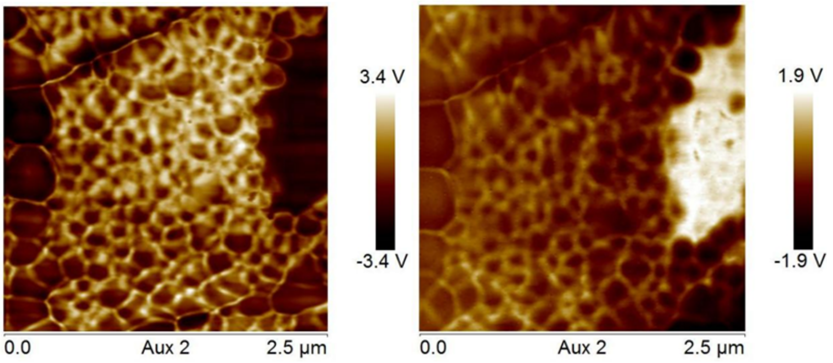

(c) 691kHz (d) 714kHz

Figure B.5: AFM images of a set of particles from *C0SoC*. (a) shows the topography and (b) is an amplitude image of the cantilever under transducer excitation at 691kHz. (c) is a another scan at 691kHz of the region marked in red in (a). (d) depicts the same area but under an excitation of 714kHz.

B.3 Electrochemical strain microscopy model

The electric and chemical boundaries are schematically shown in fig. B.6.

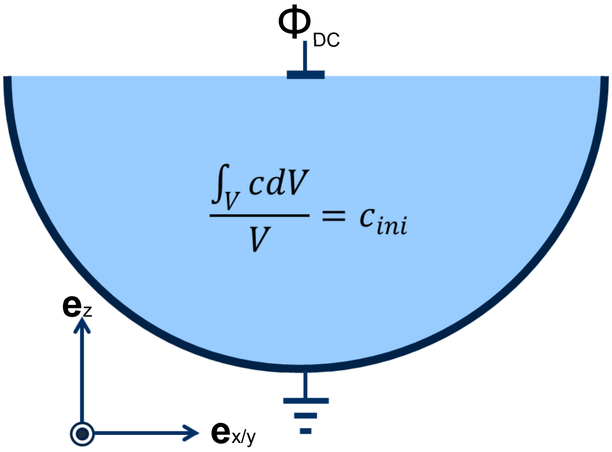

Figure B.6: Electrical and chemical boundary condition, side view of the particle.

Figure B.7 represents the concentration under the tip during the first loop using the simple model. The color coding is used only as a guide to compare it directly with fig. 16.5. One can see how the surface area for $0.7 < c_{Li} < 0.98$ is much bigger and regular in this case. The concentration also reaches deeply delithiated values (black area).

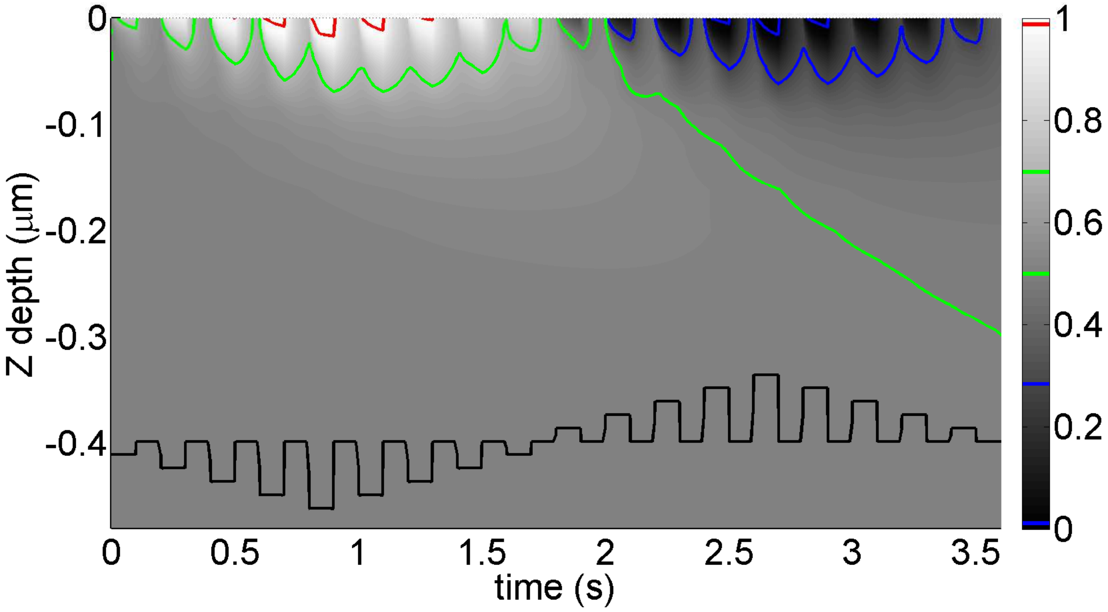

Figure B.7: Evolution of the concentration of lithium ions below the tip down to a depth of 0.5μm during the first loop with a constant $D_{\text{eff}} = 1$. The brightness is correlated with the concentration of lithium c_{Li} as indicated by the colorbar. Colored contours represent each phase of spinel $\text{Li}_x\text{Mn}_2\text{O}_4$, with blue for poorly lithiated spinel, green for the middle phase and red for lithiated spinel. These boundaries represent c_{Li} when $D_{\text{eff}}(c_{\text{Li}}) \sim 1$ in fig. 11.1 and is only intended to be compared with fig. 16.5.

Bibliography

Akimoto, J; Takahashi, Y; Mizuta, S (2000): *Single Crystal X-ray Diffraction Study of the Spinel-type LiMn2O4.* In: Chem. Mater., 12:3246–3248.

Allnatt, AR; Lidiard, AB (1993): *Atomic Transport in Solids.* Cambridge University Press. doi:10.1017/cbo9780511563904.

Amanieu, HY; Rosato, D; Sebastiani, M; Massimi, F; Lupascu, DC (2014): *Mechanical property measurements of heterogeneous materials by selective nanoindentation: Application to LiMn2O4 cathode.* In: Mater. Sci. Eng. A, 593: 92–102.

Amanieu, HY; Aramfard, M; Rosato, D; Batista, L; Rabe, U; Lupascu, DC (2015a): *Mechanical properties of commercial Mn2O4 cathode under different States of Charge.* In: Acta Materialia, 89(0):153–162. doi:10.1016/j.actamat.2015.01.074.

Amanieu, HY; Sebastiani, M; Mughal, MZ; Rosato, D; Lupascu, DC (2015b): *Fracture properties of LiMn2O4 cathode at the microscale.* to be submitted, 2015b.

Amanieu, HY; Thai, HN; Luchking, SY; Rosato, D; Lupascu, DC; Keip, MA; Schröder, J; Kholkin, AL (aug 2015c): *Electrochemical strain microscopy time spectroscopy: Model and experiment on LiMn2O4.* In: J. Appl. Phys., 118(5):055101. doi:10.1063/1.4927747.

Ang, SF; Schulz, A; Fernandes, RP; Schneider, GA (2012): *Sub-10-micrometer toughening and crack tip toughness of dental enamel.* In: Journal of the Mechanical Behavior of Biomedical Materials, 4(3):423–432.

Anstis, G; Chantikul, P; Lawn, B; Marshall, D (sep 1981): *A Critical Evaluation of Indentation Techniques for Measuring Fracture Toughness: I, Direct Crack Measurements.* In: Journal of the American Ceramic Society, 64(9):533–538. doi:10.1111/j.1151-2916.1981.tb10320.x.

Balke, N; Jesse, S; Kim, Y; Adamczyk, L; Tselev, A; Ivanov, I; Dudney, N; Kalinin, S (2010): *Real space mapping of Li-ion transport in amorphous Si anodes with nanometer resolution.* In: Nano Letters, 10(9):3420–3425.

Berg, H; Thomas, J (1999): *Neutron diffraction study of electrochemically delithiated LiMn2O4 spinel.* In: Solid State Ionics, 126:227–234.

Berg, H; Göransson, K; Noläng, B; Thomas, J (1999): *Electronic structure and stability of the LixMn2O4 $(0 < x < 2)$ system.* In: J. Mater. Chem., 9:2813–2820.

Binnig, G; Quate, CF; Gerber, C (Mar 1986): *Atomic Force Microscope.* In: Phys. Rev. Lett., 56:930–933. doi:10.1103/PhysRevLett.56.930.

Bohn, E; Eckl, T; Kamlah, M; McMeeking, R (2013): *A Model for Lithium Diffusion and Stress Generation in an Intercalation Storage Particle with Phase Change.* In: Journal of the Electrochemical Society, 160(10):1638–1652.

Bohn, E (2011): *Partikel-Modell für Lithium-Diffusion und mechanische Spannungen einer Interkalationselektrode.* PhD thesis, Karlsruher Institut für Technologie.

Bolotovskii Boris M andSero, AV (1994): *Details of the motion of charged nonrelativistic particles in a variable field.* In: Physics-Uspekhi, 37(5):515–516.

Bolshakov, A; Pharr, GM (1997): *Influences of pileup on the measurement of mechanical properties by load and depth sensing indentation techniques.* In: J. Mater. Res., 13(4):1049–1057.

Bolshakov, A; Oliver, WC; Pharr, GM (1996): *Influences of stress on the measurement of mechanical properties using nanoindentation: Part II. Finite element simulations.* In: J. Mater. Res., 11(3):760–768.

Brodd, RJ (2009): *Innovation and Intellectual Property Rights.* In: Yoshio, M; Brodd, RJ; Kozawa, A (Eds.): Lithium-Ion Batteries, chapter 1. Springer New York, 2009. doi:10.1007/978-0-387-34445-4.

Chan, CK; Peng, H; Liu, G; McIlwrath, K; Zhang, XF; Huggins, RA; Cui, Y (dec 2007): *High-performance lithium battery anodes using silicon nanowires.* In: Nature Nanotech, 3(1):31–35. doi:10.1038/nnano.2007.411.

Chen, D; Indris, S; Schulz, M; Gamer, B; Moenig, R (2011): *In situ scanning electron microscopy on lithium-ion battery electrodes using an ionic liquid.* In: J Power Sources, 196:6382–6387.

Chen, QN; Ou, Y; Ma, F; Li, J (2014): *Mechanisms of electromechanical coupling in strain based scanning probe microscopy.* In: Applied Physics Letters, 104(24):242907.

Cheng, YT; Cheng, CM (1998): *Further analysis of indentation loading curves: Effects of tip rounding on mechanical property measurements.* In: J. Mater. Res., 13(4): 1059–1064.

Cho, J; Losego, MD; Zhang, HG; Kim, H; Zuo, J; Petrov, I; Cahill, DG; Braun, PV (jun 2014): *Electrochemically tunable thermal conductivity of lithium cobalt oxide.* In: Nat Comms, 5. doi:10.1038/ncomms5035.

Choudhury, S; Zhang, JX; Li, YL; Chen, LQ; Jia, QX; Kalinin, SV (2008): *Effect of ferroelastic twin walls on local polarization switching: Phase-field modeling.* In: Applied Physics Letters, 93(16):162901. doi:10.1063/1.2993330.

Chudoba, T; Schwaller, P; Rabe, R; Breguet, J; Michler, J (2006): *Comparison of nanoindentation results obtained with Berkovich and cube-corner indenters.* In: Philos. Mag., 86(33-35 SPEC. ISSUE):5265–5283.

Chung, DW; Balke, N; Kalinin, SV; García, RE (2011a): *Virtual Electrochemical Strain Microscopy of Polycrystalline LiCoO2 Films.* In: Journal of the Elecgrochemical Society, 158(10):1083–1089.

Chung, M; Seo, J; Zhang, X; Sastry, A (2011b): *Implementing Realistic Geometry and measured Diffusion Coefficients into Single Particle Electrode Modeling Based Experiments with Single LiMn2O4 Spinel Particles.* In: J. Electrochem. Soc., 158(4): A371–A378.

Constantinides, G; Ravi Chandran, K; Ulm, FJ; Van Vliet, K (2006): *Grid indentation analysis of composite microstructure and mechanics: Principles and validation.* In: Mater. Sci. Eng. A, 430:189–202.

Cuadradoa, N; Casellasa, D; Angladac, M; Jiménez-Piquéc, E (2012): *Evaluation of fracture toughness of small volumes by means of cube-corner nanoindentation.* In: Scr Mater, 66(9):670–673.

Dal, H; Miehe, C (2015): *Computational electro-chemo-mechanics of lithium-ion battery electrodes at finite strains.* In: Computational Mechanics, 55(2):303–325. doi:10.1007/s00466-014-1102-5.

Darul, J; Nowicki, W; Piszora, P (2012): *Unusual Compressional Behavior of Lithium?Manganese Oxides: A Case Study of Li4Mn5O12.* In: J. Phys. Chem. C, 116: 17872–17879.

Deiss, E (2002): *Spurious potential dependence of diffusion coefficients in Li+ insertion electrodes measured with PITT.* In: Electrochimica Acta, 47(25):4027–4034.

Dericioglu, AF; Boccaccini, AR; Dlouhy, I; Kagawa, Y (2005): *Effect of Chemical Composition on the Optical Properties and Fracture Toughness of Transparent Magnesium Aluminate Spinel Ceramics.* In: MATERIALS TRANSACTIONS, 46(5): 996–1003. doi:10.2320/matertrans.46.996.

Devreese, J (1996): *Polarons.* In: Encyclopedia of Applied Physics, 14:383–409.

Doerner, M; Nix, W (1986): *A method for interpreting the data from depth-sensing indentation instruments.* In: Journal of Materials Research, 1:601–609. doi:10.1557/JMR.1986.0601.

Dridi-zrelli, Y (2012): *Electrochimie et Spectroscopie Raman de matériaux d'électrodes positives pour batteries lithium ion.* PhD thesis, Université Paris Est-Créteil.

Fischer-Cripps, A (2006): *Critical review of analysis and interpretation of nanoindentation test data.* In: Surface and Coatings Technology, 200(14–15): 4153–4165. doi:10.1016/j.surfcoat.2005.03.018.

García, RE; Chiang, YM; Carter, WC; Limthongkul, P; Bishop, CM (2005): *Microstructural Modeling and Design of Rechargeable Lithium-Ion Batteries.* In:

Journal of the Electrochemical Society, 152:A255–A263.

Ghosh, D; Subhash, G; Orlovskaya, N (2010): *Slip-line spacing in ZrB2-based ultrahigh-temperature ceramics.* In: Scr Mater, 62:839–842.

Grechnev, GE; Ahuja, R; Johansson, B; Eriksson, O (Apr 2002): *Electronic structure, magnetic, and cohesive properties of* $\mathrm{Li}_x\mathrm{Mn}_2\mathrm{O}_4$ *:Theory.* In: Phys. Rev. B, 65:174408. doi:10.1103/PhysRevB.65.174408.

Griffith, AA (jan 1921): *The Phenomena of Rupture and Flow in Solids.* In: Philosophical Transactions of the Royal Society A: Mathematical, Physical and Engineering Sciences, 221(582-593):163–198. doi:10.1098/rsta.1921.0006.

Guan, J; Liu, M (1998): *Transport properties of LiMn O electrode materials for lithium-ion batteries.* In: Solid State Ionics, 110:21–28.

Guo, S; Jesse, S; Kalnaus, S; Balke, N; Daniel, C; Kalinin, SV (2011): *Direct Mapping of Ion Diffusion Times on LiCoO2 Surfaces with Nanometer Resolution.* In: Journal of the Electrochemical Society, 158(8):A982–A990.

Guyomard, D; Tarascon, J (1992): *Li metal-free rechargeable LiMn2O4/carbon cells: their understanding and optimization.* In: J. Electrochem. Soc., 139(4):937–948.

Hao, X; Lin, X; Lu, W; Bartlett, B (2014): *Oxygen vacancies lead to loss of domain order, particle fracture, and rapid capacity fade in lithium manganospinel (LiMn2O4) batteries.* In: ACS Applied Materials and Interfaces, 6(14):10849–10857.

Harvard University, dop (2007): *A Summary of Error Propagation.* http://ipl.physics.harvard.edu/wp-uploads/2013/03/PS3_Error_Propagation_sp13.pdf, 2007. [Online ; accessed first June 2014].

Hay, J; G.M., P (1999): *A critical examination of the fundamental relations used in the analysis of nanoindentation data.* In: J. Mater. Res., 14(6):2296–2305.

Hay, J; Pharr, G (2000): *Instrumented Indentation Testing.* In: ASM Handbook, 8: 232–243.

Hoang, K (2014): *Understanding the electronic and ionic conduction and lithium over-stoichiometry in LiMn2O4 spinel.* In: Journal of Materials Chemistry A, 2(43): 18271–18280.

Huang, MR; Lin, CW; Lu, HY (2001): *Crystallographic facetting in solid-state reacted LiMn2O4 spinel powder.* In: Applied Surface Science, 177(1–2):103–113.

Huggins, RA (2009): *Advanced batteries.* Springer US. doi:10.1007/978-0-387-76424-5.

Huggins, RA; Nix, WD (jan 2000): *Decrepitation model for capacity loss during cycling of alloys in rechargeable electrochemical systems.* In: Ionics, 6(1–2):57–63. doi:10.1007/bf02375547.

Hurley, D (2009): *Contact Resonance Force Microscopy Techniques for Nanomechanical Measurements*, chapter 5, pp.97–138. eds. B. Bhushan and H. Fuchs.

Iguchi, E; Nakamura, N; Aoki, A (1998): *Electrical transport properties in LiMn2O4.* In: Philosophical Maganzine Part B, 78(1):65–77.

Iguchi, E; Tokuda, Y; Nakatsugawa, H; Munakata, F (2002): *Electrical transport properties in LiMn2O4, Li0.95Mn2O4, and LiMn1.95B0.05O4 (B=Al or Ga) around room temperature.* In: Journal of Applied Physics, 91(2149):2149–2154.

Iqbal, F; Ast, J; Göken, M; Durst, K (2012): *In situ micro-cantilever tests to study fracture properties of NiAl single crystals.* In: Acta Materialia, 60(3):1193–1200. doi:10.1016/j.actamat.2011.10.060.

Irwin, GR (1957): *Analysis of Stresses and Strains near the End of a Crack Traversing a Plate.* In: Journal of Applied Mechanics, 24:361–364.

Jakes, J (2008): *Experimental method to account for structural compliance in nanoindentation measurements.* In: J. Mater. Res., 23(4):1113–1127.

Jakes, J (2009): *Nanoindentation near the edge.* In: J. Mater. Res., 24(3):1016–1031.

Jesse, S; Balke, N; Eliseev, E; Tselev, A; Dudney, NJ; Morozovska, AN; Kalinin, SV (2011): *Direct Mapping of Ionic Transport in a Si Anode on the Nanoscale: Time Domain Electrochemical Strain Spectroscopy Study.* In: ACS Nano, 5(12):9682–9695.

Joslin, D; Oliver, W (1990): *A new method for analyzing data from continuous depth-sensing microindentation tests.* In: J. Mater. Res., 5(1):123–126.

Julien, C; Massot, M (2003): *Lattice vibrations of materials for lithium rechargeable batteries III. Lithium manganese oxides.* In: Mater. Sci. Eng. B, 100(1):69–78.

Julien, C; Mauger, A; Zaghib, K; Groult, H (2014): *Comparative Issues of Cathode Materials for Li-Ion Batteries.* In: inorganics, 1:132–154.

Kalinin, SV; Morozovska, AN (2014): *Electrochemical strain microscopy of local electrochemical processes in solids: mechanism of imaging and spectroscopy in the diffusion limit.* In: J Electroceram, 32:51–59.

Kanamaru, K; Naito, H; Yao, T; Takehara, Zu (1996): *Structural change of the LiMn2O4 spinel structure induced by extraction of lithium.* In: J. Mater. Chem., 6: 33–36.

Kese, K; Li, Z (2005): *Method to account for true contact area in soda-lime glass during nanoindentation with the Berkovich tip.* In: Mater. Sci. Eng. A, 404:1–8.

Kim, YH; Pyun, SI; Go, JY (2005): *An investigation of intercalation-induced stresses generated during lithium transport through sol-gel derived LixMn2O4 film electrode using a laser beam deflection method.* In: Electrochimica Acta, 51(3):441–449.

Kitta, M; Akita, T; Kohyama, M (2013): *Preparation of a spinel LiMn2O4 single crystal film from a MnO wafer.* In: J Power Sources, 232:7–11.

Kumar, A; Ciucci, F; Morozovska, A; Kalinin, S; Jesse, S (2011): *Measuring oxygen reduction/evolution reactions on the nanoscale.* In: Nature Chemistry, 3(9): 707–713.

LaManna, JA; Oliver, WC; Pharr, GM (2004): *On the Measurement of Material Creep Parameters by Nanoindentation.* In: Symposium R – Fundamentals of Nanoindentation and Nanotribology III (MRS Proceedings, 841), 2004. doi:10.1557/PROC-841-R4.7.

Landi, BJ; Ganter, MJ; Cress, CD; DiLeo, RA; Raffaelle, RP (2009): *Carbon nanotubes for lithium ion batteries.* In: Energy Environ. Sci., 2:648–654. doi:10.1039/B904116H.

Lavela, P; Tirado, J; Vidal-Abarca, C (nov 2007): *Sol–gel preparation of cobalt manganese mixed oxides for their use as electrode materials in lithium cells.* In: Electrochimica Acta, 52(28):7986–7995. doi:10.1016/j.electacta.2007.06.066.

Lawn, B; Evans, A; Marshall, D (1980): *Elastic/Plastic Indentation Damage in Ceramics: The Median/Radial Crack System.* In: J Am Ceram Soc, 63(9–10):574–581.

Lawn, B (1993a): *Fracture of brittle solids. – 2nd edition*, chapter 2. Cambridge University Press.

Lawn, B (1993b): *Fracture of brittle solids. – 2nd edition*, chapter 8. Cambridge University Press.

Lee, S; Park, J; Sastry, A; Lu, W (2013): *Molecular dynamics simulations of SOC-dependent elasticity of Li xMn2O4 spinels in Li-ion batteries.* In: Journal of the Electrochemical Society, 160(6):A968–A972.

Lei, J; Li, L; Kostecki, R; Muller, R; McLarnon, F (2005): *Characterization of SEI Layers on LiMn2O4 Cathodes with In Situ Spectroscopic Ellipsometry.* In: Journal of the Electrochemical Society, 152(4):A774–A777.

Leisen, D; Kerkamm, I; Bohn, E; Kamlah, M (2012): *A novel and simple approach for characterizing the Young's modulus of single particles in a soft matrix by nanoindentation.* In: J. MAter. Res., 27(24):3073–3082.

Li, T; Song, B; Lu, L; Zeng, K (2015): *Voltage induced electrochemical reactions in the single lithium-rich layer-oxide nanoparticles.* In: Phys. Chem. Chem. Phys., 17(15): 10257–10264. doi:10.1039/c5cp00230c.

Lin, Y; Yang, Y; Ma, H; Cui, Y; Mao, W (2011): *Compressional Behavior of Bulk and Nanorod LiMn2O4 under Nonhydrostatic Stress.* In: J. Phys. Chem. C, 115: 9844–9849.

Liu, LY; Gu, HM; Shen, HT; Zhai, YC (2009): *Study on the structure and stability of LiMn2O4 by first-principle method.* In: Dongbei Daxue Xuebao/Journal of Northeastern University, 30(SUPPL. 2):190–192.

Loubet, J; Georges, J; Marchesini, O; Meille, G (1984): *VICKERS INDENTATION CURVES OF MAGNESIUM OXIDE (MgO).* In: Journal of Tribology, Transactions of the ASME, 106(1):43–48.

Luchkin, SY; Romanyuk, K; Ivanov, M; Kholkin, AL (2015): *Li transport in fresh and aged LiMn2O4 cathodes via Electrochemical Strain Microscopy.* In: Journal of Applied Physics, p. to appear.

Maier, J (2005): *Kinetics and Irreversible Thermodynamics*, pp.268–398. John Wiley & Sons, Ltd. doi:10.1002/0470020229.ch6.

Marzec, J; Świerczek, S; Przewoźnik, J; Molenda, J; Simon, D; Kelder, E; Schoonman, J (2002): *Conduction mechanism in operating a LiMn2O4 cathode.* In: Solid State Ionics, 146(3–4):225–237.

Maxisch, T; Zhou, F; Ceder, G (2006): *Ab initio study of the migration of small polarons in olivine LixFePO4 and their association with lithium ions and vacancies.* In: Phys. Rev. B, 73(104301):1–6.

Menčík, J (1997): *Determination of elastic modulus of thin layers using nanoindentation.* In: J. Mater. Res., 12(9):2475–2484.

Meschke, F; Alves-Riccardo, P; Schneider, GA; Claussen, N (1997): *Failure behavior of alumina and alumina/silicon carbide nanocomposites with natural and artificial flaws.* In: Journal of Materials Research, 12:3307–3315. doi:10.1557/JMR.1997.0435.

Momma, K; Izumi, F (2011): *VESTA 3 for three-dimensional visualization of crystal, volumetric and morphology data.* In: J. Appl. Crystallogr., 44:1272–1276.

Moon, H; Lee, W (2003): *Effect of film stress on electrochemical properties of lithium manganese oxide thin films lithium manganese oxide thin films.* In: J Power Sources, 119–121:710–712.

Morozovska, AN; Eliseev, EA; Balke, N; Kalinin, SV (2010): *Local probing of ionic diffusion by electrochemical strain microscopy: Spatial resolution and signal formation mechanisms.* In: Journal of Applied Physics, 108(53712):1–21.

Morozovska, AN; Eliseev, EA; Bravina, SL; Ciucci, F; Svechnikov, GS; Chen, LQ; Kalinin, SV (2012a): *Frequency dependent dynamical electromechanical response of mixed ionic-electronic conductors.* In: J. Appl. Phys., 111(1):014107. doi:10.1063/1.3673868.

Morozovska, AN; Eliseev, EA; Kalinin, SV (2012b): *Electrochemical strain* *microscopy with blocking electrodes: The role of electromigration and diffusion.* In: J. Appl. Phys., 111(14114):1–18.

Mukhopadhyay, NK; Paufler, P (2006): *Micro- and nanoindentation techniques for mechanical characterisation of materials.* In: Int. Mater. Rev., 51(4):209–245.

Nguyen, TD; Mao, S; Yeh, YW; Purohit, PK; McAlpine, MC (jan 2013): *Nanoscale Flexoelectricity.* In: Adv. Mater., 25(7):946–974. doi:10.1002/adma.201203852.

Nix, WD; Gao, H (1998): *Indentation Size Effects in Crystalline Materials: A law For Strain Gradient Plasticity.* In: J. Mech. Phys. Solids, 46(3):411–425.

Ohzuku, T; Tomura, H; Sawai, K (1997): *Monitoring of particle fracture by acoustic emission during charge and discharge of Li/MnO2 cells.* In: Journal of the Electrochemical Society, 144(10):3496–3500.

Oliver, WC; Pharr, G (1992): *An improved technique for determining hardness and elastic modulus using load and displacement sensing indentation experiments.* In: J. Mater. Res., 7(6):1564–1583.

Oliver, WC; Pharr, G (2004): *Measurement of hardness and elastic modulus by instrumented indentation: Advances in understanding and refinements to methodology.* In: J. Mater. Res., 19(1):43891.

Ouyang, C; Deng, H; Ye, Z; Lei, M; Chen, L (2006): *Pulsed laser deposition prepared LiMn2O4 thin film.* In: Thin Solid Films, 503(1–2):268–271.

Park, M; Zhang, X; Chung, M; Less, GB; Sastry, AM (2010): *A review of conduction phenomena in Li-ion batteries.* In: J Power Sources, 195:7904–7929.

Park, Y; Kim, J; Kim, M; Kim, H; Chung, H; Park, Y (2000): *Electrochemical properties of LiMn2O4 thin films: suggestion of factors for excellent rechargeability.* In: Journal of Power Sources, 87(1):69–77.

Pavel Trtik, P; Münch, B; Lura, P (2009): *A critical examination of statistical nanoindentation on model materials and hardened cement pastes based on virtual experiments.* In: Cem. Concr. Compos., 31(10):705–714.

Pelletier, H (2005): *Predictive model to estimate the stress-strain curves of bulk metals using nanoindentation.* In: Tribology International, 39(7):593–606.

Pharr, G (1998): *Measurement of mechanical properties by ultra-low load indentation.* In: Mater. Sci. Eng. A, A253:151–159.

Pharr, G (May 2013): *Nanoindentation: from theory to practice.* Agilent Nanoindentation Users' Meeting, May 2013. Lecture. Hosted by Roma Tre University, Rome, Italy.

Qi, Y; Hector, LGJ; James, C; Kim, KJ (2014): *Lithium Concentration Dependent Elastic Properties of Battery Electrode Materials from First Principles Calculations.* In: Journal of the Electrochemical Society, 161(11):F3010–F3018.

Qu, M; Woodford, WH; Maloney, JM; Carter, WC; Chiang, YM; Vliet, KJV (may 2012): *Nanomechanical Quantification of Elastic, Plastic, and Fracture Properties of LiCoO2.* In: Advanced Energy Materials, 2(8):940–944. doi:10.1002/aenm.201200107.

Rabe, U; Arnold, W (1994): *Acoustic microscopy by atomic force microscopy.* In: Applied Physics Letters, 64(12):1493–1495.

Rabe, U; Amelio, S; Kopycinska, M; Hirsekorn, S; Kempf, M; Göken, M; Arnold, W (2002): *Imaging and measurement of local mechanical material properties by atomic force acoustic microscopy.* In: Surf. Interface Anal., 33:65–70.

Rabe, U (2006): *Atomic Force Acoustic Microscopy.* In: Bhushan, B; Fuchs, H (Eds.): Applied Scanning Probe Methods II (NanoScience and Technology,), chapter Atomic Force Acoustic Microscopy, pp.37–90. Springer Berlin Heidelberg, 2006. doi:10.1007/3-540-27453-7_2.

Rice, JR (1968): *MATHEMATICAL ANALYSIS IN THE MECHANICS OF FRACTURE*, chapter 3, pp.191–311. Academic Press, N.Y.

Rödel, J; Kelly, JF; Lawn, BR (1990): *In Situ Measurements of Bridged Crack Interfaces in the Scanning Electron Microscope.* In: J. Am. Ceram. Soc., 73(11): 3313–3318.

Rösler, J; Harders, H; Bäker, M (2008): *Mechanisches Verhalten der Werkstoffe* (Vieweg Studium.). Vieweg+Teubner Verlag. ISBN:9783835192454.

Roy, DW; Gay G. Martin, J (dec 1992): *Advances in spinel optical quality, size/shape capacity, and applications.* In: Klocek, P (Ed.): Window and Dome Technologies and Materials III. SPIE, dec 1992. doi:10.1117/12.130781.

Schmidt, R; Basu, A; Brinkman, A (2005): *Small polaron hopping in spinel manganates.* In: Physical Review B - Condensed Matter and Materials Physics, 72(11).

Scrosati, B; Garche, J (2010): *Lithium batteries: Status, prospects and future.* In: J Power Sources, 195:2419–2430.

Sebastiani, M; Johanns, K; Herbert, E; Carassiti, F; Pharr, G (2014): *A novel pillar indentation splitting test for measuring fracture toughness of thin ceramic coatings.* In: Philosophical Magazine.

Sebastiani, M; Johanns, K; Herbert, E; Pharr, G (apr 2015): *Measurement of fracture toughness by nanoindentation methods: Recent advances and future challenges.* In: Current Opinion in Solid State and Materials Science. doi:10.1016/j.cossms.2015.04.003.

Shim, S; il Jang, J; Pharr, G (sep 2008): *Extraction of flow properties of single-crystal silicon* *carbide by nanoindentation and finite-element simulation.* In: Acta Materialia, 56(15): 3824–3832. doi:10.1016/j.actamat.2008.04.013.

Sneddon, I (1965): *The relation between load and penetration in the axisymmetric boussinesq problem for a punch of arbitrary profile.* In: International Journal of Engineering Science, 3 (1):47–57.

Stone, D; Yoder, K; Sproul, W (1991): *Hardness and elastic modulus of TiN based on continuous indentation technique and new correlation.* In: J. Vac. Sci. Technol., 9(4): 2543–2547. doi:10.1116/1.577270.

Sugiyama, J; Tamura, T (1995): *Elastic/anelastic behaviour during the phase transition in spinel LiMn2O4.* In: J Phys Condens Matter, 7:9755–9764.

Swadener, JG; Taljat, B; Pharr, G (jul 2001): *Measurement of residual stress by load and depth sensing indentation with spherical indenters.* In: Journal of Materials Research, 16(07): 2091–2102. doi:10.1557/jmr.2001.0286.

Swallow, JG; Woodford, WH; McGrogan, FP; Ferralis, N; Chiang, YM; Vliet, KJV (jan 2014): *Effect of Electrochemical Charging on Elastoplastic Properties and Fracture Toughness of LiXCoO2.* In: Journal of the Electrochemical Society, 161(11):F3084–F3090. doi:10.1149/2.0141411jes.

Takahashi, Y; Kijima, N; Akimoto, J (2006): *Crystal growth and structural properties of the spinel-type Li1+xMn2 - xO4 (x=0.10, 0.14).* In: Solid State Ionics, 177:691–695.

Tang, W; Yang, X; Kanoh, H; Ooi, K (2001): *Formation and growth of spinel-type LiMn2O4 Single Crystals by LiCl-MnCl2 Flux evaporation.* In: Chemistry Letters, 30(6):524–525.

Tang, XC; Song, XW; Shen, PZ; Jia, DZ (2005): *Capacity intermittent titration technique (CITT): A novel technique for determination of Li+ solid diffusion coefficient of LiMn2O4.* In: Electrochimica Acta, 50(28):5581–5587.

tateishi, K; du Boulay, D; Ishizawa, N (2004): *The effect of mixed Mn valences on Li migration in LiMn2O4 spinel: A molecular dynamics study.* In: Appl. Phys. Lett., 84(4): 529–531.

Tselev, A; Morozovska, AN; Udod, A; Eliseev, EA; Kalinin, SV (2014): *Self-consistent modeling of electrochemical strain microscopy of solid electrolytes.* In: Nanotechnology, 25 (44):445701.

Tsui, TY; Pharr, GM; Oliver, WC; Bhatia, CS; White, RL; Anders, S; Anders, A; Brown, IG (1995): *Nanoindentation and Nanoscratching of Hard Carbon Coatings for Magnetic Disks.* In: Symposium I: Mechanical Behavior of Diamond and Other Forms of Carbon, 1995.

Ulm, FJ; Vandamme, M (2007): *Statistical Indentation Techniques for Hydrated Nanocomposites: Concrete, Bone, and Shale.* In: J. Am. Ceram. Soc., 90(9):2677–2692.

Ulm, FJ; Vandamme, M (2010): *Does microstructure matter for statistical nanoindentation techniques?* In: Cem. Concr. Compos., 32:92–99.

Van Der Ven, A; Bhattacharya, J; Belak, A (2013): *Understanding Li diffusion in Li-intercalation compounds.* In: Accounts of Chemical Research, 46(5):1216–1225.

Vetter, J; Novak, P; Wagner, M; Veit, C; Müller, KC; Besenhard, J; Winter, M; Wohlfahrt-Mehrens, M; Vogler, C; Hammouche, A (2005): *Ageing mechanisms in lithium-ion batteries.* In: J Power Sources, 147:269–281.

Veyssiére, P.; Kirby, S. H.; Rabier, J. (1980): *Plastic deformation of MgO : n Al2O3 spinels at temperatures below 1000 °C (0.5 Tm).* In: J. Phys. Colloques, 41(C6):C6–175–C6–178. doi:10.1051/jphyscol:1980645.

Vlassak, JJ; Nix, WD (1993): *Indentation modulus of elastically anisotropic half spaces.* In: Philosophical Maganzine A, 67(5):1045–1056.

Waldmann, T; Gorse, S; Samtleben, T; Schneider, G; Knoblauch, V; Wohlfahrt-Mehrens, M (jan 2014): *A Mechanical Aging Mechanism in Lithium-Ion Batteries.* In: Journal of the Electrochemical Society, 161(10):A1742–A1747. doi:10.1149/2.1001410jes.

Wang, H (1999): *TEM Study of Electrochemical Cycling-Induced Damage and Disorder in LiCoO[sub 2] Cathodes for Rechargeable Lithium Batteries.* In: J. Electrochem. Soc., 146(2): 473. doi:10.1149/1.1391631.

Watanabe, N; Nakayama, H; Fukao, F; Munakata, F (2012): *Effects of metal substitution on the electric and thermoelectric properties in (Ni 1-xM x)Mn 2O 4 (M = Zn and Mg).* In: Thermochimica Acta, 532:56–59.

Wikimedia Commons (2009): *Atomic force microscope block diagram*, 2009. https://en.wikipedia.org/wiki/File:Atomic_force_microscope_block_diagram.svg. [Online; accessed 05-02-2013].

Xia, Y; Yoshio, M (1996): *An Investigation of Lithium Ion Insertion into Spinel Sfructure Li-Mn-O Compounds.* In: J. Electrochem. Soc., 143(3):825–833.

Xu, B; Meng, S (2010): *Factors affecting Li mobility in spinel LiMn2O4 – A first-principles study by GGA and GGA+U methods.* In: J Power Sources, 195:4971–4976.

Yamanaka, K; Ogiso, H; Kolosov, O (1994): *Ultrasonic force microscopy for nanometer resolution subsurface imaging.* In: Applied Physics Letters, 64(2):178–180.

Yan, W; Pun, C (2011): *Some issues on nanoindentation method to measure the elastic modulus of particles in composites.* In: Composites: Part B, 42:2093–2097.

Yan, W; Pun, C (2012): *Conditions of applying Oliver and Pharr method to the nanoindentation of particles in composites.* In: Composites Science and Technology, 72:1147–1152.

Yoshio, M; Noguchi, H (2009): *Innovation and Intellectual Property Rights.* In: Yoshio, M; Brodd, RJ; Kozawa, A (Eds.): Lithium-Ion Batteries, chapter 2. Springer New York, 2009. doi:10.1007/978-0-387-34445-4.

Yoshio, M; Brodd, RJ; Kozawa, A (Eds.) (2009): *Lithium-Ion Batteries.* Springer New York.

doi:10.1007/978-0-387-34445-4.

Zhao, K; Pharr, M; Vlassak, JJ; Suo, Z (2010): *Fracture of electrodes in lithium-ion batteries caused by fast charging.* In: J. Appl. Phys., 108(7):073517. doi:10.1063/1.3492617.

Zhu, J (2011): *Nanomechanical characterization of sputtered RuO2 thin film on silicon substrate for solid state electronic devices.* In: Thin Solid Films, 519:1914–1922.

Zhu, J; Zeng, K (2012): *Cycling effects on surface morphology, nanomechanical and interfacial reliability of LiMn2O4 cathode in thin film lithium ion batteries.* In: Electrochimica Acta, 15: 52–59.

Glossary

aging The permanent loss of capacity due to passage of time. Aging is however colloquially used by the electrochemical community to depict fatigue. The latter only is used in the thesis.

anode The electrode in an electrochemical cell where oxidation takes place. During discharge, the negative electrode of the cell is the anode. During charge, the positive electrode is the anode this time. It is colloquially used only for the negative electrode.

battery Set of one or several electrochemical cells delivering a certain capacity and voltage depending on the series/parallel arrangement of the cells.

C-rate Also known as Hourly Rate, it is a unit defining a normalized current. It is a multiple of the rated capacity in ampere-hours. 1 C-rate corresponds to the current necessary to fill up a cell in one hour. Often abbreviated as the letter C

capacity It corresponds to the charge of the cell and is measured in Ampere-hour (Ah). See also energy.

cathode The electrode in an electrochemical cell where reduction takes place. During discharge, the positive electrode of the cell is the cathode. During charge, the negative electrode is the cathode this time. It is colloquially used only for the positive electrode.

charge Conversion of electrical energy into electrochemical energy.

constant current It is a way of charging or discharging a cell where the current is kept constant until the voltage reaches a specified cut-off voltage. The procedure is then stopped.

constant current constant voltage It is a way of charging or discharging a cell where the current is kept constant until the voltage reaches a specified threshold. Then the voltage is kept constant by reducing the current until it reaches a specified cut-off current.

current collector Inert inner element of a cell with high electrical conductivity. It is used to conduct electrical current from and to an electrode. It is usually made of copper on the negative side and aluminum on the positive side.

cycle life The cycle life performance is commonly defined as the number of cycles necessary before the cell capacity reaches 80 % of its initial capacity. A different percentage can be stated.

depth of discharge It is a percentage corresponding to the discharged capacity of the cell. Its reciprocal is SoC.

discharge Conversion of electrochemical energy into electrical energy.

electrolyte Medium which provides the ion transport mechanism between the anode and the cathode.

electromotive force It is measured in volts and corresponds to the open circuit voltage generated by a battery.

energy Energy stored in the cell and measured in Watt-hour (Wh). There is a linear relationship between the energy and the capacity where the slope is the cell potential.

fatigue The permanent loss of capacity due to repeated use of an electrochemical cell. The electrochemical community usually uses the colloquial term aging to refer to this phenomenon.

polaron Quasi-particle used to describe an electron (or a hole) which polarizes its environment in a dielectric crystal

scanning electron microscope Microscope imaging samples by scanning with high energy electrons. Two modes of scanning were used: secondary electron mapping which gives information on relief; back scattered electron mapping which contrasts areas with different chemical compositions.

state of charge It is a percentage corresponding to the remaining energy of the cell. Its reciprocal is DoD.

Acronyms

AFM atomic force microscopy

CC constant current

CCCV constant current constant voltage

CDF cumulative distribution function

COD crack-opening displacement

CR-AFM contact-resonance atomic force microscopy

DoD depth of discharge

EBSD Electron backscatter diffraction

EDX energy dispersive X-ray analysis

EMF electromotive force

ESM electrochemical strain microscopy

FEM finite element modeling

ICP-OES inductively coupled plasma optical emission spectrometry

IIT instrumented indentation testing

LiB lithium-ion batteries

OCV open-circuit voltage

SEI secondary electrolyte interface

SEM scanning electron microscopy

SoC state of charge

XRD X-ray diffraction

Symbols

Greek symbols

α	Indentation load constant	$[\mathrm{N\cdot m^{-m}}]$
β	Indentation correction factor	[1]
$\Delta\psi$	Difference of potential in an electrochemical cell	[V]
η	Ohmic tip contact coefficient (see MOROZOVSKA ET AL. 2010)	[1]
η_{e}	Electrochemical potential of electrons	$[\mathrm{J\cdot mol^{-1}}]$
η_{Li}	Electrochemical potential of Li	$[\mathrm{J\cdot mol^{-1}}]$
ϵ	Indentation sink-in coefficient	[1]
ε	Total strain	[1]
$\boldsymbol{\varepsilon}$	Total strain field	[1]
ϵ_j	Fitting error	[Pa]
γ_s	Surface energy per unit surface	$[\mathrm{J\cdot m^{-2}}]$
κ_e	Electronic conductivity	$[\mathrm{S\cdot m^{-1}}]$
ν	Poisson’s ratio	[1]
ν_s	Sample Poisson’s ratio	[1]
ν_d	Tip (diamond) Poisson’s ratio	[1]
μ_0	Reference chemical potential of Li	$[\mathrm{J\cdot mol^{-1}}]$
μ_{Li}	Chemical potential of Li	$[\mathrm{J\cdot mol^{-1}}]$
Ω_{Li}	Partial molar volume	$[\mathrm{m^3\cdot mol^{-1}}]$
ω	ESM excitation frequency	[Hz]
Φ_0	Applied voltage	[V]
ϕ	Electric potential	[V]
$\underline{\phi}_{AC}$	Local RMS electric potential	[V]
$\underline{\phi}_0$	Time dependent applied voltage	[V]
$\underline{\phi}_{AC}$	Applied AC voltage	[V]
$\underline{\phi}_{DC}(x,y)$	Lorentz distribution of the applied voltage	[V]
ϕ_{AC}^{rms}	Root mean square of the applied AC voltage	[V]
ψ	Gibbs free energy per unit volume	$[\mathrm{J\cdot m^{-3}}]$
ψ^{chem}	Chemical energy per unit volume	$[\mathrm{J\cdot m^{-3}}]$
ψ^{elec}	Electric energy per unit volume	$[\mathrm{J\cdot m^{-3}}]$
ψ^{mech}	Mechanical energy per unit volume	$[\mathrm{J\cdot m^{-3}}]$
ψ^{anode}	Potential of the anode	[V]
ψ^{cathode}	Potential of the cathode	[V]
σ	Uniaxial stress	[Pa]

$\boldsymbol{\sigma}$	Stress tensor	[Pa]
σ_c	Critical stress	[Pa]
σ_i	Standard deviation of the sigmoid i in $D_{fit}(x)$	[Pa]
σ_h	Hydrostatic stress	[Pa]
ρ	Mass density	[kg·m^{-3}]
ρ	Charge density	[C·m^{-3}]

Latin symbols

$A(h)$	Indenter projected area at depth h	[m^{2}]
a	AFM tip/sample Hertzian contact radius	[m]
a_i	Quadratic fitting parameters, $i = [1 \cdots 3]$	[m$^{2\text{-}i}$]
b	AFM cantilever thickness	[m]
C	Indentation contact compliance, $1/S$	[m·N^{-1}]
$\mathbb{C}$	Fourth-order elasticity tensor	[Pa]
C_m	Indenter machine compliance	[m·N^{-1}]
C_n	Fitting parameters of $A(h)$, $n \in [0 \cdots 8]$	[m$^{2^{n}}$]
C_s	Indentation structural compliance	[m·N^{-1}]
$\hat{c}$	Normalized lithium concentration	[1]
c_0	Initial concentration of lithium ions	[mol]
c_B	Cantilever resonance parameter	[s$^{1/2}$.m^{-1}]
c_{e}	Concentration of electrons	[mol]
$\hat{c}_{ini}$	Normalized initial concentration of lithium ions	[1]
c_{Li}	Concentration of Lithium ions	[mol]
c_{max}	Maximum concentration of Lithium ions	[mol]
D_0	Diffusion coefficient of Lithium ions (constant)	[m^{2}·s^{-1}]
$D(X_t)$	Experimental accumulation function	[1]
$D_{fit}(x)$	Sum of Gaussian sigmoids	[1]
D_{Li}	Diffusion coefficient of Lithium ions	[m^{2}·s^{-1}]
D_{eff}	Normalized effective diffusion coefficient of Li^{+}	[1]
E	Elastic modulus	[Pa]
$\boldsymbol{E}$	Electric field	[V·m^{-1}]
$\boldsymbol{E}_{AC}$	Mean AC electric field	[V·m^{-1}]
E_d	Tip (diamond) elastic modulus	[Pa]
E_{eff}	Effective elastic modulus	[Pa]
E_m	Matrix elastic modulus	[Pa]
E_p	Particle elastic modulus	[Pa]
E_{ref}	Elastic modulus of the reference sample	[Pa]
E_s	Sample elastic modulus	[Pa]
erf	Error function	[1]
F	Faraday constant, 96485	[m^{2}·s^{-1}]
$\mathfrak{F}_{AC}$	Mean Lorentz electric force	[N]

f_n^0	nth free flexular mode resonance frequency	[Hz]
f_n	nth contact flexular mode resonance frequency	[Hz]
G	Gibbs free energy	[J]
G_c	Griffith critical energy release rate	[J·m^{-2}]
g	Lithium occupancy function	[1]
H	Indentation hardness	[Pa]
h	Indentation depth	[m]
h_c	Indentation contact depth	[m]
h_f	Indentation residual depth	[m]
h_p	Particle dominated indentation depth	[m]
h_{max}	Indentation depth at full load	[m]
h_s	Indentation sink-in depth	[m]
$\boldsymbol{I}_\mathrm{e}$	Electric current density	[A·m^{-3}]
$\boldsymbol{I}_\mathrm{Li}$	Ionic current density	[A·m^{-3}]
$\boldsymbol{J}_0$	Joslin-Oliver parameter	[m^{2}·N^{-1}]
$\boldsymbol{J}_\mathrm{e}$	Flux of electrons	[mol·m^{-2}·s^{-1}]
J_Li	Flux of lithium ions	[mol·m^{-2}·s^{-1}]
K	Stress intensity factor	[Pa·m$^{1/2}$]
K_C	Fracture toughness	[Pa·m$^{1/2}$]
K_{IC}	Fracture toughness, mode I	[Pa·m$^{1/2}$]
K_{IIIC}	Fracture toughness, mode III	[Pa·m$^{1/2}$]
K_i	Surface fraction of phase i in D_{fit}	[1]
k	AFM tip/sample contact stiffness	[N·m^{-1}]
k_{ref}	AFM tip/reference sample contact stiffness	[N·m^{-1}]
k_lever	AFM cantilever spring constant	[N·m^{-1}]
L	Indentation load	[N]
L	AFM cantilever length	[m]
L_{max}	Maximum indentation load	[N]
L_j	Experimental load observation j	[Pa]
$\widehat{L}_j$	Fitted load observation j	[Pa]
M	Indentation modulus	[Pa]
M_e	Mobility of electrons	[m^{2}·mol·J^{-1}]
M_Li	Mobility of lithium ions	[m^{2}·mol·J^{-1}]
m	Indenter geometry constant, [1, 2]	[1]
m_i	Mean value of the sigmoid i in $D_{fit}(x)$	[Pa]
N	Total amount of lithium ions	[mol]
$\boldsymbol{n}$	surface unit vector	[1]
R	AFM tip curvature radius	[m]
R	Ideal gas constant	[J·mol^{-1}·K^{-1}]
R	Particle radius	[m]

R_{tip}	AFM tip contact radius	[m]
R^2	Coefficient of determination	[1]
S	Indentation contact stiffness at unloading	[N·m^{-1}]
S_{CSM}	Continuous indentation contact stiffness	[N·m^{-1}]
S_{Total}	ESM signal	[1]
$S_{\mathrm{Background}}$	ESM signal background	[1]
S_{Li}	Time dependent ESM signal	[1]
T	Absolute temperature	[K]
T_i	Set i of indentation tests	[1]
t	Indentation test	[1]
t	Time	[s]
t_0	ESM DC pulse length	[s]
$\boldsymbol{u}$	Displacement field	[m]
V	Particle volume	[m^3]
V_0	Unit volume	[m^3]
W	Strain energy per unit volume	[Pa]
w	AFM cantilever width	[m]
X_t	Experimental materials property, H or E	[Pa]
x	Number of Li or e$^-$ in a compound or a reaction	[1]
x	Variable of D_{fit}	[Pa]
x	Position scalar along x-axis	[m]
x_0	Tip position	[m]
x_n^0	nth free flexular mode wave number	[m^{-1}]
Y	Yield strength	[Pa]
y	Position scalar along y-axis	[m]
y_0	Tip position	[m]
z_{e}	Electron charge	[1]
z_{Li}	Lithium ion charge	[1]

Summary

This document deals with the research that the author, Hugues-Yanis Amanieu, carried out between 2012 and 2015 in order to obtain the academic grade of Doctor of Engineering (Dr.-Ing.) delivered by the University of Duisburg-Essen, Germany. The present work was included in two larger projects: *Nanomotion*, funded by the European Commission through a Marie-Curie actions program, and *ReLiOn*, funded by the German Federal Ministry of Education and Research. The goal of the former is to design new nanoscale characterization techniques to study electrochemical systems. The latter has for objective to better understand mechanical reliability of battery materials. The work described in this manuscript consequently had for objective to develop new characterization techniques in order to obtain material parameters which are fundamental to numerical simulations allowing a better understanding of mechanical failure in active particles of lithium-ion batteries.

In part I, there is a description of the functioning of lithium-ion batteries (LiB) and of the state-of-the-art of the most important characterization techniques.

As explained in section 1.1, LiB is an electrochemical system where two electrodes exchange ions within the system and electrons in an external circuit. These electrodes contain active particles where lithium can reversibly intercalate. The ions are extracted and reintroduced repeatedly which can lead to mechanical failure of the particles (see section 1.2). In fact the speed of ions in the host material controls the gradient of ionic concentration upon cycling. This gradient provokes tensile and compressive stresses. The former can reach a critical value where fracture or disordering occurs. This process depends on some key material parameters, namely the elastic modulus E, the fracture toughness K_C, and the diffusion coefficient D_{Li}. The material of study is spinel lithium manganese(III,IV) oxide ($LiMn_2O_4$), which is described in section 1.3.

Instrumented indentation testing (IIT), or nanoindentation, is then outlined in section 2.1. It is a tool which consists in driving a stiff diamond tip into a sample surface. Using the Oliver and Pharr (1992) method, the elastic modulus and the hardness of a homogeneous sample can be quantified. It was extended by Ulm and Vandamme (2007) for heterogeneous materials by implementing statistical deconvolution on a large data set. Section 2.2 deals with atomic force microscopy (AFM)-based techniques. The first one consists of measuring the topography of a crack in order to determine its crack-opening displacement (COD) and subsequently estimate the fracture toughness using Irwin's near field theory. Then contact-resonance atomic force microscopy (CR-AFM) is introduced. The elastic properties can be estimated through the resonance frequency of the cantilever when in contact with the sample surface. Last electrochemical strain microscopy (ESM) is presented. Here the AFM cantilever vibration amplitude is measured during application of a AC excitation between the AFM tip and the sample. The vibration is mediated via a mechanism which depends on the lithium concentration. *Time spectroscopy* measurements can be carried out by monitoring the signal after applying a DC pulse: a typical relaxation process is detected and its speed depends on the ionic diffusion coefficient D_{Li}. However the underlying mechanisms are still unknown to quantify it. A Vegard's deformation generated by ionic diffusion was first assummed but it seems unlikely as the displacement would not be detectable.

As listed in part II, the objectives of the work were to implement Ulm's nanoindentation statistical method and to suggest alternative methods such as CR-AFM in order to quantify E, to propose new instruments to estimate the K_C of micro-metric particles, and last to suggest a new model in order to make ESM a quantitative technique.

Sample preparation and experiments are described in part III. $LiMn_2O_4$ cathodes obtained from fresh cells and from aged cells at different states of charge were embedded in epoxy and then prepared as polished cross-sections. Laboratory-grade reference powders of SiO_2, MnO_2 and $LiMn_2O_4$ were also similarly prepared. A $LiMn_2O_4$-based wafer oriented in the {111} direction was synthesized (see chapter 3). The different instruments used in the course of the work are mentioned in chapter 4. Among these, AFM topography measurements of the COD were numerically modeled as described in chapter 5.

It is shown in part IV that Ulm's statistical deconvolution technique cannot be directly used on the battery samples as many spurious peaks appear in the distribution of the measurements. This part therefore relates to a method, called *selective nanoindentation*, that was specifically developed in order to obtain reliable measurements of the elastic moduli and the hardnesses of each phase of heterogeneous samples. It consists of filtering each experimental data by checking its consistency with the Oliver and Pharr method. First it is checked if the load-displacement curve has a quadratic shape. Second it is checked if no structural compliance induced by the epoxy matrix influences the measured stiffness. Third the filtered data are deconvoluted and compared to scanning electron microscopy (SEM) micrograms of the indented surfaces. The SiO_2-based sample was used to verify the reliability of the method.

Part V deals with the modeling of the ESM system. A COMSOL model was developed to describe the change in the lithium concentration field in a $LiMn_2O_4$ body during and after the application of a DC pulse. Its novelty is twofold. D_{Li} is not constant but depends on the lithium concentration. More importantly, the ESM signal is not physically described like in previous work where Vegard's deformation in the frequency domain is computed. Instead, the signal is estimated to be linearly dependent with the mean Lorentz electric force applied by the AC excitation on the lithium ions, denoted $\mathfrak{F}_{AC}$.

All of the results are listed in part VI.

First, chemical analyzes of the samples are given in chapter 13. X-ray diffraction (XRD) measurements showed that every sample contains a single spinel phase. This result was nuanced by energy dispersive X-ray analysis (EDX) and inductively coupled plasma optical emission spectrometry (ICP-OES) as cobalt oxide particles (up to 2 %) were detected but also other impurities. SEM showed also that these commercial particles can be porous agglomerates of nanoparticles as well as large single grains. The wafer exhibited two phases: the main one is spinel $LiMn_2O_4$ as expected but also a Mn_2O_3 bixbyite phase was found. Only the former was characterized by the other methods.

Nanoindentation results are reported in chapter 14. The particles are quite brittle: chipping occurs around the indents and cracks grow from them. Electron backscatter diffraction (EBSD) qualitatively revealed that the mechanisms depend on the crystal orientation. IIT measurements reported an elastic modulus of around 90 GPa and a Berkovich hardness of 7 GPa. This is lower than what was previously reported on $LiMn_2O_4$ thin films by ZHU AND ZENG (2012), certainly because they did not take pile-up into account, hence overestimating the properties, but also because our samples are made of factory-grade particles of lower quality. These two properties increase of more than 10 % upon delithiation. We associated this behavior with Mn−O bonds which are stiffer when the valence of the transition metal increases. The average Mn valence goes from +3.5 for $LiMn_2O_4$ to +4 for $\lambda{-}MnO_2$. An exception was detected for the specimen obtained from a 25 % SoC cell where the hardness was much lower (6.5 GPa), which could be caused by a less hard non-stoichiometric $LiMn_2O_4$. Micro-Raman spectroscopy combined with CR-AFM revealed that neighboring particles can have different lithium concentrations, hence difference stiffnesses accordingly with the nanoindentation results. CR-AFM was also used on the reference $LiMn_2O_4$ powder and it was shown that the spinel is isotropic, at least within the detection limit of the instrument. Quantitative implementation of CR-AFM was unsuccessful.

Using the traditional crack-length measurement method on the wafer, a K_C of 0.23 MPa·m$^{1/2}$ was found. As the unusual crack configuration around the indents of the particles do not allow this method to be used, COD measurements were carried out. A K_C of about 0.9 MPa·m$^{1/2}$ was measured for the commercial particles and of about 0.8 MPa·m$^{1/2}$ for the wafer. It was also found by EBSD that cracks always propagate in the $<121>$ direction in the wafer. They open {101} planes just below the surface and deviate of 30 to 40° after about 100 nm. These data are given in chapter 15.

ESM measurements as well as data from the model are reported in chapter 16. It was demonstrated that the experimental signal is qualitatively similar to $\mathfrak{F}_{AC}$. The concentration dependent D_{Li} can explain the asymmetrical hysteresis loops. Using a constant D_{Li}, it was established that time spectroscopy relaxation of $\mathfrak{F}_{AC}$ follows a power law of the form $(at+1)^{1/p}$. Here p is only slightly dependent on the diffusivity and the contact radius while a strongly depends on them and is linear with $D_{\mathrm{Li}}^{1/2}/R_{\mathrm{tip}}$. Experimentally, the relaxation process was much slower for the aged sample while no significant differences were reported for the fresh samples with different states of charge (SoCs).

Discussions of the different results are depicted in part VII.

A critique of the Ulm and Vandamme (2007) method of is discussed in chapter 17. Pavel Trtik et al. (2009) consider indeed that spurious peaks cannot be avoided when indenting heterogeneous materials. A response is given by Ulm and Vandamme (2010) which proves that their results are due to the three-dimensional configuration of their model. In our case, spurious peaks were detected nonetheless but could simply be eliminated using the *selective nanoindentation* method. An important drawback is that much more measurements must be performed to reach statistically significant numbers. In the same chapter, it was discussed that CR-AFM was a valuable extension to nanoindentation as qualitative stiffness maps with a nanoscale precision can be acquired within minutes. Nanoindentation still has the advantage of quantification as the AFM-based method was unreliable and much too slow. Last the COD measurements are discussed. It was shown that the user interpretation of the data is not so significant as a sample of 9 analysts found similar K_{IC} and K_{IIIC} on the simulated cracks as well as on two real measurements. However it is believed that the method greatly overestimates the toughness as one of the Irwin's condition is not met: the crack walls are not traction-free due to residual tensile stresses originating from the indent plastic zone. This explains the discrepancy between the two values measured on the wafer. It was suggested to use instead the pillar splitting method developed by Sebastiani et al. (2014), as they found a likely K_C of about 0.3 MPa·m$^{1/2}$ on our samples.

The origin of the ESM signal is discussed in chapter 18. It is suggested that other electromechanical couplings, such as electrostriction or flexoelectricity, should be considered. Moreover, the AC electric field could hypothetically interact with the transition metals rather than with the lithium ions.

The coupling between the mechanical properties and the lithium concentration is compared with that of other similar ceramics in chapter 19. In general, a longer bond length lead to a more compliant material, whether it is induced by an increasing or decreasing lithium concentration. Then the fracture toughness is compared with that of $LiCoO_2$. It was reported to be higher for the pristine material: 1 MPa·m$^{1/2}$. But as soon as the material is electrochemically activated, the K_C drops to similar values as ours, about 0.25 MPa·m$^{1/2}$.

In the end a brief conclusion is given that first sums up the key results for people working with battery simulation. Secondly, an overview of the reliability of the different characterization methods is given.

Zusammenfassung

Thema dieser Dissertation ist die Forschungsarbeit, die der Verfasser Hugues-Yanis Amanieu von 2012 bis 2015 zur Erlangung des akademischen Grades eines Doktors der Ingenieurwissenschaften (Dr.-Ing.) an der Universität Duisburg-Essen durchführte. Die Arbeit fand im Rahmen zweier Projekte statt: *Nanomotion*, ein von der EU-Kommission durch eine Marie-Curie Maßnahme finanziertes Projekt, und das vom Bundesministerium für Bildung und Forschung geförderte Projekt *ReLiOn*. Das Ziel des erstgenannten ist es, neue Nano-Charakterisierungstechniken zur Untersuchung elektrochemischer Systeme zu entwerfen. Letzteres hat zum Ziel, die mechanische Zuverlässigkeit von Batteriematerial besser zu verstehen. Die hier beschriebene Arbeit bringt beide Projekte zusammen: ihr Ziel die Entwicklung neuer Charakterisierungstechniken für die Erlangung von Materialparametern, die grundlegend für numerische Simulationen sind. Diese Simulationen ermöglichen ein besseres Verstehen mechanischer Brüche in den aktiven Partikeln von Lithium-Ionen-Batterien (LiB).

Teil I enthält eine Beschreibung der Funktionsweise von LiB und der modernsten und wichtigsten Charakterisierungstechniken.

Wie in Abschnitt 1.1 erklärt wird, ist LiB ein elektrochemisches System, bei dem zwei Elektroden Ionen im Inneren der Batterie und Elektronen in einem äußeren Stromkreis austauschen. Diese Elektroden enthalten aktive Partikel, in denen Lithium in einem reversiblen Prozess interkalieren kann. Die Ionen werden wiederholt geladen und entladen, was zu mechanischen Brüchen der Partikel führen kann (siehe Abschnitt 1.2). Tatsächlich kontrolliert die Geschwindigkeit der Ionen im Interkalationsmaterial den Gradienten der Ionenkonzentration beim Zyklisieren der Zelle. Dieser Gradient verursacht Zug- und Druckspannungen. Sie können einen kritischen Wert erreichen, bei dem es zu Rissen oder Phasenumwandlungen kommt. Der Prozess ist abhängig von einigen entscheidenden Materialparametern, namentlich vom Elastizitätsmodul E, der Bruchzähigkeit K_c und dem Diffusionskoeffizienten D_{Li}. Das Untersuchungsmaterial $\mathrm{LiMn_2O_4}$ wird in Abschnitt 1.3 beschrieben.

In Abschnitt 2.1 wird die Nanoindentierung geschildert. Dabei handelt es sich um ein Werkzeug, welches eine harte Diamantspitze in eine Probenoberfläche bohrt. Durch die Oliver und Pharr (1992) Methode können das Elastizitätsmodul und die Härte eines homogenen Materials gemessen werden. Ulm und Vandamme (2007) erweiterten die Methode um heterogene Materialien. Hierbei wird eine statistische Entfaltung der Daten von großen Indentierungsmatrizen durchgeführt.

Verschiedene auf Atomkraftmikroskopie (AFM) basierende Techniken werden in Abschnitt 2.2 dargelegt. Die erste besteht in der Messung der Topographie eines Risses, um die Breite der Rissöffnung (COD) zu bestimmen und anschließend die Bruchzähigkeit K_c durch die Nahfeld-Theorie von Irwin zu berechnen. Anschließend wird die Technik der Ultraschallkraftmikroskopie (CR-AFM) dargelegt. Wenn die Spitze des Cantilevers in Kontakt mit der Materialoberfläche ist, kann anhand der Resonanzfrequenz das Elastizitätsmodul berechnet werden. Zuletzt wird die Electrochemical Strain Microscopy (ESM) vorgestellt. Hierbei wird die Schwingungsamplitude des Cantilevers während einer Wechselspannungsanregung (AC-Anregung) zwischen AFM-Spitze und Probe gemessen. Die Schwingung wird durch einen Mechanismus hervorgerufen, der von der Lithiumkonzentration abhängig ist. Durch beobachten des Signals nach Anlegen eines DC-Puls können Zeitspektroskopy-Messungen durchgeführt werden: es lässt sich ein typischer Relaxations-Prozess feststellen, dessen Geschwindigkeit vom Li-Diffusionskoeffizienten D_{Li} abhängt. Die der Methode zugrundeliegenden Mechanismen zur quantitativen Bestimmung von D_{Li} sind aber immer noch unbekannt. Eine durch Li-Diffusion hervorgerufene Vegards Verformung wurde anfangs vermutet. Sie erscheint jedoch unwahrscheinlich, da die Verschiebung nicht messbar wäre.

Wie in Teil II aufgeführt ist es das Ziel der Arbeit, die statistische Methode von Ulm zu verändern, alternative Methoden für die Quantifizierung von E, wie beispielsweise CR-AFM, zu finden und neue Geräte zur Messung der Bruchzähigkeit micrometrischer Partikel vorzuschlagen. Zudem sollen neue Modelle entworfen werden, um ESM zu einer quantitativen Technik zu machen.

In Teil III werden Probenvorbereitungen und Versuche beschrieben. Aus neuen und gealterten Zellen in verschiedenen Ladungszuständen gewonnene $LiMn_2O_4$ Kathoden wurden in Epoxidharz eingebettet und als Schleifproben vorbereitet. Auf selbe Weise wurden laborreine Referenzproben von SiO_2, M_nO_2 und $LiMn_2O_4$ erstellt. Ein Wafer aus $LiMn_2O_4$ wurde in {111} Richtung synthetisiert. Die verschiedenen, im Laufe der Forschungsarbeit verwendeten Messgeräte werden in Kapitel 4 genannt, darunter AFM-Topologiemessungen der COD, deren numerische Modelle in Kapitel 5 beschreiben werden.

Wie in Teil IV gezeigt wird, kann die statistische Methode von Ulm und Vandamme (2007) nicht direkt auf Batterieproben angewendet werden, da mehrere unberechtigte Scheitelpunkte in der Verteilung der Messungen wirken. Deshalb verweist dieser Teil auf eine Methode, die *selective Nanoindentierung*, die speziell entwickelt wurde, um verlässliche Messungen des E-Moduls und der Härte zu erhalten. Sie besteht darin, jede Versuchsdatei mittels einer Überprüfung ihrer Kompatibilität durch die Oliver und Pharr Methode zu filtern. Zunächst wird überprüft, ob die Kraft-Eindringtiefe-Kurve quadratisch ist. Dann wird geprüft, ob keinerlei strukturelle Flexibilität die gemessene Steifheit beeinflusst. In einem dritten Schritt werden die gefilterten Daten entfaltet und mit Hilfe eines Rasterelektronenmikroskops (SEM) mit jeder Phase der heterogenen Probe verknüpft. Die SiO_2-Probe wurde verwendet, um die Zuverlässigkeit der Methode zu testen.

Teil V behandelt die Modellierung des ESM-Systems. Um die Veränderung des Lithiumkonzentrationsfeldes eines $LiMn_2O_4$-Körpers während und nach Anlegen eines

DC-Pulses zu beschreiben, wurde ein COMSOL-Modell entwickelt. Die Neuartigkeit im Vergleich zu anderen Modellen liegt darin, dass D_{Li} keine Konstante darstellt, sondern von der Lithiumkonzentration abhängt. Darüberhinaus wird das ESM-Signal nicht physikalisch beschrieben wie bisher, wo Vegards Verformung im Frequenzbereich berechnet wird. Stattdessen nimmt man an, dass das Signal linear abhängig ist von der durchschnittlichen elektrischen Lorenztkraft, bezeichnet als $\mathfrak{F}_A C$, die durch die AC-Anregung auf die Lithium-Ionen ausgeübt wird.

Sämtliche Ergebnisse werden in Teil VI aufgelistet.

In Kapitel 13 werden chemische Analysen der Proben gegeben. XRD-Messungen zeigen, dass jede Probe eine einzelne Spinellphase enthält. Das Ergebnis wurde durch EDX und ICP-OES ausdifferenziert, da Kobaltoxidpartikel (bis zu 2 %) aber auch andere Unreinheiten gefunden wurden. SEM-Abbildungen haben außerdem gezeigt, dass diese Partikel sowohl poröse Agglomerate von Nanopartikeln als auch große einzelne Körnchen sein können. Der Wafer wies zwei Phasen auf: die Hauptphase bildet wie erwartet der Spinell $LiMn_2O_4$, aber es wurde auch eine Mn_2O_3-Bixbyit-Phase gefunden. Nur erstere wurde von den anderen Methoden charakterisiert.

Die Ergebnisse der Nanoindentierung sind in Kapitel 14 aufgeführt. Es wurde herausgefunden, dass die Partikel relativ brüchig sind: um die Eindrücke herum kommt es zu Absplitterungen und Risse gehen von ihnen aus. Die EBSD zeigte in qualitativer Hinsicht, dass die Mechanismen von der Ausrichtung der Kristalle abhängig sind. Nanoindentierungsmessungen zeigten ein E-Modul von etwa 90 GPa und eine Berkovich-Härte von 7 GPa an. Dieses Ergebnis ist niedriger als das zuvor auf $LiMn_2O_4$-Dünnschicht gemessene Ergebnis von Zhu und Zeng (2012). Das ist sicher deshalb der Fall, weil sie nicht die Aufstockung berücksichtigten und folglich die Eigenschaften überschätzten, aber auch weil unsere Proben aus weniger hochwertigen Partikeln bestehen. Das E-Modul und die Härte steigen um mehr als 10 % bei schwächeren Lithium-Konzentrationen. Wir brachten dieses Verhalten mit Mn—O-Bindungen in Zusammenhang. Diese sind steifer, wenn die Valenz des Übergangsmetalls zunimmt. Die durchschnittliche Mn-Valenz wächst um von +3,5 für $LiMn_2O_4$ bis +4 für $\lambda-MnO_2$. Eine Ausnahme bildet die aus einer 25 % SoC-Zelle gewonnene Probe, wo die Härte viel niedriger war (6,5 GPa). Dies könnte durch ein weniger hartes nicht-stöchiometrisches $LiMn_2O_4$ verursacht werden. Wie die Micro-Raman-Spektroskopie in Kombination mit CR-AFM zeigte, können benachbarte Partikel unterschiedliche Lithium-Konzentrationen haben, folglich unterschiedliche Steifheit in Einklang mit den Ergebnissen der Nanoindentierung. CR-AFM wurde auch auf die Referenzprobe von $LiMn_2O_4$-Pulver angewendet. Wie sich herausgestellt hat, ist der Spinell isotrop, zumindest innerhalb der Nachweisgrenze des Messgeräts. Eine quantitative Durchführung von CR-AFM hat sich als erfolglos erwiesen.

Durch Anwendung einer traditionellen Technik, die darin besteht, die Länge der durch Indentierung ausgelösten Risse zu messen, hat sich für die Bruchzähigkeit des

Wafers ein Wert von 0.23 MPa·m$^{1/2}$ ergeben. Da die ungewöhnliche Konfiguration der Risse um die Eindrücke der Partikel herum es nicht erlaubt, diese Methode anzuwenden, wurden COD-Messungen durchgeführt. Für die kommerziellen Partikel wurde eine Bruchzähigkeit von etwa 0,9 MPa·m$^{1/2}$ gemessen, für den Wafer eine Bruchzähigkeit von etwa 0,8 MPa·m$^{1/2}$. EBSD hat außerdem gezeigt, dass Risse sich immer in $<$121$>$ Richtung des Waferkristalls ausbreiten. Sie legen {101}-Kristallebenen direkt unter der Oberfläche frei und weichen dann nach etwa 100 nm um 30°bis 40°ab. Diese Daten finden sich in Kapitel 15.

Die ESM-Messungen und Ergebnisse des numerischen Modells sind in Kapitel 16 aufgeführt. Wir konnten zeigen, dass das Versuchssignal qualitativ ähnlich ist zu der von unserem Modell berechneten durchschnittlichen elektrischen Lorentzkraft $\mathfrak{F}_{AC}$. Die konzentrationsabhängige D_{Li} erklärt die asymmetrischen Hystereseschleifen. Durch Verwendung einer konstanten D_{Li} wurde festgestellt, dass die Relaxation während der Zeitspektroskopie-Messung einem Potenzgesetz in Form der Funktion $(at+1)^{1/p}$ folgt. Hierbei hängt p nur leicht vom Diffusionsvermögen und dem Kontaktradius ab, während a stark davon abhängt und linear zu $D_{\mathrm{Li}}^{1/2}/R_{\mathrm{tip}}$ verläuft. Im Versuch war der Relaxationsprozess bei der gealterten Probe viel langsamer, wohingegen keine signifikanten Unterschiede bei den neuen Proben in verschiedenen Ladungszuständen (SoCs) festgestellt werden konnten.

Die Diskussion der unterschiedlichen Ergebnisse findet sich in Teil VII.

In Kapitel 17 wird eine Kritik der Methode von Ulm und Vandamme (2007) diskutiert. Pavel Trtik et al. (2009) sind in der Tat der Ansicht, dass unberechtigte Scheitelpunkte bei der Indentierung heterogener Materialien nicht vermieden werden können. Die Antwort von Ulm und Vandamme (2010) zeigt, dass ihre Ergebnisse auf eine dreidimensionalen Konfiguration ihres Modells zurückzuführen sind. In unserem Fall wurden dennoch unberechtigte Scheitelpunkte festgestellt, die jedoch durch die *selektive Nanoindentierung* einfach beseitigt werden konnten. Ein wesentlicher Nachteil besteht darin, dass weitaus mehr Messungen durchgeführt werden müssen, um statistisch signifikante Zahlen zu erhalten. Im selben Kapitel wird erörtert, dass CR-AFM eine wertvolle Erweiterung der Nanoindentierung darstellt, da sich innerhalb weniger Minuten qualitativ hochwertige Karten über die Steifheit mit einer Genauigkeit im Nanobereich herstellen lassen. Doch anders als die Indentierungstechnik erlaubt die CR-AFM keine ebenso einfache und zuverlässige qualitative Messung. Zuletzt werden die COD-Messungen diskutiert. Die simulierten Topographien sowie experimentelle Risstopographien wurden neun Analytikern vorgelegt, die den COD von jeder schätzen sollten. Es wurden ähnliche K_{IC} und K_{IIIC} berechnet, was zeigte, dass die Benutzerauslegung der Daten nur begrenzte Auswirkungen hat. Der Bruchzähigkeit wird jedoch ein zu großer Wert beigemessen, da eine der Bedingungen der Theorie von Irwin nicht erfüllt zu sein scheint: aufgrund von verbleibenden Zugspannungen, die von der durch Eindrücke entstandenen plastischen Zone ausgehen, sind die Risswände nicht traktionsfrei. Dies erklärt die Abweichung zwischen den beiden auf dem Wafer gemessenen Werten. Stattdessen wurde vorgeschlagen, die von SEBASTIANI ET AL. (2014) entwickelte Pfeiler-Spaltungs-Methode zu verwenden, da sie bei unseren Proben einen wahrscheinlicheren K_C von etwa 0,3 MPa·m$^{1/2}$ gemessen haben.

Der Ursprung des ESM-Signals wird in Kapitel 18 diskutiert. Es wird vermutet, das andere elektromechanische Kopplungen wie Elektrostriktion oder Flexoelektrizität berücksichtigt werden sollten. Außerdem besteht die Hypothese, dass das elektrische Feld eher mit dem Übergangsmetall als mit den Lithium-Ionen interagieren könnte.

In Kapitel 19 wird die Kopplung zwischen den mechanischen Eigenschaften und der Lithium-Konzentration mit der von anderen, ähnlichen Keramiken verglichen. Im Allgemeinen führt eine längere Bindungslänge, ob durch eine zu- oder eine abnehmende Lithium-Konzentration hervorgerufen, zu einem weniger steifen Material. Anschließend wird die Bruchzähigkeit mit der von $LiCoO_2$ verglichen. Sie ist bei den ursprünglichen Partikeln höher: 1 MPa·m$^{1/2}$. Sobald das Material jedoch elektrochemisch aktiviert wird, sinkt der K_C auf ähnliche Werte wie die unseren, etwa 0,25 MPa·m$^{1/2}$.

Das Ende des Manuskripts bildet ein kurzes Fazit, welches zunächst die wesentlichen Ergebnisse für jene Personen zusammenfasst, die sich mit der numerischen Modellierung von Elektroden befassen. Darüberhinaus wird ein Überblick über die Zuverlässigkeit der verschiedenen Charakterisierungstechniken gegeben.

Résumé

Ce document a pour sujet la recherche doctorale que l'auteur, Hugues-Yanis AMANIEU, a effectué de 2012 à 2015 afin d'obtenir le diplôme de docteur en ingénierie (Dr.-Ing.) délivré par l'Université de Duisburg-Essen en Allemagne. Ce travail s'inscrit dans deux projets: d'une part *Nanomotion*, financée par la Commission Européenne via une action Marie Curie, et d'autre part *ReLiOn*, financé par le ministère fédéral de l'éducation et de la recherche allemand. L'objectif du premier projet est de développer des outils de caractérisation à l'échelle nanométrique afin d'étudier les matériaux électrochimiques. Le second a pour but de mieux comprendre la fiabilité mécanique des matériaux pour batteries au lithium. Le travail décrit dans ce manuscrit a donc un objectif qui rassemble les deux projets : développer de nouvelles techniques de caractérisation afin de mesurer les propriétés physiques indispensables aux simulations numériques permettant une meilleure compréhension de la dégradation mécanique des particules actives des batteries.

Dans la partie I se trouvent la description du fonctionnement des batteries au lithium et l'état de l'art concernant les techniques de caractérisation les plus importantes.

Comme expliqué au chapitre 1, une batterie est un système électrochimique dans lequel deux électrodes échangent des ions via un circuit intérieur et des électrons via un circuit extérieur. L'échange ionique n'est possible que lorsque les électrodes contiennent des particules actives qui peuvent absorber les ions de manière réversible. De par les cycles répétitifs d'absorption et d'extraction du lithium, ces particules peuvent se fracturer (voir la section 1.2). Cela s'explique par le fait qu'un gradient de concentration ionique est généré lorsque la batterie est soumise à des courrants élevés, ce qui entraîne des stress de compression et de tension. Ils peuvent atteindre une valeur critique où une fissure ou un désordre structurel se produit. Cette suite de processus est contrôlée par les paramètres clés que sont le module de Young E, la ténacité à la fracture K_C et le coefficient de diffusivité D_{Li}. Le matériau choisi pour cette étude est l'oxyde de manganèse(III,IV) de lithium ($\mathrm{LiMn_2O_4}$), comme nous le verrons dans la section 1.3.

La technique d'indentation instrumentée, plus communément appelée *nanoindentation*, est décrite dans la section 2.1. Elle consiste à déformer la surface d'un échantillon à l'aide d'une pointe dure en diamant. Le module de Young E et la dureté peuvent être calculés pour un matériau homogène en utilisant la méthode d'OLIVER et PHARR (1992). ULM et VANDAMME (2007) l'ont étendue aux matériaux hétérogènes en utilisant une déconvolution statistique des données issues de large matrices d'indentation. Les techniques qui reposent sur la microscopie à force atomique (AFM) sont présentées en section 2.2. La première d'entre elles consiste à mesurer la topographie d'une fissure afin de déterminer sa courbe d'ouverture (COD). En appliquant la théorie des champs proches d'Irwin, K_C peut être déterminée. La deuxième technique, l'AFM à résonance de contact (CR-AFM), permet d'estimer les propriétés élastiques en mesurant le changement de fréquence de résonance du levier lorsque la pointe de l'AFM est en contact avec l'échantillon. La dernière technique, la microscopie à déplacement électrochimique (ESM), consiste à mesurer l'amplitude de vibration du levier pendant qu'une excitation électrique alternative (AC) est appliquée entre la pointe et l'échantillon. Cette vibration est causée par un mécanisme qui dépend de la concentration d'ions lithium dans le matériau. C'est pourquoi lorsqu'une impulsion de courant continu (DC) est appliquée avant la mesure, une relaxation du signal peut être observée car l'impulsion a localement changé la concentration d'ions lithium. Cette expérience s'appelle la *spectroscopie temporelle*. D_{Li} pourrait ainsi être estimé car la vitesse de relaxation dépend de la diffusivité. Une déformation de Vegard a été premièrement proposée pour expliquer le signal mais cela semble dorénavant improbable car une excitation de 200 à 400 kHz provoquerait un déplacement indétectable.

Les objectifs du travail sont listés en partie II. La méthode d'Ulm sera modifiée et d'autres méthodes comme le CR-AFM seront proposées afin de quantifier le module d'élasticité de $LiMn_2O_4$. De nouveaux instruments seront suggérés pour mesurer K_C. Enfin, une modélisation numérique sera développée afin de rendre l'ESM quantitatif.

La préparation des échantillons ainsi que les procédures expérimentales sont décrites dans la partie III. Des échantillons de cathodes de $LiMn_2O_4$ issues de batteries commerciales cyclées et non cyclées sont noyés dans une matrice de résine d'époxy puis préparés en coupes transversales polies. Des échantillons de référence de haute pureté sont préparés de la même manière : des particules de SiO_2, de MnO_2 et de spinelle de $LiMn_2O_4$. Un wafer de $LiMn_2O_4$ avec une orientation cristallographique verticale {111} est synthétisé en interne. Ensuite les différents instruments de mesure utilisés dans ce travail sont mentionnés dans le chapitre 4. Parmi ceux-ci, la mesure topographique du COD a été simulée (voir le chapitre 5).

Dans la partie IV, il est démontré que la méthode de déconvolution statistique d'Ulm ne peut être directement utilisée sur les échantillons car de nombreuses mesures sont erronées, ne correspondant à aucune phase. Une méthode, appelée *nanoindentation sélective*, a donc été développée afin d'obtenir des mesures fiables. Les données de mesures d'indentation sont filtrées par contrôle de leur compatibilité avec les hypothèses de la méthode d'Oliver et Pharr. En premier lieu, la forme quadratique de la courbe de force est examinée. Ensuite, on vérifie si une souplesse structurelle influence la mesure. Enfin, les données filtrées sont déconvoluées et associées à chaque phase du matériau hétérogène à l'aide d'un microscope électronique à balayage (SEM). L'échantillon de référence de SiO_2 a été utilisé pour vérifier la validité de cette méthode de filtrage.

Le modèle numérique de l'ESM, décrit dans la partie V. Le logiciel COMSOL a été utilisé pour décrire le changement dans le champ de concentration d'atomes de lithium dans un corps de $LiMn_2O_4$ pendant et après l'impulsion DC. L'originalité de ce travail est de considérer que D_{Li} n'est pas constant mais dépend de la concentration de lithium.

Plus important, le signal mesuré n'est pas calculé via une déformation de Vegard dans le domaine fréquentiel. Il est en fait considéré comme linéairement proportionnel à la force moyenne électrique de Lorentz, notée $\mathfrak{F}_{AC}$, exercée sur les ions de lithium.

Tous les résultats se trouvent dans la partie VI.

Tout d'abord, les résultats de l'analyse chimique des échantillons sont présentés dans le chapitre 13. Une phase unique de spinelle de $LiMn_2O_4$ a été détectée par diffractométrie de rayons X (XRD). Ce résultat est tempéré par l'analyse dispersive en énergie (EDX) et par la spectroscopie d'émission optique par torche à plasma (ICP-OES) pour lesquelles des particules d'oxyde de cobalt ont été détectées (jusqu'à 2 %) ainsi que d'autres impuretés. Des images par SEM ont aussi établi que ces particules commerciales peuvent être aussi bien des agglomérats poreux de nanoparticules comme de larges monocristaux. Le wafer quant à lui présente une phase principale de spinelle de $LiMn_2O_4$ et une phase secondaire de bixbyite de Mn_2O_3. Seule cette première phase a été caractérisée par les autres méthodes.

Un compte-rendu des résultats de nanoindentation est donné au chapitre 14. Les particules sont fragiles : la surface s'écaille autour de l'indentation et des fissures se développent depuis celle-ci. Des mesures par diffraction d'électrons rétrodiffusés (EBSD) ont révélé que ce phénomène dépend de l'orientation cristalline. Par ailleurs, un module d'élasticité d'environ 90 GPa et une dureté (pointe de Berkovich) de 7 GPa ont été mesurés. C'est en decà de ce qui a été rapporté auparavant pour des couches minces de $LiMn_2O_4$ (Zhu et Zeng (2012)), certainement à cause d'un phénomène d'empilement de matière (*pile-up*) non pris en considération par les chercheurs et surestimant ainsi la mesure. De plus, nos échantillons ont une pureté moindre ce qui pourrait les rendre moins rigides. Le module de Young et la dureté augmentent de plus de 10 % pour des concentrations plus faibles de lithium. Ce phénomène pourrait avoir pour origine la rigidité plus grande des liaisons Mn—O lorsque la valence du métal de transition augmente. La valence moyenne de Mn augmente depuis +3,5 pour $LiMn_2O_4$ jusqu'à +4 pour $\lambda{-}MnO_2$. Une exception a été trouvée pour le spécimen originaire d'une cellule chargée à 25 %: la dureté était bien en-dessous (6,5 GPa), ce qui pourrait indiquer une phase moins dure de $LiMn_2O_4$ non stœchiométrique. La spectroscopie Raman, combinée au CR-AFM, a révélé que des particules voisines peuvent avoir une concentration de lithium différente, par conséquent une rigidité différente en accord avec les résultats de nanoindentation. Le CR-AFM a aussi été utilisé sur l'échantillon de référence de poudre de $LiMn_2O_4$ et il a été démontré que ce spinelle a une élasticité isotrope, tout du moins selon la limite de détection du système. Une utilisation quantitative de ce même instrument s'est révélée infructueuse.

Une valeur de 0,23 $MPa{\cdot}m^{1/2}$ a été mesurée pour la ténacité à la fracture du wafer par l'application d'une technique traditionnelle qui consiste à mesurer la longueur des cracks provoqués par indentation. Cette méthode n'a pas pu être utilisée sur les autres échantillons car la configuration des fissures est inhabituelle. A la place, la mesure du COD a été utilisée. Une K_C d'environ 0,9 MPa·m$^{1/2}$ a été mesurée pour les particules commerciales et d'environ 0,8 MPa·m$^{1/2}$ pour le wafer. A l'aide de l'EBSD, il a été déterminé que les fissures dans le wafer se propagent toujours dans la direction cristalline $<$121$>$. Elles ouvrent des plans {101} juste sous la surface puis dévient de 30 à 40° après environ 100 nm. Ces mesures sont données au chapitre 15.

Les mesures par ESM ainsi que les résultats du modèle numérique sont donnés dans le chapitre 16. Il a été montré que le signal expérimental est similaire à $\mathfrak{F}_{AC}$. Un D_{Li} dépendant de la concentration de Li peut expliquer la forme assymétrique des boucles d'hystérésis. En utilisant un D_{Li} constant, il a été établi que la relaxation de $\mathfrak{F}_{AC}$ pendant une mesure de spectroscopie temporelle a la forme d'une loi mathématique de type $(at+1)^{1/p}$. p ne dépend que légèrement des paramètres du modèle. En revanche, a est très dépendant du coefficient de diffusion et du rayon de contact entre la pointe d'AFM et la surface de l'échantillon, R_{tip}. a est linéairement proportionnel à $D_{\mathrm{Li}}^{1/2}/R_{\mathrm{tip}}$. Expérimentalement, le processus de relaxation du signal d'ESM est beaucoup plus lent pour l'échantillon issu d'une batterie cyclée que pour ceux issus de nouvelles batteries. Autrement, aucune différence significative n'a été détectée pour différents états de charge des batteries non cyclées.

La partie VII traite des discussions des différents résultats.

Une critique de la déconvolution statistique d'Ulm est discutée dans le chapitre 17. En effet, Pavel Trtik et al. (2009) considèrent que des pics artificiels dans la distribution (c-à-d associés à aucune phase) ne peuvent être évités quand un matériau hétérogène est indenté. Une réponse est donnée par Ulm et Vandamme (2010) qui prouvent que c'est la configuration tridimensionnelle de leur modèle qui est responsable de ces pics et que ce n'est pas systématique. Dans notre cas, des pics artificiels ont été toutefois détectés. Cependant, la méthode de *nanoindentation sélective* a pu les filtrer. Mais de très nombreuses mesures doivent être effectuées afin d'atteindre un nombre statistiquement significatif. Dans ce même chapitre, il est dit que le CR-AFM est un ajout utile à la nanoindentation car il permet de faire des cartes qualitatives de l'élasticité de la surface en quelques minutes et avec une précision nanométrique. Mais contrairement à la technique d'indentation, le CR-AFM ne permet pas une mesure *quantitative* aussi facile et fiable. Enfin les mesures de K_C par l'application de la théorie des champs proches d'Irwin sont reconsidérées. Les topographies simulées ainsi que des topographies réelles de fissures ont été soumises à neuf analystes. Il leur a été demandé d'estimer le COD de chacune. Des K_{IC} et K_{IIIC} similaires ont été calculées, démontrant que l'interprétation de l'utilisateur n'a qu'un impact limité. Cependant, la méthode surestime de beaucoup la valeur de la ténacité car une des conditions d'Irwin ne semble pas être remplie. En effet, les surfaces des cracks ne sont pas libres de traction à cause d'un stress en tension résiduel provoqué par la déformation plastique de l'indentation. Cela explique l'écart entre les deux valeurs mesurées pour le wafer. Une méthode développée par Sebastiani et al. (2014) est proposée comme meilleure alternative. Ils trouvent un

K_C plus probable de 0,3 MPa·m$^{1/2}$.

L'origine du signal de l'ESM est traitée au chapitre 18. Il y est suggéré que d'autres couplages électromécaniques que la déformation de Vegard, comme l'électrostriction ou la flexoélectricité, devraient être considérés. De plus, le champ électrique alternatif pourrait hypothétiquement intéragir avec les métaux de transition plutôt qu'avec les ions lithium.

La tendance du module d'élasticité et de la dureté à monter pour des concentrations plus grandes de lithium est comparée aux données trouvées dans la littérature pour d'autres matériaux similaires dans le chapitre 19. En général, des liaisons inter-atomiques plus longues mènent à un matériau moins rigide, que ce soit par l'augmentation ou la diminution de concentration de lithium. Ensuite la ténacité à la fracture est comparée à celle de $LiCoO_2$. Elle est plus haute pour les particules immaculées: 1 MPa·m$^{1/2}$. Dès le premier cycle électrochimique, elle baisse jusqu'à une valeur proche de celle trouvée ici pour le $LiMn_2O_4$: 0,25 MPa·m$^{1/2}$.

A la fin de l'ouvrage, une conclusion succincte résume les résultats les plus importants pour les personnes travaillant à la modélisation numérique des électrodes. Elle donne également un apercu de la fiabilité des différentes techniques utilisées pour la caractérisation de matériaux électrochimiques.

List of publications and conferences

publications

As first author

- **Amanieu, HY; Rosato, D; Sebastiani, M; Massimi, F; Lupascu, DC (2014)**: *Mechanical property measurements of heterogeneous materials by selective nanoindentation: Application to LiMn2O4 cathode.* In: Mater. Sci. Eng. A, 593:92–102
- **Amanieu, HY; Aramfard, M; Rosato, D; Batista, L; Rabe, U; Lupascu, DC (2015a)**: *Mechanical properties of commercial Mn2O4 cathode under different States of Charge.* In: Acta Materialia, 89(0):153–162. doi:10.1016/j.actamat.2015.01.074
- **Amanieu, HY; Thai, HN; Luchking, SY; Rosato, D; Lupascu, DC; Keip, MA; Schröder, J; Kholkin, AL (aug 2015c)**: *Electrochemical strain microscopy time spectroscopy: Model and experiment on LiMn2O4.* In: J. Appl. Phys., 118(5):055101. doi:10.1063/1.4927747
- **Amanieu, HY; Sebastiani, M; Mughal, MZ; Rosato, D; Lupascu, DC (2015b)**: *Fracture properties of LiMn2O4 cathode at the microscale.* to be submitted, 2015b

As co-author

- **Luchkin,SY;Amanieu,HY;Rosato,D;Kholkin,AL(dec2014)**: *Li distribution in graphite anodes: A Kelvin Probe Force Microscopy approach.* In:Journal of Power Sources,268:887–894.
  doi:10.1016/j.jpowsour.2014.06.143

Conferences

Oral presentations

- **Amanieu, Hugues-Yanis; Rosato, daniele; Aramfard, Mohammad; Batista, Leonard; Rabe, Ute**: *Nanomechanics of Battery composites: From nanoindentation to AFM*. Presented at: Materials Science Engineering 2014; Sept 23–25, 2014; Darmstadt, Germany.

- **Amanieu, Hugues-Yanis; Thai, Huy; Luchkin, Sergey; Rosato, Daniele; Schröder, Jörg; Kholkin, Andrei**: *Electrochemical Strain Microscopy Time Spectroscopy: Model and Experiment on $LiMn_2O_4$*. Presented at: 2015 Materials Research Society Spring Meeting; April 6–10, 2015; San Francisco, CA, USA.

Poster presentations

- **Amanieu, Hugues-Yanis**: *Micro- and nano-mechanics of lithium-ion battery materials*. Presented at: Nanomotion meeting; August 26, 2013; Prague, Czech Republic.

- **Amanieu, Hugues-Yanis; Rosato, Daniele; Sebastiani, Marco**: *Mechanical property measurements of heterogeneous materials by selective nanoindentation: application to battery composites.*. Presented at: Nanomechanical Testing in Materials Research and Development IV; October 6–11, 2013; Albufeira, Portugal.

Hugues-Yanis AMANIEU
French citizen, male, 27
1 rue du Ruisseau Bleu
67100 Strasbourg, France
email: hy.amanieu@uni-due.de
LinkedIn: de.linkedin.com/in/hyamanieu

ENGINEER
Materials science

Mechanics, electrochemistry
OO programming, Characterisation

Education

2012→2015 **Doctorate degree (Dr.-Ing.)**, candidate
Duisburg-Essen University, Essen (Germany)

Topic: “nanomechanics of lithium-ion battery electrodes”

2006→2011 **Master's degree in Physics Engineering (M.Sc., Diplôme d'ingénieur)**
graduation Sept 2011 INSA, French 5-year engineering school, Toulouse (France)
Materials science, instrumentation, solid state physics, project management

2005→2006 **First year of Business & Management**, IUT GEA, Toulouse (France)

2005 **High school graduation**, Lycée de l'Edit, Rousillon (France)

Specialization in mathematics, baccalauréat with merit

Work Experience

2012→2015 **R&D ENGINEER** – Robert Bosch GmbH, Stuttgart (Germany)

Materials analyst within a team aiming at simulating devices. Developing methods and models to extract properties of materials used in batteries.
Reference upon request: Dr. Daniele Rosato (project leader)

02→08/2011 **R&D engineer** – internship, Philips Research, Eindhoven (Netherlands)

7 months Life-cycle performance of lithium-ion battery cells for automotive application.
Reference upon request: Dr. Jiang Zhou

Personal skills

Languages English: proficient user (TOEFL iBT:109/120; TOEIC: 980/990)
German: proficient user (B2, C1)

Techniques Expert: indentation, scanning probe microscopy, SEM, battery testing
Intermediate: XRD, wet labs, glove box, thin film techniques

IT Expert: Matlab, data manipulation, office software, LaTeX
Intermediate: Python, LabVIEW, CVI, Basic

Management PhD project: project management, student supervision, knowledge transfert
Theater club head: 5-person team, 50 actors, 600 sold tickets

Interests

Intercultural experience: travelling, couchsurfing.org project, language learning.
Surfing, theatre playing, music, e-sport, energy and sustainable development.

Statutory Declaration

The statutory declaration needs to be in German, so the following excerpt is in German:

Eidesstattliche Versicherung

Ich versichere an Eides statt durch meine Unterschrift, dass ich die vorstehende Arbeit selbständig und ohne fremde Hilfe angefertigt und alle Stellen, die ich wörtlich oder annährend wörtlich aus Veröffentlichungen entnommen habe, als solche kenntlich gemacht habe, mich auch keiner anderen als der angegebenen Literatur oder sonstiger Hilfsmittel bedient habe. Die Arbeit hat in dieser oder ähnlicher Form noch keiner anderen Prüfungsbehörde vorgelegen. Dem Promotionsverfahren gehen keinerlei andere Promotionsverfahren voraus.

Essen, 6. November 2015
Ort, Datum

Unterschrift